# SOLUTION STRATEGIES FOR NONLINEAR MULTISCALE MULTIPATCH PROBLEMS WITH APPLICATION TO ANALYSIS OF LOCAL SINGULARITIES

by

**Yaxiong Chen**

**A Dissertation**

*Submitted to the Faculty of Purdue University*

*In Partial Fulfillment of the Requirements for the degree of*

**Doctor of Philosophy**

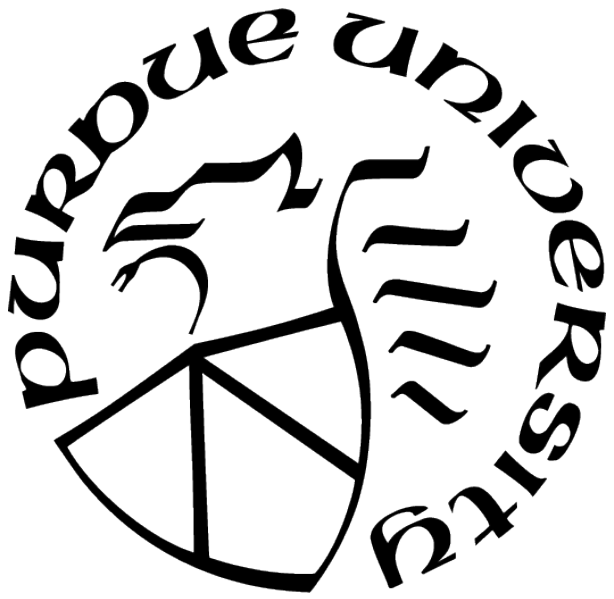


School of Mechanical Engineering

West Lafayette, Indiana

August 2021

# THE PURDUE UNIVERSITY GRADUATE SCHOOL
# STATEMENT OF COMMITTEE APPROVAL

**Dr. Ganesh Subbarayan, Chair**

School of Mechanical Engineering

**Dr. Marcial Gonzalez**

School of Mechanical Engineering

**Dr. Rodrigo Salgado**

School of Civil Engineering

**Dr. Arun Prakash**

School of Civil Engineering

**Approved by:**

Dr. Nicole Key

To my family

for their unconditional support and love

# ACKNOWLEDGMENTS

It is a milestone in my life to finish my PhD dissertation. When looking back for the past four years at School of Mechanical Engineering, I am thankful to all who have appeared in my life and made me a better individual. I feel extremely privileged to have the chance to work with my advisor, Professor Ganesh Subbarayan. When I lost funding at school of civil engineering and was going to pack to go back home, it was him who gave a chance to continue pursuing my dream. During my PhD study, there are many moments I could feel his consideration to students. I still remember how he took notes for me during the individual meeting. I also remember how we discussed on my research until late night, even though he has to get up 4:00 in the morning. His unwaivering patience, insightful thoughts and profound knowledge and artful teaching skills will always inspire me. I owe my deep gratitude to his enlightened guidance in all respects.

I want to sincerely thank my esteemed committee members: Prof. Marcial Gonzalez, Prof. Rodrigo Salgado and Prof. Arun Prakash for their constructive suggestions and advices.

I am also grateful to the financial support from Semiconductor Research Corporation and Purdue University. I have also been benefited from the internship at Intel during the summer 2020. I am thankful to their support and meaningful discussion on maximum entropy fracture model. I deeply appreciate the support from Torsten Hauck and Sandeep Shantaram at NXP semiconductors during the time when I wrote my thesis.

I want to acknowledge the group members for the unforgettable time we spent in the lab. I would like to thank lab-alumni – Tao Song, Kritika Upreti for their help and support during my early days in the lab. I am thankful to lab-alumni – Chun-Pei Chen for our productive collaboration, Pavan Vaitheeswaran for his insightful discussion , Travis Dale and Yuvraj Singh for their readiness to help. I am thankful to the lab mates: Huanyu Liao, Sudarsan Prasad, Sai Sanjit Ganti, Sukshitha Achar, Chetan S Jois, David Halbrook and Colin Greene, for the valuable time we spent together in the HiDAC group.

I would like to thank my friends: Fei Tao and Chen Ma for their constant encouragement and support which made my life much more cheerful at West Lafayette, especially thanks

for their accompany during the boring days of the unprecedented pandemic. I would like to express my heartfelt gratitude to my parents. They have shown their unconditional supports and unwavering love since I was a child. They know how to respect my choice and how to inspire me to pursue my dream. I left home to study in another city when I was 15, and since then I stayed away from them for most of the time. They can only show their concern by phone, but I know how sincere the love is.

# TABLE OF CONTENTS


LIST OF TABLES . . . . . 11

LIST OF FIGURES . . . . . 12

ABSTRACT . . . . . 18

1 INTRODUCTION . . . . . 20

1.1 Literature Review . . . . . 22

1.1.1 Boundary Condition Application in IGA . . . . . 22

1.1.2 Smooth Coupling of Incompatible Subdomains with Extraordinary vertex . . . . . 23

1.1.3 Modeling Corner Singularities and Interface Crack . . . . . 25

1.1.4 Domain Decomposition Method . . . . . 27

1.2 Gaps in Existing Literature . . . . . 29

1.3 Research Objectives . . . . . 30

1.4 Outline . . . . . 30

2 ANALYSIS OF PLASTIC RATCHETING-INDUCED FRACTURE IN SEMICONDUCTOR DEVICES . . . . . 31

2.1 Introduction . . . . . 31

2.2 Background: Analytical Model for Plastic Ratcheting Induced Passivation Cracking . . . . . 33

2.3 Asymptotic Analysis of Metal Line-Passivation Corner Singularity . . . . . 35

2.4 Finite Element Model of BEOL Structure . . . . . 40

2.4.1 Model Configuration . . . . . 40

2.5 Mechanastic understanding of failure in BEOL . . . . . 43

2.5.1 Unreversed Shear Direction . . . . . 43

2.5.2 Ratcheting-Induced Stress Accumulation . . . . . 45

2.5.3 Influence of Metal Line Width . . . . . 45

2.6 Structure improvement . . . . . 47

2.7 Summary . . . 49

3 NON-INTRUSIVE TWO-WAY COUPLING MODEL . . . 51
3.1 Overview Methodology for Iterative Two-Way Coupling . . . 52
3.2 Interface Data Transfer between Sub-Domains with Mismatched Mesh . . . 53
3.2.1 Governing Equations . . . 54
3.2.2 Variational Principles for Interfaces . . . 54
Global Lagrange Multiplier Method . . . 54
Local Lagrangian Multiplier Method . . . 56
3.2.3 Derivation of Local-Global Displacement and Force Projection Matrix 58
Global Lagrange Multiplier method . . . 58
Local Lagrange Multiplier Method . . . 60
3.2.4 Comments on GLM and LLM . . . 63
3.3 Iterative Solution to Interfacial Unknowns . . . 63
3.3.1 Algorithm for Iterative Solution . . . 65
3.3.2 Step Length Determination: Bisection Method . . . 66
3.4 Acceleration Technique and Non-intrusive implementation . . . 67
3.4.1 Symmetric Rank One Update . . . 69
3.4.2 BFGS Update . . . 69
3.4.3 Non-Intrusive Implementation . . . 69
3.5 Numerical Examples . . . 70
3.5.1 L-Shaped Domain . . . 70
3.5.2 Fracture Propagation using XFEM . . . 73
3.5.3 Plastic ratcheting in BEOL . . . 77
3.5.4 Ductile fracture in solder joint using Maximum Entropy Fracture Model 79
3.5.5 Two-way Coupling through mixed computational platform: Copper Bump shear . . . 84
3.6 Summary . . . 88

4 IMMERSED ISOGEOMETRIC ANALYSIS WITH DIRECT BOUNDARY CONDITION IMPOSITION . . . 90

4.1 Immersed B-rep Analysis using Enriched . . . 90
4.2 Boundary Condition Application . . . 92
4.2.1 Enriched Isogeometric analysis . . . 93
4.2.2 Boundary Conditions as Enrichments . . . 95
4.2.3 Dirichlet Boundary Conditions . . . 97
4.2.4 Neumann Boundary Conditions . . . 99
4.2.5 Illustration with a One-Dimensional Example . . . 100
4.2.6 Patch Test . . . 102
4.3 Algebraic Level Sets for Distance Measures And Point Classification . . . 105
4.4 Numerical Examples . . . 108
4.4.1 Plate with a Single Hole . . . 108
4.4.2 Plate with Multiple Holes . . . 111
4.4.3 Curved T-structure . . . 112
4.4.4 Loaded wheel . . . 113
4.5 Summary . . . 114

5 PARAMETRIC STITCHING FOR SMOOTH COUPLING OF SUB-DOMAINS . 116
5.1 Methodology for Smooth Field Coupling . . . 116
5.1.1 Construction of Enriched Field Appoximations . . . 117
5.1.2 Construction of Hierarchically Enriched Approximations . . . 119
5.1.3 Continuity Conditions for Enriched Field Approximations . . . 121
Continuity Across a Stitching Edge Connecting Two Patches . . . 122
Continuity Across Blending Edges within a Patch . . . 123
5.2 P-Stitching Formulation for Elasto-Static Problems . . . 126
5.2.1 Discretization for Blending of Two Patches . . . 128
5.2.2 Discretization for Hierarchical Blending of Multiple Patches . . . 129
5.3 Patch Tests . . . 131
5.3.1 Two-Patch Domains . . . 132
5.3.2 Generalization to Patches with Curved Edges . . . 133
5.3.3 Three- and Four-Patch Domains . . . 137

5.3.4 Multi-Patch Domains with Extraordinary Vertices . . . 138
5.4 Boundary Condition Application . . . 140
5.4.1 Neumann Boundary Conditions . . . 143
5.4.2 Dirichlet Boundary Conditions . . . 144
5.5 Numerical Examples . . . 145
5.5.1 Bi-quadratic Geometry Representation . . . 145
5.5.2 Quadratically Loaded Patch . . . 147
5.5.3 Timoshenko Beam . . . 150
5.5.4 L-shaped Domain . . . 151
5.6 Summary . . . 153

6 ENRICHED ISOGEOMETRIC ANALYSIS FOR CORNER SINGULARITIES . . 155
6.1 Isogeometric Enrichments for Singular Fields . . . 155
6.2 Stress analysis for homogeneous sharp corner . . . 160
6.3 Stress Analysis of Bi-Material Corner with Two Bonded Interfaces . . . 165
6.4 Stress analysis for interface crack . . . 169
6.5 Numerical example: Iteraitve Global-local Analysis on BEOL Structure . . . 177
6.6 Summary . . . 180

7 CLOSURE . . . 181
7.1 Summary and Novel Contributions . . . 181
7.2 Recommendationa for Future Work . . . 183
7.2.1 Non-Intrusive Coupling Algorithm on Multiple Geometrically Identical Sub-Structures using Machine Learning . . . 183
7.2.2 Complex Solution for Arbitrary Wedge Angle Corners using EIGA . . 184
7.2.3 Unified Failure Mechanism and Crack Propagation Simulation . . . 184

REFERENCES . . . 186

A MULTI-SCALE ANALYSIS OF PACKAGE AND SOLDER JOINT FRACTURE SIMULATION . . . 202
A.1 The Maximum Entropy Fracture Model . . . 202

A.2 Numerical Implementation . . . . . 204
A.3 Mesh Dependence Mitigation . . . . . 205
A.4 Extrapolation to accelerate . . . . . 209

# LIST OF TABLES


2.1 The calculated strengths of singularities obtained through asymptotic analysis at the six corners of the BEOL structure for room temperature. . . . . 39

2.2 Elastic and thermophysical properties of die attach material. . . . . 41

2.3 Elastic and thermophysical properties of mold compound. . . . . 41

2.4 Temperature independent properties of other materials. . . . . 42

2.5 Relative shear rigidity $\bar{E}\bar{t}\bar{\alpha}$ at different temperatures. . . . . 44

2.6 Properties of Polymer at room temperature. . . . . 49

3.1 Elastic properties of die attach material. . . . . 78

3.2 Elastic properties of mold compound. . . . . 78

3.3 Temperature independent properties of other materials. . . . . 78

3.4 properties of materials . . . . . 83

3.5 properties of materials . . . . . 86

6.1 Coefficients of angular function associated with bi-material corner with bonded interface obtained through asymptotic analysis. . . . . 168

A.1 Properties of materials. . . . . 208

# LIST OF FIGURES


1.1 (a) crack at sharp corner in copper/low-$\kappa$ dual damascene integrated structures[1], [2], (b) Elamination in device layers of a die induced by dicing [3] (c) Delamination of chip pad from encapsulating epoxy resin[4]. . . . . 21

2.1 Schematic of film cracking induced by thermal cycling. . . . . 31

2.2 Observations of ratcheting-induced passivation cracking. Images adapted from [86]–[88]. . . . . 32

2.3 A schematic illustration of the stress state in the film . . . . . 33

2.4 The Bree diagram for an elastic and perfectly plastic film [90] . . . . . 34

2.5 A schematic illustration of the BEOL structure showing susceptible corners. . . 36

2.6 The material sets constituting the six different corners identified in the BEOL structure. . . . . 39

2.7 Cross Section of a 3D package model. Inserted figure shows the region enclosing the BOEL structure that was analyzed in the local model . . . . . 40

2.8 Thermal loading history. . . . . 42

2.9 Finite element discretization of the simplified two-dimensional model. . . . . 43

2.10 Local deformation in passivation (20 times amplified). . . . . 43

2.11 Schematic illustration of shear stress existing at mold compound-BEOL and Si-BEOL interfaces. . . . . 44

2.12 Contours of accumulated plastic strain during different cycles in the aluminum line. 46

2.13 Accumulated shear plastic strain vs. number of cycles on the upper right corner of the aluminum metal line. . . . . 46

2.14 Principal stress and deformation in the passivation corner. . . . . 47

2.15 Evolution of the first principal stress against the number of cycles (a) in the TEOS films, and (b) in the silicon nitride films. . . . . 48

2.16 Corner opening of different metal width at -65°C in the first cycle (displacement 50 times amplified) . . . . . 48

2.17 2D package model with inserted polymer layer . . . . . 49

2.18 Principal Stress the silicon nitride films with different thickness of polymer layer 50

3.1 Problem overview: iterative two-way coupling global-local. model . . . . . 52

3.2 Connection for non-matched mesh interface by LLM . . . . . 61

3.3 Dicretization of (a) global and local model (b) refined full model . . . . . 71

3.4 Flow of data transfer during iterative solution. . . . . 72

3.5 Von Mises Stress in the local region (a) Initial guess (global-local solution) (b) final solution (iterative two-way coupling) (c)reference solution (refined full model). 73

3.6 Convergence of residual force . . . . . 73

3.7 Test case for crack propagation using XFEM (a) Boundary conditions (b) Global and local mesh. . . . . 74

3.8 Crack growth simulation: acceleration techniques comparison. (a) Crack spreading: dependence between crack length and convergence (b) Final crack propagation step: residual evolution. . . . . 75

3.9 Comparison of crack propagation. . . . . 76

3.10 Convergence of relative residual by using different step length. . . . . 76

3.11 Cross section of the Package model. Insert figure shows the region enclosing the BEOL structure $\Omega_L$ that was analyzed in the local model. . . . . 77

3.12 Discretization for (a) Global and local model (b) Refined full model . . . . . 79

3.13 Maximum Principal Stress in the Passivation Corner at 150° C (left) and -65°C (right) of (a) One-way global local model (b) Two-way coupling and ?? Refined full model. . . . . 80

3.14 Comparison of principal stress at passivation corner . . . . . 80

3.15 Boundary condition for two-dimensional solder joints under thermal cycling . . . 84

3.16 Dicretization for (a) Global and local model (b) Refined full model . . . . . 84

3.17 Crack propagation at 1001th cycle (left) and 2201th cycle (right) for (a) One-way global local model (b) Two-way coupling and (c) Refined full model. . . . . 85

3.18 Comparison of relative crack length . . . . . 85

3.19 Bump shear: model setup . . . . . 86

3.20 Discretization of (a) Global model in ANSYS and Local model using ABAQUS (b) Refined full model in ABAQUS . . . . . 87

3.21 Displacement field of (a) Global model using ANSYS and (b) Local model using ABAQUS . . . . . 87

3.22 Crack propagation for (a) One-way global local model (b) Two-way coupling and (c) Refined full model. . . . . 88

4.1 Graphical illustration of constructing Enriched Isogeometric approximation . . . 94

4.2 Possible mathematical forms of the weight functions . . . . . 95

4.3 Boundary reparametrization (The subregions of the boundary where Dirichlet or Neumann conditions are applied are extracted and reparametrized so boundary conditions may be directly imposed on the newly generated control points) . . . 98

4.4 A one-dimensional immersed boundary example (a) Case 1: Immersed domain conforming to background discretization (b) Case 2: Immersed domain not conforming to background discretization . . . . . 100

4.5 B-spline basis functions of the background domain . . . . . 101

4.6 Basis functions of the enriched approximations (a) Immersed boundary conforming to the background discretization (b) Immersed boundary not conforming to the background discretization . . . . . 102

4.7 Illustration of boundary condition application (a) Dirichlet condition (b) Neumann condition . . . . . 104

4.8 Convergence study for the Dirichlet condition . . . . . 104

4.9 Convergence study for the Neumann condition . . . . . 105

4.10 Role of algebraic level sets in CAD-CAE integration . . . . . 106

4.11 Procedure to construct algebraic distance field for Bezier curves . . . . . 107

4.12 Procedure to construct algebraic distance field for NURBS curves . . . . . 107

4.13 Procedure to construct signed algebraic level sets . . . . . 107

4.14 CAD-EIGA integration: flow of control during analysis . . . . . 109

4.15 Example 1: Plate with a single hole (a)Problem description (b) Problem domain and boundaries that are enriched (c) Immersed geometry (d) Algebraic distance field (e) Point classification (f) Weight field (g) Von Mises stress . . . . . 110

4.16 Convergence of $\sigma_{22}$ . . . . . 111

4.17 Example 2: Plate with multiple holes (a) Problem description (b)Problem domain and boundaries that are enriched (c)Point classification (d)Von Mises stress . . 112

4.18 Example 3: Curved T-shape (a) Problem description(b)Problem domain and boundaries that are enriched(c)Immersed geometry(d)Point classification(e)Weight field(f)Von Mises stress on deformed shape . . . . . 113

4.19 Example 4: Curved T-shape (a) Problem description(b)Problem domain and boundaries that are enriched(c)Immersed geometry(d)Point classification(e)Weight field(f)Von Mises stress on deformed shape . . . . . 114

5.1 Illustration of non-matching parametric domains. The interfaces are shown separated for clarity, but $\Gamma_e \equiv \Gamma_i$. . . . . 117

5.2 A domain decomposed into multiple patches with pairwise edge enrichments. . . 119

5.3 (a) Weight function of adjacet patches (b) weight function within one patch . . 123

5.4 Problem domain consisting two subdomains that need to be smoothly coupled. . 126

5.5 Integration cell in the parametric space (left) and in Euclidean space (right). In general, the integration cell corresponding to the first non-zero knot-span does not coincide with the edge of the blending region. . . . . 127

5.6 Illustration of Hierarchical Blending . . . . . 130

5.7 (a) Patch test setup and (b) expanded view of the individual subdomains and the coupling interface. . . . . 133

5.8 (a) $u_y$ solution and (b) $\sigma_{yy}$ solution on two-patches with regular edges . . . . . 133

5.9 (a) The relative $L_2$ norm of error in displacement on a two-patch domain with a regular edge (a) The relative energy norm of error on a two-patch domain with a regular edge (c) Illustration of the coarsest mesh used in the study. . . . . 134

5.10 Point projection near regions of high curvature (a) Regularly spaced spatial points project to a narrow range of parametric values (b) Projected points are discontinuous. . . . . 135

5.11 Issue of integration over a cell with a piece-wise function description. . . . . 135

5.12 (a) $u_y$ solution on two-patches with curved edges estimated with 6-point qudrature in the cells, (d) $\sigma_{yy}$ solution estimated with 6-point qudrature in the cells, (a) $u_y$ solution estimated with 21-point qudrature in the cells, and (b) $\sigma_{yy}$ solution estimated with 21-point qudrature in the cells. The grid of knot spans were not overlaid on the displacement contour plots to enable easier reading of the contours. 136

5.13 (a) The relative $L_2$ norm of error in displacement on a two-patch domain with a curved edge (b) Illustration of the coarsest mesh used in the study. . . . . 137

5.14 (a) Three- and four-patch test setup (b) expanded view of the individual subdomains and the coupling interfaces of the four patch domain (c) expanded view of the individual subdomains and the coupling interface of three patch domain. . . 138

5.15 (a) $u_y$ solution on three-patches with orthogonal, straight edges, (b) $\sigma_{yy}$ on the three-patch geometry, (c) $u_y$ on the four-patch geometry with orthogonal straight edges, and (d) $\sigma_{yy}$ solution on the four-patch geometry. . . . . 139

5.16 (a) Relative $L_2$ norm of error in displacement and (b) strain energy for patch tests on a domain with three or four patches coupled along orthogonal, straight edges (c) Illustration of the coarsest mesh of three- and four-patch domains. . . 140

5.17 (a) $u_y$ contours on the three-patch geometry with curved edges, (b) $\sigma_{yy}$ on the three-patches, (c) $u_y$ solution on the four-patch geometry with curved edges, and (d) $\sigma_{yy}$ solution on the four-patch geometry. The grid of knot spans were not overlaid on the displacement contour plots to enable easier reading of the contours. 141

5.18 (a) Relative $L_2$ norm of error in displacement and (b) The coarsest mesh used in the patch test. . . . . 142

5.19 (a) Fifteen patch NURBS geometry with extraordinary vertices (b) edge enrichments and vertex enrichments used to build the approximation (c) $u_y$ solution and (d) $\sigma_{yy}$ solution. . . . . 142

5.20 Enrichment of a patch by two edges joined at a vertex. Edges joined at an (a) acute angle (b) obtuse angle . . . . . 143

5.21 Illustration of the application of the boundary conditions. . . . . 143

5.22 Modified basis functions on the boundary of the geometry illustrated in Section 5.4. 144

5.23 Solution to $f(x, y) = y^2$(a) geometry - the color contours represent the function values (b) error distribution. The fit was accurate to within machine precision. . 147

5.24 Solution to $f(x, y) = -(x^2 - x)(y^2 - y + 1)$ (a) geometry - the color contours represent the function values (b) error distribution on coarser discretization (c) error distribution reduces with finer discretization. . . . . 148

5.25 Deformation of quadratically loaded domain (a) without vertex enrichment (b) with vertex enrichment . . . . . 149

5.26 Deformation of interfaces (a) in Figure 5.25a without vertex enrichment (b) in Figure 5.25b with vertex enrichment. . . . . 150

5.27 (a) Dimensions, boundary conditions, and (a) NURBS discretization of Timoshenko beam. . . . . 151

5.28 (a) Vertical displacements $u_y$ and (b) its relative error $u_y/|u_{max}|$ in the Timoshenko beam using three patches . . . . . 152

5.29 (a) Geometry and boundary condition (b) NURBS descretization (c) FEM mesh in ABAQUS . . . . . 152

5.30 Simulation result: $u_y$ obtained by (a) the present method (b) ABAQUS; $\sigma_{xx}$ obtained by (c) the present method (d) ABAQUS; $\sigma_{yy}$ obtained by (e) the present method (f) ABAQUS . . . . . 153

6.1 Illustration of conversion from local polar coordinates to global cartesian coordinate 157

6.2 Sharp corner with opening angle $2\beta$ in polar coordinates ($r$,$\theta$). . . . . 162

6.3 Notched plate subject to mode I load . . . . . 165

6.4 Von-Mises stress distribution in the plate with V-shaped Notch . . . . . 165

6.5 Convergence of generalized stress intensity factor for V-shaped notch. . . . . 166

6.6 Sharp corner with opening angle $2\beta$ in polar coordinate ($r$,$\theta$) . . . . . 167

6.7 Boundary condtions on the structure with bi-material corner. . . . . 169

6.8 Von-Mises stress distribution near the bi-material corner. . . . . 169

6.9 Convergence of generalized stress intensity factor for bi-material corner with bonded interface. . . . 170
6.10 Bi-material corner with one bonded interface . . . 170
6.11 Illustration of enrichment for bi-material problem. . . . 175
6.12 Boundary condition on the structure containing an interfacial crack. . . . 176
6.13 Von Mises Stress around the interface crack. . . . 177
6.14 Convergence of generalized stress intensity factor for interface crack. . . . 177
6.15 Corner singularity: model setup. . . . 178
6.16 FE-IGA coupled analysis (a) Nodal force at the $1^{st}$ iteration (b) Nodal force at the $20^{th}$ iteration(c) Convergence of relative residual (d) Maximum principal stress distribution in the local model. . . . 179
6.17 Convergence of the generalized stress intensity factors obtained directly using the EIGA procedure. . . . 180
A.1 Illustration of process zone and crack surface. . . . 207
A.2 (a) Simplified 2D test setup and (b) Von Mises Stress Distribution (Deformation 50 times amplified). . . . 208
A.3 Comparison of crack propagation without mitigation. . . . 209
A.4 Comparison of crack propagation with different mesh sizes. . . . 210
A.5 Comparison of relative crack length with different mesh sizes. . . . 211
A.6 Comparison of crack propagation with different acceleration time step. . . . 211

# ABSTRACT

Many Engineering structures, including electronic component assemblies, are inherently multi-scale in nature. These structures often experience complex local nonlinear behavior such as plasticity, damage or fracture. These local behaviors eventually lead to the failure at the macro length scale. Connecting the behavior across the length scales to develop an understanding of the failure mechanism is important for developing reliable products.

To solve multi-scale problems in which the critical region is much smaller than the entire structure, an iterative solution approach based on domain decomposition techniques is proposed. Two independent models are constructed to model the global and local substructures respectively. The unbalanced force at the interface is iteratively reduced to ensure force equilibrium of the overall structure in the final solution. The approach is non-intrusive since only nodal values on the interface are transferred between the global and local models. Solution acceleration using SR1 and BFGS updates is also demonstrated. Equally importantly, the two updates are applied in a non-intrusive manner, meaning that the technique is implemented without needing access to the codes using which the sub-domains are analyzed. Code- and mesh-agnostic solutions for problems with local nonlinear material behavior or local crack growth are demonstrated. Analysis in which the global and local models are solved using two *different* commercial codes is also demonstrated.

Engineering analysis using numerical models are helpful in providing insight into the connection between the structure, loading history, behavior and failure. Specifically, Isogeometric analysis (IGA) is advantageous for engineering problems with evolving geometry compared to the traditional finite element method (FEM). IGA carries out analysis by building behavioral approximations isoparametrically on the geometrical model (commonly NURBS) and is thus a promising approach to integrating Computer-Aided Design (CAD) with Computer-Aided Engineering (CAE).

In enriched isogeometric Analysis (EIGA), the solution is enriched with known behavior on lower dimensional geometrical features such as crack tips or interfaces. In the present research, enriched field approximation techniques are developed for the application of bound-

ary conditions, coupling patches with non-matching discretizations and for modeling singular stresses in the structure.

The first problem solution discussed is to apply Dirichlet and Neumann boundary conditions on boundary representation (B-rep) CAD models immersed in an underlying domain of regular grid points. The boundary conditions are applied on the degrees of freedom of the lower dimensional B-rep part directly. The solution approach for the immersed analysis uses signed algebraic level sets constructed from the B-rep surfaces to blend the enriched field with the underlying field. The algebraic level sets provide a surrogate for distance, are non-iteratively (or algebraically) computed and allow implicit Boolean compositions.

The methodology is also applied to couple solution approximations of decomposed patches by smoothly blending incompatible geometries to an arbitrary degree of smoothness. A parametrically described frame or interface is introduced to "stitch" the adjacent patches. A hierarchical blending procedure is then developed to stitch multiple unstructured patches including those with T-junctions or extraordinary vertices.

Finally, using the EIGA technique, a computational method for analyzing general multi-material sharp corners that enables accurate estimations of the generalized stress intensity factors is proposed. Explicitly modeled geometries of material junctions, crack tips and deboned interfaces are isogeometrically and hierarchically enriched to construct approximations with the known local behavior. specifically, a vertex enrichment is used to approximate the asymptotic field near the re-entrant corner or crack tip, Heaviside function is used to approximate the discontinuous crack face and the parametric smooth stitching technique is used to approximate the behavior across material interface. The developed method allows direct extraction of generalized stress intensity factors without needing a posteriori evaluation of path independent integrals for decisions on crack propagation. The numerical implementation is validated through analysis of a bi-material corner, interface crack and growth of an inclined crack in a homogeneous solid. The developed procedure demonstrates rapid convergence to the solution stress intensity factors with relatively fewer degrees of freedom, even with uniformly coarse discretizations.

# 1. INTRODUCTION

Local nonlinear behaviors (e.g., fracture, plasticity) are a critical concern for the reliability of engineering structures. These behaviors usually occur at micro scale, but finally leads to the failure of the whole structure. For example,The back end of line (BEOL) in semiconductor device, is susceptible to cracking. It is consisted of multiple layered material including dieletrics, metal lines and over-coating passivation layer. The reliability of the device relies on the structural integrity. However, during the manufacturing process or usage, different types of local nonlinear behavior are often observed: singular stress at the re-entrant corner, delamination of multi-layered structure, crack propagating and so on (Figure 1.1). To evaluate and minimize the risk of failure, one needs to understand how severe stress concentrates and how non-linearity evolves. Due to the complexity of the structure, an accurate and efficient numeral tool is necessary to implement the analysis.

A common approach to model this kind of phenomenon is to use the classical finite element method (FEM) with a dense mesh at the local region. However, single-scale solution to a structure with refined mesh is computationally expensive when the behavior is nonlinear, even if the nonlinearity is confined to a local region. One method to reduce the computational cost is global-local modeling (or submodeing). Global-local modeling applies computed global solution as boundary condition on the refined local model. However, this method has a significant challenge - lack of two-way communication between the global model and local model. In other words, it ignores the effect of local stress evolution on the global structure and thus leads to inaccuracy in prediction of stress state or crack path. A multi-scale model that allows data transfer between different models will enable not only efficient analysis but can also improve the accuracy of nonlinear simulation at the local scale.

In general, any finite element solution is hampered by the need to generate the mesh when geometries evolve as CAD and CAE methods are poorly integrated at the present time. Currently, most CAD system use Non-Uniform Rational B-Spline (NURBS) representations while CAE commonly employs Lagrangian interpolations that are central to finite element analysis. The idea to apply identical representations in both CAD and CAE can narrow the

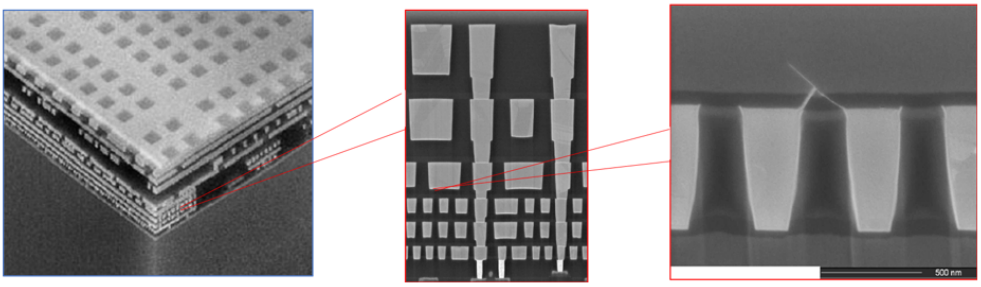

(a)

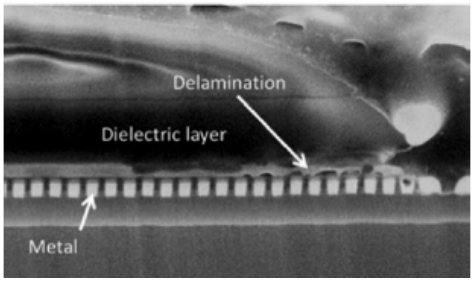


(b)

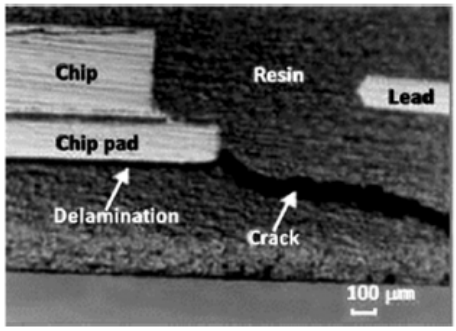


(c)

**Figure 1.1.** (a) crack at sharp corner in copper/low-$\kappa$ dual damascene integrated structures[1], [2], (b) Elamination in device layers of a die induced by dicing [3] (c) Delamination of chip pad from encapsulating epoxy resin[4].

gap between design and analysis[5], [6]. The use of such approximation is now referred to as Isogeometric Analysis (IGA)[7].

The early IGA research was largely concerned with a single volumetric patch. But, most current CAD modelers generate not a volumetric representation, but a boundary presentation (B-rep). To make the model analysis suitable, it is necessary to convert the B-rep into a volumetric NURBS model. This volumetric (or trivariate) NURBS is also a volumetric discretization, and therefore vitiates the original intention of IGA. Converting the the B-rep model into an analysis ready form is a key issue in current IGA research. One solution is the so-called Immersed Boundary Method, in which the B-rep model is immersed into a regular grid of NURBS background mesh. In the Immersed Boundary Method, applying boundary conditions is a critical challenge.

In the B-rep solid modeling, it is difficult to represent a complex geometry with single NURBS patch. B-rep CAD models generated by commercial CAD systems contain uncou-

pled NURBS patches and are therefore not suitable for analysis directly. It is necessary to couple adjacent patches in order to implement further analysis. $C^0$ smoothness across the interface between adjacent patches is a trivial task. However, It is challenging to realize $C^1$ or higher smoothness across a shared edge of patches, which is desirable in both design and analysis.

Another is to capture the accurate local field at multi-material corner and crack tip. Due to the stress singularity at the sharp corner, large amounts of degrees of freedom are required in the model for stress analysis if using the conventional FEM. As an alternative approach, the local feature can be enriched with a priori knowledge using the Partition of Unity Finite Element Method (PUFEM)[8]. The PUFEM theory is the foundation of the Generalized Finite Element Method (GFEM)[9] as well as the eXtended Finite Element Method (XFEM)[10]. The idea of enrichment can be also applied on general sharp corners and wedges as long as the there exists a priori known form to approximate the local field. To evaluate the risk of failure, a posteriori evaluation of path independent integrals is often needed to extract generalized stress intensity factors (SIFs) from the simulation result. Such tedious task can be avoided if the SIFs are included in the solution directly.

## 1.1 Literature Review

### 1.1.1 Boundary Condition Application in IGA

In the original description of isogeometric analysis [7], the essential boundary conditions were directly applied to the control variables. This approach is referred as direct imposition of Dirichlet boundary conditions. A direct application of boundary conditions on control points is reasonable if control points coincide with points of application of the essential boundary condition on the domain.

In the immersed boundary method, the essential boundary conditions are often applied using a weak form, in which the integral of the displacement constraint on the boundary is set to zero. That is, the constraint is enforced in an averaged sense than on each point on the boundary. The weak form constraint is most commonly enforced using Lagrange multipliers [11]. However, the use of Lagrange multipliers to enforce the constraint may cause the

solution matrix system to become ill-conditioned. The alternatives to Lagrange multipliers, namely the penalty method [12] and Nitsche's method [13] require the selection of a scalar parameter, but that value of the parameter is typically model-dependent. In the penalty method, the selected parameter must be large enough to ensure the accurate enforcement of the essential boundary conditions, while too large a value leads to ill-conditioned system of equations. In comparison, Nitsche's method does not suffer from ill-conditioning, however, an empirical stabilization parameter is needed, so the implementation of Nitsche's method is not as trivial as the Lagrange multiplier method or the penalty method. The choice of the stabilization parameter will depend on the problem at hand. In this study, a new method to apply boundary conditions based on the theory of Enriched Isogeometric Analysis (EIGA) is proposed. In EIGA, the boundaries are treated as lower-dimensional enrichments. Extra degrees of freedom are added to the control points of the boundary. The field approximation on the domain is enriched with an approximation near the enriching boundaries through a blending function. The method also allows the direct application of the boundary condition on the enrichment.

### 1.1.2 Smooth Coupling of Incompatible Subdomains with Extraordinary vertex

Stitching incompatible parametric subdomains is a critical research need in both CAD and CAE. Due to the complexity of geometric models and the need for local refinement to capture complex free-form shapes, it is necessary to use multiple trimmed patches to construct the boundary representation (B-rep) of solid objects [14]. Consequently, trimmed surfaces resulting from commercial CAD systems are rarely compatible or "watertight."

In the CAD community, different new spline techniques are proposed to enable local refinement without losing water-tightness. These approaches include sub-division surfaces that enable the modeling of complex free-form surfaces [15]–[18]. HB-splines [19], T-splines [20], [21], PHT-splines [22], THB-splines [23], LR B-splines [24] and the recently developed U-splines [25]. The ability to perform local refinement allows the use of single patch to represent a geometry that would be otherwise described by multiple incompatible NURBS

patches. Due to the elimination of the need to use multiple patches, geometries represented by these new spline methods naturally achieve watertightness without gaps and overlaps.

The aforementioned alternative spline methods provide an upstream solution that allow seamless integration with downstream CAE operations (see for instance, [26]–[28]). Their utility lies in enabling a single bi-variate or tri-variate spline patch to describe the geometry, which in turn may be used directly for isogeometric analysis. However, such geometries need to be analysis aware [29], [30] or analysis-suitable [31]–[33]. Arguably, new spline technologies would have greater impact if they are compatible with NURBS based B-rep paradigm that is widely prevalent in commercial CAD software at the present time. While direct generation of tri-variate spline subdomains from B-rep CAD models has been recently demonstrated [34] and may hold a potential solution for the future, the coupling of volumetric spline subdomains remains a critical unsolved need at the present time.

Similar to the application of boundary conditions, constraint enforcement strategies can also be applied to couple subdomain discretizations. Penalty formulations, Lagrange multiplier methods [35], [36] as well as Nitsche's method [37] are among the most common approaches. These methods enforce weak coupling of behavioral field values such that compatibility and consistency conditions are satisfied in an average sense along the interface.

In domains assembled using multiple patches, $C^0$ smoothness across the interface between adjacent patches is easily achieved. However, $C^1$ or higher smoothness across a shared edge of patches is desirable during design as well as analysis, but is challenging to achieve. Towards this end, recently, constructing $C^1$ continuous smooth approximation spaces over geometrically complex multi-patch domains has been an important focus in the isogeometric analysis community. An early comparison of such approaches was provided by Nguyen et al. [38]. The approaches are broadly aimed at assuring $C^1$ continuity over the complex domain by utilizing $G^1$ continuity across the patches [39]–[42]. These methods are argued as providing "full approximation power" even at extraordinary vertices, where subdivision methods' convergence rate is reduced. Their relative merits are often discussed in terms of their ability to generate approximations that possess desirable properties such as non-negativity, smoothness, partition of unity as well as local support that NURBS basis functions are known to provide, and therefore are argued as being useful for isogeometric analysis [41], [43].

### 1.1.3 Modeling Corner Singularities and Interface Crack

The simulation of sharp corner problem is a non-trivial task due to the complex stress field near the tip. The traditional FEM needs very fine mesh near the corner to capture the field accurately and thus makes analysis computationally expensive. The difficulty has been discussed in the fracture mechanics literature for a long time and different approaches have been proposed to approximate the singular field more efficiently. Malenk and Bubuska proposed Partition of Unity Finite Element Method (PUFEM)[44] that enables one to enrich the approximation with the known singular behavior. The method was later extended to generalized finite element method (GFEM)[45]. Based on the idea, Dolbow and Moes et al.[10] further developed the technique for fracture problem termed the eXtended Finite element method (XFEM). XFEM and GFEM have also been demonstrated in the context isogeometric analysis. Benson *et al.* and De Luycker *et al.* [46], [47] developed a similar formulation using IGA. Ghorashi *et al.* focused on fracture modeling using a similar formulation and termed the technique as eXtended Isogeometric Analysis (XIGA) [48].

The idea of integrating the asymptotic analytical solution into basis function has also been applied for general problems with corner singularities. There are many theoretical studies that provide the foundation for numerical solution development. Williams[49], [50] was the first one to apply Eigenfunction Expansion Method to solve biharmonic equation by describing the Airy stress function as a product of $r^{\lambda+1}$ and a angular function $f(\theta)$. This method was later extended by Seweryn and Molski [51] by proposing a general equation for displacement. Luo and Subbarayan [52] extended the displacement method to bi-material and multi-material wedges with de-bonded or bonded interfaces. Other relevant theoretical studies can be found in the review of asymptotic analysis on wedge-shaped domain [53]. As a special case for bi-material wedge, interface crack problem has received significant attention over the past a couple of decades. Williams's Eigenfunction Expansion Method [54] was applied to the interface crack problem again to illustrate the complex singularity. He showed that the singular field around the crack tip is composed of square-root singularity and an oscillatory part. Later, Malyshev and Salganik[55] related energy release rate to a complex SIF. Rice and Sih [56] solved the stress field for two typical interface crack problems and

defined the complex SIF. There are also important discussions in the literature on contact zone[57] and oscillatory field[58], [59].

Despite the considerable theoretical understanding, it is still challenging to accurately *compute* the asymptotic stress field for structures with complex geometries. Within the framework of finite element method (FEM), specific singular parametric elements have been developed to approximate singular field near the sharp corner or crack tip[60], [61]. In general, for the bi-material wedge with an arbitrary wedge angle, there is no explicit form of the singular solution. However, the analytical solution for the asymptotic stress may be obtained by solving the eigenvalue and eigenvector problem, which then can be used to enrich the finite element solution. Chen [62] developed an enriched element method, in which the singular field with its oscillatory characteristic was embedded into the basis function at the crack tip. A hybrid finite element analysis was also demonstrated to solve bi-material wedge problems[63], in which both the theoretical solution of stress and displacement were used in the basis function. Yi et al[64] carried out stress analysis on bi-material V-notch using the XFEM framework. Eight or sixteen (denpending on real or complex singularity) branch functions were employed to enrich the nodes surrounding the notch-tip. Chen et al. [65] proposed a general, explicit geometry isogeometric analysis procedure for singular enrichment at bi-material corner.

Another challenge to the analysis of corner singularities is the extraction of the generalized stress intensity factor (SIF). In general, the SIF provide the far-field influence that complements the asymptotic singular stress solution of the form $\sigma(2\pi r)^{1-\lambda}$. Usually, the far-field influence is estimated post analysis, that is, post-processing is needed to extract SIFs. The common method used in FEM to determine the value of SIFs include i. stress and strain correlation, ii, strain energy release rate, iii.virtual crack closure technique[66], and iv. J-integral[67]. For example, in [64], the SIF was evaluated using a conserved integral. To avoid the post processing step of carrying out the contour integration, Liu et al. [68] used stress intensity factors at the crack tip directly as the unknowns in FEA. Similar approach was also implemented by Leung et al. [69], in which the degrees of freedom at the nodes are condensed to unknowns associated with the crack tip in the nonlinear region. This approach was extended to sharp notches with arbitrary opening angle by Treifi et al. [70]. In the

enriched isogeometric analysis technique for multi-material wedges developed by Chen et al [65], the SIFs were directly extracted from the unknowns associated with the bi-material sharp corner.

### 1.1.4 Domain Decomposition Method

In many engineering applications, including in semiconductor chip assemblies, failures in small local features occur due to forces applied far field. Also, many times, the nonlinear material behavior or cracks are confined to local regions. Generally, the accurate modeling of local phenomenon such as singularity at a material corner or crack tip requires refined meshing. However, a single finite element model domain with mesh spanning the local refined region to the larger length scale far field region is computationally prohibitive. Commonly, in engineering practice, these problems are modeled using a global-local (or sub-modeling) strategy. The global-local finite element modeling procedure involves two steps. First, a coarse, quasi-uniform global mesh is constructed to get a coarse (global) solution. Next, sub-domains containing local features of interest such as cracks or other stress raisers are extracted from the global domain and analyzed while applying the global solution as boundary condition on the local domain. A significant challenge in the above global-local modeling strategy is the lack of two-way communication between the global model and the local model. In other words, as the state of stress in the local model evolves due to material non-linearity or crack propagation, the effect of this evolution is not communicated back to the global model. As a result, the state of stress, the crack initiation site/path predicted in the local model is often inaccurate. Alternative, iterative solution approach for these problems exists in the literature [71], [72], but their application is limited to elastic problems, and often requiring the mesh to match at the interface between the sub-domains.

In general, two types of methods have been proposed to improve the global-local procedure. The first one is based on the generalized finite element method (GFEM) [73]. In the classical GFEM framework, apriori known field for lower dimensional features, usually based on an analytical solution, is applied to expand the solution space. With the enrichment of a carefully selected basis function, even a coarse mesh can capture complex local

behavior. When an analytical solution is not readily available for local enrichment, the local approximation is used as an enrichment function for the global problem. This enriched solution method is termed GFEM with global-local enrichment functions ($GFEM^{gl}$) [74], [75]. Numerical and mathematical analysis of the $GFEM^{gl}$ have shown that the solution of $GFEM^{gl}$is as accurate as direct global simulation on a fine scale mesh. However, the above described enrichment technique is generally intrusive since access to the FEM software is needed. This need for access to the source code of the FE software limits the method's wider applicability.

The second type of global-local procedure relies on model coupling, in which the sub-domain coupling is achieved through the Mortar method [76], Langrangian multiplier method [77], or the Nitsche method [78]. In general, these methods also require access to the FE software. To alleviate the requirement for FE code access, a non-intrusive coupling method was proposed by Gendre et al.[79]. Similar to the $GFEM^{gl}$ method, the local solution was used to improve the global solution. But, instead of enriching the global domain, the non-intrusive coupling updates the displacement at the common interface, applied as boundary conditions on the coupled sub-domains. Since the application of the boundary condition does not require access to the source code, the method is easy to implement. As long as the interface nodal value is accessible, the method can be used to couple models constructed by different codes. The non-intrusive coupling technique of Gendre et al. may be regarded as a modification of the non-overlapping domain decomposition method (DDM) [80]–[82].

There are two fundamental issues that must be addressed in any efficient and robust non-intrusive algorithm. The first one is the method to transfer data between two arbitrarily discretized sub-models. In the original work of Gendre et al. [79], only coupling at an interface with a matched mesh was demonstrated. Liu et al. [83] proposed data transfer using radial basis functions (RBF) [84] for non-matching discretizations. Duval et al. [85] described a general interface projection like operator based on the Lagrangian multiplier method. The second issue that must be addressed is global solution correction. At each iteration, unbalanced force or mismatched displacement will be generated at the interface between the coupled sub-domains. Essentially, the objective of the iterations is to reduce to zero the unbalanced force or mismatched displacement. A critical advantage of non-intrusive

coupling is the capability to couple a custom code with commercial software without inner access to either code. As a result, the user can still take advantage of the efficiency and robustness of commercial software to obtain the solution on the sub-domains. The custom code may provide specialized failure modeling in the local region of interest.

## 1.2 Gaps in Existing Literature

Non-intrusive techniques in the literature for global-local analysis are relatively few. Generally, the prior studies have not demonstrated non-intrusive two-way coupling with acceleration of the solution, on domains with mismatched meshes, using commercial finite element codes. The solution presented in this thesis addresses these issues.

Direct application of boundary condition is an issue for mesh free approximation of fields, specifically for the immersed boundary method. Weak imposition may lead to an ill-conditioned matrix system. One goal of the current research is to develop a general methodology for applying boundary conditions for immersed isogemetric analysis, or more generally, for any mesh-free method.

The existing techniques for stitching NURBS patches are similar to boundary application; they enforce the compatibility in a weak sense. Weakly enforcing compatibility condition results in an ill-conditioned system or a need for method-specific parameters. The other solution is to convert the NURBS geometry to new spline types. But this requires assessment of analysis suitability and compibality with the current NURBS-based commercial CAD systems. Clearly, there is a need for a novel technique to couple NURBS patches that have the following characteristics. First, the technique should allow the geometry to be represented in the original spline system, NURBS. Second, the technique should yield a system with an acceptable condition number, yet without the need to determine method-specific parameters.

Another challenge is the modeling of stress singularity at multi-material wedges or corners. The enrichment strategies that currently exist do not provide a solution for arbitrary wedge angles. It is also desired to develop a general and convenient approach to extract the generalized stress intensity factors (SIF) without post-processing.

## 1.3 Research Objectives

The goals of this research are to develop computational strategies for complex engineering structure enabling stitching of non-matching discretizations, corner singularities and fracture. The following topics are studied:

1. Non-intrusive iterative global-local model based on domain decomposition
2. General strategy for applying boundary conditions on immersed boundaries using enrichment
3. Smooth coupling methodology for NURBS patches
4. Unified enriched isogeometric formulation for corner and crack singularity
5. Numerical procedure for local nonlinear analysis on heterogeneous structures

In general, the methodology proposed in the current work would provide more accurate modeling methodology for complex structures containing heterogeneity and critical local features.

## 1.4 Outline

The thesis document is organized as follows. In Chapter 2, the mechanistic failure mechanism for ratcheting induced fracture in BEOL structures is studied by the conventional global-local model. This is to show the effort needed by the traditional method to solve complex engineering problems and propose potential improvements. Chapter 3 describes iterative two way coupling methodology for multi-scale local nonlinear analysis.Chapter 4 proposes a novel way to apply boundary conditions on immersed boundaries using the Enriched Isogemtric Analysis (EIGA). Chapter 5 uses the same enriching strategy for stitching two NURBS patches to an arbitrary degree of smoothness. The parametric stitching method is then extended for multi- patches. Chapter 6 propose a general approach to evaluate the singular stress for bi-material wedges. the work will be summarized in Chapter 7 with discussion of novel contributions and potential future work.

# 2. ANALYSIS OF PLASTIC RATCHETING-INDUCED FRACTURE IN SEMICONDUCTOR DEVICES

Many engineering structures are inherently multi-scale with complex geometry and material heterogeneity. Fracture initiates usually at a micro scale but leads eventually to observable macroscale. One example in semiconductor industry is the Back End of Line (BEOL) structures on silicon chips encased in epoxy mold compounds that are in very wide spread use at the present time. When metal lines plastically deform due to ratcheting, the passivation overcoat accumulates stress at the corner upon temperature cycling and is eventually susceptible to fracture. Since packaging materials' interaction with the silicon die is the cause of the failure, the problem is inherently multiscale in nature requiring bridging from package dimension to BEOL length scale. In this chapter, the mechanistic cause for the stress accumulation is elucidated using the global-local finite element method. It reveals the mechanical problem in such structures as well as the difficulties in modeling such multi-scale structures.

## 2.1 Introduction

One failure mechanism observed in molded packages during accelerated thermal cycling is the cracking of passivation films deposited on the BEOL metal lines. Specifically, cracking occurs in the TEOS film at the die corner after hundreds or thousands of temperature cycles. Figure 2.1 is a schematic of the observed fractures, and Figure 2.2 shows observations of such failure in the literature.

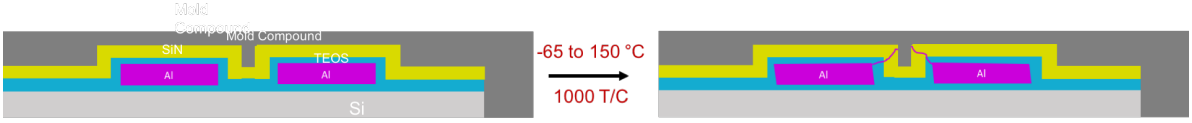


**Figure 2.1.** Schematic of film cracking induced by thermal cycling.

The mechanism for the above described fracture has often been attributed to metal line ratcheting [89]–[91]. The above literature largely relies on qualitative reasoning in proposing

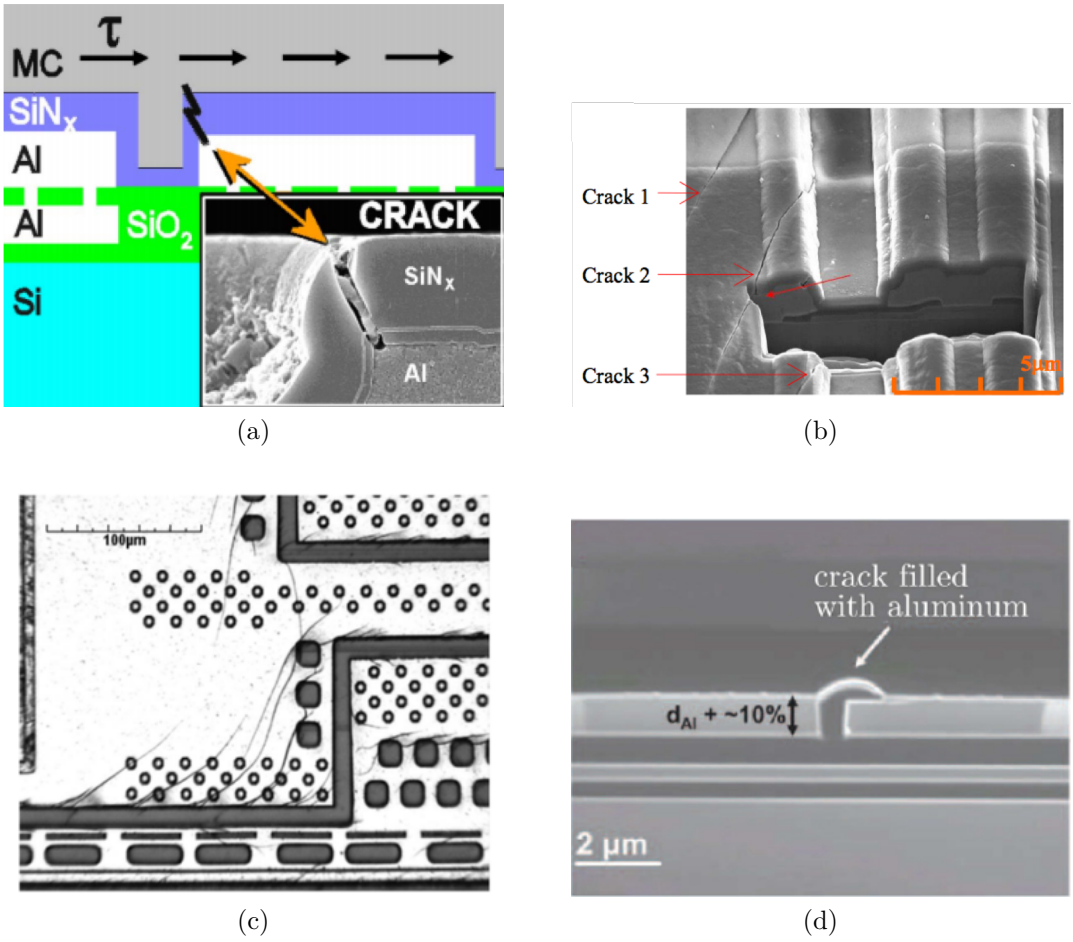


**Figure 2.2.** Observations of ratcheting-induced passivation cracking. Images adapted from [86]–[88].

the failure mechanism, and therefore, questions of why passivation cracks initiate only upon significant thermal cycling and the reason for the path they follow are not fully understood. Thus, the details of the suggested mechanism have not been clearly explained in prior literature through predictive modeling. Numerical models are usually necessary for more detailed understanding of failure phenomenon. Commercial finite element analysis (FEA) software, such as ANSYS®and Abaqus®, have been used extensively to analyze stress in electronic components. However, as the model needs to span length scales from a few micrometer to a few mm to relate failure in BEOL structures due to package causes, computational cost becomes significant. Therefore, multiscale modeling techniques such as the global-local

modeling (also referred as sub-modeling) technique, with coarse global model and fine local model, is popular in modeling microelectronic packages[92]–[94].

## 2.2 Background: Analytical Model for Plastic Ratcheting Induced Passivation Cracking

Ratcheting plastic deformation occurs in devices when under thermal cycling, the metal film monotonically accumulates a small amount of plastic strain with each cycle causing the metal line to "crawl." This metal line plastic deformation then transfers the load to the passivation film causing its fracture. In reference [90], an idealized model was developed for stress accumulation in the passivation film that is briefly reviewed below.

In Figure 2.3, a schematic illustration of the modeled region of the metal line is shown. The film is assumed to experience equi-biaxial stress in the plane and a shear stress on the top surface.

$$\sigma_{11} = \sigma_2 = \sigma, \sigma_{13} = \tau_0 \tag{2.1}$$

$\alpha_f$ and $\alpha_s$ are the thermal expansion coefficients of film and the substrate with $\alpha_f > \alpha_s$.

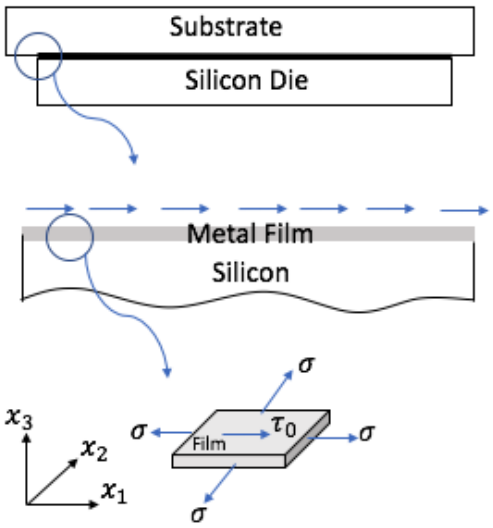


**Figure 2.3.** A schematic illustration of the stress state in the film

Assuming that the material of the line has a constant yield strength, $Y$, a plot of the normalized shear stress and the normalized temperature range may be constructed as shown

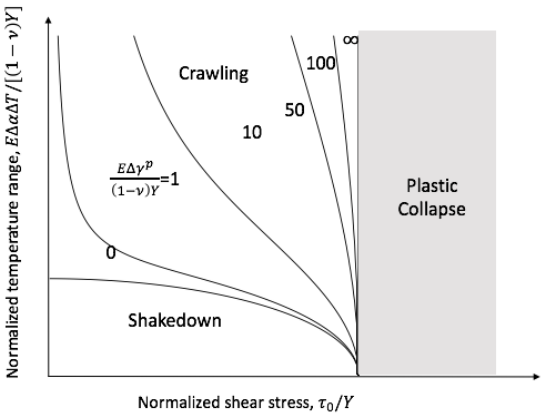


**Figure 2.4.** The Bree diagram for an elastic and perfectly plastic film [90]

in Figure 2.4. Three regimes of deformation are identified in this plot: shake down, ratcheting and plastic collapse.

If $\tau_0/Y < \frac{1}{\sqrt{3}}$ and the temperature range is small enough, the metal only yields in the first cycle and deforms elastically in the subsequent cycles. If $(\tau_0/Y) > (1/\sqrt{3})$, excessive shear stresses cause a plastic collapse.

The film will crawl if it satisfies the following three conditions: (i) the thermal expansion mismatch causes the film to yield (ii) during yielding, the film gains a finite plastic shear strain, as well as a finite plastic in-plane strain and (iii) the plastic shear strain is always in the same direction as the shear stress.

In the crawling (ratcheting) regime in Figure 2.4, at each thermal cycle, over a temperature excursion of $dT$, a small in-plane plastic strain increment is accumulated:

$$d\epsilon^p = -(\alpha_f - \alpha_s)dT - \frac{1-\nu}{E}d\sigma \tag{2.2}$$

Applying the $J_2$ plasticity theory, an increment in plastic shear strain may also be estimated due to the temperature excursion:

$$d\gamma^p = -\frac{6\tau_0}{\sigma}[(\alpha_f - \alpha_s)dT + \frac{1-\nu}{E}d\sigma] \tag{2.3}$$

The accumulation of plastic strain leads to the yielding of the metal film and a change in the stress state of the passivation layer. In their other related work [89], the authors propose that after several thermal cycles, the metal film no longer sustains shear stress due to plastic yielding and that all the shear load is transferred to the passivation film. The earlier model is then updated as follows. Denoting $\sigma_0$ as the magtitute of the normal stress in the passivation film, $W$ as the width of the metal line and $t$ as the thickness of the passivation film, force balance between the plastically yielded metal line and the passivation film yields

$$\sigma_0 = \frac{\tau_0 W}{2t} \tag{2.4}$$

Thus, a large ratio of $W/t$ is suggested to yield a significant increase in normal stress $\sigma_0$ even if the shear stress $\tau_0$ is small. The normal stress in the passivation film is predicted to vary linearly with the position

$$\sigma(x) = -2\sigma_0 x/W \tag{2.5}$$

where $x$ is the distance from the center of the metal line, thus making the corners more susceptible for fracture.

The above described model provides an idealization for metal line plastic ratcheting induced stress accumulation in passivation films. However, a more quantitative explanation is needed for the following reasons: the model does not take into account (i) complex geometry of real devices (ii) complex temperature dependent thermal expansion coefficient and elastic modulus of the mold compound (iii) complex load distribution in the passivation film (iv) metal film-passivation corners that are potentially stress raisers and (v) precise mode of fracture at the corner of the passivation film. Thus, while the idealized model provides some insight to understand ratcheting induced fracture, its applicability for real devices needs verification. In the present paper, detailed numerical models are used to explain the local behavior leading to passivation film fracture.

## 2.3 Asymptotic Analysis of Metal Line-Passivation Corner Singularity

A schematic passivated BEOL structure as shown in Figure 2.5. The interconnect struc-

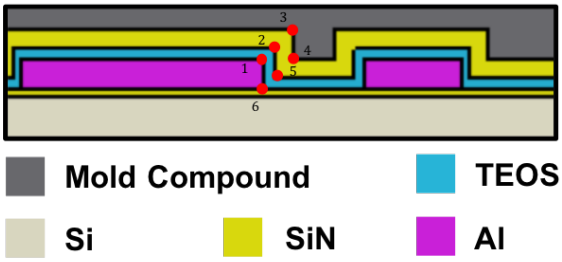


**Figure 2.5.** A schematic illustration of the BEOL structure showing susceptible corners.

ture shown in the figure is complex and contains many interfaces between dissimilar materials and therefore, stress concentration under temperature change is expected. Singular stress fields are known to arise at geometric discontinuities such as interfaces, corners, and free edges. This may lead to failure during fabrication or test. In this section, we examine the nature of stresses at the multimaterial corners, specifically under thermal excursion.

The stress fields at multi-material corners are known to exhibit a singular behavior (for a linear elastic material) that is proportional to $\frac{1}{r^{1-\lambda}}$ [95]–[97], where $r$ is the distance from the interface corner, and $1-\lambda$ is the strength of the singularity. The stresses near the edge of an interface can be described asymptotically as:

$$\sigma_{\mathrm{ij}} = \sum_{n=1}^{N} \frac{K_n}{r^{1-\lambda_n}} f_{\mathrm{ij}n(\theta)} + \sigma_{\mathrm{ij}0}(\theta) \tag{2.6}$$

The above stress field arises from the general solution of the displacement in the neighborhood of multi-material wedge [52]:

$$\begin{aligned} u_r = r_{\mathrm{i}}^{\lambda}[&A_{\mathrm{i}} cos(1+\lambda)\theta_{\mathrm{i}} + B_{\mathrm{i}} sin(1+\lambda)\theta_{\mathrm{i}} \\ &+ C_{\mathrm{i}} cos(1-\lambda)\theta_{\mathrm{i}} + D_{\mathrm{i}} sin(1-\lambda)\theta_{\mathrm{i}}], \end{aligned} \tag{2.7}$$

$$\begin{aligned} u_\theta = r_{\mathrm{i}}^{\lambda}[&B_{\mathrm{i}}(\kappa_{\mathrm{i}}-\lambda) cos(1+\lambda)\theta_{\mathrm{i}} - A_{\mathrm{i}}(\kappa_{\mathrm{i}}-\lambda) sin(1+\lambda)\theta_{\mathrm{i}} \\ &+ D_{\mathrm{i}}(\kappa_{\mathrm{i}}+\lambda) cos(1-\lambda)\theta_{\mathrm{i}} \\ &- C_{\mathrm{i}}(\kappa_{\mathrm{i}}+\lambda) sin(1-\lambda)\theta_{\mathrm{i}}]/(\kappa_{\mathrm{i}}-\lambda) \end{aligned} \tag{2.8}$$

where, the subscript i refers to the different materials present in the wedge. In general, each loading mode is associated with a strength of singularity in a multi-material wedge. The coefficients of the angular function are the eigenvectors associated with each order of singularity. To accurately capture the stress near the interface, it is necessary to obtain the order of the singularity $\lambda$. While it is known [52] that the singularity is determined by the elastic moduli of the materials that form the corner, it is not clear whether thermal strains influence the corner singularity. To study this question, the methodology described by Luo and Subbarayan [52] is expanded here by applying the asymptotic analysis procedure to an isotropic thermoelastic material described by the generalized Hooke's law:

$$\sigma_{\mathrm{ij}} = 2\mu\epsilon_{\mathrm{ij}} + [\Lambda\epsilon_{kk} - (3\Lambda + 2\mu)\alpha\Delta T]\delta_{\mathrm{ij}} \tag{2.9}$$

We begin the analysis by considering the strain displacement relation, constitutive behavior and equilibrium equation in polar coordinates (Eqs. (2.10) to (2.12)):

$$\begin{aligned} \epsilon_{r_{\mathrm{i}}} &= \frac{\partial u_{r_{\mathrm{i}}}}{\partial r_{\mathrm{i}}} \\ \epsilon_{\theta_{\mathrm{i}}} &= \frac{1}{r_{\mathrm{i}}}\frac{\partial u_{r_{\mathrm{i}}}}{\partial r_{\mathrm{i}}} + \frac{u_{r_{\mathrm{i}}}}{r_{\mathrm{i}}} \\ \epsilon_{r_{\mathrm{i}}} &= \frac{\partial u_{r_{\mathrm{i}}}}{\partial r_{\mathrm{i}}} \end{aligned} \tag{2.10}$$

$$\begin{aligned} \sigma_{r_{\mathrm{i}}} &= \Lambda_{\mathrm{i}}(\epsilon_{r_{\mathrm{i}}} + \epsilon_{\theta_{\mathrm{i}}}) + 2\mu_{\mathrm{i}}\epsilon_{r_{\mathrm{i}}} - (3\Lambda_{\mathrm{i}} + 2\mu_{\mathrm{i}})\alpha_{\mathrm{i}}\Delta T \\ \sigma_{\theta_{\mathrm{i}}} &= \Lambda_{\mathrm{i}}(\epsilon_{r_{\mathrm{i}}} + \epsilon_{\theta_{\mathrm{i}}}) + 2\mu_{\mathrm{i}}\epsilon_{\theta_{\mathrm{i}}} - (3\Lambda_{\mathrm{i}} + 2\mu_{\mathrm{i}})\alpha_{\mathrm{i}}\Delta T \\ \tau_{r\theta_{\mathrm{i}}} &= \mu_{\mathrm{i}}\epsilon_{r\theta_{\mathrm{i}}} \end{aligned} \tag{2.11}$$

$$\frac{\partial \sigma_{r_i}}{\partial r_i} + \frac{1}{r}\frac{\partial \tau_{r\theta_i}}{\partial \theta_i} + \frac{\sigma_{r_i} - \sigma_{\theta_i}}{r_i} = 0 \qquad (2.12)$$
$$\frac{\partial \tau_{r_i}}{\partial r_i} + \frac{1}{r}\frac{\partial \sigma_{\theta_i}}{\partial \theta_i} + 2\frac{\tau_{r\theta_i}}{r_i} = 0$$

Substituting Eq. (2.11) into Eq. (2.12), we notice that the $\alpha_i \Delta T$ term, which is not a function of $r_i$ or $\theta_i$, drops out in the expressions. Thus, the thermal strain has no influence on the corner singularity, and the only source of singularity is the mismatch in elastic modulus between Al metal line and the TEOS passivation layer. Combining the above three sets of equations, the stress equilibrium equations may be written in terms of displacements as follows:

$$(\Lambda_i + 2\mu_i)\frac{\partial}{\partial r_i}\left(\frac{\partial u_{r_i}}{\partial r_i} + \frac{1}{r_i}\frac{\partial u_{\theta_i}}{\partial \theta_i} + \frac{u_{r_i}}{r_i}\right) - \mu_i \frac{\partial}{r_i}\frac{\partial}{\partial \theta_i}\left(\frac{\partial u_{\theta_i}}{\partial r_i} - \frac{1}{r_i}\frac{\partial u_{r_i}}{\partial \theta_i} + \frac{u_{\theta_i}}{r_i}\right) = 0 \qquad (2.13)$$

$$(\Lambda_i + 2\mu_i)\frac{1}{r}\frac{\partial}{\partial \theta_i}\left(\frac{\partial u_{r_i}}{\partial r_i} + \frac{1}{r_i}\frac{\partial u_{\theta_i}}{\partial \theta_i} + \frac{u_{r_i}}{r_i}\right) + \mu_i \frac{\partial}{\partial r_i}\left(\frac{\partial u_{\theta_i}}{\partial r_i} - \frac{1}{r_i}\frac{\partial u_{r_i}}{\partial \theta_i} + \frac{u_{\theta_i}}{r_i}\right) = 0 \qquad (2.14)$$

Assuming now displacement fields of the form:

$$u_{r_i} = r^\lambda f(\theta) u_{\theta_i} = r^\lambda g(\theta) \qquad (2.15)$$

where, $\theta$ is the angle around the corner, the solution given in Eq. (2.7) results. With the appropriate application of symmetric or anti-symmetric boundary conditions (as described in [52]), solution for $\lambda$ and the coefficients $A_i$, $B_i$, $C_i$ and $D_i$ are obtained as the eigen-value/eigenvector pair of the system. The coefficients representing the eigenvector are in general determined to within a constant, which is the stress intensity factor obtained by considering the far-field loading conditions.

There are in total six different geometric corners in the passivated BEOL structure as shown in Figure 2.5. The combinations of materials and associated angles in each wedge are

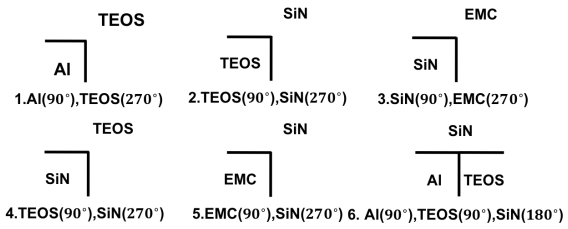


**Figure 2.6.** The material sets constituting the six different corners identified in the BEOL structure.

**Table 2.1**. The calculated strengths of singularities obtained through asymptotic analysis at the six corners of the BEOL structure for room temperature.

| **Corner** | $\lambda_1$ | $\lambda_2$ |
|---|---|---|
| 1 | 0.000 | 0.000 |
| 2 | 0.150 | 0.017 |
| 3 | 0.163 | 0.159 |
| 4 | 0.120 | 0.028 |
| 5 | 0.277 | 0.053 |
| 6 | 0.000 | 0.000 |

illustrated in Figure 2.6. The orders of singularities and their associated angular functions are obtained by solving corresponding eigenvalue problem described in reference [52]. The asymptotic solution to all the singularities at the corners identified in Figure 2.6 are listed in Table 2.1. Material properties used to determine Table 2.1 are based on their value at room temperature. Within the working temperature range of package, only mold compound and die attach are regarded as temperature dependent. It is interesting to note that Corner 1 and Corner 6 do not exhibit singular behavior due to well matched elastic modulus of TEOS and Aluminum. However, as mentioned earlier, cracks are often observed to initiate at point 1 and propagate though the passivation layer. A possible explanation is that when aluminum line begins to plastically yield, the material becomes soft and introduces a stress concentration that was initially not present.

## 2.4 Finite Element Model of BEOL Structure

### 2.4.1 Model Configuration

In packaged components, often, only a small region undergoes plastic behavior while most of the structure behaves elastically. In the nonlinear finite element method that is commonly applied to analyze packages, the whole domain is meshed and solved without any special solution procedure that takes into account regions of plastic behavior. In the nonlinear finite element method that is commonly applied to analyze packages, the whole domain is meshed and solved without any special solution procedure that takes into account regions of plastic behavior. During the nonlinear solution, the finite element solver applies the load in several increments while iterating to convergence using the Newton Raphson method. However, this methodology is computationally expensive for complex geometries, especially when critical regions of nonlinear behavior are much smaller than the structure domain. One way to alleviate this computational expense is to create a smaller sub-domain containing the nonlinearly behaving materials that is meshed much finer than the remainder of the domain that is elastic in behavior. This is called global-local modeling (or submoddeling).

In this section, the global-local model technique is used to explore the mechanism of plastic ratcheting induced crack. The global model is analyzed first, following by a local nonlinear "zoom" centered on the critical zone and driven by global displacement. For simplicity, a plane strain model is used to model a cross-section of the half-package with a single metal line Figure 2.9.

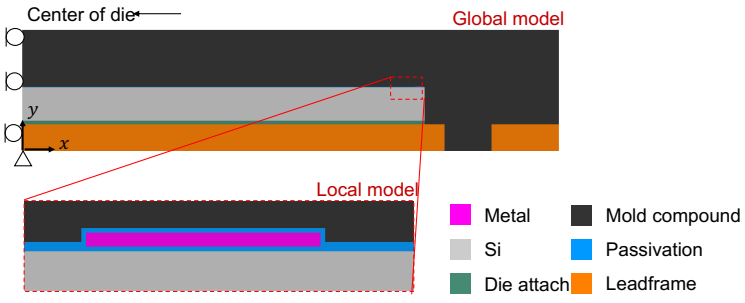


**Figure 2.7.** Cross Section of a 3D package model. Inserted figure shows the region enclosing the BOEL structure that was analyzed in the local model .

Aluminum lines with a thickness of 3 $\mu m$, and widths of 20, 35 and 50 $\mu m$ were modeled. The BEOL structure in the package contains passivation (composed of TEOS and SiN), Al, and epoxy mold compound materials. In the present study, all the materials except the Al line were treated as elastic. The yield strength of 100 MPa was used for Al. The Al metal line's temperature-independent yield strength, elastic modulus and CTE were based on values reported in the literature [87], [98].

As for the cyclic plastic response of aluminum, isotropic hardening model was assumed upon yielding. The mold compound and die attach were modeled as temperature-dependent elastic materials that were strain rate-independent. This assumption was felt to be reasonable, and allowed one to capture the change due to glass transition of the epoxy mold compound under a quasi-static thermal loading. The temperature dependent behavior of mold compound was felt to be critical to the observed behavior, but the material's strain rate dependence was perceived to be not as important owing to the slower response in time relative to the cycling time. The elastic behavior of die attach and mold compound materials was described through three temperature-dependent transition steps as listed in Table 3.1 and Table 3.2, respectively. The mechanical properties of other material used in the model may be found in Table 3.3.

**Table 2.2**. Elastic and thermophysical properties of die attach material.

| Temperature(°C) | $E$ (GPa) | $\nu$ | $\alpha$ (ppm/°C) |
|---|---|---|---|
| -65 | 10 | 0.35 | 50 |
| 75 | 10 | 0.35 | 50 |
| 125 | 0.5 | 0.35 | 100 |
| 260 | 0.5 | 0.35 | 100 |

**Table 2.3**. Elastic and thermophysical properties of mold compound.

| Temperature(°C) | $E$ (GPa) | $\nu$ | $\alpha$ (ppm/°C) |
|---|---|---|---|
| -65 | 30 | 0.35 | 10 |
| 85 | 30 | 0.35 | 10 |
| 115 | 1 | 0.35 | 40 |
| 260 | 1 | 0.35 | 40 |

**Table 2.4**. Temperature independent properties of other materials.

| **Mateiral** | $E$ (GPa) | $\nu$ | $\alpha$ (ppm/°C) |
|---|---|---|---|
| Leadframe | 123 | 0.34 | 17.6 |
| SiN | 160 | 0.25 | 0.69 |
| TEOS | 68 | 0.18 | 0.54 |
| Al | 70 | 0.33 | 23 |
| Si | 131 | 0.28 | 2.61 |

The test structure was assumed stress-free at 175°C, at which temperature the last step of fabrication occurred. Complete thermal cycles of the package from -65°C to 150°C (Figure 2.8) up to five hundred cycles were simulated. Such elaborate simulations were necessary to accurately account for the accumulation of plastic strains in the metal lines due to ratcheting.

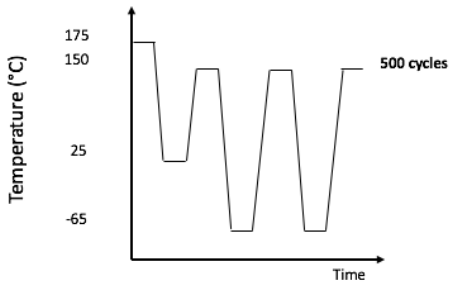


**Figure 2.8.** Thermal loading history.

The global finite element model used to identify the most critical loading mode and to extract displacement was based on commercial tool ABAQUS/Standard&CAE [99]. The model was discretized using plane strain elements since the out of plane deformation was expected to be constrained by the geometry. Figure 2.9 demonstrates the discretizations of the overall package model as well as the submodel at the BEOL level to more accurately characterize the local state of stress. The densities of mesh were carefully selected such that simulation of five hundred thermal cycles is within computational and temporal limits using available resources. Overall, the global model used 11,783 nodes and the submodel used 10,744 nodes. The minimum element size was 1 $\mu m$ and 0.3 $\mu m$ for global model and submodel, respectively.

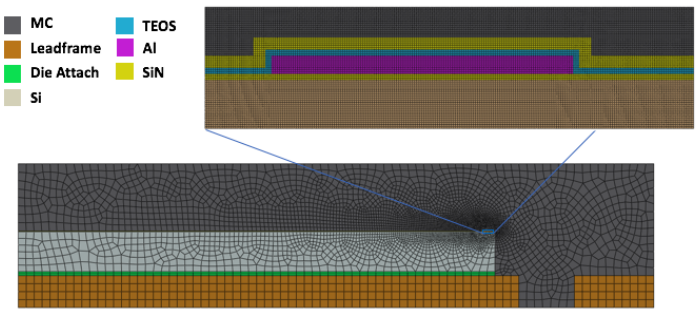


**Figure 2.9.** Finite element discretization of the simplified two-dimensional model.

## 2.5 Mechanastic understanding of failure in BEOL

From the previous section, it is clear that shear of the BEOL structure is the likely cause of cracking in the passivated structures. In this section, further insights from the global-local simulation is discussed to shed light on the mechanism causing the fracture of the passivation layer.

### 2.5.1 Unreversed Shear Direction

During the thermal cycling, it is observed that the shear stresses on the die surface are always directed towards the die center, and *do not reverse direction* (Figure 2.10) when the temperature excursion reverses from cooling to heating.

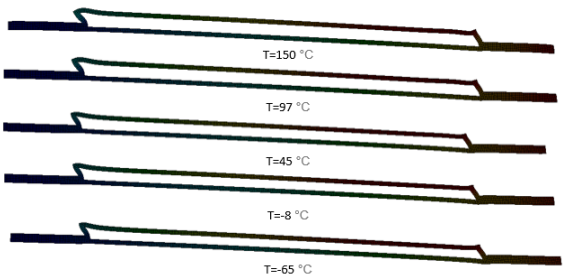


**Figure 2.10.** Local deformation in passivation (20 times amplified).

This can be explained by the fact that the stress-free temperature for the package, at the application of the mold compound, is 175°$C$. During thermal cycling, the temperature varies between 150 °$C$ to -65°$C$. During the whole temperature cycle, stress state in the package

is dominated by the contraction of the die, mold compound and leadframe, which possess significantly larger stiffness compared to the BEOL structure. Considering the thickness $t$, Young's modulus $E$ and thermal expansion coefficient $\alpha$ of the Si, mold compound and the lead frame, let the $\bar{E}\bar{t}\bar{\alpha}$ represent the relative effective shear rigidity when compared to Si. The corresponding value of $\bar{E}\bar{t}\bar{\alpha}$ for the three materials at different temperatures are listed in table 2.5.

**Table 2.5**. Relative shear rigidity $\bar{E}\bar{t}\bar{\alpha}$ at different temperatures.

| | -65°C | 25°C | 150°C |
|---|---|---|---|
| Mold compound | 1.709 | 2.071 | 5.528 |
| Si | 1.000 | 1.000 | 1.000 |
| Leadframe | 4.690 | 4.690 | 4.690 |

The mold compound as well as the leadframe contract more than silicon on account of their larger cofficient of thermal expansion. Thus the top surface of silicon will experience shear towards the die center as will the thin layer of BEOL between silicon and mold compound. The effect of relative difference in shear deformation between mold compound, Si and lead frame is illustrated in Figure 2.11. Since the deformation in the local model is driven by the stiffer mold compound, lead frame and Si interfacing with it, the BEOL structure in the local model experiences the net shear indicated in Figure 2.11.

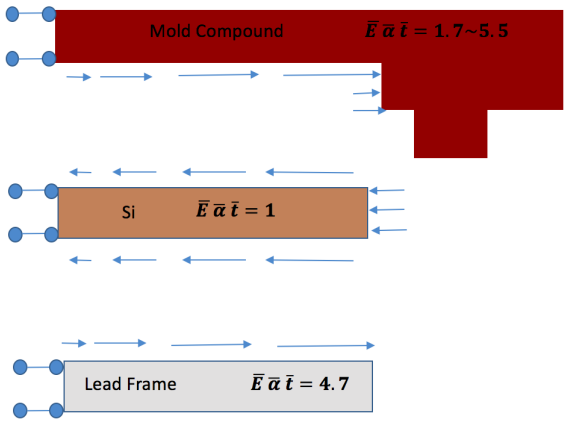


**Figure 2.11.** Schematic illustration of shear stress existing at mold compound-BEOL and Si-BEOL interfaces.

### 2.5.2 Ratcheting-Induced Stress Accumulation

It is clear from the results of the previous section that the BEOL structure is under overall shear stress that does not change direction. If the shear stress exceeds the yield strength of aluminum, the metal will experience shakedown (accumulates plastic strain only in the first cycle and deforms elastically thereafter) or ratcheting (plastic strain accumulates in every cycle). The results of the modeling in the present study show that temperature-dependent expansion of the mold compound as well as the rigidity of the mold compound and the lead frame are critical to the observed failure mechanism. As a result, aluminum metal line experiences ratcheting and accumulates plastic strain during each temperature cycling. Due to the geometrical complexity of the BEOL structure, the stress is not uniform. In Figure 2.12 it is seen that the plastic strain accumulates near the metal line corner after the 50th cycle. Irreversible plastic deformation accumulates in the aluminum line every cycle. Figure 2.13 shows the corresponding accumulation of plastic strain at the metal line corner away from the die center.

The global-local model results show that the shear plastic strain on the upper right corner of metal line increases rapidly in the first several cycles and the increment is smaller (Figure 2.13) during each cycle afterwards. After the first few cycles, all of the metal line yields and begins to gain a constant increment of plastic strain during each cycle. Figure 2.14 shows the principal stress value and direction at the corner of interest. The principal stress contour clearly indicates that the stress direction has the potential to cause opening mode fracture along the 45 degree line. Figure 2.15 shows a steady increase in principal stress as the temperature cycles continue. When the appropriate measure of strength of the brittle passivation layer is exceeded, crack will initiate. Thus, the risk of ratcheting-induced fracture does not occur immediately after fabrication, but increases with cyclic thermal loading.

### 2.5.3 Influence of Metal Line Width

The magnitude of principal stress at the corner of TEOS film is also positively correlated to the width of the aluminum line as shown in Figure 2.15. The stress in the passivation layer builds up at a higher rate when the aluminum line is wider in dimension. This may

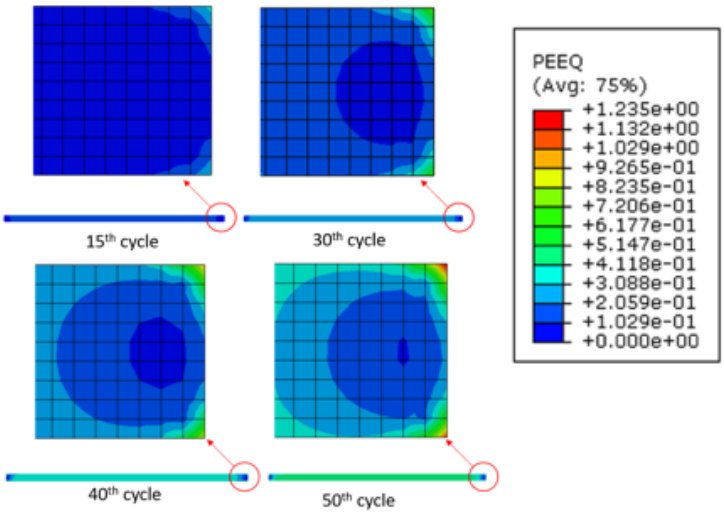


**Figure 2.12.** Contours of accumulated plastic strain during different cycles in the aluminum line.

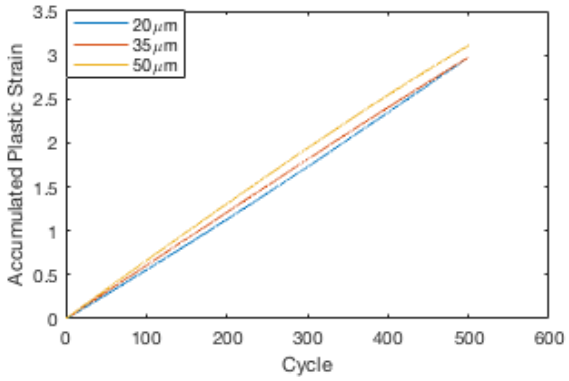


**Figure 2.13.** Accumulated shear plastic strain vs. number of cycles on the upper right corner of the aluminum metal line.

be explained by the fact that metal is softer than other surrounding materials and a wider line causes larger local shear deformation which in turn manifests as higher corner principal stress. As can be seen in Figure 2.16, the initial corner angle is 90 °C. In the first cycle at -65°C, but this angle increases to 91.88°C for a metal line width of 100 $\mu m$. While for metal line width of 20 $\mu m$, the angle is 91.27° after deformation.

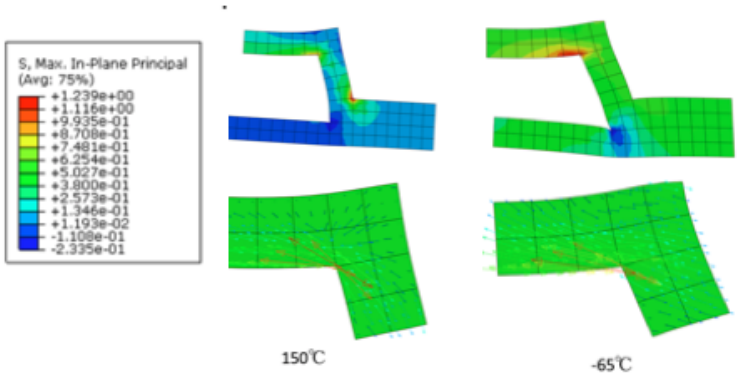


**Figure 2.14.** Principal stress and deformation in the passivation corner.

## 2.6 Structure improvement

Several useful rules for improved design are evident from the present study. First, one should aim to avoid metal layer ratcheting altogether. Under thermal cycling, the metal layer deforms elastically only with in a specific temperature range. If the temperature range exceeds a threshold, ratcheting occurs and stress increases until reaching a steady state. Preventing the failure before reaching the steady state is important

Shear displacement driven by mismatch of CTE between mold compound and silicon is the major source of ratcheting. The difference in CTE between these two materials can be as high as 19 to 38 $\times 10^{-6}$ $^{\circ}C^{-1}$ (Table 3.2 and Table 3.3). Replacing mold compound with other material (e.g., ceramic) which has closer CTE to silicon or higher stiffness may be a potential direction, but the high cost limits its application.

One may also reduce stress concentration in passivation layer. [91] proposes a design for metal layer geometry such that the passivation layer can sustain the steady state. But it is hard to manipulate perforated metal line at such a small scale and of course such modification will influence the electrical properties.

An alternative approach is to adding a polymer layer between mold compound and passivation layer.The property of the polymer is as follow in Table 2.6

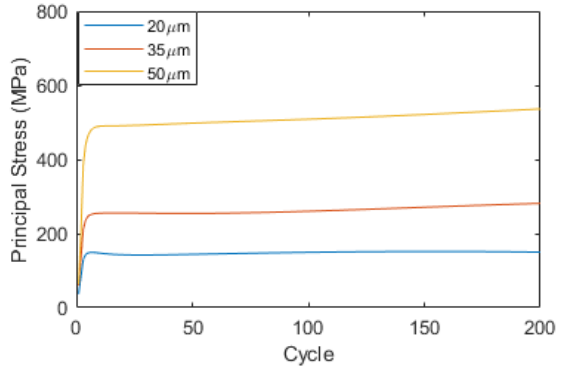


(a)

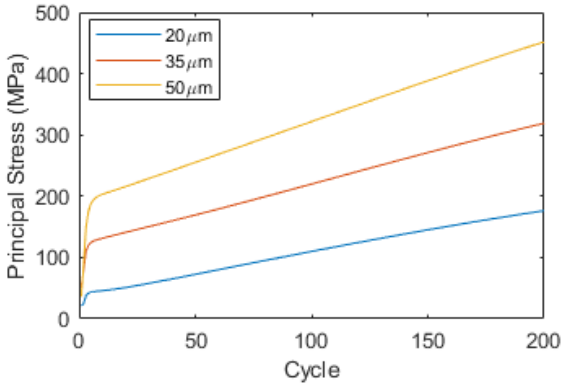


(b)

**Figure 2.15.** Evolution of the first principal stress against the number of cycles (a) in the TEOS films, and (b) in the silicon nitride films.

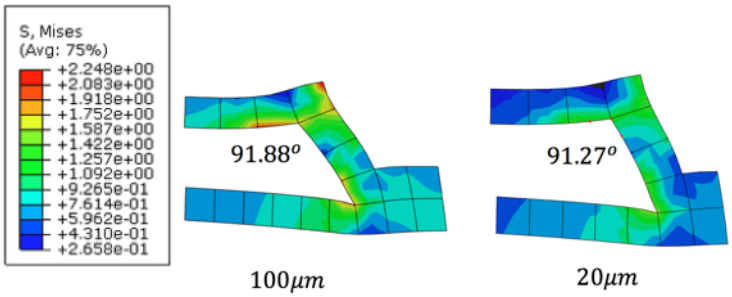


**Figure 2.16.** Corner opening of different metal width at -65°C in the first cycle (displacement 50 times amplified)

The influence of thickness of polymer layer is studied: the thickness of polymer is denoted as $h$, is used to replace mold compound just above the passivation layer(Figure 2.17). The principle stress in the TEOS after

**Table 2.6**. Properties of Polymer at room temperature.

| **Mateiral** | $E$ (GPa) | $\nu$ | $\alpha$ (ppm/°C) | $\sigma_Y$ (MPa) |
|---|---|---|---|---|
| Polymer | 5 | 0.3 | 2.1 | - |

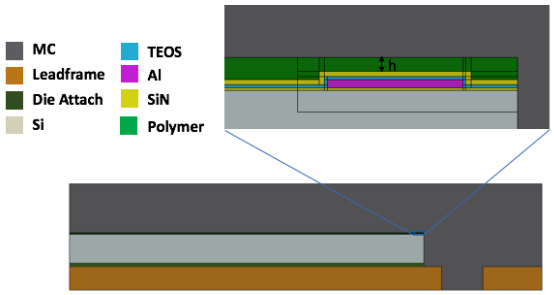


**Figure 2.17.** 2D package model with inserted polymer layer

Figure 2.18 shows the influence of polymer thickness on the principal stress in the TEOS film. The thickness ranges from $2\mu m$ to $10\mu m$. The principal stress with thin polymer layer ($2\mu m$) leads to higher principal stress than that without polymer layer. It may caused by the singular stress at the corner between polymer and mold compound. But with the increase of polymer thickness, the principal stress in TEOS film is decreasing.This is because polymer layer is less thermal sensitive than mold compound and provide a buffer zone to reduce the shear load directly applied on passivation.

## 2.7 Summary

This chapter explored the mechanism of ratcheting induced crack in passivation layer during temperature cycling. The study demonstrates that thermal excursion has no influence on the corner singularity and that mechanical stress concentration at the multi-material junction is not the reason for the observed fractures. Based on the global-local finite element model, it is observed that mismatch of thermal expansion between substrate and silicon causes repeating (non-reversed) shear stress in the BEOL structure. Ratcheting in aluminum line causes plastic strain accumulation and finally results in high corner stress in passivation

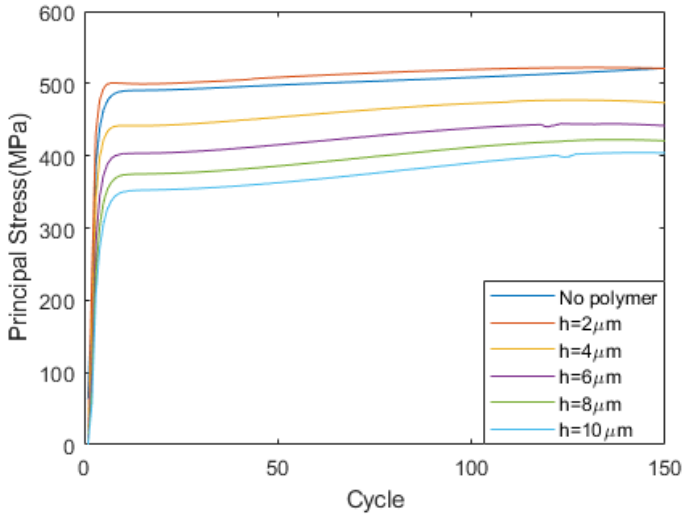


**Figure 2.18.** Principal Stress the silicon nitride films with different thickness of polymer layer

layer. During the entire thermal cycle, shear remains the loading mode most correlated with the observed cracks.

# 3. NON-INTRUSIVE TWO-WAY COUPLING MODEL

Global, coarse mesh and local, refined mesh modeling strategy is a common solution approach for domains spanning many orders in length scale. However, a single finite element model domain with mesh spanning the local refined region to the larger length scale far field region is computationally prohibitive. Commonly, in engineering practice, these problems are modeled using a global-local (or sub-modeling) strategy. A significant challenge in the above global-local modeling strategy is the lack of two-way communication between the global model and the local model. In other words, as the state of stress in the local model evolves due to material non-linearity or crack propagation, the effect of this evolution is not communicated back to the global model. As a result, the state of stress, the crack initiation site/path predicted in the local model is often inaccurate.

In this chapter, a non-intrusive computational strategy for iterative solution to the non-linear behavior in the sub-domains is proposed. This method uses quasi-Newton iterative updates to correct displacements on the interface connecting the different sub-domains until equilibrium is reached. The developed method is suitable for the modular construction of sub-models with non-matching discretizations, and even allows coupling between sub-domains analyzed using different (commercial or custom) codes. A Symmetric Rank 1 update as well as the BFGS update are considered for accelerating the solution convergence. To estimate the residual force on the interface connecting the sub-domains with non-matching discretizations, variational principles with an intermediate framework is proposed to transfer nodal force from one mesh to the other. Both global Lagrangian multiplier (GLM) and local Lagrangian multiplier (LLM) methods are discussed. The iterative global-local coupling strategy is validated on several examples including an L-shaped domain with local non-linearity and a rectangular plate with a propagating crack. Another example illustrating the coupling of domains independently analyzed using commercial finite element codes ANSYS and ABAQUS is next demonstrated. Finally, the method is demonstrated to analyze semiconductor chip assemblies where plastic ratcheting of the interconnect line causes passivation coating fracture, and thermal cycling causes fatigue fracture in solder joints.

## 3.1 Overview Methodology for Iterative Two-Way Coupling

The non-intrusive coupling allows two-way data transfer, that is to say, the local solution is used to correct the global field and in turn it updates the local boundary condition. The core idea of the proposed iterative two-way coupling is as follows:

Consider a global model with purely linear elastic behavior in the domain $\Omega = \Omega_G \cup \Omega_{\tilde{G}}$. Local features such as cracks, inclusions, re-entrant corners are not included in this global model although they may exist in the local refined model. The detailed local model is then built on $\Omega_L$, whose boundary geometry coincides with that of $\Omega_{\tilde{G}}$, namely $\Gamma$. The objective of the method is to replace global solution on $\Omega_{\tilde{G}}$ by the one on local region $\Omega_L$ without changing or modifying the global linear system $\boldsymbol{K}$ on $\Omega$. The final solution obtained by the method is:

$$\boldsymbol{u} = \begin{cases} \boldsymbol{u}_G \;\; in \;\; \Omega_G \\ \boldsymbol{u}_L \;\; in \;\; \Omega_L \end{cases} \tag{3.1}$$

The two models are also discretized independently as illustrated in Figure 3.1. The sub-models can even use approximations other than finite element interpolations, such as iso-geometric approximations or even finite differences, as long as the the field is explicitly represented on the interface.

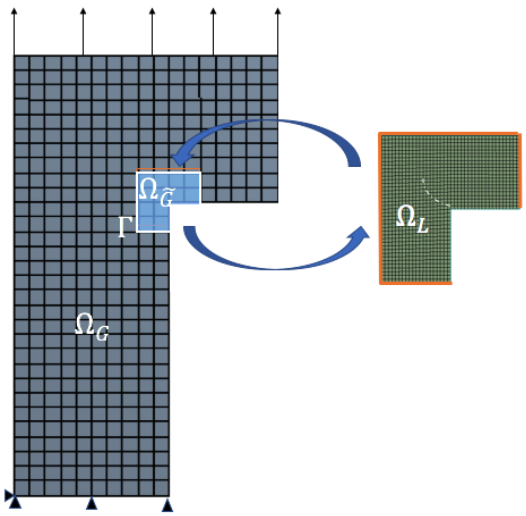


**Figure 3.1.** Problem overview: iterative two-way coupling global-local. model

As can be seen in Figure 3.1, two distinct models corresponding to the two regions $\Omega_G$ and $\Omega_L$ are constructed based on domain decomposition methods (DDM) [80]–[82]. But the two sub-models may differ in interior geometrical details, mesh refinement, as well as the material constitutive behavior. Displacement boundary conditions are iteratively updated on the interface $\Gamma$ between the two models until static equilibrium is achieved. The solution in region $\Omega_{\tilde{G}}$ is not used but is used to update the interface displacement as elaborated later.

In the present study, beginning with an initial guess of a global elastic solution on $\Omega$, the following iterative procedure is applied:

- Local Analysis: Dirichlet boundary conditions corresponding to a guessed displacement solution are applied at the interface to carryout a full nonlinear analysis on the local model.

- Residual Computation: The nodal force at the interface resulting from the analysis of the local model is then mapped to the global mesh to compute the unbalanced force vector at the interface. The iterations will terminate when the unbalanced force is smaller than the chosen convergence criterion.

- Global Correction: The unbalanced force will be applied on the global model as an additional load. Since the global model is linear elastic in behavior, all degrees of freedom except for those of the interface are "condensed" out to reduce the stiffness matrix. The displacement corresponding to the unbalanced force is then used to update the guessed displacement. The process is repeated until convergence.

In the next section, the theory behind the proposed method and its detailed implementation is discussed.

### 3.2 Interface Data Transfer between Sub-Domains with Mismatched Mesh

We begin with the governing equations for the domain, which is followed by a discussion of variational principles for decomposed domains. The discretized solution strategy is then discussed.

### 3.2.1 Governing Equations

As stated earlier, the domain $\Omega$ is divided in to a local sub-domain $\Omega_L$ that may behave nonlinearly or possess a crack, and a global, elastically behaving domain $\Omega_G$. The problem to be solved is as follows:

$$\nabla \cdot \sigma + \bar{f} = 0 \quad in \quad \Omega \tag{3.2}$$

$$u = u_d \quad on \quad \Gamma_d \tag{3.3}$$

$$\sigma \cdot \boldsymbol{n} = \bar{t} \quad on \quad \Gamma_n \tag{3.4}$$

$$\tag{3.5}$$

where $\bar{f}$, $u_d$ and $\bar{t}$ are body force, prescribed displacement and surface traction with $\boldsymbol{n}$ being the outward normal direction. $\Gamma_d$ and $\Gamma_n$ are boundaries over which Dirichlet and Neumann conditions are applied.

### 3.2.2 Variational Principles for Interfaces

Two variational principles are derived in this section for coupling *nonlinearly* behaving sub-domains. Following the terminology common in mechanics (see for instance, Park and Felippa [100]), the first of the two methods is termed the Global Lagrange Multiplier (GLM) method, while the second is termed the Local Lagrange Multiplier (LLM) method.

#### Global Lagrange Multiplier Method

To link the two domains, Lagrange multipliers can be introduced on the interface between the two domains, leading to the Global Lagrange Multiplier method ([100]), or the Mortar method [101]. The multiplier may be physically interpreted as traction on the interface computed on the boundary of either the domain $\Omega_{\tilde{G}}$ or the domain $\Omega_L$ with their shared boundary $\Gamma$.

Posing virtual work statements on the global domain, we get the following:

$$\delta I^G(u^G) = \int_{\Omega^G} \sigma^G : \delta\varepsilon^G d\Omega - \int_{\Omega^G} \bar{f}^G \delta u^G d\Omega - \int_{\partial\Omega^G} \bar{t}^G \delta u^G dS \tag{3.6}$$

where, $\bar{f}^G$ and $\bar{t}^G$ are body force and external traction respectively. Similarly, the virtual work on the local domain yields:

$$\delta I^L(u^L) = \int_{\Omega^L} \sigma^L : \delta\varepsilon^L d\Omega - \int_{\Omega^L} \bar{f}^L \delta u^L d\Omega - \int_{\partial\Omega^L} \bar{t}^L \delta u^L dS \tag{3.7}$$

Introducing Lagrangian multiplier $\lambda$ on the interface of global and local models, the variation of the constraint on the displacements at the interface $\Gamma$ yields:

$$\delta I^\Gamma(\lambda) = \int_\Gamma \lambda(\delta u^G - \delta u^L) d\Gamma + \int_\Gamma \delta\lambda(u^G - u^L) d\Gamma \tag{3.8}$$

where, the sign on $\lambda$ is arbitrary. The variational principle that must be satisfied for the coupled problem is

$$\delta I \equiv \delta I^G + \delta I^L + \delta I^\Gamma = 0 \tag{3.9}$$

Thus, integrating by parts and applying the divergence theorem on the global and local domains, the governing condition becomes:

$$\begin{aligned}
\delta I(u^G, u^L, \lambda) = 0 = &- \int_{\Omega^G} (\nabla \cdot \sigma^G + \bar{f}^G) \delta u^G d\Omega + \int_{\partial\Omega^G \setminus \Gamma} \left(\sigma^G \cdot \boldsymbol{n} - \bar{t}^G\right) \delta u^G d\partial\Omega \\
&- \int_{\Omega^L} (\nabla \cdot \sigma^L + \bar{f}^L) \delta u^L d\Omega + \int_{\partial\Omega^L \setminus \Gamma} \left(\sigma^L \cdot \boldsymbol{n} - \bar{t}^L\right) \delta u^L d\partial\Omega \\
&+ \int_\Gamma (u^G - u^L) \delta\lambda d\Gamma \\
&+ \int_\Gamma (\sigma^G \cdot \boldsymbol{n} + \lambda) \delta u^G d\Gamma + \int_\Gamma (\sigma^L \cdot \boldsymbol{n} - \lambda) \delta u^L d\Gamma
\end{aligned} \tag{3.10}$$

At the coupling interface $\Gamma$, if displacements are imposed, then $\delta u^G = \delta u^L = 0$ on $\Gamma$. It is important to note here that integrals on $\Gamma$ involve fields from both sub-domains requiring them to be carried out on one of the sub-domains with fields communicated from the other. Thus, it is necessary to identify master and slave interfaces.

The stationary of $\delta I$ with respect to the independent variables $\delta u^G$, $\delta u^L$ and $\delta\lambda$ yields the following conditions:

$$\nabla \cdot \sigma + \bar{f} = 0 \quad \text{on } \Omega_G \cup \Omega_L \tag{3.11}$$

$$\sigma \cdot \boldsymbol{n} = \bar{t} \quad \text{on } \Gamma_n \tag{3.12}$$

$$u^L = u^G \quad \text{on } \Gamma \tag{3.13}$$

$$\lambda = -\sigma^G \cdot \boldsymbol{n} \text{ or } \delta u^G = 0 \quad \text{on } \Gamma \tag{3.14}$$

$$\lambda = \sigma^L \cdot \boldsymbol{n} \text{ or } \delta u^L = 0 \quad \text{on } \Gamma \tag{3.15}$$

Eq. (3.11) ensures stress equilibrium, Eq. (3.12) is the Neumann boundary condition, Eq. (3.13) represents the interface compatibility, Eqs. (3.14) and (3.15) relate the Lagrange multiplier to tractions on the sub-domains.

### Local Lagrangian Multiplier Method

In contrast to the global lagrange multiplier method, more flexibility is achieved by introducing an intermediate frame and constraining the frame displacements with those of the sub-domains on both sides. Such an approach is termed Local Lagrangian Method [100]. An appealing feature of the LLM method is that a virtual frame is introduced between two neighboring meshes, which dissociates (from each other) details of the sub-domain meshes such as element shape functions. The hiding of sub-domain mesh details from each other makes LLM convenient for non-intrusive coupling.

Using Eq. (3.6) and Eq. (3.7) as global and local model virtual work statements, we introduce Lagrange multipliers $\lambda^G$ and $\lambda^L$ to constrain the displacements on the sub-domains to that of the frame displacement field $u^B$ on $\Gamma$. Analogous to Eq. (3.9), the virtual work statement now becomes $\Omega$ is:

$$\delta I \equiv (u^G, u^L, u^B, \lambda^G, \lambda^L) \equiv \delta I^G + \delta I^L + \delta I^B = 0 \tag{3.16}$$

where,

$$\delta I^B = \int_{\partial\Omega^G} \lambda^G(\delta u^G - \delta u^B)d\Gamma + \int_{\partial\Omega^L} \lambda^L(\delta u^L - \delta u^B)d\Gamma \tag{3.17}$$

$$+ \int_{\partial\Omega^G} \delta\lambda^G(u^G - u^B)d\Gamma + \int_{\partial\Omega^L} \delta\lambda^L(u^L - u^B)d\Gamma \tag{3.18}$$

As with the GLM, integrating by parts and applying the divergence theorem, the stationary condition is derived as:

$$\begin{aligned}
\delta I(u^G, u^L, u^B, \lambda^G, \lambda^L) = 0 = &- \int_{\Omega^G} (\nabla \cdot \sigma^G + \bar{f}^G)\delta u^G d\Omega + \int_{\partial\Omega^G \setminus \Gamma} \left(\sigma^G \cdot \boldsymbol{n} - \bar{t}^G\right) d\partial\Omega \\
&- \int_{\Omega^L} (\nabla \cdot \sigma^G + \bar{f}^G)\delta u^G d\Omega + \int_{\partial\Omega^L \setminus \Gamma} \left(\sigma^G \cdot \boldsymbol{n} - \bar{t}^L\right) d\partial\Omega \\
&+ \int_\Gamma (u^G - u^B)\delta\lambda^G d\Gamma + \int_\Gamma (u^L - u^B)\delta\lambda^L d\Gamma \\
&+ \int_\Gamma (\sigma^G \cdot \boldsymbol{n} + \lambda^G)\delta u^G d\Gamma + \int_\Gamma (\sigma^L \cdot \boldsymbol{n} - \lambda^L)\delta u^L d\Gamma \\
&- \int_\Gamma (\lambda^G + \lambda^L)\delta u^B d\Gamma
\end{aligned} \tag{3.19}$$

The above stationary principle yields the necessary conditions:

$$\nabla \cdot \sigma + \bar{f} = 0 \quad \text{on } \Omega_G \cup \Omega_L \tag{3.20}$$

$$\sigma \cdot \boldsymbol{n} = \bar{t} \quad \text{on } \Gamma_n \tag{3.21}$$

$$u^L = u^G = u^B \quad \text{on } \Gamma \tag{3.22}$$

$$\lambda^G = -\sigma^G \cdot \boldsymbol{n} \text{ or } \delta u^G = 0 \quad \text{on } \Gamma \tag{3.23}$$

$$\lambda^L = \sigma^L \cdot \boldsymbol{n} \text{ or } \delta u^L = 0 \quad \text{on } \Gamma \tag{3.24}$$

$$\lambda^G + \lambda^L = 0 \quad \text{on } \Gamma \tag{3.25}$$

As before, Eq. (3.20) ensures stress equilibrium, Eq. (3.21) is the Neumann boundary condition, Eq. (3.22) represents the interface compatibility, Eqs. (3.23) and (3.24) relate the Lagrange multipliers to tractions on the sub-domains and Eq. (3.25) provides the compatibility of tractions across the interface.

### 3.2.3 Derivation of Local-Global Displacement and Force Projection Matrix

In this section, the unknown fields in the governing principles of Eqs. (3.10) and (3.19) are discretized to develop a force projection matrix that allows transfer of fields between mismatched meshes of the two sub-domains.

#### Global Lagrange Multiplier method

The displacement on the interface $\Gamma$ is approximated using its discretized values on the sub-domains:

$$\begin{aligned} u^L &= \boldsymbol{N}^L \boldsymbol{u}^L \\ u^G &= \boldsymbol{N}^G \boldsymbol{u}^G \end{aligned} \tag{3.26}$$

where $\xi$ is the parametric description of the element edges along the boundary, $\boldsymbol{N}^G$ and $\boldsymbol{N}^L$ are row vectors containing the shape functions of the discretization in the global and local models respectively. In the present paper, $\boldsymbol{N}$ quantities alone are assumed to be row vectors in keeping with the common finite element convention; all other vectors are column vectors. To relate the nodal displacement values between the sub-domains, $\lambda$ needs to be discretized as well:

$$\delta\lambda = \boldsymbol{N}^\lambda \boldsymbol{u}^\lambda \tag{3.27}$$

We next substitute the above discretization into the interface compatibility condition

$$\int_\Gamma (u^G - u^L)\delta\lambda d\Gamma = 0 \tag{3.28}$$

along with the displacement approximations at the interface to obtain a relation between nodal quantities $\boldsymbol{u}^L$ and $\boldsymbol{u}^G$:

$$\boldsymbol{u}^L = \boldsymbol{P}\boldsymbol{u}^G \tag{3.29}$$

where, the mapping matrix is

$$\boldsymbol{P} = \boldsymbol{C}^{L^+}\boldsymbol{C}^G \tag{3.30}$$

where, $+$ denotes the general Moore–Penrose inverse, and the matrices on the right hand side are defined as

$$\boldsymbol{C}^L = \int_\Gamma \boldsymbol{N}^{\lambda^T} \boldsymbol{N}^L d\Gamma \tag{3.31}$$

$$\boldsymbol{C}^G = \int_\Gamma \boldsymbol{N}^{\lambda^T} \boldsymbol{N}^G d\Gamma \tag{3.32}$$

where, $\boldsymbol{N}^L$, $\boldsymbol{N}^G$ denote the shape functions of local and global models at the interface, respectively.

We note that satisfaction of Eq. (3.10) requires the following two conditions to hold:

$$\int_\Gamma (\lambda + \sigma^G \cdot \boldsymbol{n}) \delta u^G d\Gamma = 0 \tag{3.33}$$

$$\int_\Gamma (\lambda - \sigma^L \cdot \boldsymbol{n}) \delta u^L d\Gamma = 0 \tag{3.34}$$

Summing the above two equations yields the condition:

$$\int_\Gamma \left[ \left( \sigma^G \cdot \boldsymbol{n} \right) \delta u^G + \left( \sigma^L \cdot \boldsymbol{n} \right) \delta u^L \right] d\Gamma = \int_\Gamma \lambda (-\delta u^G + \delta u^L) d\Gamma \tag{3.35}$$

Now, substituting the discretized fields into the above condition gives,

$$\int_\Gamma \left( \sigma^G \cdot \boldsymbol{n} \right) \left( \boldsymbol{N}^G \delta \boldsymbol{u}^G \right) + \left( \sigma^L \cdot \boldsymbol{n} \right) \left( \boldsymbol{N}^L \delta \boldsymbol{u}^L \right) d\Gamma = \int_\Gamma \left( \boldsymbol{\lambda}^T \boldsymbol{N}^{\lambda^T} \right) \left( -\boldsymbol{N}^G \delta \boldsymbol{u}^G + \boldsymbol{N}^L \delta \boldsymbol{u}^L \right) d\Gamma \tag{3.36}$$

The validity of Eq. (3.29) implies that

$$\delta \boldsymbol{u}^L = \boldsymbol{P} \delta \boldsymbol{u}^G \tag{3.37}$$

Thus, the right hand side of Eq. (3.36) vanishes due to the definition of the mapping matrix in Eq. (3.30). Now, denoting

$$\boldsymbol{F}^G = \int_\Gamma \boldsymbol{N}^{G^T} \left( \sigma^G \cdot \boldsymbol{n} \right) d\Gamma \tag{3.38}$$

$$\boldsymbol{F}^L = \int_\Gamma \boldsymbol{N}^{L^T} \left( \sigma^L \cdot \boldsymbol{n} \right) d\Gamma \tag{3.39}$$

where, $\boldsymbol{F}^G$ and $\boldsymbol{F}^L$ represent the nodal force on the interface of global and local models. Thus, Eq. (3.36) reduces to

$$\delta \boldsymbol{u}^{L^T} \boldsymbol{F}^L + \delta \boldsymbol{u}^{G^T} \boldsymbol{F}^G = 0 \tag{3.40}$$

Using Eq. (3.37), the above equation yields the relation between local and global nodal forces on the interface

$$\boldsymbol{F}^G = -\boldsymbol{P}^T \boldsymbol{F}^L \tag{3.41}$$

with $\boldsymbol{P}^T = \boldsymbol{C}^{G^T} \boldsymbol{C}^{L^{+T}}$.

### Local Lagrange Multiplier Method

The stationary principle of Eq. (3.19) yields the following condition:

$$\int_\Gamma \left[ (u^L - u^B)\delta\lambda^L + (u^G - u^B)\delta\lambda^G \right] d\Gamma = 0 \tag{3.42}$$

$$\int_\Gamma (\lambda^G + \lambda^L)\delta u^B d\Gamma = 0 \tag{3.43}$$

We next dicretize the displacement fields as before:

$$\begin{aligned} u^L &= \boldsymbol{N}^L \boldsymbol{u}^L \\ u^G &= \boldsymbol{N}^G \boldsymbol{u}^G \\ u^B &= \boldsymbol{N}^B \boldsymbol{u}^B \end{aligned} \tag{3.44}$$

where, $\boldsymbol{N}^B$ is the row vector containing the shape functions associated with the frame, and $\boldsymbol{u}^B$ are its associated nodal degrees of freedom.

To derive the relation between nodal unknowns on the sub-domains, one needs to discretize $\lambda^G$ and $\lambda^L$. By a special choice of discretization of the Lagrange multipliers $\lambda^G$ and

$\lambda^L$ integration in Eq. (3.43) may be avoided as shown by Park and Felippa [100]. The specific choice for the approximation is to use the Dirac-delta function $\delta$ as shown below:

$$\begin{aligned} \lambda^L &= \sum_{\mathrm{i}=1}^{n^L} \delta(\xi - \xi_{\mathrm{i}}) \boldsymbol{\lambda}_{\mathrm{i}}^L \\ \lambda^G &= \sum_{\mathrm{i}=1}^{n^G} \delta(\xi - \xi_{\mathrm{i}}) \boldsymbol{\lambda}_{\mathrm{i}}^G \end{aligned} \tag{3.45}$$

Thus, the multiplier becomes a point force applied at the sub-domain displacement nodes (see Figure 3.2). Also, the discretizations of the variations $\delta\lambda^L$ and $\delta\lambda^G$ follow those of $\lambda^L$ and $\lambda^G$.

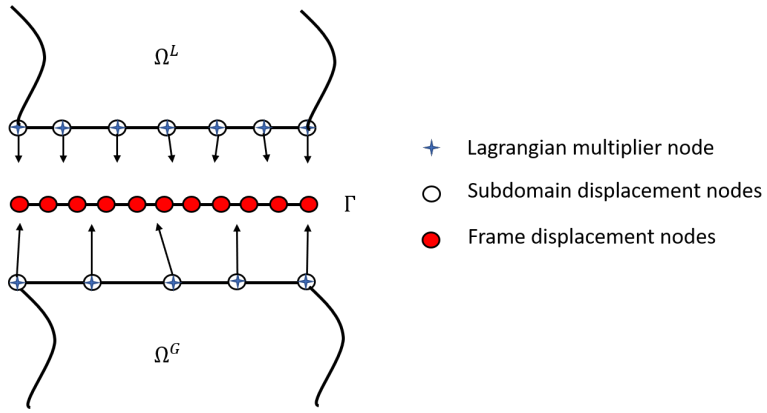


**Figure 3.2.** Connection for non-matched mesh interface by LLM

Substituting the discretization of the variation of the multipliers, the terms in Eq. (3.43) become

$$\begin{aligned} \int_\Gamma u^L \delta\lambda^L d\Gamma &= \delta\boldsymbol{\lambda}^{L^T} \boldsymbol{u}^L \\ \int_\Gamma u^G \delta\lambda^G d\Gamma &= \delta\boldsymbol{\lambda}^{G^T} \boldsymbol{u}^G \end{aligned} \tag{3.46}$$

Similarly, the terms associated with the frame displacement field are obtained as:

$$\begin{aligned} \int_\Gamma \delta\lambda^L u^B &= \delta\boldsymbol{\lambda}^{L^T} \boldsymbol{L}^{BL} \boldsymbol{u}^B \\ \int_\Gamma \delta\lambda^G u^B &= \delta\boldsymbol{\lambda}^{G^T} \boldsymbol{L}^{BG} \boldsymbol{u}^B \end{aligned} \tag{3.47}$$

where,

$$\begin{aligned} \boldsymbol{L}_{\mathrm{ij}}^{BL} &= \int_{\Gamma} \delta(\xi - \xi_{\mathrm{i}}) N_{\mathrm{j}}^{B} d\gamma = N_{\mathrm{j}}^{B}(\xi_{\mathrm{i}}) \\ \boldsymbol{L}_{\mathrm{ij}}^{BG} &= \int_{\Gamma} \delta(\xi - \xi_{\mathrm{i}}) N_{\mathrm{j}}^{B} d\gamma = N_{\mathrm{j}}^{B}(\xi_{\mathrm{i}}) \end{aligned} \tag{3.48}$$

Substituting Eq. (3.46) and Eq. (3.47) into Eq. (3.42), we get:

$$\begin{bmatrix} \delta\boldsymbol{\lambda}^{L^T} & \delta\boldsymbol{\lambda}^{G^T} \end{bmatrix} \left\{ \begin{Bmatrix} \mathbf{u}^{L} \\ \mathbf{u}^{G} \end{Bmatrix} - \begin{bmatrix} \mathbf{L}^{BL} \\ \mathbf{L}^{BG} \end{bmatrix} \mathbf{u}^{B} \right\} = 0 \tag{3.49}$$

which leads to the condition

$$\begin{Bmatrix} \mathbf{u}^{L} \\ \mathbf{u}^{G} \end{Bmatrix} - \begin{bmatrix} \mathbf{L}^{BL} \\ \mathbf{L}^{BG} \end{bmatrix} \mathbf{u}^{B} = 0 \tag{3.50}$$

Similarly, discretizing Eq. (3.43) yields

$$\begin{bmatrix} \boldsymbol{\lambda}^{L^T} & \boldsymbol{\lambda}^{G^T} \end{bmatrix} \left\{ \begin{Bmatrix} \delta\mathbf{u}^{L} \\ \delta\mathbf{u}^{G} \end{Bmatrix} - \begin{bmatrix} \mathbf{L}^{BL} \\ \mathbf{L}^{BG} \end{bmatrix} \delta\mathbf{u}^{B} \right\} = 0 \tag{3.51}$$

The above equation can be simplified by substituting the variation of displacement relation obtained in Eq. (3.50)

$$\begin{bmatrix} \mathbf{L}^{BL^T} & \mathbf{L}^{BG^T} \end{bmatrix} \begin{Bmatrix} \boldsymbol{\lambda}^{L} \\ \boldsymbol{\lambda}^{G} \end{Bmatrix} = 0 \tag{3.52}$$

Finally, using Eqs. (3.50) and (3.52), one can relate the nodal unknowns at the subdomainn interface to obtain:

$$\boldsymbol{u}^{L} = \boldsymbol{P}\boldsymbol{u}^{G} \tag{3.53}$$

and

$$\boldsymbol{\lambda}^{G} = \boldsymbol{P}^{T}\boldsymbol{\lambda}^{L} \tag{3.54}$$

where, $\boldsymbol{P} = \boldsymbol{L}^{BL}(\boldsymbol{L}^{BG})^{+}$ is the mapping matrix, with $+$ denoting the general Moore-Penrose inverse. Note that in LLM, local Lagrangian field is discretized by collocation on the displacement nodes, and the nodal values $\boldsymbol{\lambda}^{G}$ and $\boldsymbol{\lambda}^{L}$ in Eq. (3.54) are the same as nodal force.

$\boldsymbol{L}$ matrix is also determined by collocation on the basis function of $u^B$. The discretization of $u^B$ in Eq. (3.44) can be through finite element or other approximations including isogeometric spline approximations.

### 3.2.4 Comments on GLM and LLM

The advantages and disadvantages of the GLM and LLM methods are briefly discussed.

1. The GLM method has two unknown fields corresponding to the displacement fields of the two partitioned sub-domains and that of the connecting Lagrange multiplier field on the boundary $\Gamma$, and is therefore a two-field method. LLM on the other hand adds a third independently varied displacement field at the interface – that of the frame. Thus, the LLM will require higher number of degrees of freedom as compared to GLM method, but the method eliminates the need for master-slave sub-domain identification.

2. The calculation of the mapping matrix $\boldsymbol{P}$ is computationally less expensive in LLM because integration in Eq. (3.48) reduces to evaluating the frame displacement shape functions at interface nodes. Computing the mapping matrix in Eq. (3.30) requires integration along the boundary. Since LLM does not need to evaluate the shape functions of elements of the sub-domains along the interface to compute the mapping matrix, it is more flexible. GLM, on the other hand, requires the shape functions of the sub-domain element shape functions to compute $\boldsymbol{P}$.

3. In general, GLM yields more accurate solution because of the quadrature over the boundary.

## 3.3 Iterative Solution to Interfacial Unknowns

In Section 3.2, two variational formulations and the discretized form for transferring displacements across the interface were discussed. The described methods are valid even when the meshes of the local and global domains do not match at the interface. Once the mapping matrix $\boldsymbol{P}$ is computed, the nodal force on the local mesh can be transferred to the

equivalent nodal force on the global mesh to calculate the unbalanced force at any iteration:

$$\boldsymbol{r} = \boldsymbol{P}^T \boldsymbol{F}^L + \boldsymbol{F}^G \tag{3.55}$$

Since $\boldsymbol{u}^G$ and $\boldsymbol{u}^L$ are connected by $\boldsymbol{P}$, finding the equilibrium state is equivalent to solving the following optimization problem for variable $\boldsymbol{u}^G$

$$min \quad f(\boldsymbol{u}^{\boldsymbol{G}}) = \left\| \boldsymbol{r} \right\| \tag{3.56}$$

The above minimization problem problem is generally solved using a direct search algorithm that updates the solution guess iteratively until convergence:

$$\boldsymbol{u}^G_{\mathrm{i}+1} = \boldsymbol{u}^G_{\mathrm{i}} + \alpha_{\mathrm{i}} \boldsymbol{\Delta u}^G_{\mathrm{i}} \tag{3.57}$$

where, the increment $\boldsymbol{\Delta u}^G_{\mathrm{i}}$ is typically a quasi-Newton direction of descent for the objective and $\alpha_{\mathrm{i}}$ is a step length along the search direction. The gradient of the objective function with respect to the unknown displacements $\boldsymbol{u}^G$ is

$$\nabla f = \frac{\nabla \boldsymbol{r} \ \boldsymbol{r}}{\left\| \boldsymbol{r} \right\|} \tag{3.58}$$

A general quasi-Newton search direction for the unconstrained optimization problem of Eq. (3.56) is [102]:

$$\boldsymbol{\Delta u}^G = -\boldsymbol{A}^{-1} \nabla f = -\boldsymbol{A}^{-1} \frac{\nabla \boldsymbol{r} \ \boldsymbol{r}}{\left\| \boldsymbol{r} \right\|} \tag{3.59}$$

where, $\boldsymbol{A}$ is a symmetric positive definite matrix. The simplest choice for $\boldsymbol{A}$ is an identity matrix, which yields the steepest descent search direction, but choosing $\boldsymbol{A}$ to be the Hessian of the objective, one obtains the Newton search direction. Since computing the gradient $\nabla \boldsymbol{r}$ is in general non-trivial and requires access to the internals of the analysis codes used for the sub-domains, we choose an alternative search direction dependent only on the unbalanced force:

$$\boldsymbol{\Delta u}^G = -\boldsymbol{A}^{-1} \frac{\boldsymbol{r}}{\left\| \boldsymbol{r} \right\|} \tag{3.60}$$

Here, beginning with an identity matrix Quasi-Newton updates to $\boldsymbol{A}$ are constructed using Symmetric Rank 1 and BFGS formulae [102]. For the above-chosen search direction, the first order change in the objective is:

$$\boldsymbol{\Delta u}^{G^T} \nabla f = -\frac{\boldsymbol{r}^T (\boldsymbol{A}^{-1} \nabla \boldsymbol{r}) \boldsymbol{r}}{\left\| \boldsymbol{r} \right\|^2} \tag{3.61}$$

Therefore, the chosen search direction is a direction of descent ($\boldsymbol{\Delta u}^T \nabla f < 0$) provided $\boldsymbol{A}^{-1} \nabla \boldsymbol{r}$ is a symmetric positive definite matrix.

### 3.3.1 Algorithm for Iterative Solution

To solve the problem with additive global displacement correction, the following two-way iterative algorithm is proposed:

**Initialization**: An admissible initial guess of $\mathbf{u^G}$ is generated. This step can be easily implemented through an elastic analysis of the domain $\Omega_G \cup \Omega_{\tilde{G}}$:

$$\boldsymbol{K}^{G+\tilde{G}} \boldsymbol{u} = \boldsymbol{f} \tag{3.62}$$

Where $\boldsymbol{K}^{G+\tilde{G}}$ is the stiffness matrix of the whole coarse model. Only the displacement and nodal force on the global interface $\boldsymbol{u}_0^G$ and $\boldsymbol{F}_0^G$ are extracted and used as the initial guess for the start of the iterations.

**Step 1**: The global displacement field is mapped to the local interface:

$$\boldsymbol{u}^L = \boldsymbol{P} \boldsymbol{u}^G \tag{3.63}$$

$\boldsymbol{u}^L$ is imported as boundary condition for the nonlinear local problem. The local model solution may be obtained using a commercial finite element software or a custom solver. The nodal force on the local interface, $\boldsymbol{F}^L$, is obtained through the local analysis.

**Step 2**: The residual force at the interface is defined as:

$$\boldsymbol{r} = -\int_\Gamma \boldsymbol{N}^T [\sigma^L \cdot \boldsymbol{n}^L + \sigma^G \cdot \boldsymbol{n}^G] d\Gamma \tag{3.64}$$

where, $\sigma^G$ and $\sigma^L$ are the stress states on the interface of global and local model, $\boldsymbol{n}^L$ and $\boldsymbol{n}^G$ are the normal vectors and $\boldsymbol{N}$ is the finite element shape function. The local nodal force on the interface is projected to the global interface through matrix $\boldsymbol{P}^T$. The residual nodal force is:

$$\boldsymbol{r} = \boldsymbol{P}^T \boldsymbol{F}^L + \boldsymbol{F}^G \tag{3.65}$$

The iteration will be terminated if magnitude of $\|\boldsymbol{r}\|$ is small as defined by the following convergence criterion:

$$f_{err} = \frac{\|\boldsymbol{r}_{\mathrm{i}}\|}{\|\boldsymbol{F}^G_{\mathrm{i}}\|} < tol \tag{3.66}$$

where, $f_{err}$ is the relative residual and $tol$ is the user specified tolerance.

**Step 3**: The quantity $\Delta \boldsymbol{u}^G = [\boldsymbol{S}]^{-1}\boldsymbol{r}$ is estimated as the global correction, where $\boldsymbol{S}$ is the Schur complement of the initial elastic model of domain $\Omega$ condensed on the interface $\Gamma$. This can be done non-intrusively using the initial elastic model of the domain $\Omega_G \cup \Omega_{\tilde{G}}$ as follows. The homogeneous Dirichlet boundary condition is retained on the domain while the residual force $\boldsymbol{r}$ is applied on the corresponding nodes on the interface as the Neumann boundary condition. The output nodal displacement of the interface will be $[\boldsymbol{S}]^{-1}\boldsymbol{r}$. At the $\mathrm{i}^{\mathrm{th}}$ iteration, the global update is:

$$\boldsymbol{u}^G_{\mathrm{i}+1} = \boldsymbol{u}^G_{\mathrm{i}} + \alpha_{\mathrm{i}} \left[\boldsymbol{S}\right]^{-1} \boldsymbol{r}_{\mathrm{i}} \tag{3.67}$$

If convergence criterion Eq. (3.66) is not met, the procedure will repeat from Step 1. $\alpha_{\mathrm{i}}$ is the step length that should be small enough to guarantee convergence. In Step 2, it is desired that $\boldsymbol{r}_{\mathrm{i}} < \boldsymbol{r}_{\mathrm{i}-1}$, which provides the "globalization" [102] to assure convergence, given a descent direction. If not, the value of $\alpha_{\mathrm{i}}$ should be adjusted until the residual force in the search direction is lower than its current value.

### 3.3.2 Step Length Determination: Bisection Method

Eq. (3.67) is the line search form for updating global displacement. $\left[\boldsymbol{S}\right]^{-1} \boldsymbol{r}^G_{\mathrm{i}}$ denotes the direction for line search, though it naturally represents displacement. With little stiffness reduction, $\alpha_{\mathrm{i}} = 1$ should be a proper value. However, when the gap of stiffness between

global and local model increased, it no longer guarantees convergence without an appropriate globalization strategy. Usually, the step length is determined by the so call Goldstein-Armijo condition[103]. This condition assures "sufficient decrease" through iterations:

$$f(x^k + \alpha s^k) = f(x^{k+1}) \leq f(x^k) + c\alpha \nabla f^T(x^k) s^k \tag{3.68}$$

where $x_k$ is the variable value at $k^{th}$ iteration, $s^k$ is the search direction, $\alpha$ is the step length and $c$ is chosen to be a small value ($c$ is chosen to be $10^{-4}$ in [103]). The Goldstein-Arjimo condition guarantees that the search algorithm will converge to a local monimum while a fixed step does not assure such convergence.

However, Eq. (3.68) only gurantees local minimum. The function $f$, which is the relative residual, may not be a strict convex function. In the present algorithm, the condition is slightly relaxed so that the algorithm will not get stuck in the local minimum. A small coefficient $\beta$ (0.01 is used in the current study) is introduced and the residual of adjacent iteration should satisfy:

$$\|\boldsymbol{r}_{\mathrm{i}+1}\| < (1+\beta)\|\boldsymbol{r}_{\mathrm{i}}\| \tag{3.69}$$

This means the norm of residual is allowed to increase but within a small amount. If the condition Eq. (3.69) is not satisfied, set $\alpha_{\mathrm{i}+1} = 0.5\alpha_{\mathrm{i}+1}$ and the current iteration is computed again.

### 3.4 Acceleration Technique and Non-intrusive implementation

As described in the algorithm of the previous section, the nodal displacement on the interface of the global mesh is sequentially updated as follows:

$$\boldsymbol{u}^G_{\mathrm{i}+1} \rightarrow \boldsymbol{u}^G_{\mathrm{i}} + \alpha_{\mathrm{i}} \boldsymbol{A}^{-1}_{\mathrm{i}} \frac{\boldsymbol{r}^G_{\mathrm{i}}}{\left\|\boldsymbol{r}^G_{\mathrm{i}}\right\|} \tag{3.70}$$

where, $\boldsymbol{r}^G_{\mathrm{i}}$ is the unbalanced force mapped on the global mesh, $\boldsymbol{A}_{\mathrm{i}}$ is a symmetric positive definite matrix, which is the Schur complement of the global stiffness matrix condensed on the interface in Section 3.3.1, and $\alpha_{\mathrm{i}}$ is the step length ranging from 0 to 1. A good

approximation of the Hessian of $\|\boldsymbol{r}\|$ should be constructed to replace $\boldsymbol{A}_{\mathrm{i}}$. As discussed in Section 3.3.1, the Schur complement $\boldsymbol{S}$ of the global elastic structure condensed on the interface is used as the approximation for $\boldsymbol{A}_{\mathrm{i}}$. This is elaborated below.

Consider purely elastic behavior of the global structure. In general, the discretized stiffness matrices on the sub-domains are such that the unbalanced force may be defined in terms of the Schur complements:

$$\boldsymbol{r} = \boldsymbol{P}^T \boldsymbol{F}^L + \boldsymbol{F}^G = (\boldsymbol{P}^T \boldsymbol{S}^L \boldsymbol{P} + \boldsymbol{S}^G)\boldsymbol{u}^G \tag{3.71}$$

where $\boldsymbol{S}^G$, $\boldsymbol{S}^L$ are the primal Schur complements on the interface of the global and local models. Therefore,

$$\nabla \boldsymbol{r} = \boldsymbol{P}^T \boldsymbol{S}^L \boldsymbol{P} + \boldsymbol{S}^G \tag{3.72}$$

Now, since $\boldsymbol{S}^G$, $\boldsymbol{S}^L$ are the primal Schur complements on the interface, they are symmetric and positive definite. Extending the idea, let $\boldsymbol{S}^G$, $\boldsymbol{S}^{\tilde{G}}$ and $\boldsymbol{S}^L$ be the primal Schur complements on the interface corresponding to region $\Omega_G$, $\Omega_{\tilde{G}}$ and $\Omega_L$. Then,

$$\nabla \boldsymbol{r} = \boldsymbol{S}^G + \boldsymbol{S}^{\tilde{G}} + (\boldsymbol{P}^T \boldsymbol{S}^L \boldsymbol{P} - \boldsymbol{S}^{\tilde{G}}) \tag{3.73}$$

If the local behavior is purely elastic, then the condensed stiffness on the interface from both sides are nearly the same, and $\boldsymbol{S}^{\tilde{G}} + \boldsymbol{S}^G$ is a good approximation to $\nabla \boldsymbol{r}$. However, as the local non-linearity evolves, the local stiffness degenerates and the use of a constant $\boldsymbol{A}_{\mathrm{i}} = \boldsymbol{S}$ in Eq. (3.70) will lead to slow convergence. Therefore, it is necessary to apply acceleration techniques to improve the convergence rate. The most commonly used technique is the Quasi-Newton method of which symmetric rank one update and Broyden-Fletcher-Goldfarb-Shanno (BFGS) update are two well-known examples [102].

### 3.4.1 Symmetric Rank One Update

The classical symmetric rank one (SR1) update formula is :

$$\boldsymbol{A}_{\mathrm{i}+1} = \boldsymbol{A}_{\mathrm{i}} - \frac{\boldsymbol{r}_{\mathrm{i}}\boldsymbol{r}_{\mathrm{i}}^T}{\boldsymbol{r}_{\mathrm{i}}^T \Delta \boldsymbol{u}_{\mathrm{i}}} \tag{3.74}$$

where $\Delta \boldsymbol{u}_{\mathrm{i}}$ is the global correction of Eq. (3.67). In the current step, $\boldsymbol{A}_{\mathrm{i}+1}^{-1}$ is computed to update global correction in next iteration. Applying Sherman-Morrison formula and right multiplying residual force $\boldsymbol{r}_{\mathrm{i}}$, we get:

$$\boldsymbol{A}_{\mathrm{i}+1}^{-1} = \boldsymbol{A}_{\mathrm{i}}^{-1} + \boldsymbol{A}_{\mathrm{i}}^{-1}\boldsymbol{r}_{\mathrm{i}} \frac{\boldsymbol{r}_{\mathrm{i}}^T \boldsymbol{A}_{\mathrm{i}}^{-1}}{\boldsymbol{r}_{\mathrm{i}}^T (\Delta \boldsymbol{u}_{\mathrm{i}} - \boldsymbol{A}_{\mathrm{i}}^{-1}\boldsymbol{r}_{\mathrm{i}})} \tag{3.75}$$

### 3.4.2 BFGS Update

Another popular quasi-Newton update is that by Broyden-Fletcher-Goldfarb-Shanno (BFGS). It uses the information of global correction and residual from last iteration. The update formula is:

$$\boldsymbol{A}_{\mathrm{i}+1} = \boldsymbol{A}_{\mathrm{i}} + \frac{\Delta \boldsymbol{r}_{\mathrm{i}} \Delta \boldsymbol{r}_{\mathrm{i}}^T}{\Delta \boldsymbol{r}_{\mathrm{i}}^T \Delta \boldsymbol{r}_{\mathrm{i}}} - \frac{\boldsymbol{A}_{\mathrm{i}} \Delta \boldsymbol{r}_{\mathrm{i}} \Delta \boldsymbol{r}_{\mathrm{i}}^T \boldsymbol{A}_{\mathrm{i}}}{\Delta \boldsymbol{u}_{\mathrm{i}}^T \boldsymbol{A}_{\mathrm{i}} \Delta \boldsymbol{u}_{\mathrm{i}}} \tag{3.76}$$

Where $\Delta \boldsymbol{r}_{\mathrm{i}} = \boldsymbol{r}_{\mathrm{i}+1} - \boldsymbol{r}_{\mathrm{i}}$ and $\Delta \boldsymbol{u}_{\mathrm{i}}$ is the displacement update. This update is a rank two update and guarantees a symmetric positive definite matrix. Applying Sherman-Morrison formula again to Eq. (3.76), one gets

$$\boldsymbol{A}_{\mathrm{i}+1}^{-1} = \boldsymbol{A}_{\mathrm{i}}^{-1} + \frac{(\Delta \boldsymbol{u}_{\mathrm{i}}^T \Delta \boldsymbol{r}_{\mathrm{i}}^T + \Delta \boldsymbol{r}_{\mathrm{i}}^T \boldsymbol{A}_{\mathrm{i}}^{-1} \Delta \boldsymbol{r}_{\mathrm{i}})(\Delta \boldsymbol{u}_{\mathrm{i}} \Delta \boldsymbol{u}_{\mathrm{i}}^T)}{(\Delta \boldsymbol{u}_{\mathrm{i}}^T \Delta \boldsymbol{r}_{\mathrm{i}})^2} - \frac{\boldsymbol{A}_{\mathrm{i}}^{-1} \Delta \boldsymbol{r}_{\mathrm{i}} \Delta \boldsymbol{u}_{\mathrm{i}}^T + \Delta \boldsymbol{u}_{\mathrm{i}} \Delta \boldsymbol{r}_{\mathrm{i}}^T \boldsymbol{A}_{\mathrm{i}}^{-1}}{\Delta \boldsymbol{u}_{\mathrm{i}}^T \Delta \boldsymbol{r}_{\mathrm{i}}} \tag{3.77}$$

### 3.4.3 Non-Intrusive Implementation

In general, to compute the updates discussed above, one needs access to the sub-domain stiffness matrices. However, accessing the sitffness matrix is non-trivial in commercial finite element software. For example, in ANSYS, three different node numbering schemes are used to optimize the solution. It is therefore necessary to map the internal-order to user-order to be able manipulate any nodal quantity including the stiffness matrix. A non-intrusive strategy

does not need access to the sub-domain stiffness matrices and uses the finite element model directly to compute the displacement correction. Such an non-intrusive implementation inspired by [79] is explained below using the SR1 update as an example. To carryout a non-intrusive update, we note that $\boldsymbol{A}_{\mathrm{i}}$ is the current estimate of the Schur complement at the interface. We multiply Eq. (3.75) by the residual $\boldsymbol{r}_n$ to get:

$$\forall n \geq 1, \forall k \leq n, \boldsymbol{K}_{k+1}^{-1}\boldsymbol{r}_n = \boldsymbol{K}_k^{-1}\boldsymbol{r}_n + \boldsymbol{K}_{k-1}^{-1}\boldsymbol{r}_k \frac{\boldsymbol{r}_k^T(\boldsymbol{K}_{k-1}^{-1}\boldsymbol{r}_n)}{\boldsymbol{r}_k^T(\Delta\boldsymbol{u}_k - \boldsymbol{K}_{\boldsymbol{k-1}}^{-\boldsymbol{1}})\boldsymbol{r}_k} \tag{3.78}$$

Notice that $\boldsymbol{K}_k^{-1}r_n$ presents the displacement response when a force $\boldsymbol{r}_n$ is applied on the interface. Therefore, the global elastic finite element model can be used to replace $\boldsymbol{K}_k^{-1}$ with the displacement solution at the interface corresponding to nodal force $\boldsymbol{r}_n$. Therefore, Eq. (3.78) results in purely vector manipulation operations.

At iteration $n$, it is assumed that for any $k \leq n$, $\boldsymbol{r}_k$, $\boldsymbol{u}_k$ and $\boldsymbol{K}_{k-1}^{-1}\boldsymbol{r}_k$ have been stored from prior steps. At the first iteration, the residual force $\boldsymbol{r}_1$ is applied on the interface of model to get $\boldsymbol{K}_0^{-1}\boldsymbol{r}_1$ and then the formula is applied once to get $\boldsymbol{K}_1^{-1}\boldsymbol{r}_1$, which is the displacement update for the first iteration. At the second iteration, $\boldsymbol{K}_0^{-1}\boldsymbol{r}_2$ is obtained from the FE model and $\boldsymbol{K}_1^{-1}\boldsymbol{r}_2$ and $\boldsymbol{K}_2^{-1}\boldsymbol{r}_2$ are obtained using Eq. (3.78) recursively. In general, $\boldsymbol{K}_0^{-1}\boldsymbol{r}_k$ is firstly obtained by solving the intact FE model, and then the formula is applied k times to get final displacement update for the current iteration. The advantage of such recursive technique is that no access to FE matrix system is necessary, which makes the algorithm non-intrusive.

## 3.5 Numerical Examples

### 3.5.1 L-Shaped Domain

The procedure is validated first using the example of a perforated L-shape domain under uniform traction of 30 MPa. ABAQUS® is used to construct the global and local models (Figure 3.3a).The global model had 533 nodes and 156 quadratic elements while the local model, with three holes, contained 10043 nodes and 3253 quadratic elements. The global model was purely elastic and without the local void feature in the region $\Omega_{\tilde{G}}$. The local

model accounted for the plastic material behavior and included the voids that were left out of the global model. The local model solution captured the complex stress state of the critical region. The Young's modulus of global model was 300 GPa and the Poisson's ratio was 0.3. The local domain $\Omega_L$ was elastic-perfectly plastic, with the same elastic behavior as the global model but with a yield stress of 300 MPa. As a reference, a refined full model with plasticity and local feature was built with 110581 nodes and 36523 quadratic elements.

The coupling framework was implemented in the Matlab environment. In the iterative coupling procedure, the global model was computed first and then the displacement on the interface $\Gamma$ was interpolated and applied on the boundary nodes of the local model. The residual on the interface was then used to update the interfacial displacement. The detailed procedure is illustrated in Figure 3.4. It should be noted that $\Omega_{\tilde{G}}$ did not contribute to the final solution; it was an auxiliary domain to roughly approximate the stiffness matrix at the interface. The model over the domain $\Omega_{\tilde{G}}$ had the same geometry and discretization as the global model but different boundary conditions. The homogeneous Dirichlet boundary condition was retained in this model while the external oads are not included. In the global model, displacement on the interface $\Gamma$ was applied, while in the correction model the residual force was applied on the interface and the output displacement was used to update the corresponding global displacement.

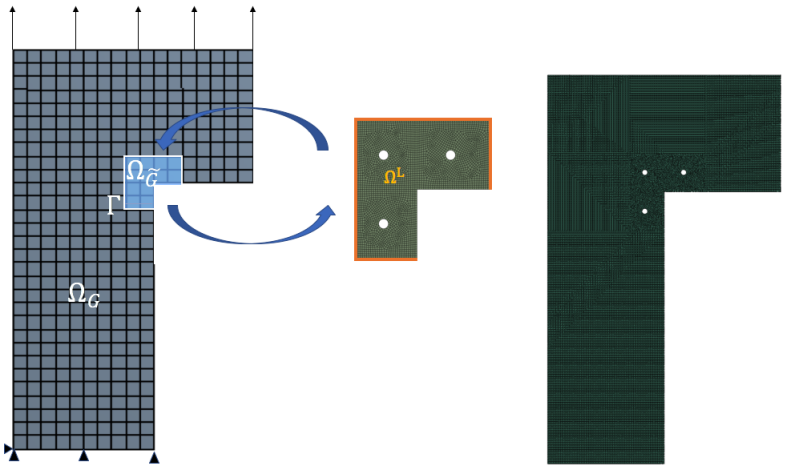


(a) (b)

**Figure 3.3.** Dicretization of (a) global and local model (b) refined full model

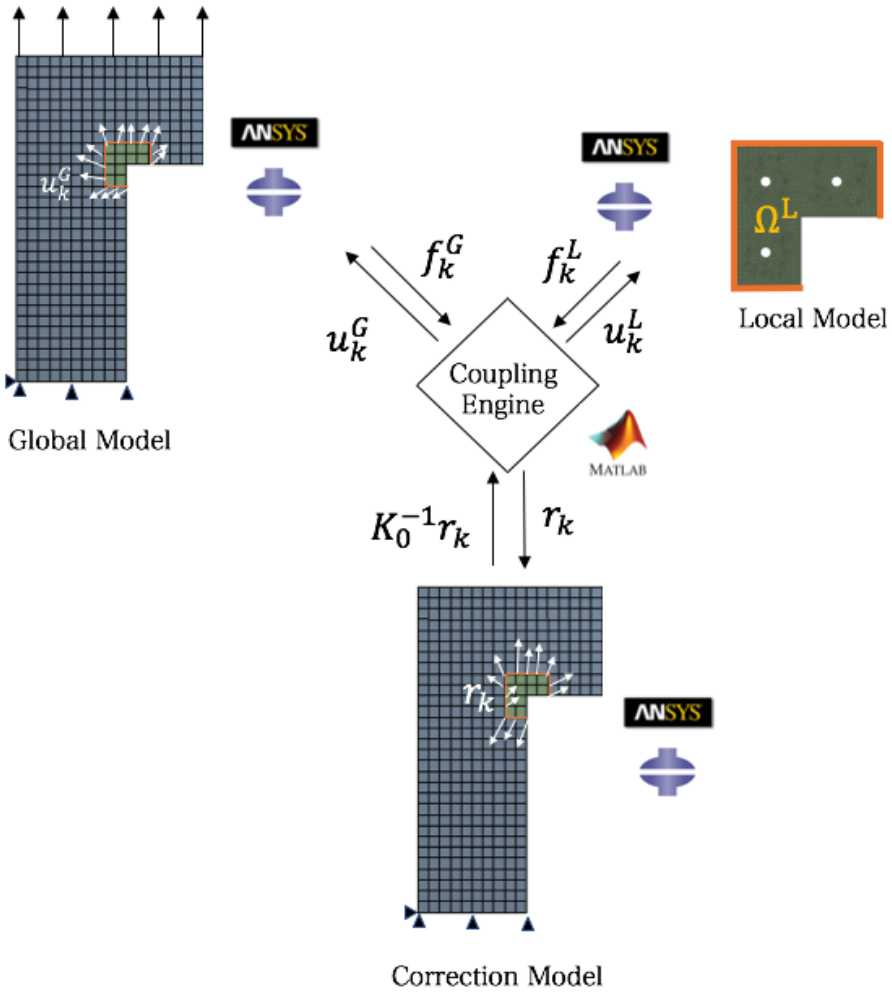


**Figure 3.4.** Flow of data transfer during iterative solution.

The initial displacement guess at the interface was from an elastic analysis of the global structure, and the convergence criterion was set as $10^{-5}$. The Von Mises Stress from the initial iterate and final solution are shown in Figure 3.5.

As can be seen from Figure 3.5, even though the initial guess does not match the reference solution, the iterative two-way coupling method will drive it towards the correct solution. The results also show that the conventional global-local model is inaccurate especially when the local region has nonlinear behavior. We argue that the iterative two-way coupling yields a solution as accurate as the refined full model, but requires fewer degrees of freedom for the same accuracy and thus needs less memory during computation. Figure 3.6 shows the

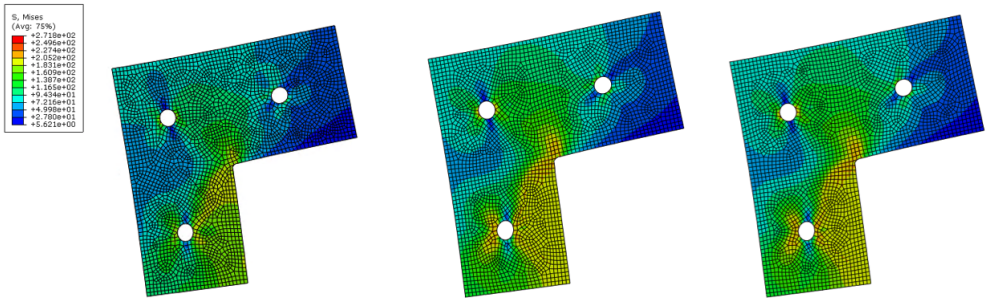


(a) (b) (c)

**Figure 3.5.** Von Mises Stress in the local region (a) Initial guess (global-local solution) (b) final solution (iterative two-way coupling) (c)reference solution (refined full model).

convergence of relative residual force using different acceleration schemes. SR1 is better than BFGS, and both and are faster than iterations using a constant Schur complement.

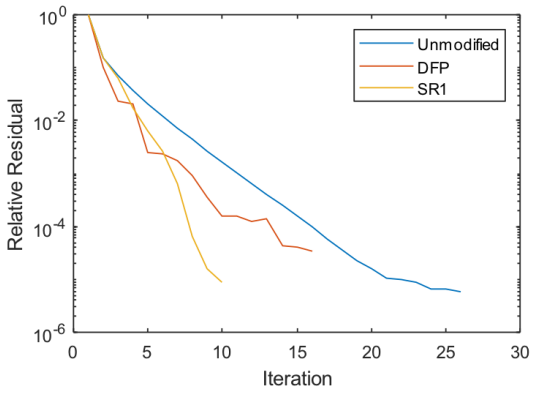


**Figure 3.6.** Convergence of residual force

### 3.5.2 Fracture Propagation using XFEM

A simple fracture propagation example is demonstrated using the iterative two-way coupling technique with the analysis being performed in ABAQUS. This example demonstrates that local evolution of fracture changes global behavior. Consider a linear elastic homogeneous plate ($E = 100GPa, \nu = 0.3$) of size $100mm \times 200mm$ under quasi-static displacement control. A total of six quasi-static crack propagation steps were carried out, with

displacement control step along the direction that $u_y = 2u_x$ and an constant increment of $\Delta u_y = 0.02mm$ at each step. A pre-existing crack with a length of $5mm$ was introduced perpendicular to the left edge in the middle as shown in Figure 3.7a. To investigate crack propagation using the two-way coupling method, the model was partitioned into two regions $\Omega_G$ and $\Omega_{\tilde{G}}$. The global model and local model mesh are illustrated in Figure 3.7b. The crack was only included in the local model. The global mesh size was set to $10mm$ and local mesh was set to $0.5mm$. Both global are local model were discretized using regular square element as shown in Figure 3.7.

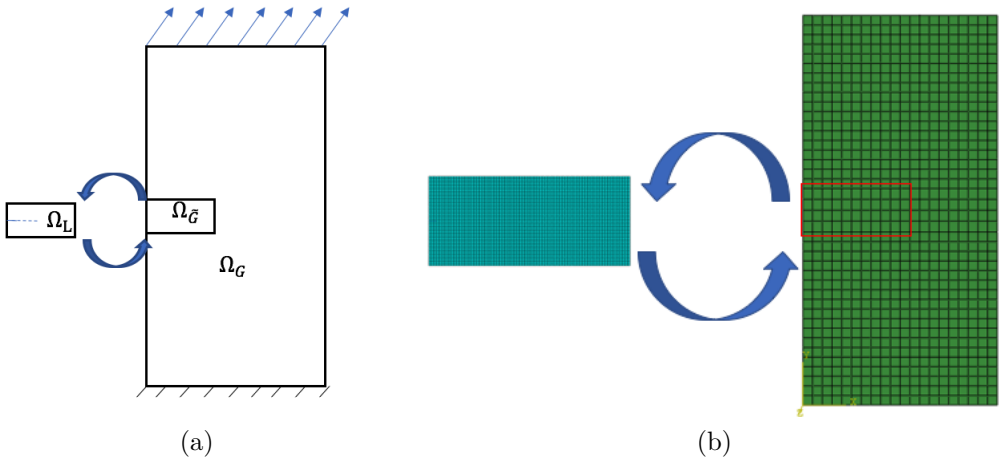


(a) (b)

**Figure 3.7.** Test case for crack propagation using XFEM (a) Boundary conditions (b) Global and local mesh.

To simulate crack propagation, eXtended Finite Element Method (XFEM)[104] implementation in ABAQUS was used in the local model. Both SR1 and BFGS updates were used along with iterations using a constant stiffness matrix. A convergence tolerance of $10^{-3}$ was chosen and a constant $\alpha = 0.1$ was used.

Figure 3.8 shows the main property of two-way coupling method and compares different acceleration techniques. Figure 3.8a illustrates the relation between crack propagation length and iteration numbers at each load step. It can be seen that the unmodified method needed more iteration to achieve equilibrium with load increasing, that is to say unmodified method was very sensitive to crack length. This is because the stiffness gap between local frac-

ture model and global model becomes larger as crack propagates. While the quasi-Newton acceleration was much less sensitive, iteration numbers for SR1 were almost unchanged.

Figure 3.8b shows the iteration numbers in the last load step. It is obvious the iteration number using unmodified method was much larger than that using quasi-newton update. It took 112 iterations for unmodified method to reduce relative error below $10^{-3}$, while it took 15 iterations for SR1 update and 22 iterations for BFGS update. In later examples, we will only use SR1 acceleration since it performs the best. Figure 3.9 compares the crack propagation length using different method. Crack initiated in load step 4. It propagated through 3 elements for unmodified global-local model method, 4 elements for both the presented non-intrusive coupling method and refined full model. In the last step, crack propagated only 8 elements for global-local model method, while it propagates 25 elements for two-way coupling and refined full model. Two-way coupling method is as accurate as full model because the local solution is commuted back to correct the global solution. The global-local model method only has one-way data transfer, since the global model could not capture the crack behavior, the local displacement is more conservative so the crack propagation is underestimated.

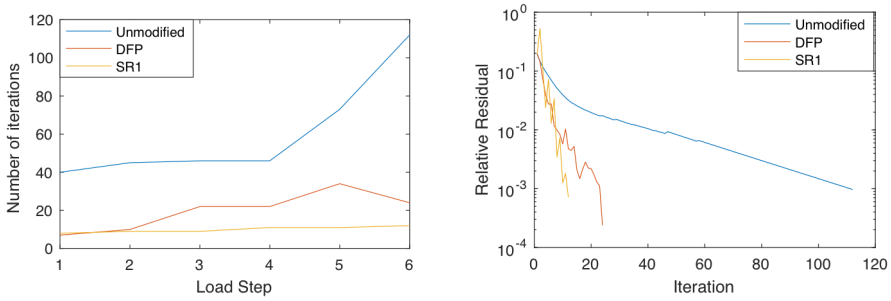


(a) (b)

**Figure 3.8.** Crack growth simulation: acceleration techniques comparison. (a) Crack spreading: dependence between crack length and convergence (b) Final crack propagation step: residual evolution.

It has been discussed that $\alpha_{\mathrm{i}}$ needs to be reduced as nonlinearity evolves. In the current case, $\alpha = 1$ leads to divergence and a smaller value is needed. This is because as nonlinearity evolves, the composed Schur complements $[\boldsymbol{A}_{\mathrm{i}}]^{-1} = \boldsymbol{S}^{G} + \boldsymbol{S}^{\tilde{G}}$ on the interface of the initial

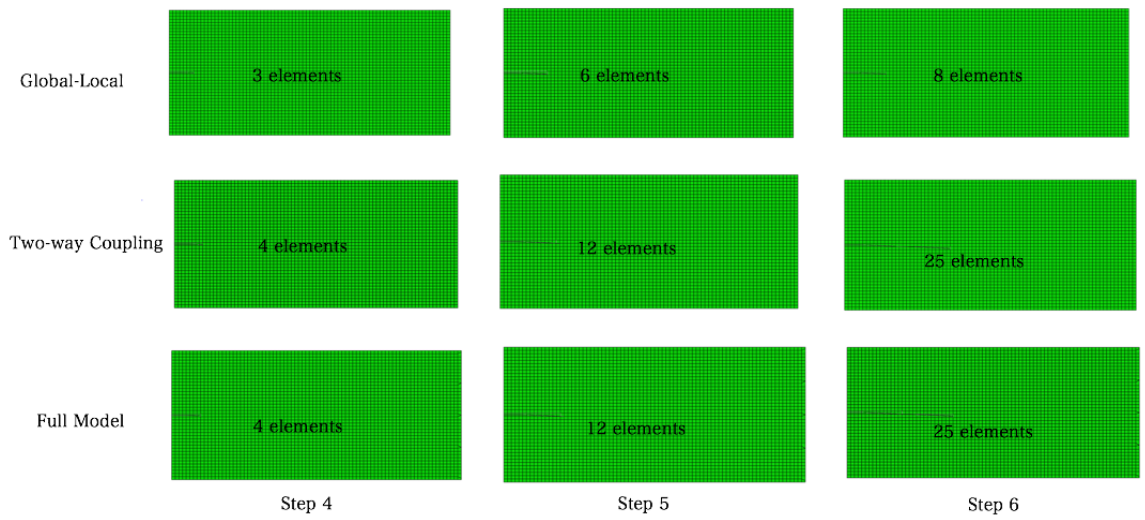


**Figure 3.9.** Comparison of crack propagation.

model is no longer a good estimate of $\nabla \boldsymbol{r}$. Reducing $\alpha_{\mathrm{i}}$ can eliminate this issue. Even though $alpha = 0.1$ led to convergence in the current case, it is not a general value. The bisection method discussed in Section 3.3.2 is the simplest approach for adaptive step length line search. It can automatically find better step length instead of using an arbitrary fixed step. The convergence study by choosing different $\alpha$ was conducted Figure 3.10. The adaptive step length converged faster than fixed step length with $\alpha = 0.1$. Moreover, it generated nearly monotonic decreasing of residual force.

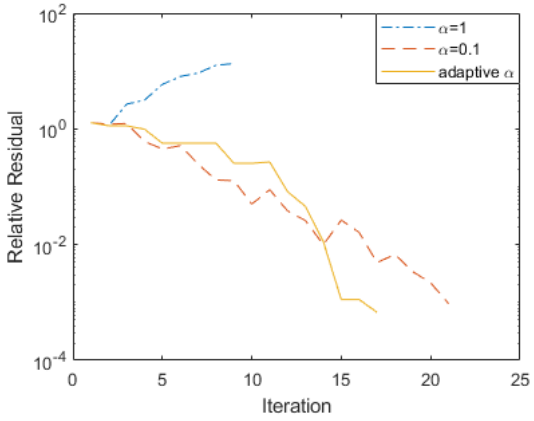


**Figure 3.10.** Convergence of relative residual by using different step length.

### 3.5.3 Plastic ratcheting in BEOL

Even though local non-linearity evolution may have great influence on the global field, it is not always the case. If the non-linear behavior is concentrated within a small region, the traditional global-local model technique will be accurate enough.

One failure mechanism observed in molded packages during accelerated thermal cycling is the cracking of passivation films deposited on the BEOL metal lines. When metal lines plastically deform due to ratcheting, the passivation overcoat accumulates stress at the corner upon temperature cycling and is eventually susceptible to fracture. This kind of failure is usually simulated using conventional global-local model method[105]. The problem was investigated using the proposed iterative two-way coupling.

A plane strain model was used to model a cross-section of the half-package shown in Figure 3.15. The size of the global model is $4000\mu m \times 900\mu m$. Aluminum lines with a thickness of 3 $\mu m$, and widths of 100 $\mu m$ were modeled.

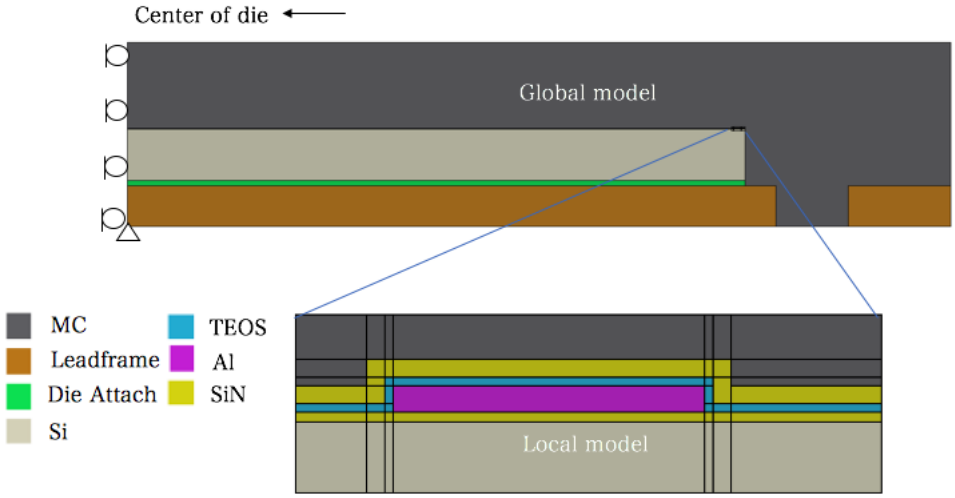


**Figure 3.11.** Cross section of the Package model. Insert figure shows the region enclosing the BEOL structure $\Omega_L$ that was analyzed in the local model.

The BEOL structure in the package contained passivation (composed of TEOS and SiN), aluminum, and epoxy mold compound materials. In the present study, all the materials except the aluminum line were treated as elastic. The yield strength of 100 MPa was used

for aluminum. The elastic behavior of die attach and mold compound materials was described through three temperature-dependent transition steps as listed in Table 3.1 and Table 3.2, respectively. The mechanical properties of other material used in the model may be found in Table 3.3.

**Table 3.1**. Elastic properties of die attach material.

| Temperature(°C) | $E$ (GPa) | $\nu$ | $\alpha$ (ppm/°C) |
|---|---|---|---|
| -65 | 10 | 0.35 | 50 |
| 75 | 10 | 0.35 | 50 |
| 125 | 0.5 | 0.35 | 100 |
| 260 | 0.5 | 0.35 | 100 |

**Table 3.2**. Elastic properties of mold compound.

| Temperature(°C) | $E$ (GPa) | $\nu$ | $\alpha$ (ppm/°C) |
|---|---|---|---|
| -65 | 30 | 0.35 | 10 |
| 85 | 30 | 0.35 | 10 |
| 115 | 1 | 0.35 | 10 |
| 260 | 1 | 0.35 | 10 |

**Table 3.3**. Temperature independent properties of other materials.

| **Mateiral** | $E$ (GPa) | $\nu$ | $\alpha$ (ppm/°C) |
|---|---|---|---|
| Leadframe | 123 | 0.34 | 17.6 |
| Passivation | 130 | 0.25 | 1.8 |
| Al | 70 | 0.33 | 23 |
| Si | 131 | 0.28 | 2.61 |

The global model was imported from a CAD geometrical model. It contained seven different materials. The global model contained 69,632 nodes defined on 23,159 quadratic elements with refined mesh around the BEOL (local) structure (Figure 3.12a). The displacements on the local region of the global model were extracted and applied as Dirichlet boundary conditions. For simplicity, structured quadrilateral mesh was adopted in meshing the local model containing 25,200 elements and 76,561 nodes. A local refined full model with 532049 nodes and 177184 elements is also computed as a reference solution(Figure 3.12b).

The test structure was assumed stress-free at 175°$C$, which is the temperature at which mold compound is applied. 20 thermal cycles from -65°$C$ to 150°$C$ were simulated. To

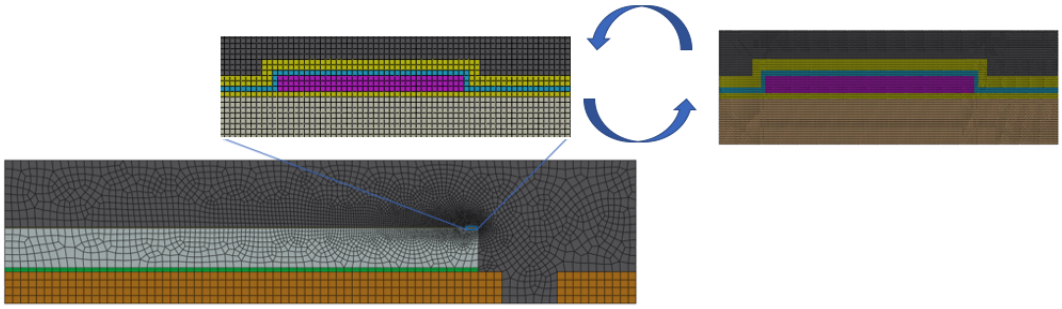

(a)

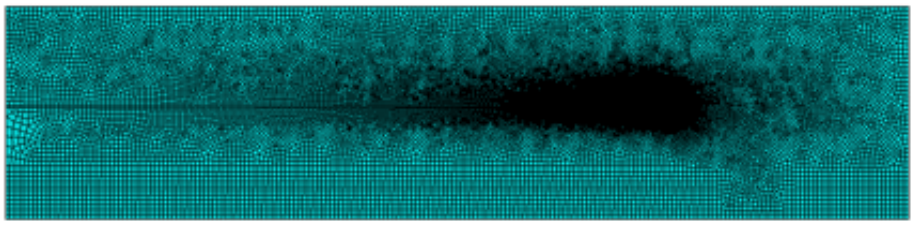

(b)

**Figure 3.12.** Discretization for (a) Global and local model (b) Refined full model

ensure equilibrium during the all process, each temperature reversal is divided into four load steps.

The relative residual tolerance is chosen to be $10^{-2}$. Figure 3.13 shows the maximum principal stress on the right corner of passivation layer at the end of $20^{th}$ cycle. It is obvious that one-way global-local method, two-way coupling model, as well as the refined full model generated almost identical solutions. Figure 3.14 illustrated the magnitude of maximum principal stress at each step on the same corner. The three curves coincided for all practical considerations. For the current example, the conventional global-local model was already accurate enough because the local non-linear behavior was only the plasticity in aluminum within a very small region, which did not have much influence on the global behavior.

### 3.5.4 Ductile fracture in solder joint using Maximum Entropy Fracture Model

Fatigue fracture is one of the major failure of solder joints in package structure under thermal cycling. However, modeling crack propagation of solder joints in electronic package is

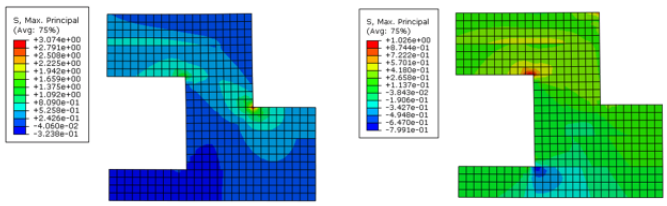

(a)

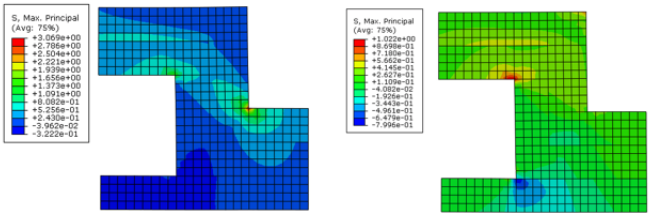

(b)

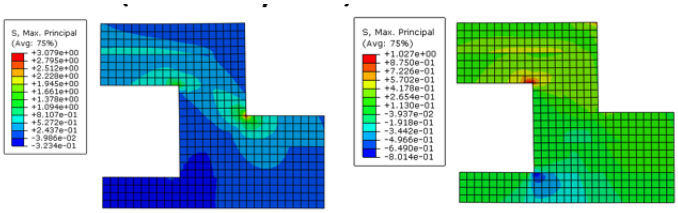

(c)

**Figure 3.13.** Maximum Principal Stress in the Passivation Corner at 150° C (left) and -65°C (right) of (a) One-way global local model (b) Two-way coupling and **??** Refined full model.

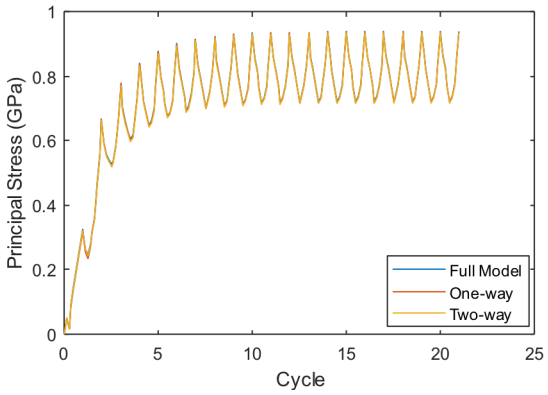


**Figure 3.14.** Comparison of principal stress at passivation corner

not a trivial task. The maximum entropy fracture model (MEFM) is a thermodynamically consistent and information theory inspired damage model for ductile solids. The model

uses a single damage accumulation parameter to relate the damage leading to fracture with accumulated entropic dissipation. It is a promising tool to predict the fatigue life of solder joints under cycling loading.

In MEFM, damage is correlated to plastic dissipation using the simplified form:

$$D = 1 - exp(\frac{W_t}{\rho k_\phi T}) \tag{3.79}$$

where $W_t$ denotes plastic dissipation, $\rho$ is density and $T$ is temperature. $k_\phi$ is called damage parameter, which is material property needs to be calibrated with experiment. At each step, Modulus of solder is updated with current damage state:

$$E = (1 - D)E_0 \tag{3.80}$$

Where $E_0$ is the initial modulus. In this method fracture path is represented by highly damage element, say $D > 0.95$. However, it is prohibitive to compute the plastic dissipation at each cycle due to computational cost.To accelerate the computational speed, inelastic dissipation is extrapolated using Taylor series expansion:

$$W_{n+1} \approx W_n + \frac{\partial W}{\partial N}(\Delta N) \tag{3.81}$$

For every pair of adjacent cycles, the increment of inelastic dissipation is computed and it is assumed to remain the same for the next $\Delta N$ cycles. For more details of the method, one can refer to the corresponding paper [106] .

To accurately capture the fracture initiation and growth, the mesh on a single solder joint needs to be sufficiently refined. However, refining the mesh of every single solder joint makes the computational cost of package-level model prohibitive.

The traditional strategy to reduce the modeling cost is to use a global-local model technique in which a coarse global package model is run to extract boundary conditions for a refined local model of the critical solder joint. This procedure is known to result in inaccurate fatigue crack because the crack growth in the solder joints influences the global behavior,

but they are not captured in the global model since the local damage is not communicated back to the global model in the sub-modeling procedure.

To consider the local influence on the global model, the two-way coupling method was applied. Consider the section of simplified package structure as shown in Figure 3.15. It was under thermal cycling ranging from $398K$ to $233K$. The initial temperature is assumed to be $398K$. Due to the mismatch of CTE between Si and PCB, solder joints was under shear during thermal cycling. Damage parameter $k_\phi$ is assumed to be $120J/(kgK)$ with $\Delta N = 100$.

The rightmost solder joint was the most critical since it underwent the largest relative shear displacement. However, local damage evolution occurred in every single joint and they all should have influenced the global behavior. To explore the influence of local non-linearity, three local models were constructed with the one, two and three rightmost solder joints respectively. The discretizaiton for global and local model of single solder joint is shown in Figure 3.16a. The global model contained 4145 nodes and 3980 elements. While the local model contained 7773 nodes and 7605 elements. A refined full model was also built with 22353 nodes and 22098 elements (Figure 3.16b).

Figure 3.17 compares the propagation of crack at $1001^{th}$ cycle and $2201^{th}$ for global-local model, two-way coupling model and full model . Fracture propagation was demonstrated by highly damage element ($d > 0.95$) marked in red. Crack initiates $1001^{th}$ cycle for all the three cases . However, the one-way global-local model underestimated the crack length compared to the full model at the $2201^{th}$ cycle. The two-way coupling was much closer to the full model solution in this case. This is because the global model failed to consider stiffness reduction of solder joints and thus the local displacement is underestimated as thermal cycles goes on. At the initial stage, there was little accumulated damage and therefore, the three methods give almost identical results for crack initiation. However, as damage accumulated, one-way global-local model failed to consider the stiffness reduction on all the solder joints and thus the relative shear displacement on the local model is underestimated. As thermal cycling went on, the gap between global-local model solution and reference solution (full model) became larger. The two way coupling method considered the local stiffness reduction and gave feedback to the global model. But there was still gap between full model and two-way

coupling method. This is because two-way coupling fails to consider the feedback from the other four solder joints, where stiffness reduction also happens. Extracting a larger local model with more solder joints can fill this gap but it is more computationally expensive.

The crack propagation on the rightmost is then compared with global-local model and full model in Figure 3.18 (two-way1, two-way2 ,two-way3 represents local models with 1, 2, 3 joints respectively). It can be seen that the relative crack length on the rightmost solder joint was highly underestimated when using global-local model, even though it was applied on the most critical solder joint. The iterative two-way coupling method, which allows feedback of nonlinear evolution from the local models with different number of solder joints, improved the accuracy by increasing the span of local model. This is because damage evolution in every solder joint contributes to the global behavior and reduce the shear stiffness between substrate and PCB. This reduction, in turn, results in more plastic dissipation and thus more damage during thermal cycling. Increasing the region of local model can mitigate this phenomenon. As can be seen in Figure 3.18, When local model includes three solder joints, the result was very close to the full model. What can be learned from this example is that when nonlinearity is spread over larger part of the domain, only considering the most critical region is not enough, because the nonlinear evolution over entire domain affects the global behavior. The iterative two-way coupling method therefore has no advantage over refined full model.

**Table 3.4**. properties of materials

| **Mateiral** | $E$ (GPa) | $\nu$ | $\alpha(ppm/K)$ |
|---|---|---|---|
| Si | 5 | 0.4 | 2.61 |
| Solder mask | 14 | 0.24 | 20 |
| Cu | 117 | 0.37 | 16.7 |
| PCB | 5 15 | 0.11 | 14.5 |
| Solder | 32 46 | 0.33 | 23 |

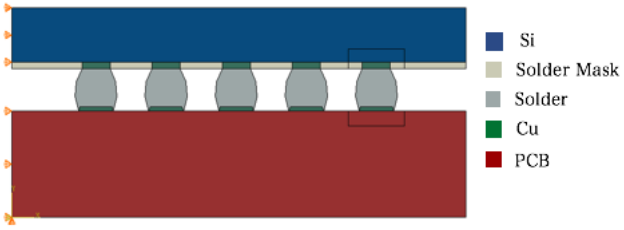


**Figure 3.15.** Boundary condition for two-dimensional solder joints under thermal cycling

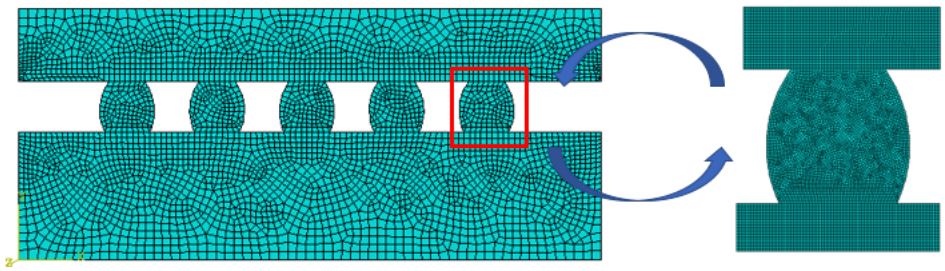

(a)

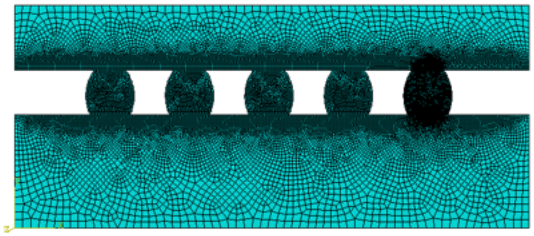

(b)

**Figure 3.16.** Dicretization for (a) Global and local model (b) Refined full model

### 3.5.5 Two-way Coupling through mixed computational platform: Copper Bump shear

The proposed method is also applicable for data transfer between different computational platform. We here demonstrate a copper bump shear example using both ABAQUS®and ANSYS®.

The structure is shown in Figure 3.19. A silicon pad of $1000\mu m \times 275\mu m$ is fixed at the bottom. The BEOL layer, redistribution layer(RDL) and polymer covered above it with thickness of $5\mu m$, $2\mu m$ and $1\mu m$ respectively. The size of Copper pillar is $80\mu m \times 50\mu m$. A

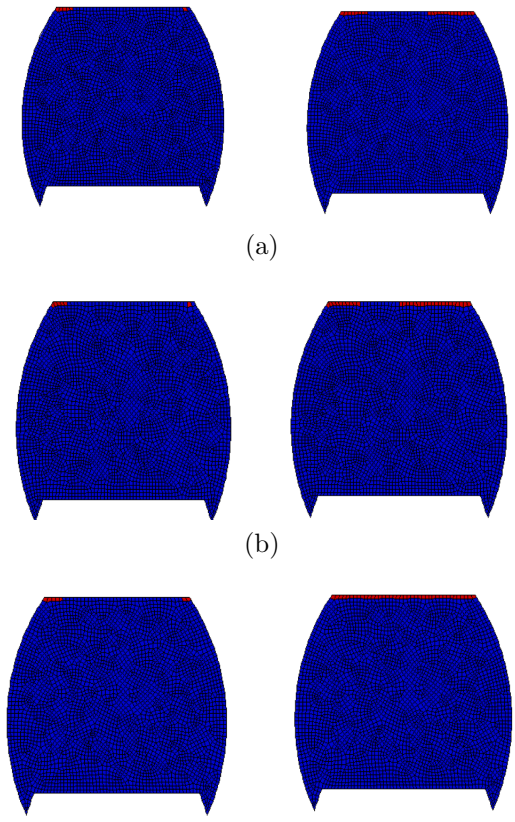

**Figure 3.17.** Crack propagation at 1001th cycle (left) and 2201th cycle (right) for (a) One-way global local model (b) Two-way coupling and (c) Refined full model.

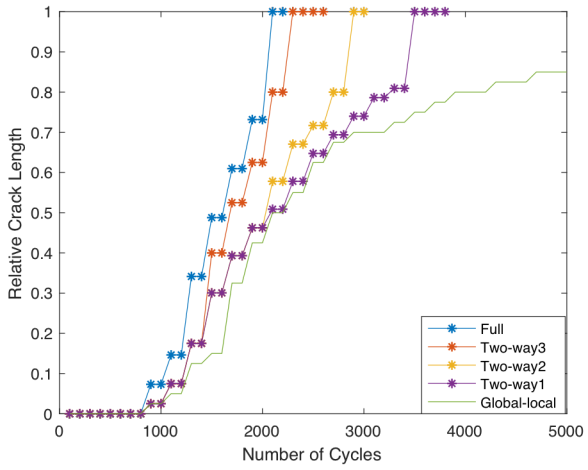


**Figure 3.18.** Comparison of relative crack length

diamond probe was used to shear the copper pillar. The magnitude of shear displacement was $0.2\mu m$. Under shear, crack initiated at the connection of copper and polymer and finally propagates into BEOL. The region near the connection was partitioned as the local model. The global model was built in ANSYS®with 1988 elements and 2069 nodes. While the local model, with pre-existing crack, was simulated by XFEM module in ABAQUS®with 8862 elements and 8547 nodes. A local refined full model was also built in ABAQUS with 18333 elements and 18475 nodes as a reference (Figure 3.20a). A pre-existing crack inserted through the polymer and RDL. The material property is listed in Table 3.5. BEOL was assumed to be homogeneous with critical maximum principal stress (maxps) to be $60MPa$. Damage evolution was displacement based and the displacement at failure was set to be $1\mu m$.

**Table 3.5**. properties of materials

| **Mateiral** | $E$ (GPa) | $\nu$ |
|---|---|---|
| Polymer | 5 | 0.4 |
| RDL | 9 | 0.2 |
| Cu | 117 | 0.34 |
| BEOL | 100 | 0.25 |
| Si | 131 | 0.28 |
| Diamond | 1000 | 0.1 |

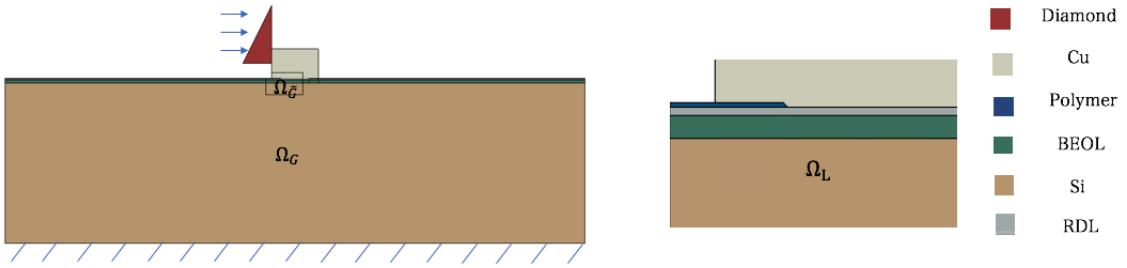


**Figure 3.19.** Bump shear: model setup

The displacement solution for both global and local model are illustrated in Figure 3.21. The solution of the entire structure will be the composition of global solution in $\Omega_G$ and local solution in $\Omega_G$.

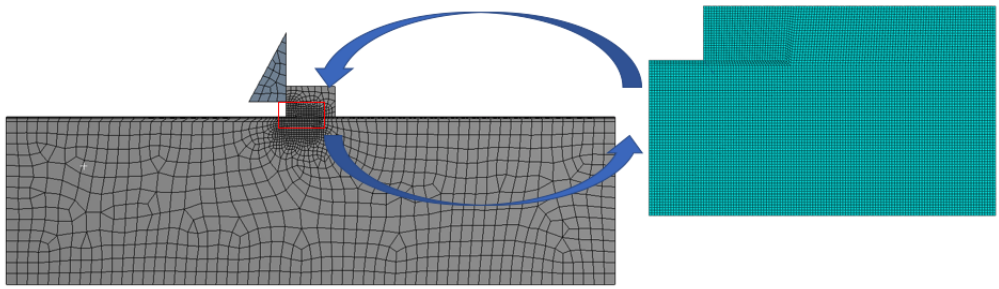

(a)

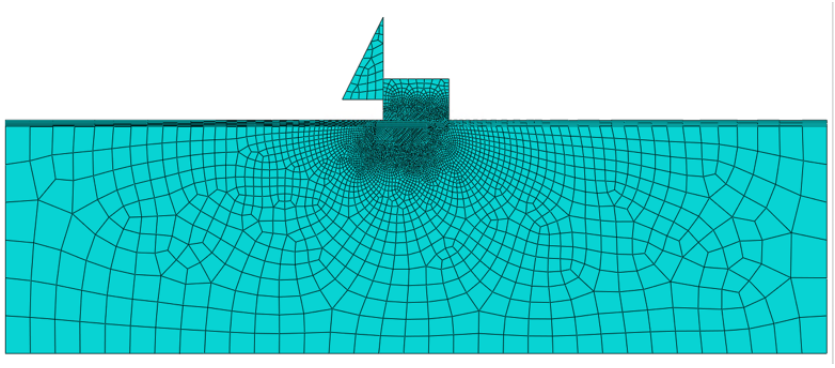

(b)

**Figure 3.20.** Discretization of (a) Global model in ANSYS and Local model using ABAQUS (b) Refined full model in ABAQUS

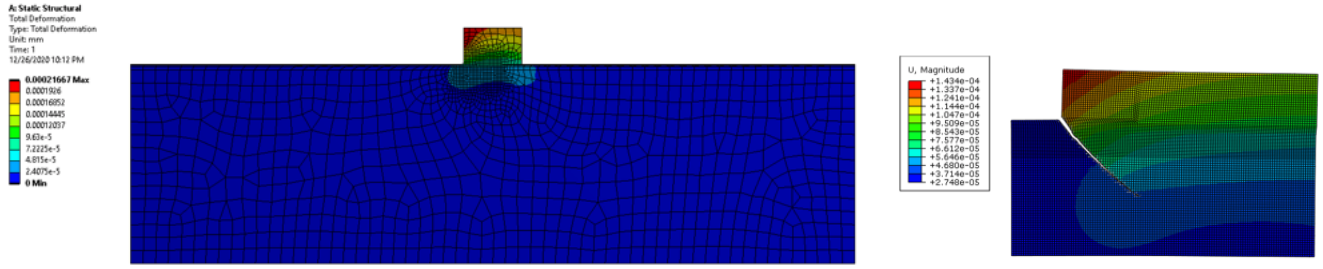


(a) (b)

**Figure 3.21.** Displacement field of (a) Global model using ANSYS and (b) Local model using ABAQUS

Figure 3.22 compares the crack propagation length using different models. Crack propagated only 16 elements for global-local model method, while it propagated 35 elements for two-way coupling and 37 elements for refined full model. As explained before, this is because the one-way global model fails to consider global influence from the local model. The iter-

ative two-way coupling highly improved the accuracy with considering feedback from local model on the global region.

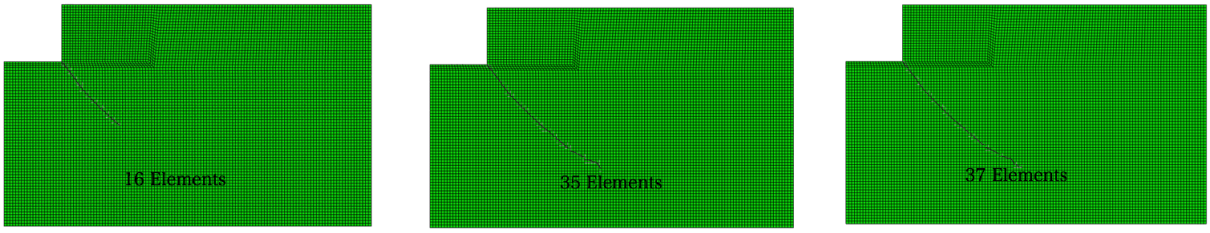


(a) (b) (c)

**Figure 3.22.** Crack propagation for (a) One-way global local model (b) Two-way coupling and (c) Refined full model.

## 3.6 Summary

In this chapter, a non-intrusive computational strategy for iterative solution to nonlinear behavior in a decomposed domain was proposed. Since the method is non-intrusive, no access to the stiffness matrix is necessary, and only the displacement at the sub-domain interface is necessary. The method allows global-local domain subdivision with the non-linearity confined to a small local region. The code- and mesh-agnostic nature of the developed method allows one to couple models with different discretizations that may be analyzed on either commercial finite element or custom solvers. In the developed method, the interfacial displacement is iteratively modified using quasi-Newton updates until convergence. The two aspects of the iterative displacement correction are (1) evaluating the unbalanced force (2) reducing the unbalance force and updating the displacement field. To calculate the unbalanced force, two methods were proposed based on variational principle with intermediate framework: global Lagrange multiplier (GLM) method and the local Lagrange multiplier (LLM) method. Overall, GLM is more accurate but since it requires integration, it is computationally more expensive. LLM is relatively less expensive but is also relatively inaccurate, especially for sub-domains with non-matching mesh. To reduce, the unbalanced force, the initial stiffness of the global model is used to approximate the Jacobian matrix, and the residual force is applied as a force input on the intact model to solve for displacement update at the

interface. In this manner, the need for access to the internals of a commercial finite element code are obviated. To accelerate the convergence, SR1 update and BFGS updates were used. Numerical examples indicated that SR1 was more efficient than the BFGS update. An adaptive step-length procedure based on the bisection method was used in the present study.

Numerical examples were solved to illustrate analysis of engineering structures. The method was first validated on several examples including an L-shaped domain with local non-linearity and a rectangular plate with a propagating crack. Plastic ratcheting in BEOL structures in a semiconductor chip as well as fatigue fracture in solder joints under thermal cycling were simulated using the developed method. It was observed that when the non-linear region is very small, a one-way global-local model is accurate enough relative to the two-way coupled solution. However, when the non-linear region nearly covers the entire domain, there is no significant advantage to domain sub-division. Finally, A bump shear example was used to demonstrate the coupling of domains analyzed using different commercial finite element software.

# 4. IMMERSED ISOGEOMETRIC ANALYSIS WITH DIRECT BOUNDARY CONDITION IMPOSITION

In engineering analysis, the task of Computer Aided Design (CAD) is to accurately capture the geometry of the modeled objects, while the task for Computer Aided Engineering (CAE) is to estimate numerical solutions to the partial differential equations (PDEs) that govern the behavior. Historically, the two phases of engineering analysis used different mathematical representations. Most CAD systems adopt Non-Uniform Rational B-Spline (NURBS) representation, while CAE commonly employs Lagrangian interpolations that are central to finite element analysis. Therefore, using identical mathematical representation for geometry and behavior would enable efficient CAD-CAE integration. Building behavioral approximations using the same parametric spline basis as geometry was proposed early by Subbarayan and co-workers among others [107]–[110]. The use of such approximations for analysis is at present popularly referred as Isogeometric Analysis (IGA) [7].

## 4.1 Immersed B-rep Analysis using Enriched

Currently, most CAD systems utilize boundary representation (B-rep) models constructed from trimmed Non-Uniform Rational B-Splines (NURBS) patches. The IGA models, on the other hand, commonly assume the availability of volumetric tensor product splines that 'mesh' the domain. The mesh generation process typically replaces the original B-rep model with a volumetric spline representation [111]–[113]. In this sense, volumetric discretization in IGA plays the same role as mesh generation in finite element analysis. Thus, although the original motivation of IGA is to narrow the gap between CAD and CAE, in practice, considerable intermediate steps remain between B-rep CAD models and analysis suitable IGA models.

An alternative approach to constructing analysis suitable tri-variate splines is to immerse the B-rep model within a regular grid in space containing analysis unknowns. This idea originates from the finite element community and is called immersed boundary method [114] (or finite cell method, fictitious domain method, embedded domain method). The fundamental

strategy is to extend the physical domain of interest beyond its complex parametric boundaries into a larger embedding domain of a simpler geometry, thus allowing for a simpler structured grid. In the immersed boundary method, the mesh does not conform to the B-rep model boundary. The challenge of generating analysis suitable mesh is converted to one of accurately representing the physical fields and carrying out numerical quadrature precisely in the immersed domain.

When the analysis grid does not conform to the B-rep model boundary, no behavioral degree of freedom exists directly on the essential boundary of the physical domain for one to apply the boundary condition directly. This challenge, common to nearly all meshfree approximations including moving least square [115] and reproducing kernel [116] methods, necessitates weak imposition of boundary conditions through one of many possible techniques including the penalty functions [12], Lagrange multipliers method [11], Augmented Lagrangian [117], or Nitsche's method [13]. The challenge of applying boundary conditions is not restricted to immersed boundaries, but also exists when volumetric NURBS patches are used for analysis since the behavioral degrees of freedom are associated with the control points and not the geometrical boundary. Similar to other mesh free method basis functions, the NURBS basis does not interpolate the control or nodal points. The non-interpolatory nature of the basis functions necessitates the earlier mentioned approaches to the application of the essential boundary conditions.

In general, direct application of boundary condition is an issue for mesh free approximation of fields, specifically, immersed boundary method. Furthermore, the point classification is tedious and computational expensive. Both task are not efficiently addressed in prior literature. So they are the goal of this paper.

In the current research, a new approach to analyze complex B-rep models immersed in regular grids is proposed. A specific form for direct boundary condition application based on Enriched Isogeometric Analysis (EIGA [118]) is proposed. In EIGA, the boundaries as well interfaces are explicitly represented by lower-dimensional NURBS entities with additional degrees of freedom directly specified on the control points of the interface geometry. Furthermore, the field approximation on the continuous domain is enriched with an approximation with known characteristics defined on the enriching boundaries. For instance, the enriching

boundary may correspond to a crack, in which case the enrichment must possess the known physical behavior such as displacement discontinuity on the boundary. The influence of any enrichment, behavioral or otherwise, is generally expected to decrease with distance (see for instance heterogeneous material modeling using distance fields [119]). Thus, the composition of the enriching boundary is restricted to a local region as dictated by a weight function that varies monotonically with respect to distance from the boundary. In our prior work, a monotonic measure of approximate distance was constructed using algebraic level sets [120], [121]. Furthermore, the sign of the algebraic level sets constructed on bounded solids enables the point membership query for CAD/CAE applications.

### 4.2 Boundary Condition Application

In the original description of isogeometric analysis [7], the essential boundary conditions were directly applied to the control variables. We refer to this approach is as direct imposition of Dirichlet boundary conditions. A direct application of boundary conditions on control points is reasonable if control points don't coincide with points of application of the essential boundary condition on the domain.

In the immersed boundary method, the essential boundary conditions are often applied using a weak form, in which the integral of the displacement constraint on the boundary is set to zero. That is, the constraint is enforced in an averaged sense than point by point. The weak form constraint is most commonly enforced using Lagrange multipliers [11]. However, the use of Lagrange multipliers to enforce the constraint may cause the solution matrix system to lose its positive definiteness. On the other hand, the penalty method [12] and Nitsche's method [13] require only the selection of one scalar parameter. In the penalty method, the selected parameter must be large enough to ensure the accurate enforcement of the essential boundary conditions, while too large a value leads to ill-conditioned system of equations. In comparison, Nitsche's method does not suffer from ill-conditioning. However, an empirical stabilization parameter is needed, so the implementation of Nitsche's method is not as trivial as the Lagrange multiplier method or the penalty method; the choice of the stabilization parameter will depend on the problem at hand. In this paper, we propose a new

method to apply boundary conditions based on the theory of Enriched Isogeometric Analysis (EIGA). In EIGA, the boundaries are treated as lower-dimensional enrichments. Extra degrees of freedom are added to the control points of the boundary. The field approximation on the domain is enriched with an approximation near the enriching boundaries through a blending function. The method also allows the direct application of the boundary condition on the enrichment.

### 4.2.1 Enriched Isogeometric analysis

The concept of enriched field approximations is enabled by Partition of Unity Finite Element Method (PUFEM) [122] and the Generalized Finite Element Method(GFEM) [123]. In GFEM, the underlying finite element approximation is generalized by adding degrees of freedom representing complex local behavior. Convergence of the approximations is ensured by the partition of unity property of the finite element shape functions. In other words, the FE approximation space is "enriched" by the known local behavior. As demonstrated by Strouboulis [123], the concept of GFEM can be applied to problems with known behaviors including boundary conditions, displacement discontinuity at a crack face, and asymptotic behavior near reentrant corners. Tambat and Subbarayan [118] proposed the so called Enriched Isogeometric Analysis wherein they enriched known behavior on the explicitly defined lower-dimensional geometric features. The base approximations are "enriched" isogeometrically on parametrically defined lower-dimensional geometrical features and by constructing distance fields from them. Both the underlying domain and the lower-dimensional geometry are represented by Non-Uniform Rational B-Splines (NURBS). The EIGA blending function for an arbitrary field is:

$$f(x) = (1 - \sum_{\mathrm{i}=1}^{n_{\mathrm{e}}} w_{\mathrm{i}}) f_{\Omega}(x) + \sum_{\mathrm{i}=1}^{n_{\mathrm{e}}} w_{\mathrm{i}} f_{\Gamma_{\mathrm{i}}}(\mathcal{P}(x)) \tag{4.1}$$

where, $\Omega$ is the underlying domain and $f_{\Omega}$ is the associated continuous field, $\Gamma_{\mathrm{i}}$ is the $\mathrm{i}^{th}$ lower dimensional geometry (internal/external boundary) with $f_{\Gamma_{\mathrm{i}}}$ being the corresponding enriching approximation. To compute $f_{\Gamma_{\mathrm{i}}}$ at a spatial point $\mathbf{x}$ in $\Omega$, it is necessary to project

the point onto the boundary $\mathbf{u_f} = \mathcal{P}(x)$ to map $\mathbf{x}$ to the parametric space of the lower-dimensional geometry $C(\mathbf{u})$. A general illustration of EIGA with single enrichment is shown in Figure 4.1. $w_{\mathrm{i}}$ is the weight function, which represents the contribution of i$^{th}$ enrichment

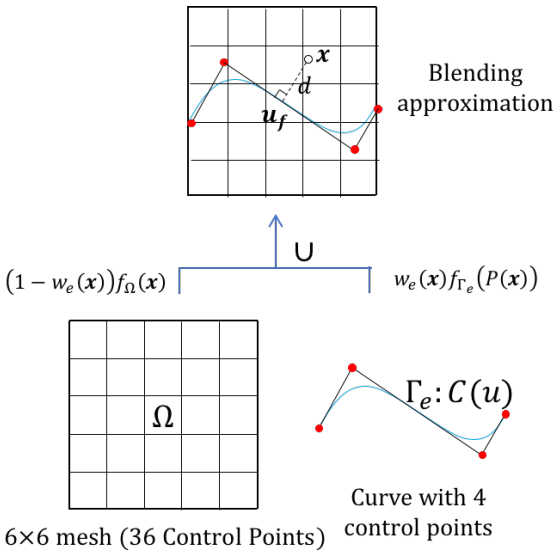


**Figure 4.1.** Graphical illustration of constructing Enriched Isogeometric approximation

to the blending function. It is a monotonically decreasing function of distance. There are multiple choices for the form of $w(d)$ including exponential, cubic and quartic among others, but they must satisfy the following conditions:

The weight functions used in the present paper are listed below and illustrated in Figure 4.1: Cubic

$$w(\bar{d}) = \begin{cases} 1 - 3\bar{d}^2 + 2\bar{d}^3 & 0 \leq \bar{d} < 1 \\ 0 & \bar{d} \geq 1 \end{cases} \tag{4.2}$$

Quartic

$$w(\bar{d}) = \begin{cases} 1 - 6\bar{d}^2 + 8\bar{d}^3 - 3\bar{d}^4 & 0 \leq \bar{d} < 1 \\ 0 & \bar{d} \geq 1 \end{cases} \tag{4.3}$$

Exponential [124]

$$w(\bar{d}) = \begin{cases} 1 - \frac{1-e^{-(\bar{d}/\alpha)^p}}{1-e^{-|1/\alpha|)^p}} & 0 \leq \bar{d} < 1 \\ 0 & \bar{d} \geq 1 \end{cases} \tag{4.4}$$

where $\bar{d} = d/d_{max}$, $d_{max}$ is the cutoff distance distance of the blending region from the enriching entity.

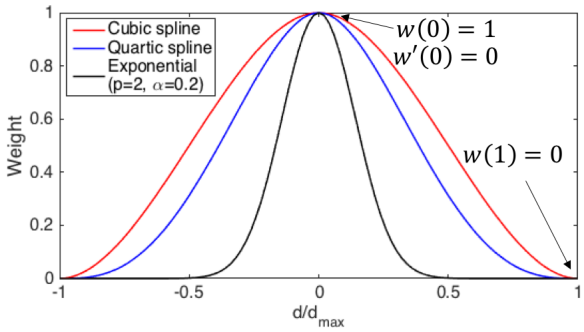


**Figure 4.2.** Possible mathematical forms of the weight functions

### 4.2.2 Boundary Conditions as Enrichments

The blending strategy of EIGA can be easily applied to enforce boundary conditions. This is especially useful when a parametric boundary is immersed into a regular analysis grid, since one can apply the boundary conditions directly on the control points of the NURBS geometry rather than weakly enforce them over the surface. To accurately capture the behavior near the boundary, an isogeometric approximation with hybrid function/derivative enrichment is proposed in the present paper. This enriched approximation is a smooth blending of $C^1$ or higher order continuous isogeometric approximation of underlying domain enriched with a $C^0$ continuous local approximation. (Eq. (4.5)) illustrates the mathematical form of the enrichment and its associated extra degrees of freedom.

$$\mathbf{u}(x) = (1 - w^e(d))\mathbf{u}^c(x) + w^e(d) * (\mathbf{u}^e(\mathcal{P}(x)) + d * \mathbf{G}^e(\mathcal{P}(x))) \tag{4.5}$$

The $\mathbf{u}^c$ term in (Eq. (4.5)) corresponds to the contribution of the approximation in the underlying domain, while the second part is from the enrichment. $\mathbf{u}_\mathrm{e}$ represents the motion of the boundary while $\mathbf{G}^\mathrm{e}$ represents the normal derivative of the displacement on the enrichment. The discretization of $\mathbf{u}^c$, $\mathbf{u}^\mathrm{e}$ and $\mathbf{G}^\mathrm{e}$ are as follows:

$$\mathbf{u}^c = \sum_{n=1}^{n^c} \mathbf{N}_\mathrm{i}{}^c \mathbf{u}_\mathrm{i}{}^c \tag{4.6}$$

$$\mathbf{u}^\mathrm{e} = \sum_{n=1}^{n^\mathrm{e}} \mathbf{N}_\mathrm{i}{}^\mathrm{e} \mathbf{u}_\mathrm{i}{}^\mathrm{e} \tag{4.7}$$

$$\mathbf{G}^\mathrm{e} = \sum_{n=1}^{n^\mathrm{e}} \mathbf{N}_\mathrm{i}{}^\mathrm{e} \mathbf{G}_\mathrm{i}{}^\mathrm{e} \tag{4.8}$$

where, $\mathbf{u}^c$, $\mathbf{u}^\mathrm{e}$, $\mathbf{G}^\mathrm{e}$ are the fields to be solved, and $\mathbf{u}_\mathrm{i}^c$, $\mathbf{u}_\mathrm{i}^\mathrm{e}$, $\mathbf{G}_\mathrm{i}^\mathrm{e}$ are the discrete unknown values at the $\mathrm{i}^{th}$ control point, $N_\mathrm{i}^c$ and $N_\mathrm{i}^\mathrm{e}$ are the rational NURBS basis functions corresponding to the underlying domain and the boundary respectively.

The matrix form of Eq. (4.5) is:

$$\mathbf{u} = \begin{bmatrix} (1 - W^\mathrm{e})\mathbf{N}^c & W^\mathrm{e} N^\mathrm{e} & W^\mathrm{e} dN^\mathrm{e} \end{bmatrix} \begin{Bmatrix} u^c \\ u^\mathrm{e} \\ G^\mathrm{e} \end{Bmatrix} \tag{4.9}$$

The corresponding strain field is

$$\varepsilon = \nabla_s \mathbf{u} = \begin{bmatrix} \mathbf{B} \end{bmatrix} \begin{Bmatrix} \mathbf{u} \end{Bmatrix} \tag{4.10}$$

with

$$\nabla_s = \begin{bmatrix} \frac{\partial}{\partial x} & 0 \\ 0 & \frac{\partial}{\partial y} \\ \frac{\partial}{\partial y} & \frac{\partial}{\partial x} \end{bmatrix} \tag{4.11}$$

$$\begin{bmatrix} \mathbf{B} \end{bmatrix} = \begin{bmatrix} B^c & B^\mathrm{e} & B^G \end{bmatrix} \tag{4.12}$$

where

$$
\begin{aligned}
B^c &= (1 - w^{\mathrm{e}})\nabla_s N^c - \nabla_s w^{\mathrm{e}} N^c \\
B^{\mathrm{e}} &= \nabla_s w^{\mathrm{e}} N^{\mathrm{e}} + w^{\mathrm{e}} \nabla_s N^{\mathrm{e}} \\
B^G &= \nabla_s d w^{\mathrm{e}} N^{\mathrm{e}} + d \nabla_s w^{\mathrm{e}} N^{\mathrm{e}} + d w^{\mathrm{e}} \nabla_s N^{\mathrm{e}}
\end{aligned}
\tag{4.13}
$$

The linear equation system resulting from the discretization that needs to be solved has the form:

$$
\begin{bmatrix} K^{cc} & K^{c\mathrm{e}} & K^{cG} \\ K^{\mathrm{e}c} & K^{\mathrm{ee}} & 0 \\ K^{Gc} & 0 & K^{GG} \end{bmatrix} \begin{Bmatrix} \mathbf{u_c} \\ \mathbf{u_e} \\ \mathbf{G} \end{Bmatrix} = \begin{Bmatrix} 0 \\ \mathbf{f_e} \\ 0 \end{Bmatrix}
\tag{4.14}
$$

where,

$$
\left[K^{IJ}\right] = \int_{\Omega} B^{I^T} D B^J d\Omega
\tag{4.15}
$$

with I,J representing $c$, e and $G$.

### 4.2.3 Dirichlet Boundary Conditions

In the immersed boundary method, the boundary in general does not coincide with the edge of the element. In the present study, the Dirichlet boundary conditions are enforced point-wise on the enrichment boundary as described below.The boundary is represented by a closed curve $\Gamma$, the Dirichlet and Neumann boundary condition are applied on part of $\Gamma$, which are marked as $\Gamma_d$ and $\Gamma_n$ in Figure 4.3. To apply the boundary condition, $\Gamma_d$ and $\Gamma_n$ are extracted from the B-rep CAD model and reparametrized as two NURBS entities $\Gamma_d(t)$ and $\Gamma_n(t)$ varying with parameter $t$. The boundary conditions are now applied on the control points of the above NURBS entities.

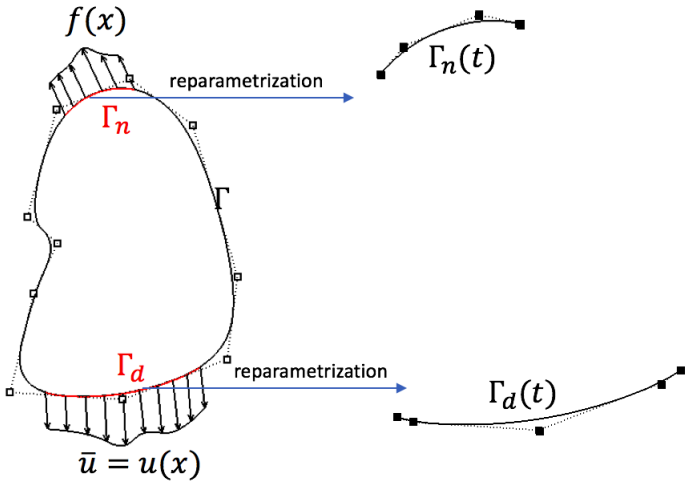


**Figure 4.3.** Boundary reparametrization (The subregions of the boundary where Dirichlet or Neumann conditions are applied are extracted and reparametrized so boundary conditions may be directly imposed on the newly generated control points)

The homogeneous boundary conditions ($\mathbf{u}^{\mathrm{e}} = 0$) can be easily applied by setting $\mathbf{u}_{\mathrm{i}}^{\mathrm{e}} = 0$ in Eq. (4.7)). Similarly, if the value of Dirichlet boundary conditions is a non-zero constant, every $\mathbf{u}_{\mathrm{i}}^{\mathrm{e}}$ in Eq. (4.7)) is set to the constant value; the partition of unity property of the basis function will ensure a constant displacement on the whole enrichment boundary. In the general case of inhomogeneous Dirichlet boundary condition, the varying value may only be enforced approximately. In the present study, a least squares solution is used to determine the value $\mathbf{u}_{\mathrm{i}}$ to be enforced on each control point of the Dirichlet boundary. Let the distribution of the displacement vector field $\mathbf{u}(\mathbf{x})$ on the boundary be of an arbitrary form $\mathbf{u}(\mathbf{x}(t))$, where, $t$ is the parametric description of the reparametrized region $\Gamma_d$, on which the condition is applied, and $\mathbf{x}$ are the cartesian coordinates corresponding to the parametric location. The problem now is to minimize the function:

$$f(\mathbf{u}_{\mathrm{i}}) = \int \left[ \mathbf{u}(\mathbf{x}(t)) - \sum_{\mathrm{i}=0}^{n} N_{\mathrm{i}}(t)\mathbf{u}_{\mathrm{i}} \right]^2 dt \tag{4.16}$$

and the optimality condition is:

$$\frac{\partial f}{\partial \mathbf{u}_\mathrm{j}} = -2 \int N_\mathrm{j} \left[ \mathbf{u}(t) - \sum_{\mathrm{i}=0}^{n} N_\mathrm{i}^T(t) \mathbf{u}_\mathrm{i} \right] dt = 0 \tag{4.17}$$

This will yield the following linear system for the unknown control point values of the vector $\mathbf{u}_\mathrm{i}$:

$$\left[ \int N_\mathrm{j}(t) N_\mathrm{i}^T(t) dt \right] \mathbf{u}_\mathrm{i} = \int N_\mathrm{j} \mathbf{u}(t) dt \tag{4.18}$$

The solution to the linear system is then enforced as the appropriate control point quantities $\mathbf{u}^\mathrm{e}$ in Eq. (4.7)).

### 4.2.4 Neumann Boundary Conditions

Let the distributed load on the boundary be of the form $\mathbf{f}(\mathbf{x})$ applied on the reparametrized region $\Gamma_n$ on which the Neumann condition is applied, and $\mathbf{x}$ is the physical coordinate. Here, we seek a work equivalent force $\mathbf{f}_\mathrm{i}$ of the form:

$$\int \mathbf{f}(\mathbf{x}) \delta \mathbf{u} d\mathbf{x} = \sum_\mathrm{i} \mathbf{f}_\mathrm{i} \delta \mathbf{u}_\mathrm{i} \tag{4.19}$$

where, $\delta \mathbf{u}(\boldsymbol{x})$ is a virtual displacement applied on the boundary $\Gamma_n$, and $\delta \mathbf{u}_\mathrm{i}$ are the control point values of the discretized virtual displacement $\delta \boldsymbol{u}(\boldsymbol{x})$. The control points here correspond to the reparametrized curve shown in Figure 4.3. Since a work equivalent force is to be defined on the control points of the boundary surface parametrized by $t$, a change of variables from $\mathbf{x}$ to $t$ is necessary to apply the Neumann condition

$$\mathbf{f}_\mathrm{i} = \int N_\mathrm{i}(\mathbf{x}) \mathbf{f}(\boldsymbol{x}) d\mathbf{x} = \int N_\mathrm{i}(t) \mathbf{f}(\boldsymbol{x}(t)) \left| \frac{d\boldsymbol{x}}{dt} \right| dt = \int N_\mathrm{i} \mathbf{f}(t) |J| dt \tag{4.20}$$

where, $J$ is the Jacobian associated with the variable change:

$$J_{pq} = \frac{\partial x_p}{\partial t_q} \tag{4.21}$$

where, $x_p$ is the $p^{\text{th}}$ component of $\mathbf{x}$. This is very similar to Neumann boundary application in FEM, where equivalent force is applied on the corresponding nodes on the Neumann boundary. Using Eq. (4.20)), the value of $\mathbf{f^e}$ is enforced in Eq. (4.14)).

### 4.2.5 Illustration with a One-Dimensional Example

To illustrate the boundary condition application, as shown in Figure 4.4, a one-dimensional bar under tension is immersed in either a domain fitting discretization (conforming boundary) or in a larger domain (non-conforming boundary). In this problem, the two end points of the bar represent the boundary. The bar is immersed in a background B-spline mesh. The background is discretized into 5 knot spans using 7 control points. The corresponding basis functions are shown in Figure 4.5, where $N_{\text{i,2}}$ refers to the i$^{th}$ basis function of degree 2. When the immersed geometry conforms to the background discretization, homogeneous Dirichlet boundary condition at point $P_0$ is enforced by constraining the end control point $P_0$. The Neumann boundary condition, on the other hand, is applied as an enrichment.

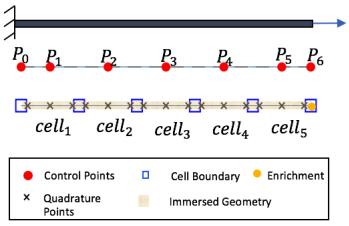


(a)

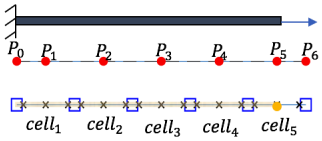


(b)

**Figure 4.4.** A one-dimensional immersed boundary example (a) Case 1: Immersed domain conforming to background discretization (b) Case 2: Immersed domain not conforming to background discretization

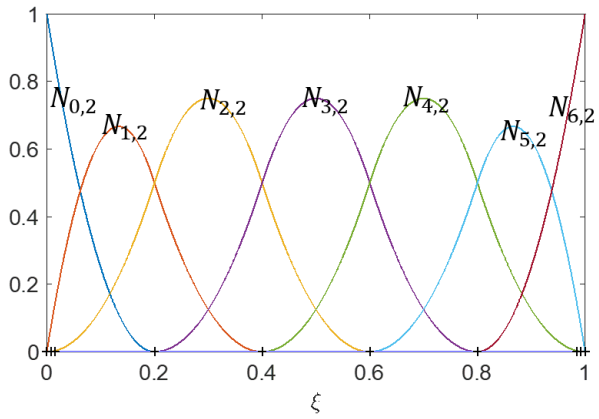


**Figure 4.5.** B-spline basis functions of the background domain

In the first case, the enrichment is conformal with the boundary of the cell (Figure 4.4a). The location of the enrichment is coincident with control point $P_6$. Two degrees of freedom, $u^{\mathrm{e}}$ and $u^{G}$ associated with the enrichment will now be added to the system. We can then rewrite Eq. (4.9) as

$$\mathbf{u} = \begin{bmatrix} \hat{\mathbf{N}}_{\mathrm{i}} & \hat{N}_{\mathrm{e}} & \hat{N}_{G} \end{bmatrix} \begin{Bmatrix} u^{c} \\ u^{\mathrm{e}} \\ G^{\mathrm{e}} \end{Bmatrix} \tag{4.22}$$

where, $\hat{\mathbf{N}}_{\mathrm{i}} = (1 - W^{\mathrm{e}})\mathbf{N}_{\mathrm{i}}^{c}$, $\hat{N}_{\mathrm{e}} = W^{\mathrm{e}}N^{\mathrm{e}}$, $\hat{N}_{G} = W^{\mathrm{e}}N^{\mathrm{e}}d$ are the modified basis functions corresponding to each degree of freedom. The influence of enrichment does not extend outside of $cell_5$. Therefore, the influence of $N_{\mathrm{e}}$ and $N_G$ also do not extend outside of $cell_5$. Due to the blending of the enrichment, the basis functions $N_4$, $N_5$, and $N_6$ in $cell_5$ are modified as shown in Figure 4.6a. In the second case, the immersed domain does not conform to the background discretization as shown in Figure 4.4b. The right end of the immersed bar is located in the middle of $cell_5$. In this case, it is not possible to apply the boundary condition directly on the end control point. The underlying domain is now enriched at the end point of the immersed bar. The basis function value at points outside the immersed domain are set to equal to zero as shown in Figure 4.6b. In this example, the blending region covers both $cell_4$ and $cell_5$, and so $N_3$ to $N_6$ require to be modified in the immersed domain. The modification ensures that the partition of unity property still holds.

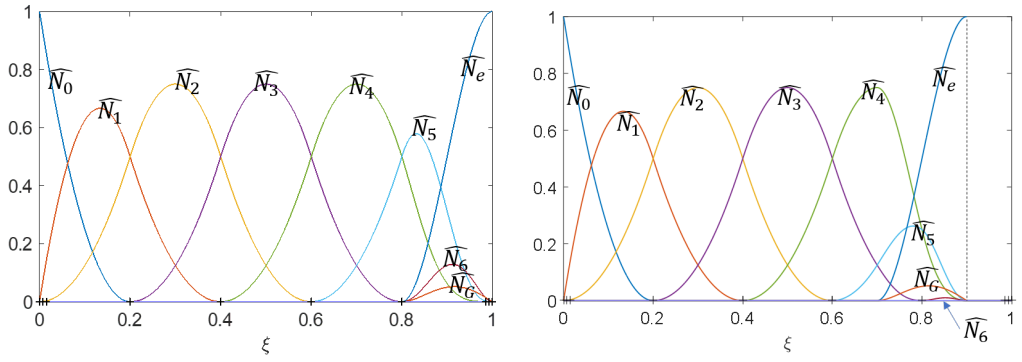


**Figure 4.6.** Basis functions of the enriched approximations (a) Immersed boundary conforming to the background discretization (b) Immersed boundary not conforming to the background discretization

### 4.2.6 Patch Test

To validate the developed method, a 'patch' test for both Dirichlet and Neumann conditions is conducted. The patch test is intended to verify that the blended numerical approximation is able to reproduce uniform displacement derivative or stress values. The chosen immersed region is of size $1 \times 1$ with a Young's modulus value of 1 and Poisson's ratio of 0.3. The bottom edge is fixed and the top edge is under tension as shown in Section 4.2.6. A homogeneous Dirichlet condition is applied at the bottom. On the top, a Dirichlet condition of constant displacement $u_y = 1$ (Figure 4.7a) or a Neumann condition of uniform stress of $f_y = 1$ (Figure 4.7b) are applied. The patch is immersed in a B-spline discretization with regularly spaced control points. A convergence study is also conducted with different cell sizes. Elasticity theory dictates identical solution with a linearly varying displacement in the vertical direction in both cases.

In the study, two error norms - energy norm (Eq. (4.23)) and displacement norm (Eq. (4.24)) - are defined to measure the error between the exact solution and numerical solution. In addition, the influence of the weight functions listed in Eq. (4.2)-(Eq. (4.4) are also evaluated.

$$error_{\mathrm{e}} = \left\{ \frac{1}{2} \int (\varepsilon^{num} - \varepsilon^{exact}) : D : (\varepsilon^{num} - \varepsilon^{exact}) d\Omega \right\}^{1/2} \tag{4.23}$$

$$error_d = \left\{ \int (\mathbf{u}^{num} - \mathbf{u}^{exact}) \cdot (\mathbf{u}^{num} - \mathbf{u}^{exact}) d\Omega \right\}^{1/2} \tag{4.24}$$

where $\mathbf{u}^{num}$ is the numerical result of displacement and $\mathbf{u}^{exact}$ is the exact solution. Three weight functions (Eq. (4.2)-Eq. (4.4)) are compared in the patch test. The blending cutoff distance is chosen to be the size of one cell. The background mesh uses uniform knot spacing on a degree-2 NURBS discretization with a regularly spaced grid of control points. The result for patch test convergence study is shown in Figure 4.8 and Figure 4.9.The cubic and quartic spline weight functions yield solutions that are accurate to machine precision even when coarse mesh is used due the exact integration of polynomials through Gaussian quadrature. Exponential weight function causes less error as cell size decreases.

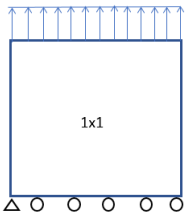


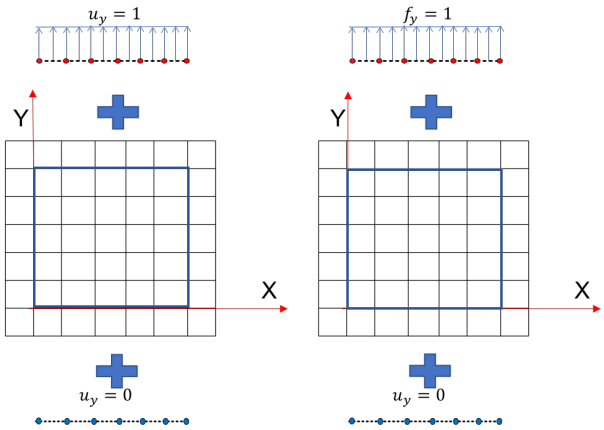


**Figure 4.7.** Illustration of boundary condition application (a) Dirichlet condition (b) Neumann condition

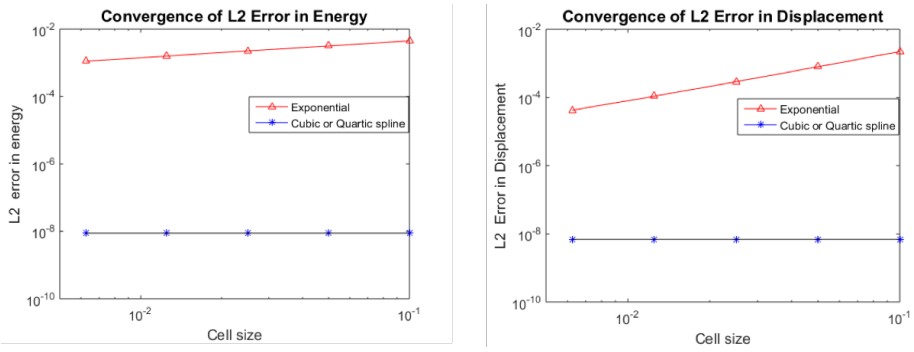


**Figure 4.8.** Convergence study for the Dirichlet condition

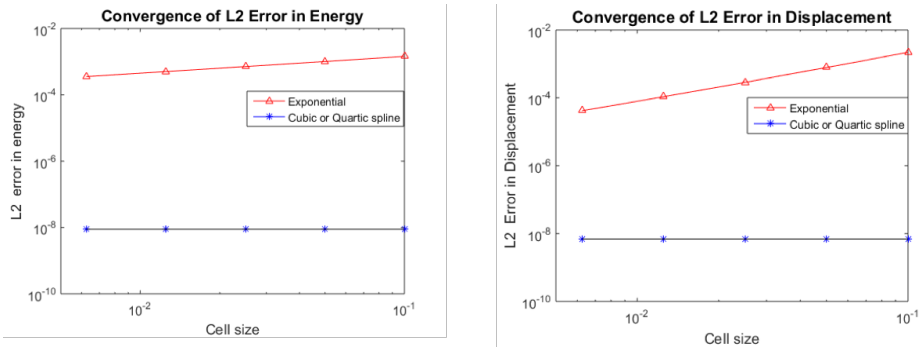


**Figure 4.9.** Convergence study for the Neumann condition

## 4.3 Algebraic Level Sets for Distance Measures And Point Classification

In the last section, an enrichment based technique for applying boundary conditions is proposed for immersed boundaries (Eq. (4.5)). In this problem, distance from the boundary or interface serves as a measure of influence of the behavior on the boundary at a point in the underlying domain. Therefore, inexpensive distance calculations from parametric boundaries are critical to the developed procedure. The need for distance measure in the present study is illustrated in Figure 4.10. An arbitrary closed boundary is immersed in the spline mesh, with the the red crosses representing the quadrature points outside the domain while the blue crosses are quadrature points inside the domain. $\Gamma_d$ and $\Gamma_n$ denote the Dirichlet and Neumann boundary.

While the use of Newton-Raphson iterations to estimate distance to a parametric boundary is most common [125], [126], the numerical iterations need to be carried out at every quadrature point. In addition, the Newton-Raphson iterations may also be non-robust in that more than one point on the immersed surface may be equidistant from a quadrature point. An alternative idea is to construct a polytope approximation to the boundary to estimate distance [127], [128]. However, a polytope approximation will not retain the parametric details of the boundary that enables computation of normals and curvatures that are critical to the evolution of the boundary under physical forces. In this study, we build on the recent work of the corresponding author and colleagues [120], [121] to construct signed algebraic level sets that provide both distance measures as well as point classification. The algebraic

level sets preserve the exact geometry of low-degree (2 or 3) NURBS curves/surface and avoid iteration. Specifically, in the present study, the algebraic level sets provide a measure of distance to the enrichment at each quadrature point.

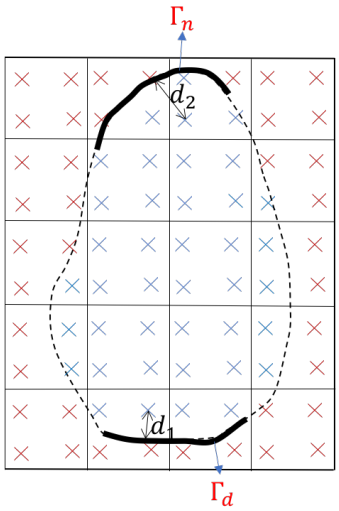


**Figure 4.10.** Role of algebraic level sets in CAD-CAE integration

The main idea behind the algebraic distance field is to implicitize the parametric entity and use the level sets of the implicitized function as a measure of distance. The implicitization of parametric entities is based on the resultant theory, which is described in the seminal research of Sederberg [129]. The resultant of a parametric entity is the determinant of a matrix of the form $det(M^B(\mathbf{x})) = 0$, which gives the implicit representation of the parametric entity. Furthermore, for any point $\mathbf{x}$ that is not on the curve, $\Gamma = det(M^B(\mathbf{x}))$ is a measure of distance from the curve. Upreti and Subbarayan [120], [121] utilized the resultant to construct signed algebraic level sets. We describe the procedure pictorially in Figure 4.11, Figure 4.12 and Figure 4.13.

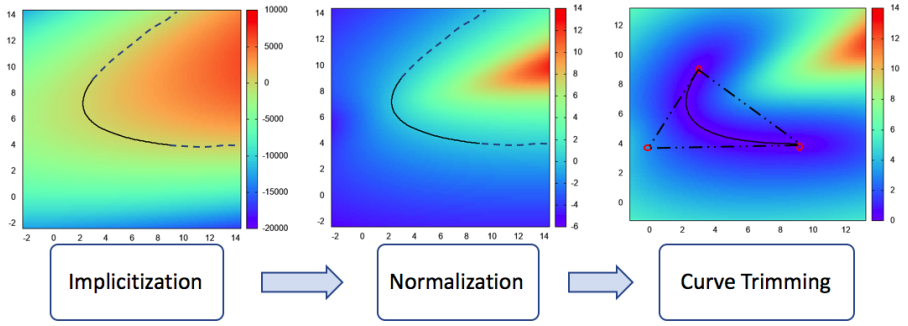


**Figure 4.11.** Procedure to construct algebraic distance field for Bezier curves

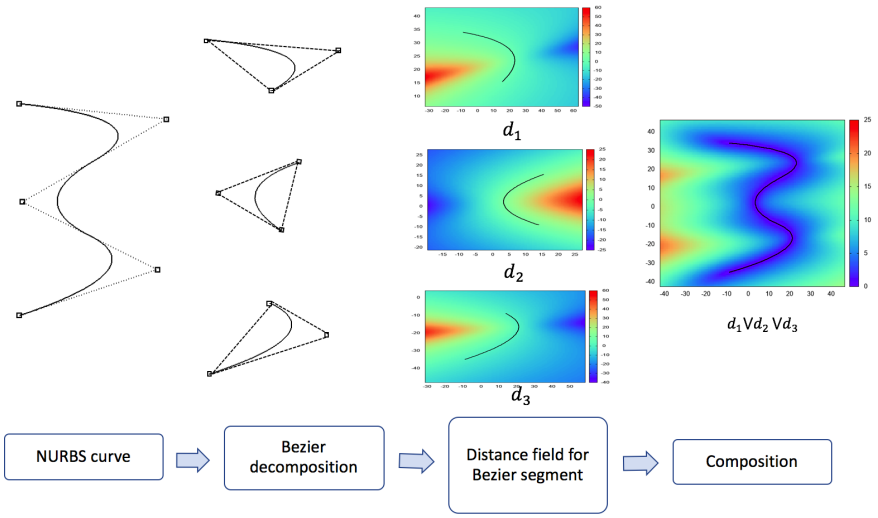


**Figure 4.12.** Procedure to construct algebraic distance field for NURBS curves

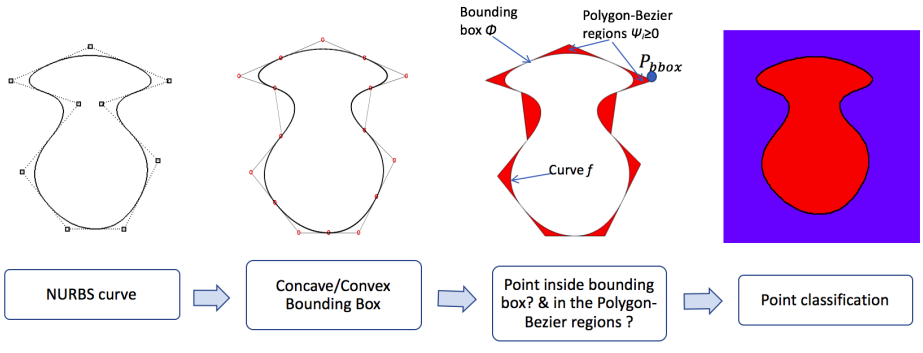


**Figure 4.13.** Procedure to construct signed algebraic level sets

Once the signed algebraic level sets are constructed, the sign is used for point membership classification. For a multiply connected domain, R-functions [130] are used to compose signed algebraic level sets.

## 4.4 Numerical Examples

Figure 4.14 describes the general procedure to implement the developed methodology. First, the B-rep model is generated in the CAD system. The geometry of the enriching boundary should also be constructed with the appropriate lower dimensional NURBS representation. This can be done by trimming the B-rep model and extracting the trimmed region where the boundary condition is to be applied. Immersing the B-rep model in the NUBRS background mesh, for each quadrature point, the signed distance field is utilized to classify the point relative to the boundary. If the quadrature point is inside, then the solid's material property is assigned to it. If not, a numerically small value $\alpha$ is used as the elastic modulus so that the contribution of the point is numerically insignificant. Ruess et al. [131] point out that for lower order splines, the resulting stiffness matrices are sufficiently well conditioned to allow the application of standard preconditioned iterative solvers. But, for higher order splines, the penalization leads to strongly ill-conditioned matrices that require the application of direct solvers. In our study, we used a direct solver and chose $\alpha$ to be $10^{-6}$. The boundary condition is assigned to the corresponding degree of freedom of the enrichment: Dirichlet bounday on $u$ and Neumann on $G$. The next step is to assemble the system following the procedure outlined in Section Section 4.2. Finally, solving the assembled matrix system, we obtain the displacement solution at each control point of the underlying domain. In the following subsections, several numerical examples are illustrated. For simplicity, all parameters are dimensionless, the size of computational region is $1 \times 1$, Young's modulus is 1 and Poisson's ratio is 0.3.

### 4.4.1 Plate with a Single Hole

The first example is of a plate with single hole under uniform tension.The geometry, loading, and boundary conditions are described in Figure 4.15a and the CAD model is shown

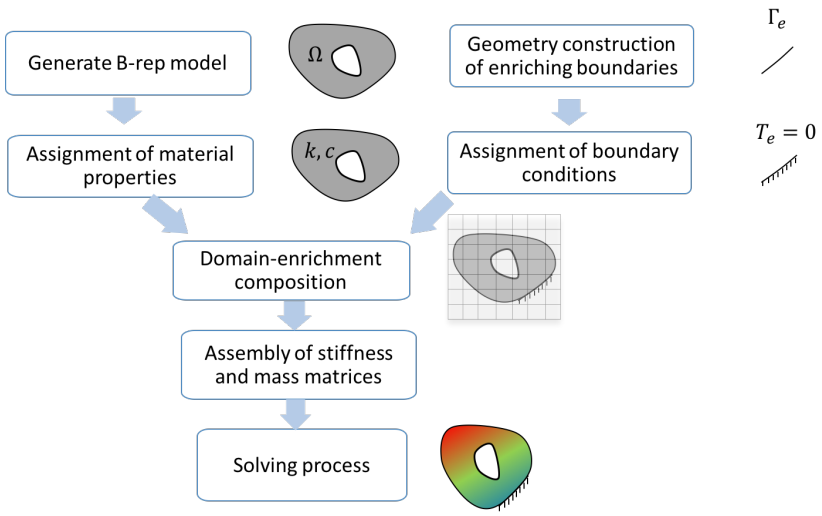


**Figure 4.14.** CAD-EIGA integration: flow of control during analysis

in Figure 4.15b. The B-rep model is immersed in the NURBS background grid shown in Figure 4.15c. In this example, we construct the NURBS grids such that the outer boundary of the CAD geometry conforms to the boundary of the grid cell. Thus, the cells in the brown region lie outside the domain of interest and may be discarded. The algebraic distance field is as shown in Figure 4.15d and the sign of algebraic distance field enables point classification. In Figure 4.15e, the red region represents the domain of interest. The weight field shown in Figure 4.15f describes the influence of the boundary condition on the underlying domain. The closer the point is to the boundary, the higher its weight. The cutoff distance for the blending region is set to two times of the element size. The Von Mises stress resulting from the analysis is shown in Figure 4.15g. The results clearly capture the stress concentration in the periphery of the hole.

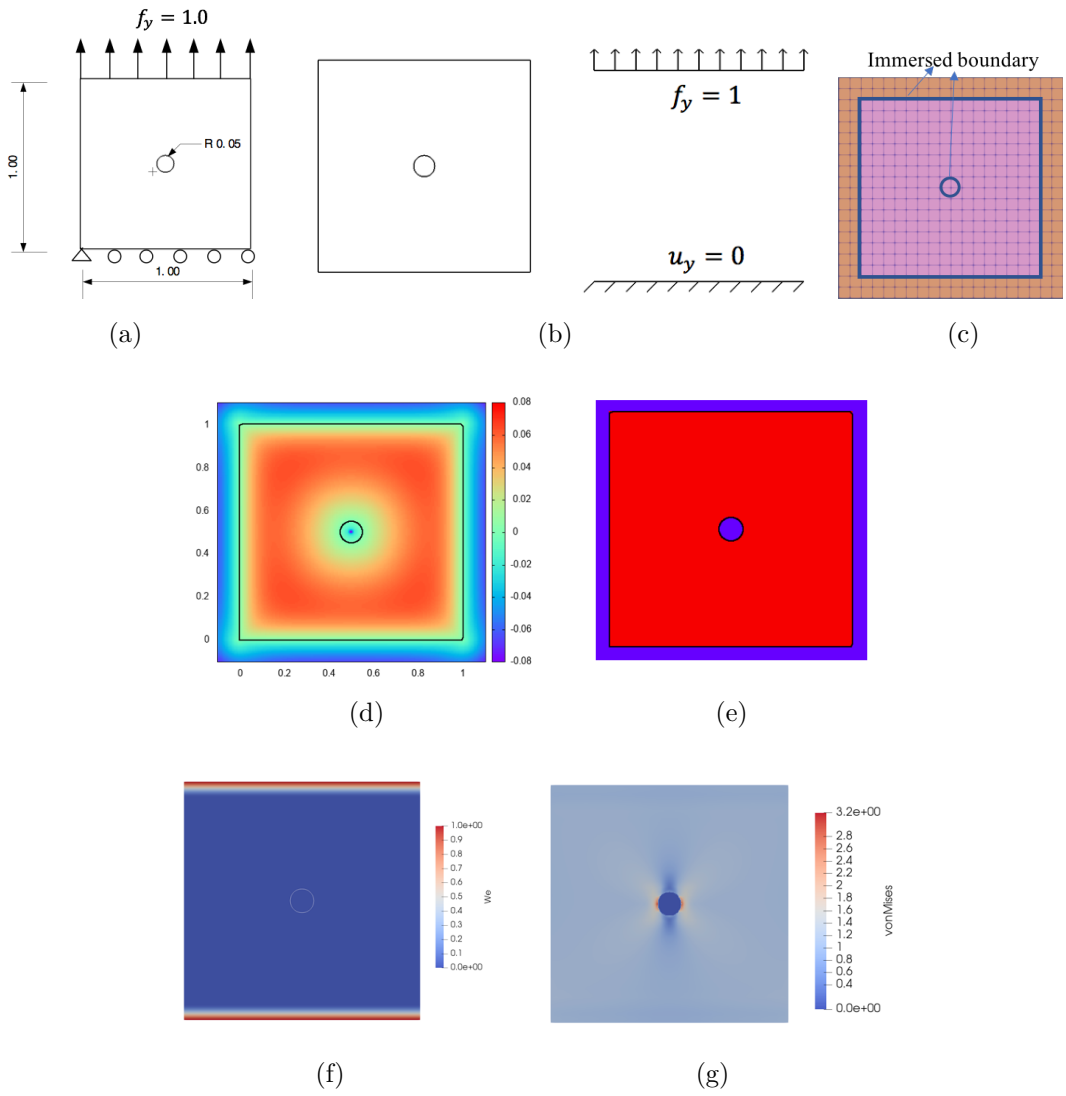


**Figure 4.15.** Example 1: Plate with a single hole (a)Problem description (b) Problem domain and boundaries that are enriched (c) Immersed geometry (d) Algebraic distance field (e) Point classification (f) Weight field (g) Von Mises stress

Figure 4.16a shows the distribution of $\sigma_{22}$ in the plate. We next carried out a convergence study by varying the spacing of the background NURBS grid and compared the solution convergence against the known analytical solution for the problem [132]. The stress concentration factor in the plot is defined as $SCF = \frac{\sigma_{max}}{\sigma_{nom}}$, where $\sigma_{nom}$ is the nominal stress due to a uniform load that one would expect on the section if there were no stress concentration. As can be seen from Figure 4.16b, with the decrease of the grid spacing or cell size, the stress concentration factor converges to the analytical result of 2.8.

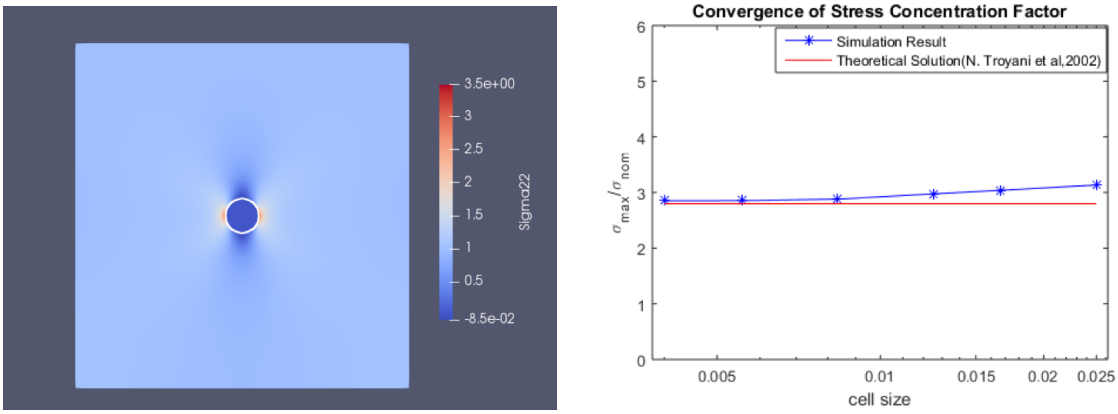


**Figure 4.16.** Convergence of $\sigma_{22}$

(a)$\sigma_{22}$ (b)Convergence of stress concentration factor

### 4.4.2 Plate with Multiple Holes

This example builds on the first one by increasing the number of holes in the domain. The external geometry, material and boundary conditions are the same as before. Interior to the plate is however different; it now contains nine holes instead of a single one. The details of this example are shown in Figure 4.17. The background NURBS grid used is $200 \times 200$. As before, the blending region is twice the grid spacing. Now, each hole causes the stress to concentrate.

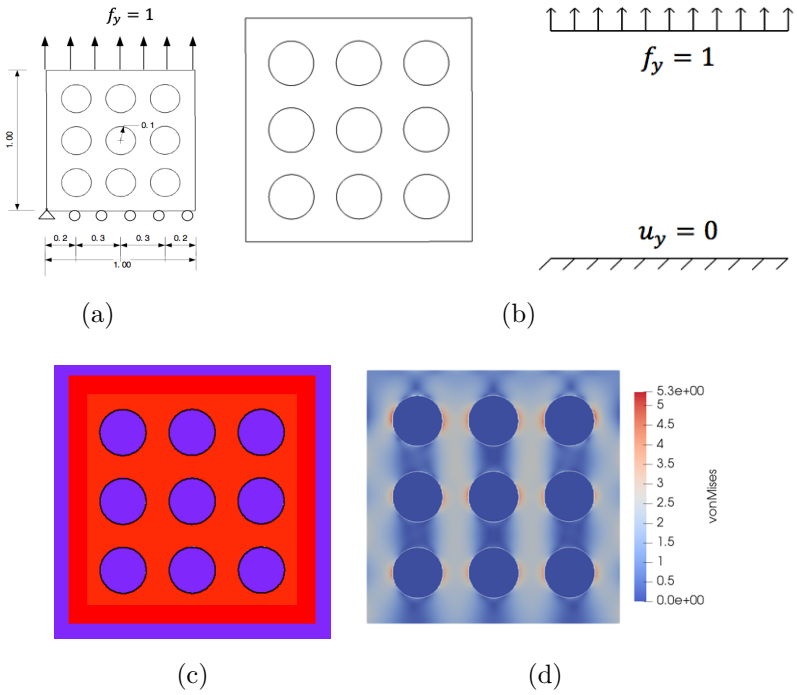


**Figure 4.17.** Example 2: Plate with multiple holes (a) Problem description (b)Problem domain and boundaries that are enriched (c)Point classification (d)Von Mises stress

### 4.4.3 Curved T-structure

In this example, a curved T-shape under uniform compressive load on the top is analyzed. Figure 4.18b shows the model geometry. The boundary of the geometry is not coincident with the edge of the background grid. Figure 4.18c shows the T-geomentry immersed in the NURBS background mesh. The signed algebraic level set that enables point classification is shown in Figure 4.18d. The weight field constructed on the boundaries is shown in Figure 4.18e. The background grid is $200 \times 200$ and the the blending region is twice the NURBS grid spacing as before. The Von mises stress generated through the analysis is shown in Figure 4.18f. It is clear that even though the applied pressure is uniform, the sharp corner is a source of significant stress concentration.

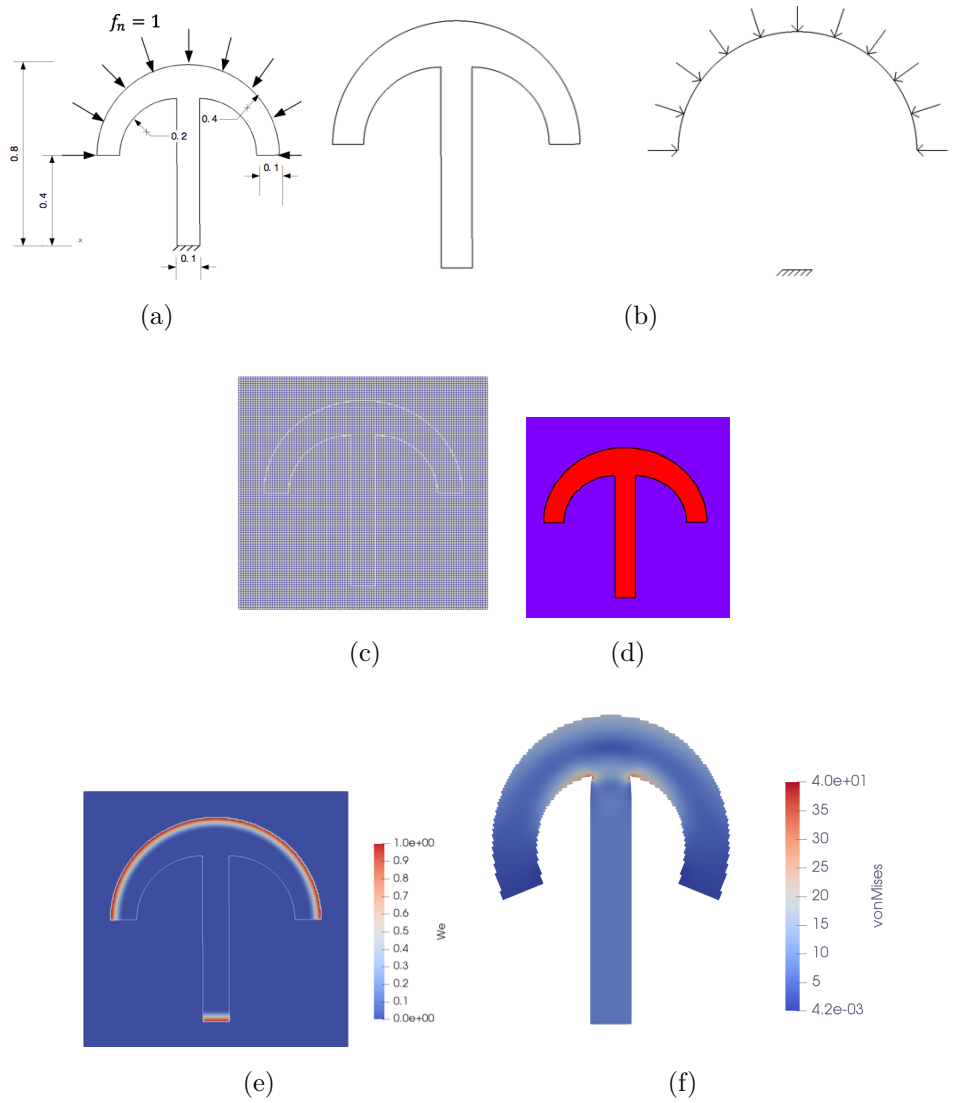


**Figure 4.18.** Example 3: Curved T-shape (a) Problem description(b)Problem domain and boundaries that are enriched(c)Immersed geometry(d)Point classification(e)Weight field(f)Von Mises stress on deformed shape

### 4.4.4 Loaded wheel

The fourth example is that of a wheel under compression. The diameter of the wheel is 0.9 units and the applied pressure on top is 1. The length of the boundary on which the pressure is applied is 0.02 units. A region of the same size is fixed on the bottom of the geometry. The background mesh is again $200 \times 200$ and the blending region is again twice the grid size. As can be seen in Fig. 4.19f, the applied load is transferred to the hub by the

nearest spokes. The deformation is consistent with the expectation that the wheel will be flattened under the load.

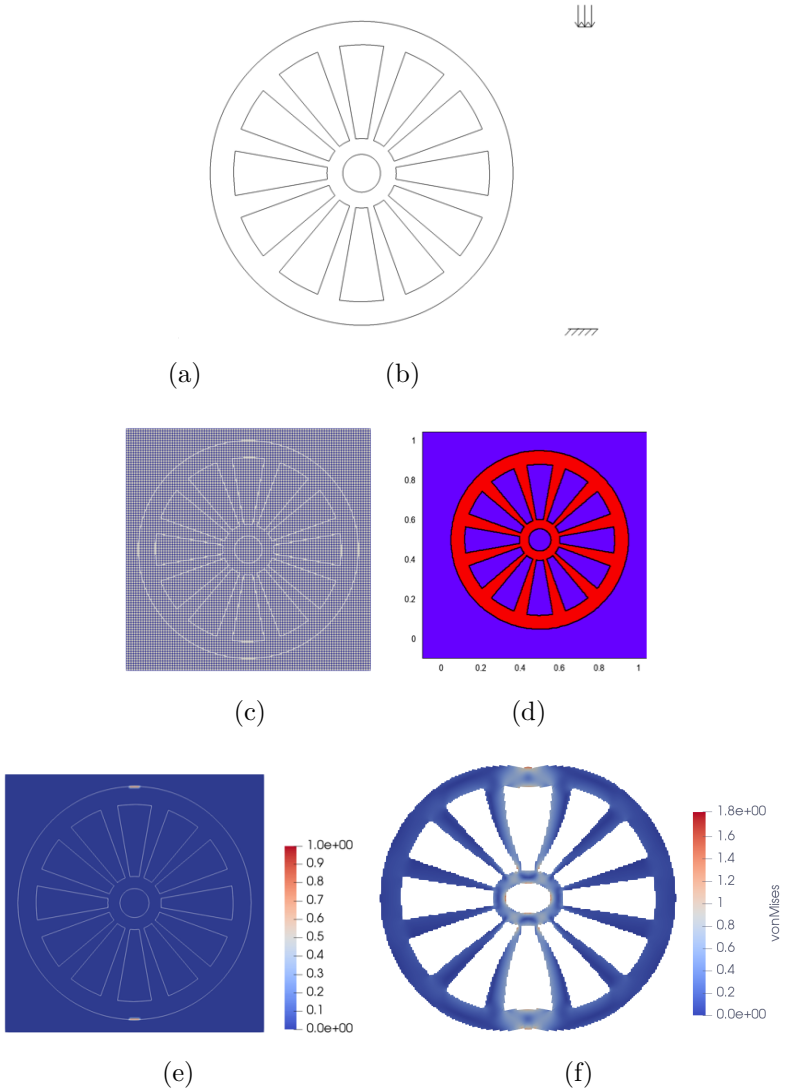


**Figure 4.19.** Example 4: Curved T-shape (a) Problem description(b)Problem domain and boundaries that are enriched(c)Immersed geometry(d)Point classification(e)Weight field(f)Von Mises stress on deformed shape

## 4.5 Summary

In this chapter, a CAD-CAE integration method that relies on immersing the CAD B-rep model into a regular NURBS analysis grid is proposed. Unlike the common weak imposition

of boundary conditions in mesh free method, the approach described here enables direct application on the degree of freedom associated with the boundary.

The analysis methodology utilizes Enriched Isogeometric Analysis, which utilizes extra degrees of freedom defined on the enriching boundary to blend fields with known behavior with those defined on the underlying analysis grid. This method avoids weak imposition of the boundary condition that is known to lead to poor numerical conditioning of the matrix system.

The proposed CAD-CAE integration approach eliminates mesh generation, retains a geometric representation of the boundaries that are exact to the CAD model, and enables exact to CAD point containment queries during analysis. The accuracy of the proposed method was demonstrated through both patch test as well as convergence analysis on a benchmark problem. In the patch test, decreasing the cell size leads to less error when using exponential weight function, while the cubic or quartic weight function yields solutions that are accurate to machine precision. In another benchmark test of a plate with hole under tension, the stress intensity factor was shown to converge to the theoretical solution with decreasing cell size. Several numerical examples were also provided to demonstrate the application and power of the developed method.

# 5. PARAMETRIC STITCHING FOR SMOOTH COUPLING OF SUB-DOMAINS

In this chapter, a new application of EIGA, termed parametric stitching, is proposed for smooth coupling of sub-domains with non-matching discretizations. The proposed technique couples NURBS patches by enforcing compatibility on the field approximations directly with a coupling interface along the shared boundary of adjacent NURBS patches. Essentially, this method uses a lower dimensional NURBS entity to join two or more NURBS patches adjacent to each other, and so it is termed parametric stitching or stitched NURBS (SNURBS).

When multiple rational spline patches combine at an T-junctions or an extraordinary vertex, interaction between multiple edge enrichments is unavoidable. To assure smoothness at such points, a vertex enrichment is used to couple two or more edges that intersect at the point. An enrichment on the intersecting edges is then used to pairwise couple patches. In general, when stitching together multiple patches, a single patch may be enriched by more than one edge, therefore a hierarchical enriching procedure is necessary and is also developed in this chapter.

The developed methodology enables a unified, isoparametric representation of geometry and behavior that closes the gaps between geometric subdomains as well as smoothly couples the fields on the (composed or) decomposed subdomains. It enables localized gradients of fields that assure arbitrary smoothness at the interface between coupled subdomains. These attributes automatically allow modular construction of coupling subdomains with arbitrary smoothness.

## 5.1 Methodology for Smooth Field Coupling

In this section, the basic methodology for stitching two patches is first described. The methodology is next extended to smoothly couple multiple patches. The continuity conditions on the fields for the coupling of multiple patches are also derived.

### 5.1.1 Construction of Enriched Field Appoximations

The coupling procedure is illustrated in Figure 5.1: $\Gamma_{\mathrm{i}}$ is the coupling interface of each patch that are part of the boundary of the associated patch $\partial\Omega_{\mathrm{i}}$. It is assumed that the two patches share a compatible interface geometry denoted by $\Gamma_{\mathrm{e}}$, i.e., $\Gamma_{\mathrm{e}} \equiv \Gamma_{\mathrm{i}}$.

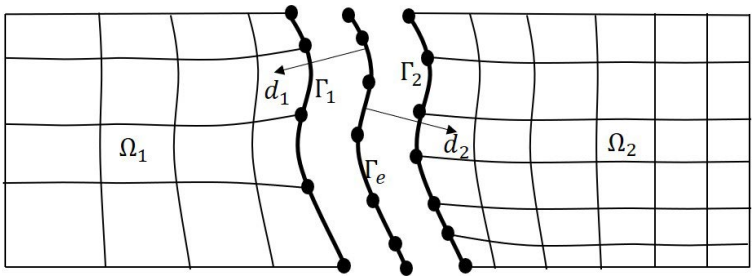


**Figure 5.1.** Illustration of non-matching parametric domains. The interfaces are shown separated for clarity, but $\Gamma_{\mathrm{e}} \equiv \Gamma_{\mathrm{i}}$.

The enriching approximation is constructed from the coupling interface $\Gamma_{\mathrm{e}}$ over the sub-domain $\Omega_{\mathrm{i}}$. The enriched field approximation (Eq. (5.1)) is constructed as a function of the normal distance from the boundary $\Gamma_{\mathrm{e}}$. Thus, at a parametric location $(\xi, \eta)$ on the enriching boundary, in the direction normal to the boundary, The enriching approximation can be expressed through a generalized Taylor's series expansion of the form:

$$f_{\Gamma_{\mathrm{e}}}(\xi, \eta, d) = f^0(\xi, \eta) + \sum_{m=1}^{\infty} \frac{1}{m!} f^m(\xi, \eta)\, d^m \tag{5.1}$$

where, $f^0$ is the constant term and $f^m = \frac{\partial^m f}{\partial n^m}$ is the $m^{\text{th}}$ directional derivative of the field in the normal direction at the parametric location $(\xi, \eta)$ of the boundary, and $d$ is the distance in the normal direction at the point on the boundary. When constructing the approximation, the term $f^0$ and the derivatives $f^m$ are in turn isoparametrically approximated as described in Eq. (5.2). Thus,

$$f^0(\xi, \eta) = \sum_{k=1}^{n_k} \sum_{l=1}^{n_l} R_{kl}(\xi, \eta) \bar{f}^0_{kl} \tag{5.2}$$

$$f^m(\xi, \eta) = \sum_{k=1}^{n_k} \sum_{l=1}^{n_l} R_{kl}(\xi, \eta) \bar{f}^m_{kl} \tag{5.3}$$

with $\bar{f}^0_{kl}, \bar{f}^m_{kl}$ being the unknowns that are obtained during the solution process.

Now, the coupling of the two subdomains at the interface is achieved by defining the function $f_{\Gamma_e}$ in Eq. (5.1) as corresponding to the interface geometry $\Gamma_e$. Thus, the approximate blended field within *each* subdomain $\Omega_i$ is

$$f_i(\boldsymbol{x}) = [1 - w(d_i(\boldsymbol{x}))]\, f_{\Omega_i}(\boldsymbol{x}) + w(d_i(\boldsymbol{x})) f_{\Gamma_e}(\xi, \eta, d_i(\boldsymbol{x})) \tag{5.4}$$

where, $d_i(\boldsymbol{x})$ and $w(d_i(\boldsymbol{x}))$ denote the distance from the boundary $\Gamma_e$ to a point in the domain $\Omega_i$, and the weight value that provides the influence of the field approximation on the boundary $\Gamma_e$ as a function distance, respectively. $f_{\Omega_i}(\boldsymbol{x})$ is the underlying field approximation in the domain $\Omega_i$, $f_{\Gamma_e}$ is the enrichment intended for subdomain $\Omega_i$, and $f_i(\boldsymbol{x})$ is the resulting blended approximation in $\Omega_i$. In general, using identical values of $\bar{f}^0_{kl}$ and $\bar{f}^m_{kl}$ in Eqs. (5.2) and (5.3) in both domains ensures the continuity of the field across the interface. However, one may choose to keep the value of $\bar{f}^0_{kl}$ the same between the two subdomains but keep two distinct values of $\bar{f}_{kl}$ to allow derivative discontinuity as at a material interface. The advantage of this formulation is that it may be expanded to arbitrary order to achieve the desired smoothness across the boundary. The constructed approximation allows arbitrary smoothness, but additional unknowns are introduced at the control points of the enriching interface $\Gamma_e$ as defined in Eqs. (5.2) and (5.3).

While the NURBS approximation for $f_{\Gamma_e}(\boldsymbol{x})$ in Eq. (5.1) is arbitrary, it may be convenient to use the approximation corresponding to the underlying approximation on $\Gamma_i$, that is, $f_{\Gamma_e}$is the value of $f_{\Omega_i}$ along the patch boundary $\Gamma_i$. In this study, we chose $f_{\Gamma_e}$ as corresponding to the boundary with the coarser discretization (for example, $\Gamma_1$ in the illustration of Figure 5.1).

This choice along with enforcement of derivative continuity leads to the value of the field at the interface being captured by a set of unknowns representing the interface, namely, $\bar{f}^0_{kl}$ and $\bar{f}^m_{kl}$. Since the normal derivatives are defined independent of the underlying subdomain approximations, the interacting physical forces are fully described by the unknowns $\bar{f}^0_{kl}$ and $\bar{f}^m_{kl}$ in each subdomain. Therefore, no interaction between the subdomains needs to be considered when constructing the system stiffness matrix – the interfacial unknowns fully

describe the coupling. Thus, the proposed methodology enables parallel assembly as well as a modular procedure to construct the coupling problem.

### 5.1.2 Construction of Hierarchically Enriched Approximations

In this section, we extend the above described procedure to a domain constructed from multiple rational spline patches. In the developed approach, an enrichment at a vertex is used to couple one or more edges that intersect at the point, an enrichment at the intersecting edge is used to couple one or more surfaces and so on. In general, when stitching together multiple patches, a single patch may be enriched by more than one edge (see Section 5.1.2). It is thus necessary to assign weights for each enrichment so that partition of unity is not violated. The procedure to construct the fields in a hierarchical manner is elaborated below.

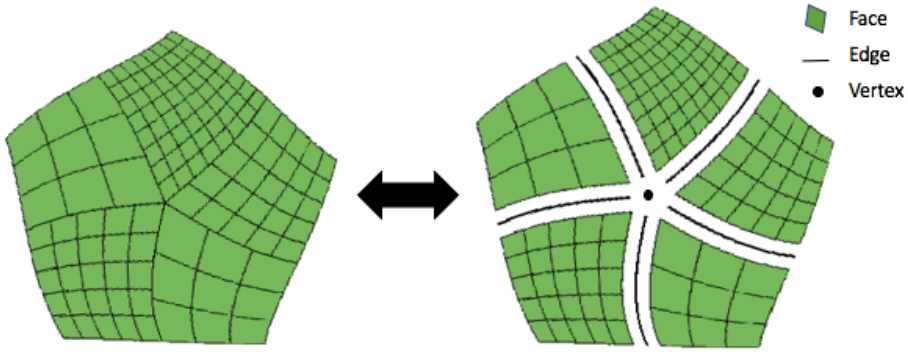


**Figure 5.2.** A domain decomposed into multiple patches with pairwise edge enrichments.

In a multi-patch domain approximation, the field approximated by each edge is blended sequentially in a patch. Without loss of generality, we consider an enriching scalar field blended with the underlying patch approximation as:

$$f(\boldsymbol{x}) = (1 - \sum_{\mathrm{i}=1}^{n} \bar{w}_{\mathrm{i}}(\boldsymbol{x}))f_{\Omega}(\boldsymbol{x}) + \sum_{\mathrm{i}=1}^{n} \bar{w}_{\mathrm{i}}(\boldsymbol{x}) f_{\Gamma_{\mathrm{i}}}(\mathcal{P}(\boldsymbol{x})) \tag{5.5}$$

where, $f_{\Gamma_\mathrm{i}}$ is the enriching approximation from the $\mathrm{i}^{th}$ enrichment defined in Eq. (5.1), $\bar{w}$ is the composite weight function for the $\mathrm{i}^{th}$ enrichment constructed as:

$$\bar{w}_\mathrm{i}(\boldsymbol{x}) = w_\mathrm{i}(\boldsymbol{x})\Pi_{\mathrm{j}=1}^{\mathrm{i}-1}(1 - w_\mathrm{j}(\boldsymbol{x})) \tag{5.6}$$

Here, $w_\mathrm{i}(\boldsymbol{x}) \equiv w(d_\mathrm{i}(\boldsymbol{x}))$ is the weight function based on normal distance from the enriching geometric entity $\Gamma_\mathrm{i}$.

Eq. (5.6) isogeometrically blends weights from multiple enriching edges at a point in the domain. However, the above expression does not construct a smooth field at the intersection of the edges surrounding the vertex (Section 5.1.2).

To achieve smoothness at these intersection points, a hierarchical enriching methodology is developed here. The core idea is to use lower dimensional enrichment to stitch higher dimensional domain. Specifically, a vertex is used to stitch edges, the composed enrichment of edges is applied to stitch faces and the composed enrichment of faces is then used to stitch bodies and so on.

The blending procedure is as follows. The scalar field at a vertex can be defined in any direction by its directional derivative as:

$$f_V(d_V) = \bar{f}_V^0 + \sum_{m=1}^{\infty} \frac{1}{m!} \bar{f}_V'^m d_V^m \tag{5.7}$$

where, $d_V \equiv d_V(\boldsymbol{x})$ is the distance to the vertex from the spatial location $\boldsymbol{x}$, $\bar{f}_V^0$ is the (unknown) value at the vertex, and $\bar{f}_V'^m$ is the unknown $m^{\text{th}}$ directional derivative at the vertex.

Next, the field approximation at the vertex is applied to enrich the edges:

$$f_{E_\mathrm{i}}^{0V}(\xi) = (1 - w_V(d_V))f_{E_\mathrm{i}}^0(\xi) + w_V(d_V)f_V(d_V) \tag{5.8}$$

where, $\xi$ is the parametric inverse of $\boldsymbol{x}$ on the edge curve, $w_V(d_V)$ is the value of the weight associated with the vertex at the point on the edge, and $f_{E_\mathrm{i}}^0(\xi)$ is the approximation to the

constant term on the i$^{\text{th}}$ edge (Eq. (5.2)). $f^{0V}_{E_\text{i}}(\boldsymbol{x})$ is the vertex enriched field for a point on the edge.

Following the above process, the approximated field near the i$^{\text{th}}$ edge can thus be expanded as:

$$f_{E_\text{i}}(d_{E_\text{i}}) = f^{0V}_{E_\text{i}}(\mathcal{P}(\boldsymbol{x})) + \sum_{m=1}^{\infty} \frac{1}{m!} f'^{m}_{E_\text{i}}(\mathcal{P}(\boldsymbol{x})) d^m_{E_\text{i}} \tag{5.9}$$

where, $d_{E_\text{i}} \equiv d_{E_\text{i}}(\boldsymbol{x})$ is the distance to the edge from $\boldsymbol{x}$. Continuing similarly, assuming that $n_E$ edges enrich the face, the edge enriched constant term for a face is:

$$f^{0E}_{F_\text{j}}(\xi,\eta) = (1 - \sum_{\text{i}=1}^{n_E} \bar{w}_{E_\text{i}}(d_{E_\text{i}})) f^0_{F_\text{j}}(\xi,\eta) + \sum_{\text{i}=1}^{n_E} \bar{w}_{E_\text{i}}(d_{E_\text{i}}) f_{E_\text{i}}(d_{E_\text{i}}) \tag{5.10}$$

where, as before, $d_{E_\text{i}} \equiv d_{E_\text{i}}(\boldsymbol{x}(\xi,\eta))$, $f^0_{F_\text{j}}(\xi,\eta)$ is the approximation to the constant term on the j$^{\text{th}}$ face, and $\bar{w}_{E_\text{i}}(\boldsymbol{x})$ is the composite weight function introduced in Eq. (5.6) with respect to the edge i. Thus, the approximated field expanded from the surface is:

$$f_{F_\text{j}}(d_{F_\text{j}}) = f^{0E}_{F_\text{j}}(\mathcal{P}(\boldsymbol{x})) + \sum_{m=1}^{\infty} \frac{1}{m!} f'^{m}_{F_\text{j}}(\mathcal{P}(\boldsymbol{x})) d^m_{F_\text{j}} \tag{5.11}$$

where, $d_{F_\text{j}} \equiv d_{F_\text{j}}(\boldsymbol{x})$ is the distance to the j$^{th}$ face. Eq. (5.11) is then used to enrich the body. Assume that there are $n_F$ faces enriching the body. The field within the body is approximated as :

$$f^{0F}_{B}(\xi,\eta,\zeta) = (1 - \sum_{\text{j}=1}^{n_F} \bar{w}_{F_\text{j}}(d_{F_\text{j}})) f^0_{B}(\xi,\eta,\zeta) + \sum_{\text{j}=1}^{n_F} \bar{w}_{F_\text{j}}(d_{F_\text{j}}) f_{F_\text{j}} \tag{5.12}$$

where, $d_{F_\text{j}} \equiv d_{F_\text{j}}(\boldsymbol{x}(\xi,\eta,\zeta))$ is the distance to the face, $\bar{w}_{F_\text{j}}$ is the composite weight function with respect to j$^{th}$ face, $f^0_B$ is the approximation to the constant term in the body.

### 5.1.3 Continuity Conditions for Enriched Field Approximations

The continuity conditions are first derived across an edge that is used to blend two subdomains. These conditions are then used to derive the continuity conditions within a subdomain at the edge of the blending region.

**Continuity Across a Stitching Edge Connecting Two Patches**

The continuity condition will be discussed for both across interfaces and within patches. In Figure 5.3a, the two subdomains $\Omega_1$ and $\Omega_2$ are connected by the interface $\Gamma$. In the blending region $\Omega_{\text{ei}}$, the field is approximated as:

$$f_{\text{i}} = (1-w) f_{\Omega_{\text{i}}} + w f_{\Gamma} \tag{5.13}$$

where, $\text{i} = 1, 2$. In the above expression, the arguments of the scalar field and the weight field are left out for ease of reading. Its directional derivative along the normal to the interface is:

$$f'_{\text{i}} = (1-w) f'_{\Omega_{\text{i}}} - w' f_{\Omega_{\text{i}}} + w f'_{\Gamma} + w' f_{\Gamma} \tag{5.14}$$

Similarly, the $m^{th}$ directional derivative $f'^{m}_{\text{i}}$ can be derived as:

$$f'^{m}_{\text{i}} = f'^{m}_{\Omega_{\text{i}}} + \sum_{\text{i}=0}^{m} \binom{m}{\text{i}} (f'^{\text{i}}_{\Gamma} - f'^{\text{i}}_{\Omega_{\text{i}}}) w'^{m-\text{i}} \tag{5.15}$$

The continuity of the $m^{\text{th}}$ derivative across the interface $\Gamma$ requires that the left and right limits be equal, that is:

$$f'^{m}_{1} = f'^{m}_{2} \quad \text{on} \quad \Gamma \tag{5.16}$$

Thus, function continuity across $\Gamma$ is assured by either of the following two conditions:

$$f_{\Omega_1} = f_{\Omega_2} \quad \text{on} \quad \Gamma \tag{5.17}$$

or

$$w = 1 \quad \text{on} \quad \Gamma \tag{5.18}$$

Generalizing, there are two sets of condition that lead to $C^m$ smoothness across the interface:

$$f_{\Omega_1} = f_{\Omega_2}, f'_{\Omega_1} = f'_{\Omega_2}, ..., f'^{m}_{\Omega_1} = f'^{m}_{\Omega_2}, \quad \text{on} \quad \Gamma \tag{5.19}$$

or

$$w = 1, w' = 0, ...w'^{m} = 0, \quad \text{on} \quad \Gamma \tag{5.20}$$

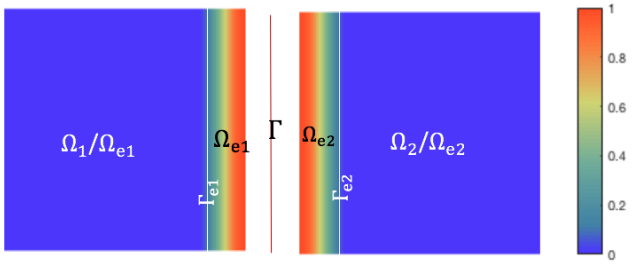


(a)

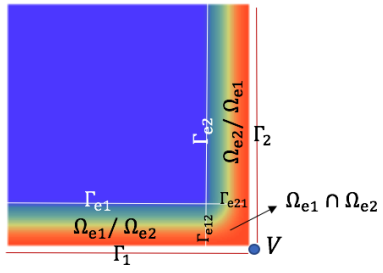


(b)

**Figure 5.3.** (a) Weight function of adjacet patches (b) weight function within one patch

In general, it is either difficult or not desirable to constrain the fields as required in Eq. (5.19). However, it is relatively easy to satisfy the required smoothness condition across the interface by choosing the weight field such that Eq. (5.20) is satisfied.

### Continuity Across Blending Edges within a Patch

The continuity within the domains requires consideration in three parts. The first is the region over which blending occurs between the underlying domain and any one enrichment($\Omega_i$ in Figure 5.3a); the second region is the intersection between any one enriched region and other enriched regions ($\Omega_{e_1} \cap \Omega_{e_2}$ in Figure 5.3b); the third part that requires attention is the vertex. The domain $\Omega_i$ is divided into the blended region $\Omega_{e_i}$ and the non-blended region

$\Omega_i/\Omega_{e_i}$. The field outside of the blended region $\Omega_{e_i}$ is clearly $f_{\Omega_i}$. Inside the blending region, the field is constructed as:

$$f_{e_i} = (1-w)f_{\Omega_i} + wf_\Gamma \tag{5.21}$$

Thus, the $m^{\text{th}}$ directional derivative in the blended region is the same as given in Eq. (5.15). The condition for $C^m$ smoothness on the boundary $\Gamma_{e_i}$ between $\Omega_i/\Omega_{e_i}$ is either

$$f_{\Omega_i} = f_{e_i}, f'_{\Omega_i} = f'_{e_i}, ..., f^{\prime m}_{\Omega_i} = f^{\prime m}_{e_i} \quad \text{on} \quad \Gamma_{e_i} \tag{5.22}$$

or

$$w = 0, w' = 0, ..., w'^m = 0, \quad \text{on} \quad \Gamma_{e_i} \tag{5.23}$$

Now consider the continuity condition across the blending regions in Figure 5.3b. $\Omega_{e_1}/\Omega_{e_2}$ and $\Omega_{e_1} \cap \Omega_{e_2}$. Outside of the intersection region $\Omega_{e_1} \cap \Omega_{e_2}$, the field is only enriched by one edge:

$$f_{e_i} = (1-w)f_\Omega + wf_{\Gamma_i} \tag{5.24}$$

Inside $\Omega_{e_1} \cap \Omega_{e_2}$, the field is enriched by two edges:

$$f_{e_{12}} = (1-w_{\Gamma_2})\left[(1-w_{\Gamma_1})f_\Omega + w_{\Gamma_1}f_{\Gamma_1}\right] + w_{\Gamma_2}f_{\Gamma_2} \tag{5.25}$$

The above blending is dependent on the sequence by which the two enrichments are blended with the underlying domain. In the above expression, the underlying field is enriched with the field $f_{\Gamma_1}$ first. By comparing the $m^{\text{th}}$ directional derivative at the boundary of this region, we get the two sets of conditions as before:

$$f_{\Gamma_1} = f_{\Gamma_2}, f'_{\Gamma_1} = f'_{\Gamma_2}, ..., f^{\prime m}_{\Gamma_1} = f^{\prime m}_{\Gamma_2}, \quad \text{on} \quad \Gamma_{e_{12}} \tag{5.26}$$

or

$$w_{\Gamma_2} = 0, w^{\prime m}_{\Gamma_2} = 0, ..., w^{\prime m}_{\Gamma_2} = 0, \quad \text{on} \quad \Gamma_{e_{12}} \tag{5.27}$$

If the sequence of blending operations is reversed so the underlying field is enriched with $f_{\Gamma_2}$ first, then the condition in Eq. (5.27) becomes:

$$w_{\Gamma_1} = 0, w'^m_{\Gamma_1} = 0, ..., w'^m_{\Gamma_1} = 0, \quad \text{on} \quad \Gamma_{e_{21}} \tag{5.28}$$

The final location that needs discussion is the vertex. The continuity condition requires that the limit of the function exits at the vertex. In the neighborhood of vertex $V$ in domain $\Omega$, the field is:

$$f = (1 - \sum_{i=1}^{n} \bar{w}_{E_i}) f_\Omega + \sum_{i=1}^{n} \bar{w}_{E_i} f_{E_i} \tag{5.29}$$

The $m^{\text{th}}$ directional derivative of the above expression is

$$f'^m = f'^m_\Omega - \sum_{p=0}^{n} \binom{m}{p} f'^p_\Omega \bar{w}'^{m-p}_{E_i} + \sum_{p=0}^{n} \binom{m}{p} f'^p_{E_i} \bar{w}'^{m-p}_{E_i} \tag{5.30}$$

From the earlier-described hierarchical blending procedure, the limit of Eq. (5.30) tends to $f'^m_V$ if either of the following conditions hold:

$$f_\Omega = f_{E_i} = f_V, f'_\Omega = f'_{E_i} = f'_V, ..., f'^m_\Omega = f'^m_{E_i} = f'^m_V \quad \text{at} \quad V \tag{5.31}$$

or

$$w_{E_i} = 1, w'_{E_i} = 0, ...w'^m_{E_i} = 0, w_V = 1, w'_V = 0, ..., w'^m_V = 0 \quad \text{at} \quad V \tag{5.32}$$

As with continuity across the interface between two subdomains, in general, it is either difficult or not desirable to constrain the fields as required in Eqs. (5.22), (5.26) and (5.31). However, it is relatively easy to satisfy the required smoothness condition by choosing the weight field such that Eqs. (5.23), (5.27), (5.28) and (5.32) are satisfied.

The basic idea is to construct the weight function such that, the weight is 1 on the interface and 0 at the edge of blending region. To ensure greater smoothness, the corresponding directional derivative should also be 0 at both the enrichment and the edge of blending region.

## 5.2 P-Stitching Formulation for Elasto-Static Problems

The proposed general formulation for coupling fields is specialized for elasto-static problems in this section. Consider an elastic body with subdomains as illustrated in Section 5.2. The body is subjected to Dirichlet boundary conditions $\bar{\boldsymbol{u}}$ on $\Gamma_u$ and traction $\bar{\boldsymbol{t}}$ is enforced on $\Gamma_t$ with $\Gamma_u \cap \Gamma_t = \emptyset$. While the developed procedure is generally valid for stitching overlapping domains, for simplicity, the domain illustrated here is composed of two non-overlapping subdomains $\Omega_1$ and $\Omega_2$ such that $\bigcup_{\alpha=1}^{2} \Omega_\alpha = \Omega$, with $\Gamma_\mathrm{e}$ as the coupling interface.

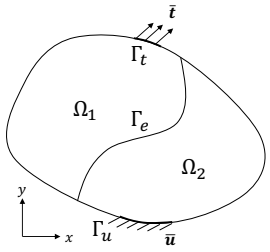


**Figure 5.4.** Problem domain consisting two subdomains that need to be smoothly coupled.

With displacement compatibility and traction reciprocity conditions enforced along the coupling interface, the elasticity problem is written as follows:

$$\nabla \cdot \sigma + \boldsymbol{b} = \boldsymbol{0} \quad \text{in} \quad \Omega \tag{5.33a}$$

$$\boldsymbol{u} = \bar{\boldsymbol{u}} \quad \text{on} \quad \Gamma_u \tag{5.33b}$$

$$\boldsymbol{t} = \bar{\boldsymbol{t}} \quad \text{on} \quad \Gamma_t \tag{5.33c}$$

$$\boldsymbol{u}^{(1)} - \boldsymbol{u}^{(2)} = 0 \quad \text{on} \quad \Gamma_\mathrm{e} \tag{5.33d}$$

$$\boldsymbol{t}^{(1)} + \boldsymbol{t}^{(2)} = 0 \quad \text{on} \quad \Gamma_\mathrm{e} \tag{5.33e}$$

For analyzing the elastic behavior, we consider the expansion of the coupling field to the first order in Eq. (5.1). The displacement field $\boldsymbol{u}(\boldsymbol{x})$ is the unknown that is required to be compatible along the coupling interface. The gradients of the displacements may or may

not be compatible depending on the nature of the materials in the two subdomains. Thus, a first-order reduction of Eq. (5.4), specialized for the current elasticity problem is:

$$\boldsymbol{u}_{\mathrm{i}}(\boldsymbol{x}) = (1 - w(d_{\mathrm{i}}))\boldsymbol{u}_{\Omega_{\mathrm{i}}}(\boldsymbol{x}) + w(d_{\mathrm{i}})(\boldsymbol{u}^0_{\Gamma_{\mathrm{e}}}(\mathcal{P}(\boldsymbol{x})) + \boldsymbol{u}_{\Gamma_{\mathrm{e}}}(\mathcal{P}(\boldsymbol{x}))\, d) \tag{5.34}$$

where, the subscript i denotes the subdomain, $\boldsymbol{u}_{\Omega_{\mathrm{i}}}$ is the displacement approximation on $\Omega_{\mathrm{i}}$, $\boldsymbol{u}^0_{\Gamma_{\mathrm{e}}}$ is the displacement approximation on the coupling boundary $\Gamma_{\mathrm{e}}$, and $\boldsymbol{u}_{\Gamma_{\mathrm{e}}}$ is the approximation of the displacement gradient normal to the coupling interface, that is, $\boldsymbol{u}_{\Gamma_{\mathrm{e}}} = \partial\boldsymbol{u}/\partial n$.

Over the support region of the associated weight field $w(d_{\mathrm{i}})$, the composed displacement is a blending of the displacement associated with neighboring domains and the first-order approximated displacement associated with the coupling boundary. For points outside of the support region, the displacement field is fully resolved by the approximation on the associated parametric domains.

Since the size of the blending region (that is, the support region of $w(d_{\mathrm{i}})$) is arbitrary, one choice is to make the support edge coincide with the Euclidean locations corresponding to the knots of the underlying domain. However, this leads to a non-uniform $d_{max}$ in **??** over the blending region. Therefore, in the present study, $d_{max}$ is held fixed while the integration is carried out over the first non-zero knot span of the domain, as illustrated in Section 5.2.

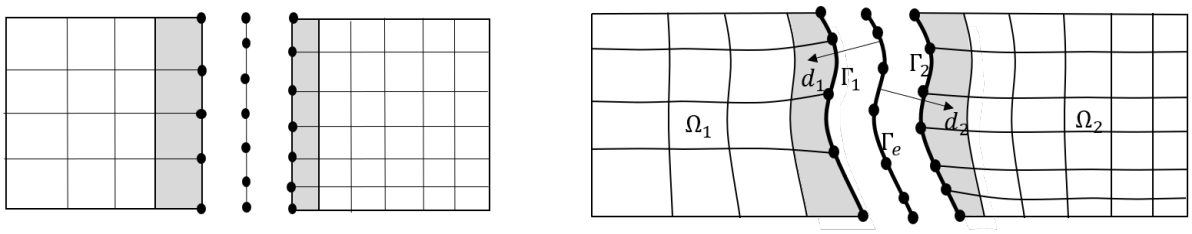


**Figure 5.5.** Integration cell in the parametric space (left) and in Euclidean space (right). In general, the integration cell corresponding to the first non-zero knot-span does not coincide with the edge of the blending region.

### 5.2.1 Discretization for Blending of Two Patches

The discretized form of the coupling approximation Eq. (5.34) is:

$$\boldsymbol{u}_{\mathrm{i}}(\boldsymbol{x}) = \Big[(1 - w(d_{\mathrm{i}}))R_{\Omega_{\mathrm{i}}}(\boldsymbol{x})\ w(d_{\mathrm{i}})R_{\Gamma_{\mathrm{e}}}(\mathcal{P}(\boldsymbol{x}))\ w(d_{\mathrm{i}})d_{\mathrm{i}}R_{\Gamma_{\mathrm{e}}}(\mathcal{P}(\boldsymbol{x}))\Big] \begin{Bmatrix} \bar{\boldsymbol{u}}_{\Omega_{\mathrm{i}}} \\ \bar{\boldsymbol{u}}^0_{\Gamma_{\mathrm{e}}} \\ \bar{\boldsymbol{u}}_{\Gamma_{\mathrm{e}}} \end{Bmatrix} \tag{5.35a}$$

$$= [R_{\Omega_{\mathrm{i}}}\ R^0_{\Gamma_{\mathrm{e}}}\ R_{\Gamma_{\mathrm{e}}}]\{\bar{\boldsymbol{u}}\} \tag{5.35b}$$

$$= [R]\{\bar{\boldsymbol{u}}\} \tag{5.35c}$$

where, $R_{\Omega_{\mathrm{i}}}$ and $R_{\Gamma_{\mathrm{e}}}$ are the basis function matrices associated with the subdomains and the coupling interface, respectively. $\bar{\boldsymbol{u}}_{\Omega_{\mathrm{i}}}, \bar{\boldsymbol{u}}^0_{\Gamma_{\mathrm{e}}}, \bar{\boldsymbol{u}}_{\Gamma_{\mathrm{e}}}$ are the degrees of freedom corresponding to the nodal unknowns of the fields $\boldsymbol{u}_{\Omega}$, $\boldsymbol{u}^0_{\Gamma_{\mathrm{e}}}$ and $\boldsymbol{u}_{\Gamma_{\mathrm{e}}}$, respectively.

The strain field approximation is now obtained in the standard manner as:

$$\boldsymbol{\varepsilon} = \nabla_s \boldsymbol{u} = [B]\{\bar{\boldsymbol{u}}\} \tag{5.36}$$

where, $\nabla_s$ is the symmetric gradient operator and for the three-dimensional problem it is defined as

$$\nabla_s = \begin{bmatrix} \partial/\partial x & 0 & 0 \\ 0 & \partial/\partial y & 0 \\ 0 & 0 & \partial/\partial z \\ 0 & \partial/\partial z & \partial/\partial y \\ \partial/\partial z & \partial/\partial x & 0 \\ \partial/\partial y & \partial/\partial x & 0 \end{bmatrix}$$

The strain-displacement matrix $[B]$ takes the following form:

$$[B] = [B_{\Omega_\mathrm{i}} \; B^0_{\Gamma_\mathrm{e}} \; B_{\Gamma_\mathrm{e}}] \tag{5.37a}$$

$$= \begin{bmatrix} -[R_{\Omega_\mathrm{i}}]^T[\nabla w]^T + (1-w)[\nabla R_{\Omega_\mathrm{i}}]^T \\ [R_{\Gamma_\mathrm{e}}]^T[\nabla w]^T + w[\nabla R_{\Gamma_\mathrm{e}}]^T \\ d_\mathrm{i}[R_{\Gamma_\mathrm{e}}]^T[\nabla w]^T + w[R_{\Gamma_\mathrm{e}}]^T[\nabla d_\mathrm{i}]^T + wd_\mathrm{i}[\nabla R_{\Gamma_\mathrm{e}}]^T \end{bmatrix}^T \tag{5.37b}$$

The discretized weak form of Eq. (5.33) may be expressed as $[K]\{\bar{\boldsymbol{u}}\} = \{f\}$, which could be further expanded into block matrices as follows.

$$\begin{bmatrix} K_{\Omega_1\Omega_1} & 0 & K_{\Omega_1\Gamma^0_\mathrm{e}} & K_{\Omega_1\Gamma'_{\mathrm{e}1}} & 0 \\ 0 & K_{\Omega_2\Omega_2} & K_{\Omega_2\Gamma^0_\mathrm{e}} & 0 & K_{\Omega_2\Gamma^0_\mathrm{e}} \\ K^T_{\Omega_1\Gamma^0_\mathrm{e}} & K^T_{\Omega_2\Gamma^0_\mathrm{e}} & K_{\Gamma^0_\mathrm{e}\Gamma^0_\mathrm{e}} & K_{\Gamma^0_\mathrm{e}\Gamma'_{\mathrm{e}1}} & K_{\Gamma^0_\mathrm{e}\Gamma'_{\mathrm{e}2}} \\ K^T_{\Omega_1\Gamma'_{\mathrm{e}1}} & 0 & K^T_{\Gamma^0_\mathrm{e}\Gamma'_{\mathrm{e}1}} & K_{\Gamma'_{\mathrm{e}1}\Gamma'_{\mathrm{e}1}} & 0 \\ 0 & K^T_{\Omega_2\Gamma'_{\mathrm{e}2}} & K^T_{\Gamma^0_\mathrm{e}\Gamma'_{\mathrm{e}2}} & 0 & K_{\Gamma'_{\mathrm{e}2}\Gamma'_{\mathrm{e}2}} \end{bmatrix} \begin{bmatrix} \bar{\boldsymbol{u}}_{\Omega_1} \\ \bar{\boldsymbol{u}}_{\Omega_2} \\ \bar{\boldsymbol{u}}^0_{\Gamma_\mathrm{e}} \\ \bar{\boldsymbol{u}}'_{\Gamma_{\mathrm{e}1}} \\ \bar{\boldsymbol{u}}'_{\Gamma_{\mathrm{e}2}} \end{bmatrix} = \begin{bmatrix} f_{\Omega_1} \\ f_{\Omega_2} \\ 0 \\ 0 \\ 0 \end{bmatrix} \tag{5.38}$$

where, $K_{IJ} = \int_\Omega [B_I]^T[D][B_J]d\Omega$ with $I, J = \Omega_\mathrm{i}, \Gamma^0_\mathrm{e}, \Gamma'_{\mathrm{ei}}$ for $\mathrm{i} = 1, 2$ and $[D]$ is the constitutive matrix. The discrete force vector $f_{\Omega_\mathrm{i}}$ associated with the subdomains is

$$\{f_{\Omega_\mathrm{i}}\} = \int_\Omega [R]^T\{\bar{\boldsymbol{b}}\}d\Omega + \int_{\Gamma_t} [R]^T\{\bar{\boldsymbol{t}}\}d\Gamma \tag{5.39}$$

where , $\bar{\boldsymbol{b}}$ is the prescribed body force per unit volume, and $\bar{\boldsymbol{t}}$ is the prescribed traction over the Neumann boundary $\Gamma_t$.

### 5.2.2 Discretization for Hierarchical Blending of Multiple Patches

The hierarchical blending procedure for elasto-static problem is illustrated in Section 5.2.2. A new vertex enrichment is introduced at the intersection of the edges. Four extra degrees of freedom are associated with the vertex, $u_{vx}, u_{vy}, G_{vx}, G_{vy}$, corresponding to the displacement and gradient at the vertex in x and y direction.

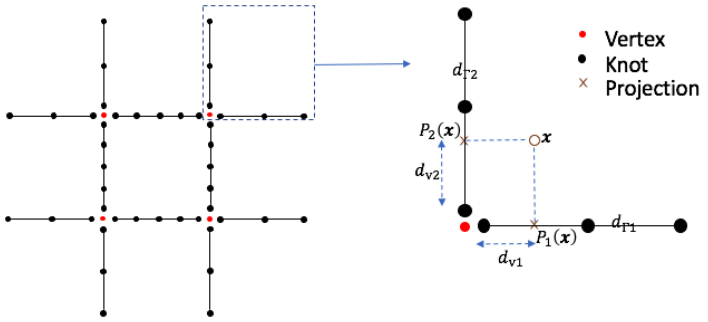


**Figure 5.6.** Illustration of Hierarchical Blending

A quadrature point is first projected to each enrichment $\Gamma_i$ with the associated distance to each enrichment being denoted as $d_{\Gamma_i}$. The blending field is now expressed as:

$$\boldsymbol{u} = (1 - w_{\Gamma_2}(d_{\Gamma_2}))[(1 - w_{\Gamma_1}(d_{\Gamma_1}))\boldsymbol{u}_\Omega + w_{\Gamma_1}(d_{\Gamma_1})\boldsymbol{u}_{\Gamma_1}] + w_{\Gamma_2}(d_{\Gamma_2})\boldsymbol{u}_{\Gamma_2} \tag{5.40}$$

where $\boldsymbol{u}_\Omega$, is the field associated with the underlying domain,$\boldsymbol{u}_{\Gamma_i}$ is the field expanded from $\Gamma_i$. Using first order expansion, the approximation of the field in the neighborhood of the edge is:

$$\boldsymbol{u}_{\Gamma_i} = \boldsymbol{u}^{0V}_{\Gamma_i} + \boldsymbol{G}_{\Gamma_i} d_{\Gamma_i} \tag{5.41}$$

where, $\boldsymbol{u}^{0V}_{\Gamma_i}$ is the vertex-enriched displacement field on the $i^{th}$ interface, $\boldsymbol{G}_{\Gamma_i}$ is the directional gradient of the field and $d_{\Gamma_i}$ is the distance. Notice that the term $\boldsymbol{u}^{0V}_{\Gamma_i}$ arises out of hierarchical blending described earlier in Eq. (5.8):

$$\boldsymbol{u}^{0V}_{\Gamma_i} = [1 - w_V(d_V)]\boldsymbol{u}^0_{\Gamma_i} + w_V(d_V)(\boldsymbol{u}_V + \boldsymbol{G}_V \boldsymbol{d}_V) \tag{5.42}$$

where $\boldsymbol{G}_V$ is a diagonal matrix of non-zero entries $\boldsymbol{G}_{vx}$ and $\boldsymbol{G}_{vy}$.

For multi-patch stitching with vertex enrichment, the discretized form on any given patch is:

$$\boldsymbol{u} = \begin{Bmatrix} (1 - w_{\Gamma_1} - w_{\Gamma_2} + w_{\Gamma_1} w_{\Gamma_2}) R_\Omega \\ w_{\Gamma_1}(1 - w_{\Gamma_2})(1 - w_{v_1}) R_{\Gamma_1} \\ (1 - w_{\Gamma_2}) w_{\Gamma_1} d_{\Gamma_1} R_{\Gamma_1} \\ w_{\Gamma_2}(1 - w_{v_2}) R_{\Gamma_2} \\ w_{\Gamma_2} d_{\Gamma_2} R_{\Gamma_2} \\ [w_{\Gamma_1}(1 - w_{\Gamma_2}) w_{v_1} + w_{\Gamma_2} w_{v_2}] I \\ w_{\Gamma_1}(1 - w_{\Gamma_2}) w_{v_1} d_{v_1} + w_{\Gamma_1} w_{v_1} d_{v_2} \end{Bmatrix}^T \begin{Bmatrix} \bar{\boldsymbol{u}}_\Omega \\ \bar{\boldsymbol{u}}^0_{\Gamma_1} \\ \bar{\boldsymbol{u}}_{\Gamma_1} \\ \bar{\boldsymbol{u}}^0_{\Gamma_2} \\ \bar{\boldsymbol{u}}_{\Gamma_2} \\ \bar{\boldsymbol{u}}^0_v \\ \bar{\boldsymbol{u}}_v \end{Bmatrix} = [N]^T \{\boldsymbol{d}\} \tag{5.43}$$

The corresponding strain-displacement $[B]$ matrix takes the following form:

$$B = \begin{bmatrix} -[R_\Omega]^T([\nabla w_{\Gamma_1}]^T + [\nabla w_{\Gamma_2}]^T) + (1 - w_{\Gamma_1} - w_{\Gamma_2} + w_{\Gamma_1} w_{\Gamma_2})[\nabla R_\Omega]^T \\ +(w_{\Gamma_1}[\nabla w_{\Gamma_2}]^T + w_{\Gamma_2}[\nabla w_{\Gamma_1}]^T)[R_\Omega]^T \\ [\nabla w_{\Gamma_1}]^T(1 - w_{\Gamma_2})(1 - w_{v_1})[R_{\Gamma_1}]^T - w_{\Gamma_1}[\nabla w_{\Gamma_2}]^T(1 - w_{v_1})[R_{\Gamma_1}]^T \\ -w_{\Gamma_1}(1 - w_{\Gamma_2})[\nabla w_{v_1}]^T[R_{\Gamma_1}]^T + w_{\Gamma_1}(1 - w_{\Gamma_2})(1 - w_{v_1})[\nabla R_{\Gamma_1}]^T \\ [\nabla w_{\Gamma_1}]^T(1 - w_{\Gamma_1}) - w_{\Gamma_1}[\nabla w_{\Gamma_2}]^T[R_{\Gamma_2}]^T + w_{\Gamma_1}(1 - w_{\Gamma_2})[\nabla R_{\Gamma_1}]^T) d_{\Gamma_1} \\ +[\nabla d_{\Gamma_1}]^T w_{\Gamma_1}(1 - w_{\Gamma_2}) R_{\Gamma_2}]^T \\ [\nabla w_{\Gamma_2}]^T(1 - w_{v_2})[R_{\Gamma_2}]^T - w_{\Gamma_2}[\nabla w_{v_2}]^T[R_{\Gamma_2}]^T + w_{\Gamma_2}(1 - w_{v_2})[\nabla R_{\Gamma_2}]^T \\ [\nabla w_{\Gamma_2}]^T d_{\Gamma_2}[R_{\Gamma_2}]^T + w_{\Gamma_2}[\nabla d_{\Gamma_2}]^T[R_{\Gamma_2}]^T + w_{\Gamma_2} d_{\Gamma_2}[\nabla R_{\Gamma_2}]^T \\ \{[\nabla w_{\Gamma_1}]^T(1 - w_{\Gamma_2}) w_{v_1} - w_{\Gamma_1} \nabla w_{\Gamma_2} w_{v_1} + w_{\Gamma_1}((1 - w_{\Gamma_2}) \nabla w_{v_1} + \nabla w_{\Gamma_2} w_{v_2} + \nabla w_{v_2} w_{\Gamma_2})\} I \\ [\nabla d_{v1}]^T w_{\Gamma_1}(1 - w_{\Gamma_2}) w_{v_1} + d_{v1}\{[\nabla w_{\Gamma_1}]^T(1 - w_{\Gamma_2}) w_{v_1} - w_{\Gamma_1}[\nabla w_{\Gamma_2}]^T w_{v_1} + w_{\Gamma_1}(1 - w_{\Gamma_2})[\nabla w_{v_1}]^T\} \\ +[\nabla d_{v2}]^T w_{\Gamma_2} w_{v_2} + d_{v2}\{[\nabla w_{\Gamma_2}]^T w_{v_2} + w_{\Gamma_2}[\nabla w_{v_2}]^T\} \end{bmatrix}^T \tag{5.44}$$

Note that in terms corresponding to the vertex, $I$ is identity matrix, $d_{v_i}$ is a vector whose components are the distance to the projected point on the edges from the vertex (Section 5.2.2).

## 5.3 Patch Tests

The developed methodology was first validated through two-dimensional and three-dimensional patch tests in which unit traction was applied as illustrated in Figure 5.7. The

non-overlapping subdomains, $\Omega_1$ and $\Omega_2$, were coupled through a stitching interface $\Gamma_e$ along the shared boundary using the above-described methodology. Subdomains with identical as well as dissimilar materials were considered to test the ability to reproduce discontinuities in the displacement derivatives across the stitching interface. Elastic modulus of $E = 1$ and Poisson's ratio of $\nu = 0.3$ were assumed when modeling homogeneous domains. The degrees of the NURBS basis functions used to approximate the subdomains, either linear or quadratic, were kept identical for both subdomains as well as the coupling interface in all the tests. Standard 3-point Legendre-Gauss numerical integration was used as the baseline quadrature scheme, but the order of quadrature depended on the chosen weight function form. Six and eight point quadrature were used when the weight function was of exponential form.

### 5.3.1 Two-Patch Domains

First we describe patch tests on coupled two-patch NURBS domains. Three types of discretization schemes including matching, hierarchical and non-matching were considered. The matching scheme assumes a conforming discretization for both subdomains with the size of $h_1 = h_2 = 1/3\text{i}$ with i taking on sequential values that produced refined meshes. The hierarchical scheme had a periodically matching discretization for $\Omega_1$ and $\Omega_2$ with $h_1 = 1/3\text{i}$ and $h_2 = 1/6\text{i}$, respectively. In the non-matching refinement, the two subdomains had a non-conforming discretization of $h_1 = 1/(4\text{i} - 1)$ and $h_2 = 1/(8\text{i} - 1)$.

To judge convergence rate, The relative $L_2$ norm of the error in displacement and strain energy as defined below:

$$\bar{\text{e}}_{L_2} = \frac{\|\boldsymbol{u}^{ex} - \boldsymbol{u}^h\|_{L_2}}{\|\boldsymbol{u}^{\text{ex}}\|_{L_2}} = \frac{\left\{\int (\boldsymbol{u}^h - \boldsymbol{u}^{\text{ex}})^T (\boldsymbol{u}^h - \boldsymbol{u}^{\text{ex}}) d\Omega\right\}^{1/2}}{\left\{\int (\boldsymbol{u}^{\text{ex}})^T (\boldsymbol{u}^{\text{ex}}) d\Omega\right\}^{1/2}} \tag{5.45a}$$

$$\bar{\text{e}}_{en} = \frac{\|\boldsymbol{u}^{ex} - \boldsymbol{u}^h\|_{en}}{\|\boldsymbol{u}^{\text{ex}}\|_{en}} = \frac{\left\{\frac{1}{2}\int (\boldsymbol{\varepsilon}^h - \boldsymbol{\varepsilon}^{\text{ex}})^T D(\boldsymbol{\varepsilon}^h - \boldsymbol{\varepsilon}^{\text{ex}}) d\Omega\right\}^{1/2}}{\left\{\frac{1}{2}\int (\boldsymbol{\varepsilon}^{\text{ex}})^T D(\boldsymbol{\varepsilon}^{\text{ex}}) d\Omega\right\}^{1/2}} \tag{5.45b}$$

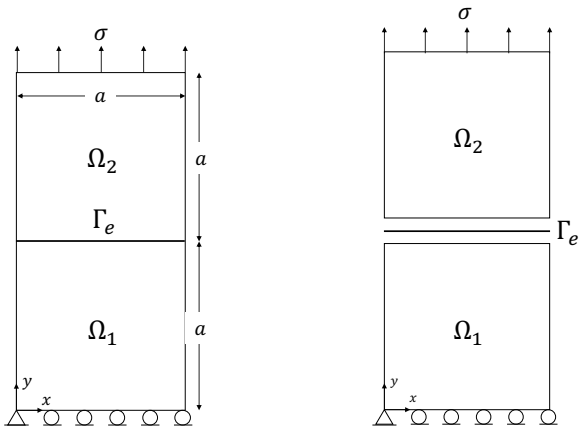


**Figure 5.7.** (a) Patch test setup and (b) expanded view of the individual subdomains and the coupling interface.

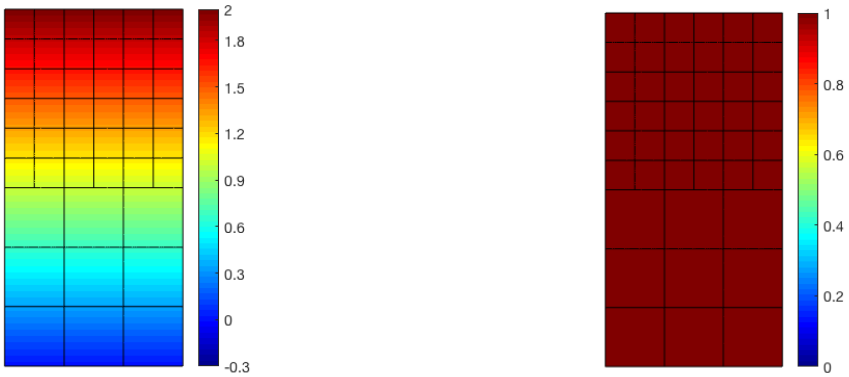


(a) (b)

**Figure 5.8.** (a) $u_y$ solution and (b) $\sigma_{yy}$ solution on two-patches with regular edges

The $u_2$ displacement and $\sigma_{yy}$ stress field in the patch test are shown in Figure 5.8 for the coarsest mesh. The convergence test result in Figure 5.9 shows that for two sub-domains with regular edge, machine precision is achieved even with the coarsest mesh.

### 5.3.2 Generalization to Patches with Curved Edges

In general, if the edges of the patches are arbitrary in shape, two issues arise: accuracy of projecting a domain point to the edge and accuracy of carrying out quadrature. These

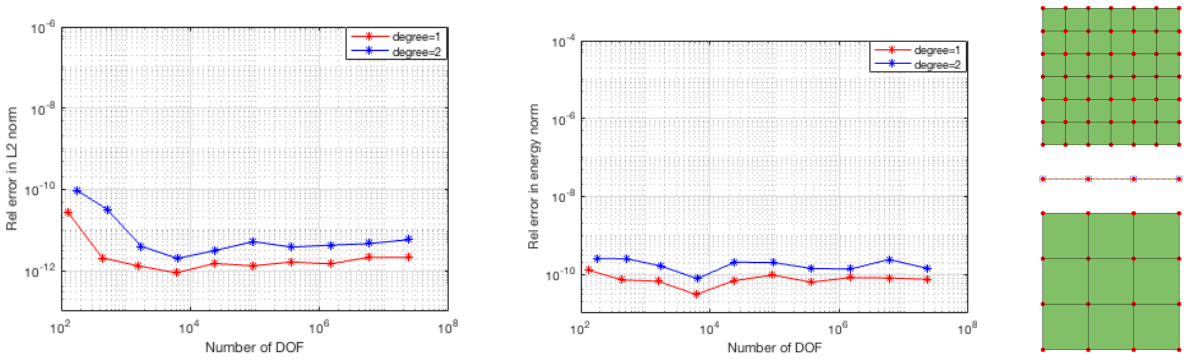


(a) (b) (c)

**Figure 5.9.** (a) The relative $L_2$ norm of error in displacement on a two-patch domain with a regular edge (a) The relative energy norm of error on a two-patch domain with a regular edge (c) Illustration of the coarsest mesh used in the study.

issues are elaborated below. Isogeometric blended field approximation was described earlier in Eq. (5.4):

$$f_{\mathrm{i}}(\boldsymbol{x}) = [1 - w(d_{\mathrm{i}}(\boldsymbol{x}))]\, f_{\Omega_{\mathrm{i}}}(\boldsymbol{x}) + w(d_{\mathrm{i}}(\boldsymbol{x})) f_{\Gamma_{\mathrm{e}}}(\xi, \eta, d_{\mathrm{i}}(\boldsymbol{x})) \tag{5.46}$$

In the above representation, to evaluate the enriching field at a spatial location $\boldsymbol{x}$, $f_{\Gamma_{\mathrm{e}}}(\xi, \eta, d_{\mathrm{i}}(\boldsymbol{x}))$, knowledge of the parametric location and distance to the parametric surface $(\xi, \eta, d_{\mathrm{i}}(\boldsymbol{x}))$ is necessary. That is, the spatial location $\boldsymbol{x}$ needs to be projected to the enriching surface. Such a projection is challenged near regions of large curvature as illustrated in Figure 5.10. These errors can be minimized when the size of the blending region is minimized so the projection is smooth.

The second issue relates to quadrature. The integration cell in Figure 5.11 is divided into two: the region blended with the enrichment $\Omega_{\mathrm{e}}$ and the region defined by the underlying field $\Omega_c$. The continuity condition (Section 5.1.3) guarantees the smoothness of the blended field across the edge of the enriching region. However, the field within the cell is a piece-wise function: This piece-wise function requires either subdivision of the integration cell or increased order of quadrature. For geometrical simplicity, the latter strategy of increased quadrature order is employed in this study.

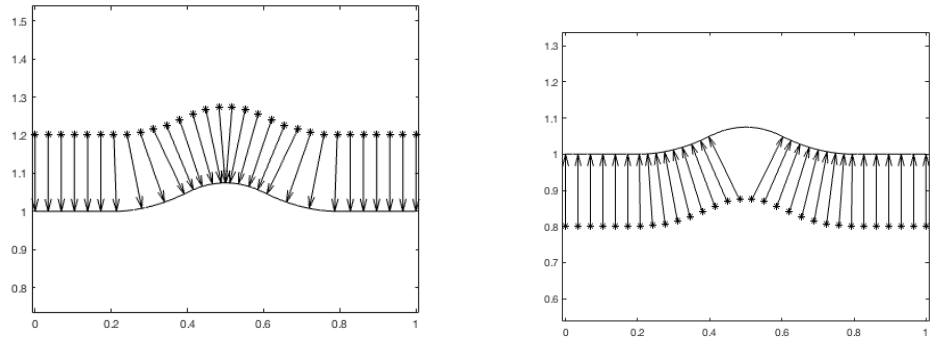

(a) (b)

**Figure 5.10.** Point projection near regions of high curvature (a) Regularly spaced spatial points project to a narrow range of parametric values (b) Projected points are discontinuous.

$$f = \begin{cases} f_c & \text{in } \Omega_c \\ (1 - w_{\mathrm{e}}) f_c + w_{\mathrm{e}} f_{\mathrm{e}} & \text{in } \Omega_{\mathrm{e}} \end{cases} \tag{5.47}$$

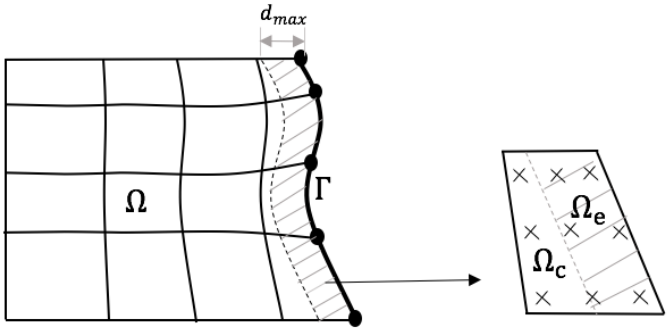


**Figure 5.11.** Issue of integration over a cell with a piece-wise function description.

We illustrate the above challenges on a two-patch geometry. Figure 5.12 shows the results of a patch test on a two-patch geometry with curved interface. In the example (and in other examples with curved edges described in this study), knots were inserted at 1% of the regular knot span close to the interface to generate the new blending region over

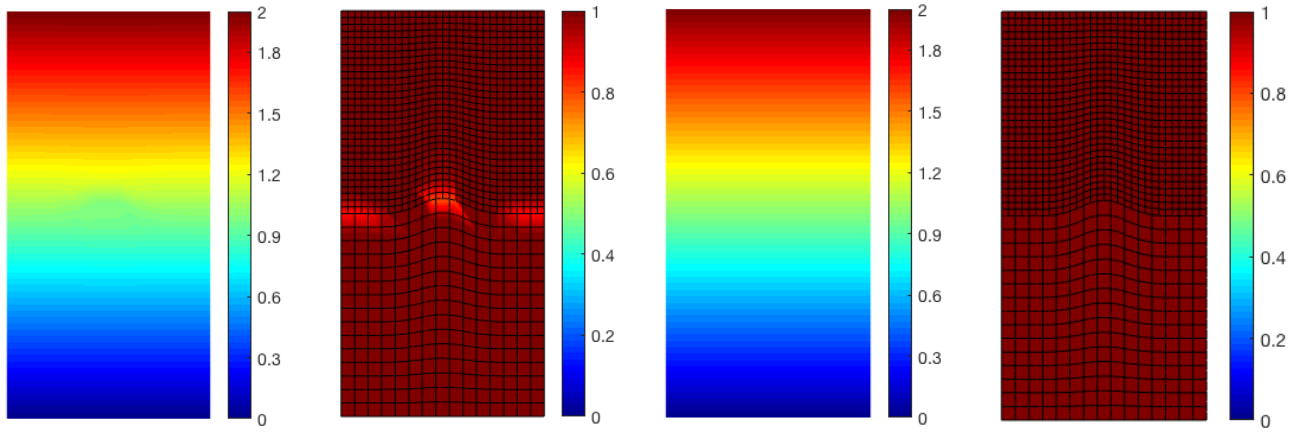


(a) (b) (c) (d)

**Figure 5.12.** (a) $u_y$ solution on two-patches with curved edges estimated with 6-point qudrature in the cells, (d) $\sigma_{yy}$ solution estimated with 6-point qudrature in the cells, (a) $u_y$ solution estimated with 21-point qudrature in the cells, and (b) $\sigma_{yy}$ solution estimated with 21-point qudrature in the cells. The grid of knot spans were not overlaid on the displacement contour plots to enable easier reading of the contours.

which integration was carried out. The example illustrates use of 6-point (Figure 5.12b) and 21-point (Figure 5.12d) quadrature in the blending knot span. In general, beginning with 6-point quadrature, the order of quadrature was increased by five until the relative error in stress decreased to below $10^{-3}$.

To quantify the influence curvature, a convergence study was carried out with edges of higher/lower curvature. The effect of using either quadratic or cubic basis functions on the patches was also studied. In Figure 5.13, the convergence of two-patch domains with a curved edge is quantified. An edge with lower curvature leads to smaller error, while the degree of the basis function has little influence on the error or the convergence rate. This is because the main source of error in the test is the projection from a domain point onto the curved edge, which depends only on the curvature of the edge. As indicated in the figure, the error decreases with curvature. When the edge is straight, the error is less than function precision as was shown earlier in Figure 5.9.

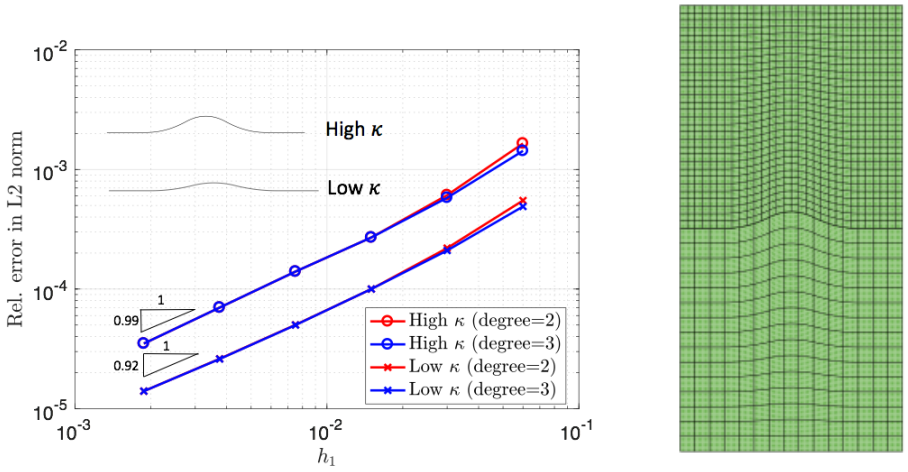


(a) (b)

**Figure 5.13.** (a) The relative $L_2$ norm of error in displacement on a two-patch domain with a curved edge (b) Illustration of the coarsest mesh used in the study.

### 5.3.3 Three- and Four-Patch Domains

We next carryout patch tests on domains composed of three and four patches with non-matching discretizations on which unit traction was applied as illustrated in Figure 5.14. Similar to the two-patch test, the non-overlapping subdomains $\Omega_i$ were coupled through stitching interfaces $\Gamma_{e_i}$ along the shared boundary. Intersecting interfaces $\Gamma_{e_i}$ were coupled at the vertex $V_1$.

In Figure 5.15, the contours of displacement $u_y$ and the normal stress $\sigma_{yy}$ are shown on the coarsest mesh. Sequential refinement by doubling the mesh density was carried out for the convergence study. The reduction in error with refinement is plotted in Figure 5.16 for both three- and four-patch domains approximated using either linear (degree=1) or quadratic (degree=2) NURBS basis functions. The error fluctuates in the range of $10^{-10}$ to $10^{-13}$, which is accurate to function precision.

Figure 5.17 shows the results of the patch test on a geometry constructed with four patches coupled along curved edges. While this solution was not accurate to function precision, the displacement and stress distribution solutions were as expected. As explained

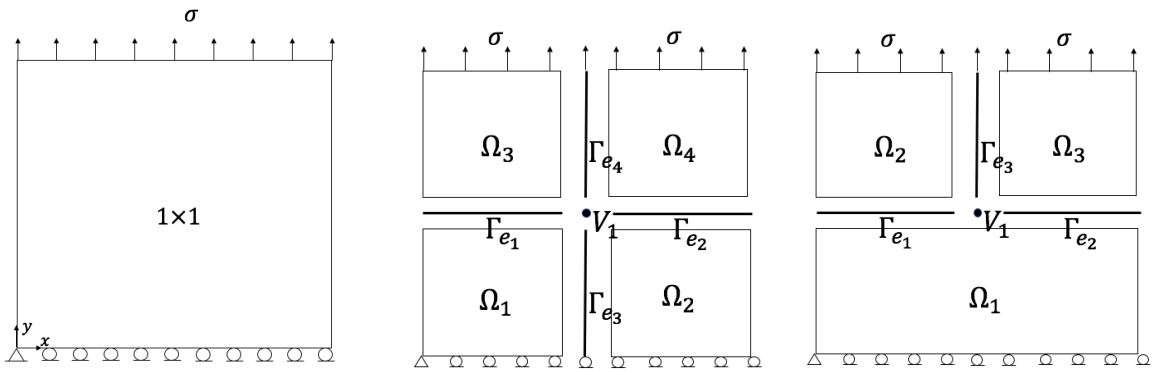


**Figure 5.14.** (a) Three- and four-patch test setup (b) expanded view of the individual subdomains and the coupling interfaces of the four patch domain (c) expanded view of the individual subdomains and the coupling interface of three patch domain.

in Section 5.3.2, a curved edge introduces two issues: inaccurate quadrature and inaccurate projection to the enriching entity. Here, 21-point quadrature was used in the knot span adjoining the coupling edge to mitigate the quadrature error. Both quadratic (degree=2) and cubic (degree=3) NURBS basis were used to approximate the underlying domain. Convergence on the four-patch domain is plotted in Figure 5.18, where, as before, $h_1$ is the knot span on patch $\Omega_1$. While the refinement reduces the error, the mangitude of the error is larger than that obtained on domains with orthogonal, straight edges. As discussed earlier on the two-patch domain coupled along a curved edge, both the solution error and the convergence rate is unaffected by the degree of the NURBS basis function used in the patches.

### 5.3.4 Multi-Patch Domains with Extraordinary Vertices

Generally, an unstructured arrangement of quadrilateral patches leads to generation of extraordinary vertices as illustrated in Figure 5.19a. In the developed method, enrichment at vertices overcomes the loss of smoothness experienced at extraordinary points in subdivision surfaces. The geometry shown in Figure 5.19a contained 15 patches, 25 edge enrichments and 11 vertex enrichments (see Figure 5.19b). In this example, multiple edges enrich a given patch, but the weight field construction described in Eq. (5.6) still applies. However, the

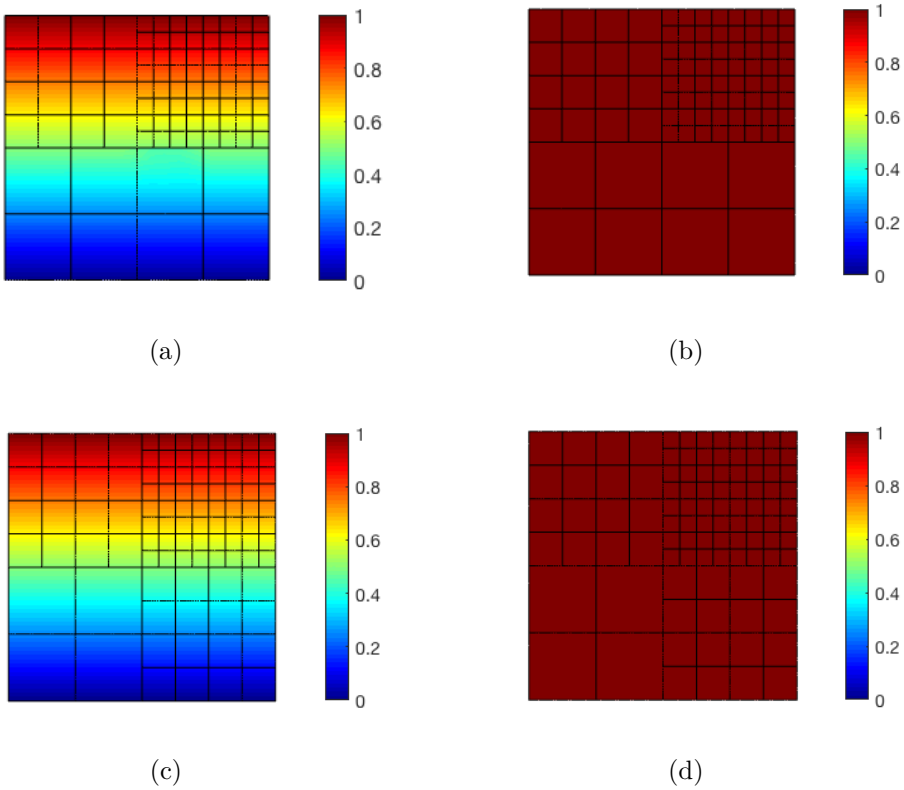


**Figure 5.15.** (a) $u_y$ solution on three-patches with orthogonal, straight edges, (b) $\sigma_{yy}$ on the three-patch geometry, (c) $u_y$ on the four-patch geometry with orthogonal straight edges, and (d) $\sigma_{yy}$ solution on the four-patch geometry.

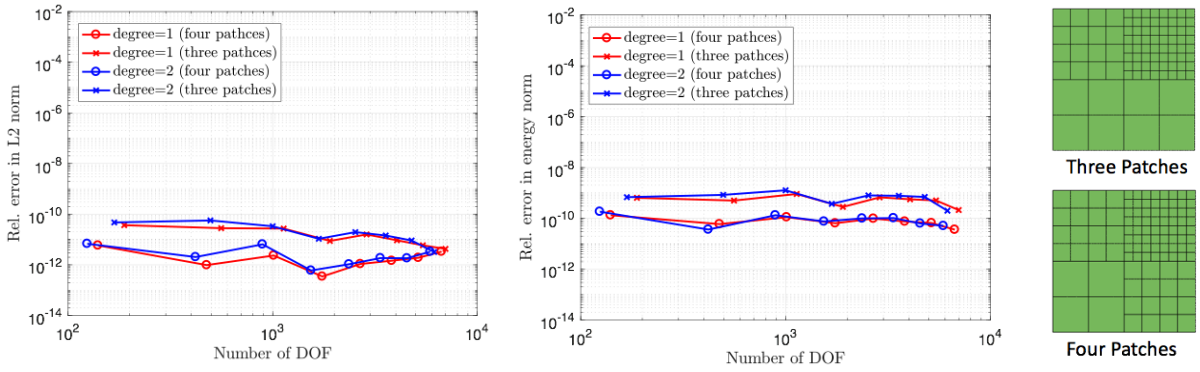


(a) (b) (c)

**Figure 5.16.** (a) Relative $L_2$ norm of error in displacement and (b) strain energy for patch tests on a domain with three or four patches coupled along orthogonal, straight edges (c) Illustration of the coarsest mesh of three- and four-patch domains.

enriching region needs to be decomposed into three sub-regions as shown in Figure 5.20: regions I and II are enriched by their corresponding edges $E_1$ and $E_2$ respectively, and region III is enriched sequentially by the two edges. The displacement $u_y$ and stress field $\sigma_{yy}$ are shown in Figure 5.19c and Figure 5.19d. The solution generated by the enriched approximation exhibits the expected smoothness in the stress.

## 5.4 Boundary Condition Application

We only consider boundary condition applied on the exterior boundary of the stitched structure. The boundary is composed of multiple patch edges as well as enrichments. Similar to boundary application in Chapter 4, Neumann boundary condition is applied by setting the corresponding value on the right hand side. Dirichlet boundary is applied by forcing the corresponding degree of freedom in the solution. In Section 5.4, which illustrates the the boundary condition application, the whole structure is composed of nine patches. The top of the structure is under distributed load $f(x)$ or displacement function $u(x)$, and it is necessary to determine the equivalent nodal value of the degree of freedom on the top. Due to the existence of boundary condition enrichment, the basis function for each control point on the top needs to be modified to $\tilde{N}_{\mathrm{i}}(x) = (1 - w_{\mathrm{e}}(x))N_{\mathrm{i}}(x)$, where $w_{\mathrm{e}}(x)$ is the weight function

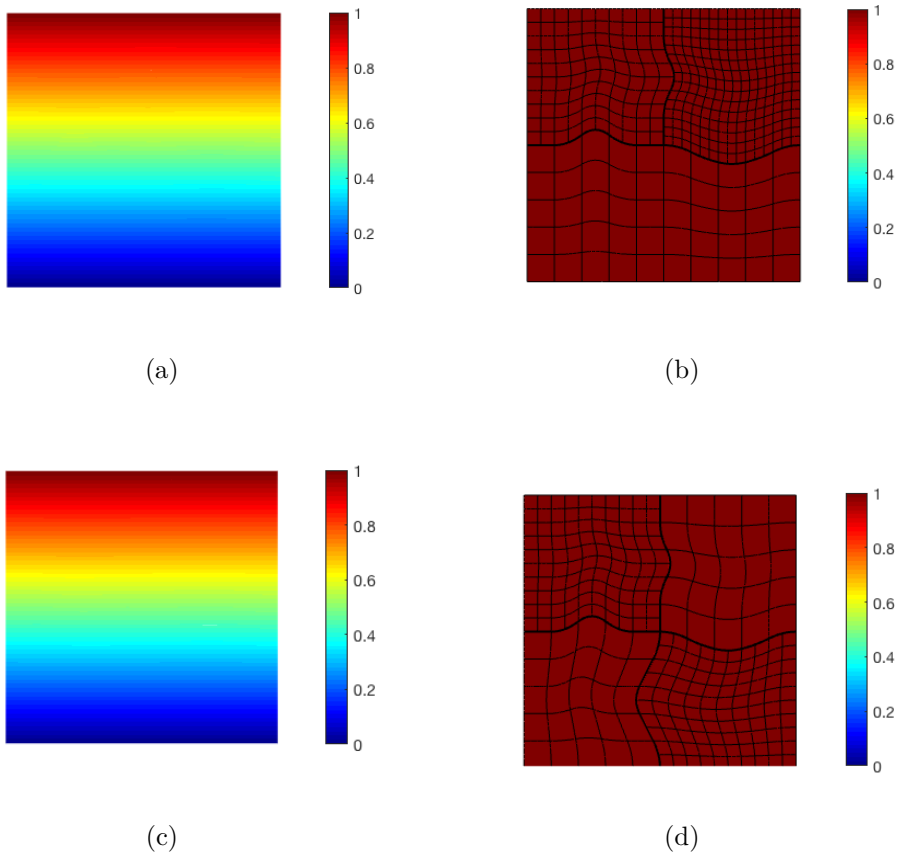


**Figure 5.17.** (a) $u_y$ contours on the three-patch geometry with curved edges, (b) $\sigma_{yy}$ on the three-patches, (c) $u_y$ solution on the four-patch geometry with curved edges, and (d) $\sigma_{yy}$ solution on the four-patch geometry. The grid of knot spans were not overlaid on the displacement contour plots to enable easier reading of the contours.

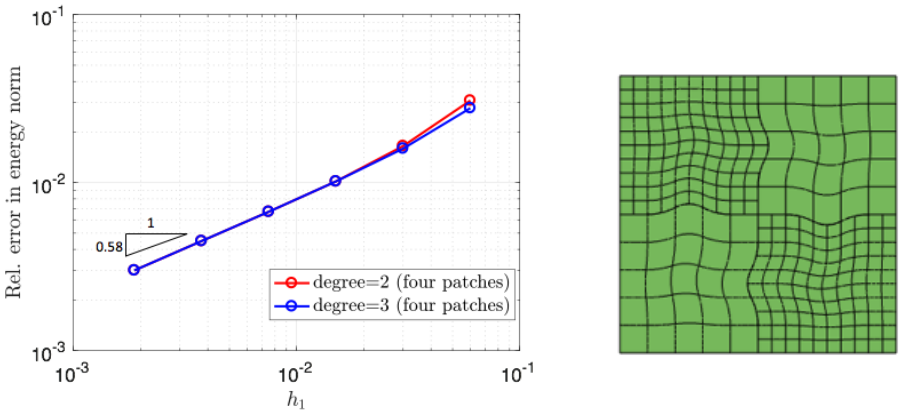


(a) (b)

**Figure 5.18.** (a) Relative $L_2$ norm of error in displacement and (b) The coarsest mesh used in the patch test.

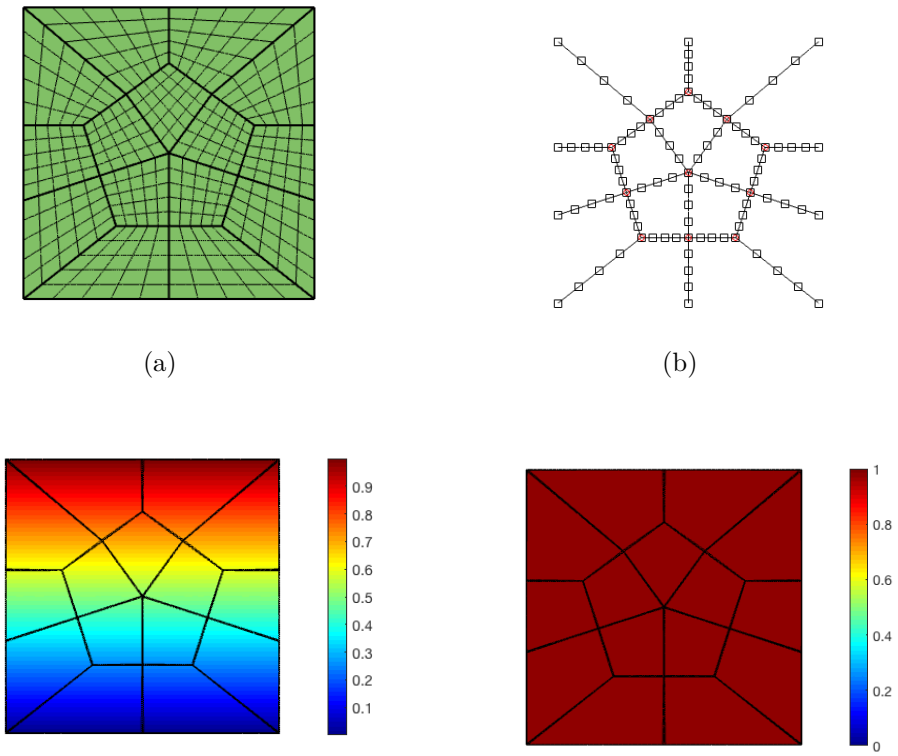


(a) (b)

(c) (d)

**Figure 5.19.** (a) Fifteen patch NURBS geometry with extraordinary vertices (b) edge enrichments and vertex enrichments used to build the approximation (c) $u_y$ solution and (d) $\sigma_{yy}$ solution.

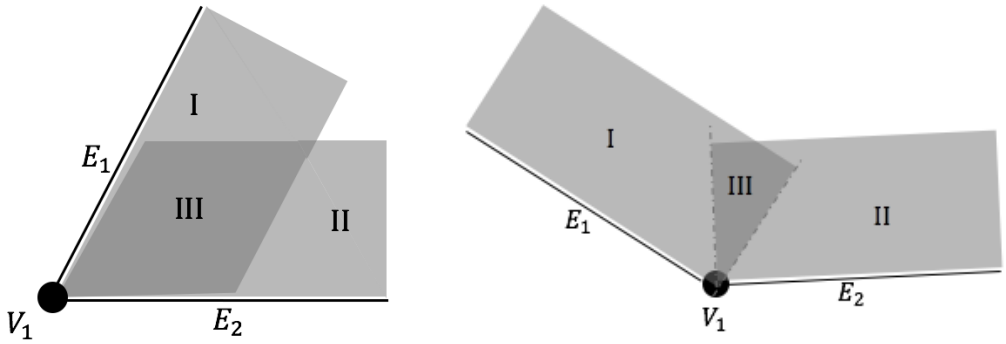


(a) (b)

**Figure 5.20.** Enrichment of a patch by two edges joined at a vertex. Edges joined at an (a) acute angle (b) obtuse angle

corresponding to the enrichment and $N_{\mathrm{i}}(x)$ is the original basis function along the boundary. The basis functions corresponding to the boundary condition enrichment are $\tilde{N}_{\mathrm{e}} = w_{\mathrm{e}}$ and $\tilde{N}_G = d_{\mathrm{e}} w_{\mathrm{e}}$. The modified basis functions for NURBS patches of degree two are shown in Section 5.4.

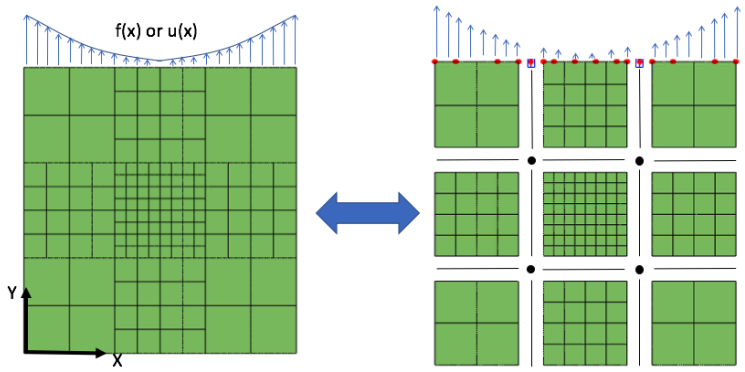


**Figure 5.21.** Illustration of the application of the boundary conditions.

### 5.4.1 Neumann Boundary Conditions

Determining the equivalent nodal force requires integrating along a one-dimensional stitched parametric curve. The technique is similar to the Neumann boundary condition application in Section 4.2.4. Since a work equivalent force is to be defined on the con-

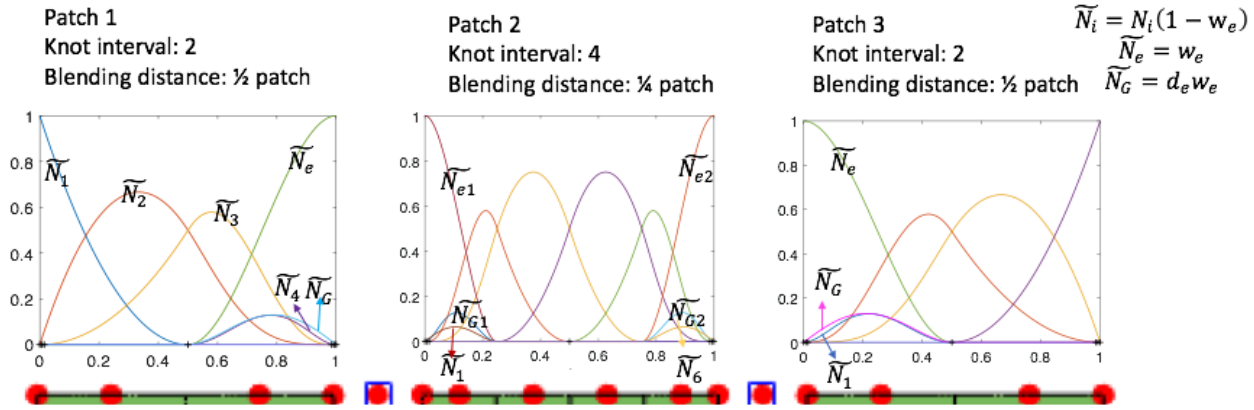


**Figure 5.22.** Modified basis functions on the boundary of the geometry illustrated in Section 5.4.

trol points of the boundary surface parametrized by $t$, a change of variables from $\mathbf{x}$ to $t$ is necessary to apply the Neumann condition

$$\mathbf{f}_{\mathrm{i}} = \int N_{\mathrm{i}}(\boldsymbol{x})\mathbf{f}(\boldsymbol{x})d\boldsymbol{x} = \int N_{\mathrm{i}}(t)\mathbf{f}(\boldsymbol{x}(t))\left|\frac{d\boldsymbol{x}}{dt}\right|dt = \int N_{\mathrm{i}}\mathbf{f}(t)|J|dt \tag{5.48}$$

where, $J$ is the Jacobian associated with the variable change:

$$J_{pq} = \frac{\partial x_p}{\partial t_q} \tag{5.49}$$

where, $x_p$ is the $p^{\mathrm{th}}$ component of $\boldsymbol{x}$.

### 5.4.2 Dirichlet Boundary Conditions

The Dirichlet boundary condition is applied by enforcing the corresponding degree of freedom by using least square approximation introduced in Section 4.2.3. The Dirichlet boundary is composed of different segments as well as nodes on the enrichments. If the value of Dirichlet boundary conditions is a non-zero constant, every $\mathbf{u}_{\mathrm{i}}$ on the corresponding edge is set to the constant value. A point to note is that in the stitching enrichment, the DOF on the edge evolves both the displacement and its normal derivative.

To apply the boundary condition, we let the distribution of the displacement vector field $\boldsymbol{u}(\mathbf{x})$ on the boundary be of an arbitrary form $\mathbf{u}(\mathbf{x}(t))$, where, $t$ is the parametric description of the reparametrized region $\Gamma_d$, on which the condition is applied, and $\mathbf{x}$ are the cartesian coordinates corresponding to the parametric location. The problem now is to minimize the function:

$$f(\mathbf{u}_\mathrm{i}) = \int \left[\mathbf{u}(\mathbf{x}(t)) - \sum_{\mathrm{i}=0}^{n} N_\mathrm{i}(t)\mathbf{u}_\mathrm{i}\right]^2 dt \tag{5.50}$$

and the optimality condition is:

$$\frac{\partial f}{\partial \mathbf{u}_\mathrm{j}} = -2\int N_\mathrm{j}\left[\mathbf{u}(t) - \sum_{\mathrm{i}=0}^{n} N_\mathrm{i}^T(t)\mathbf{u}_\mathrm{i}\right] dt = 0 \tag{5.51}$$

This will yield the following linear system for the unknown control point values of the vector $\mathbf{u}_\mathrm{i}$:

$$\left[\int N_\mathrm{j}(t)N_\mathrm{i}^T(t)dt\right]\mathbf{u}_\mathrm{i} = \int N_\mathrm{j}\mathbf{u}(t)dt \tag{5.52}$$

## 5.5 Numerical Examples

Several two-dimensional and three-dimensional examples are solved using the developed $p$-stitching procedure in the following.

### 5.5.1 Bi-quadratic Geometry Representation

The developed method is demonstrated to represent a two pre-defined quadratic surfaces in this section. The 15-patch NURBS discretization shown in Figure 5.19a is used again here. The enrichments described in Eq. (5.7) and Eq. (5.9) are used up to the quadratic term to capture the geometry:

$$f_V(d_V) = \bar{f}_V^0 + \bar{f}_V' d_V^m + \frac{1}{2}\bar{f}_V' d_V^2 \tag{5.53}$$

$$f_{E_\mathrm{i}}(d_{E_\mathrm{i}}) = f_{E_\mathrm{i}}^{0V}(\mathcal{P}(\boldsymbol{x})) + f_{E_\mathrm{i}}'(\mathcal{P}(\boldsymbol{x}))d_{E_\mathrm{i}} + \frac{1}{2}f_{E_\mathrm{i}}'(\mathcal{P}(\boldsymbol{x}))d_{E_\mathrm{i}}^2 \tag{5.54}$$

The composed field on the patch resulting from the blended enrichments is:

$$f_{F_\mathrm{j}}(\xi,\eta) = (1 - \sum_{\mathrm{i}=1}^{n_E} \bar{w}_{E_\mathrm{i}}(d_{E_\mathrm{i}}))f^0_{F_\mathrm{j}}(\xi,\eta) + \sum_{\mathrm{i}=1}^{n_E} \bar{w}_{E_\mathrm{i}}(d_{E_\mathrm{i}})f_{E_\mathrm{i}}(d_{E_\mathrm{i}}) \tag{5.55}$$

The values of the unknowns at the control points of the patches as well as the enrichments were obtained through a least square fit. Thus, given the field $f(\boldsymbol{x})$, the following function was minimized to solve for the values at the control points:

$$F(f_\mathrm{i}) = \iint \left[ f(\boldsymbol{x}(\xi,\eta)) - \sum_{\mathrm{i}=0}^{n} N_\mathrm{i}(\xi,\eta) f_\mathrm{i} \right]^2 d\xi d\eta \tag{5.56}$$

The optimality condition for the above minimization problem yields the following linear system for the unknown control point values $f_\mathrm{i}$:

$$\left[ \int N_\mathrm{j}(\xi,\eta) N_\mathrm{i}^T(\xi,\eta) d\xi d\eta \right] f_\mathrm{i} = \int N_\mathrm{j} f(\boldsymbol{x}(\xi,\eta)) d\xi d\eta \tag{5.57}$$

The enrichment at a vertex is obtained directly by evaluating the function and its derivatives at the vertex location. The edge enrichments are dependent on three sets of control point quantities: the field value, the first order directional derivative and the second order directional derivative. The directional derivatives in turn need the first and second derivative with respect to $x$ and $y$. Thus, for a given edge enrichment, the first and second order directional derivatives $f'$ and $f'$ are defined as:

$$f' = \frac{\partial f}{\partial \boldsymbol{n}} = \boldsymbol{n} \cdot \mathbf{G}, \quad f' = \frac{\partial^2 f}{\partial \boldsymbol{n}^2} = \boldsymbol{n} \cdot \mathbf{H} \cdot \boldsymbol{n} \tag{5.58}$$

where,

$$\mathbf{G} = \begin{Bmatrix} \frac{\partial f}{\partial x} \\ \frac{\partial f}{\partial y} \end{Bmatrix}, \quad \mathbf{H} = \begin{bmatrix} \frac{\partial^2 f}{\partial x^2} & \frac{\partial^2 f}{\partial x \partial y} \\ \frac{\partial^2 f}{\partial x \partial y} & \frac{\partial^2 f}{\partial y^2} \end{bmatrix} \tag{5.59}$$

Two quadratic surfaces were modeled using the above described procedure:

$$f(x,y) = y^2 \tag{5.60}$$

and

$$f(x,y) = -(x^2 - x)(y^2 - y + 1) \tag{5.61}$$

The relative error in the composed field obtained through the blending process was calculated as:

$$\epsilon(x,y) = \frac{|f(x,y) - f_F(x,y)|}{|f(x,y)|} \tag{5.62}$$

The solution for Eq. (5.60) is shown in Figure 5.23; the solution is accurate to within machine precision. For Eq. (5.61), two different discretizations of the NURBS patches was attempted: $5 \times 5$ knot span as well as a knot span of $20 \times 20$. The fitted function, and the error due to coarser/finer discretizations are shown in Figures 5.24a to 5.24c. The relative error reduces from $10^{-3}$ to $10^{-6}$ with refinement suggesting that the error is due to the accuracy of the least-squares fit and not due to the enrichment procedure.

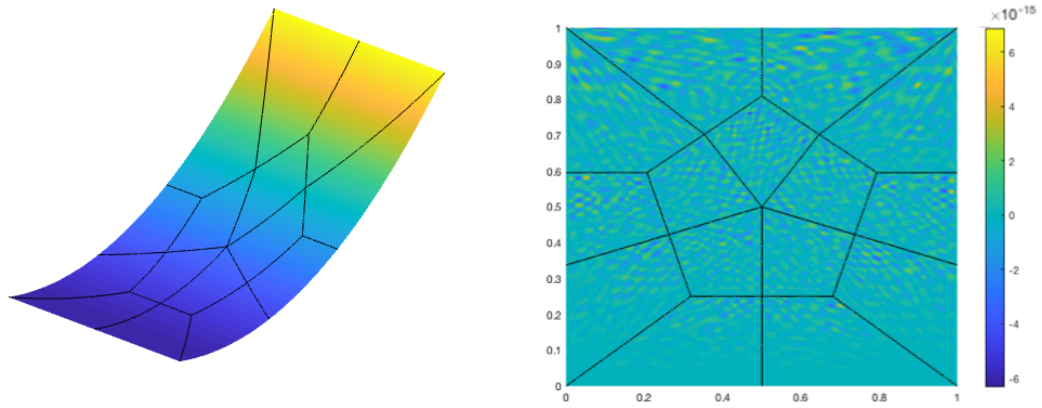


(a) (b)

**Figure 5.23.** Solution to $f(x,y) = y^2$(a) geometry - the color contours represent the function values (b) error distribution. The fit was accurate to within machine precision.

### 5.5.2 Quadratically Loaded Patch

Quadratic distributed load is applied on a domain to demonstrate the effect of the vertex enrichment. The domain size is also 1 by 1 and it is decomposed into nine patches as shown in Section 5.4. The distributed load is described as $f(x) = 4(x - 1/2)^2$ (using the coordinate

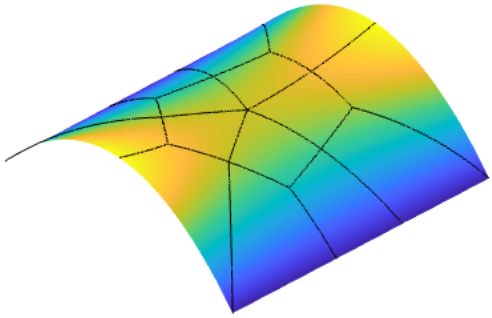

(a)

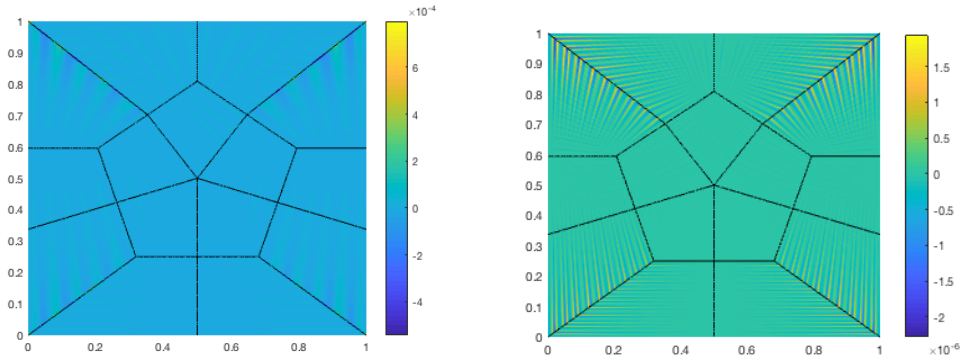

(b) (c)

**Figure 5.24.** Solution to $f(x, y) = -(x^2 - x)(y^2 - y + 1)$ (a) geometry - the color contours represent the function values (b) error distribution on coarser discretization (c) error distribution reduces with finer discretization.

system shown in Section 5.4). Two models are build for the problem: in the first one, all patches are stitched with adjacent ones through the common interface, while in the second, the interfaces are first enriched by vertexes and then the stitched interfaces are applied to stitch faces. It can seen in Figure 5.25a that gaps exist between patches if no vertex enrichment is applied. If one checks the deformation of interfaces carefully Figure 5.26a, the nodal field on the interfaces are not compatible at the intersection. Essentially, the vertices are used to construct compatible field on the incident edges, and the edges are applied to stitch adjacent patches (Figure 5.25b and Figure 5.26b).

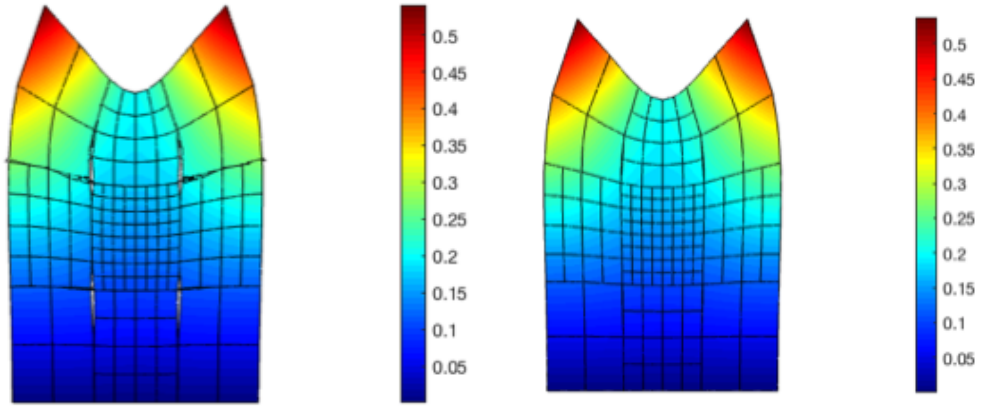


**Figure 5.25.** Deformation of quadratically loaded domain (a) without vertex enrichment (b) with vertex enrichment

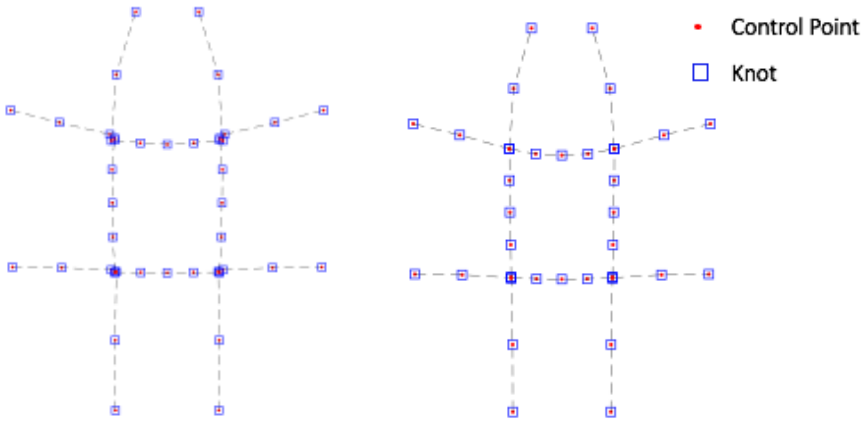


**Figure 5.26.** Deformation of interfaces (a) in Figure 5.25a without vertex enrichment (b) in Figure 5.25b with vertex enrichment.

### 5.5.3 Timoshenko Beam

Consider a beam with dimensions $L$ by $D$, and of unit thickness, subjected to parabolically distributed shear traction $t_y$ along the free end given by:

$$t_y = \frac{-P}{2I}\left(\frac{D^2}{4} - y^2\right) \tag{5.63}$$

where, $P$ is the resultant load and $I = D^3/12$ is the cross-sectional moment of inertia. Along the boundary, $\Gamma_u = \{x = 0, -D/2 \leq y \leq D/2\}$, the $x$-displacements were set to zero. The $y$-displacement was also restrained at $x = 0, y = 0$. The beam was decomposed into two equal sized halves represented by two bi-cubic NURBS patches. A coupling interface defined by $\Gamma_e = \{x = L/2, -D/2 \leq y \leq D/2\}$ was introduced between the two patches. The two subdomains were discretized into $10 \times 10$ and $21 \times 21$ uniform "elements" (non-zero knot spans), respectively. Figure 5.27 shows the geometric dimensions, boundary conditions, decomposed subdomains as well as their discretizations.

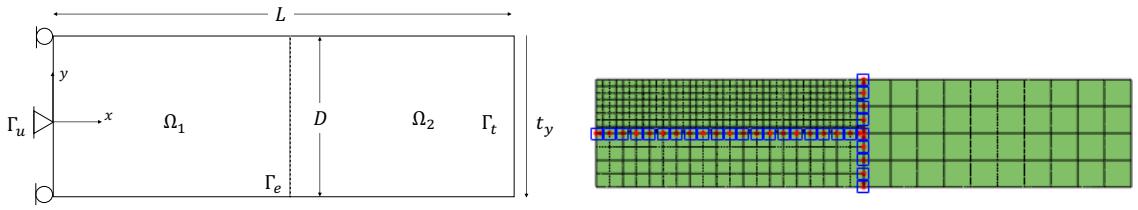


(a) (b)

**Figure 5.27.** (a) Dimensions, boundary conditions, and (a) NURBS discretization of Timoshenko beam.

The analytical solution to this problem is [133]:

$$u_x = \frac{Py}{6EI}[(6L - 3x)x + (2 + \nu)(y^2 - \frac{D^2}{4})] \tag{5.64a}$$

$$u_y = \frac{-P}{6EI}[3\nu y^2(L - x) + (4 + 5\nu)\frac{D^2}{4}x + (3L - x)x^2] \tag{5.64b}$$

$$\sigma_{xx} = \frac{P(L - x)y}{I} \tag{5.64c}$$

$$\sigma_{yy} = 0 \tag{5.64d}$$

$$\sigma_{xy} = \frac{-P}{2I}(\frac{D^2}{4} - y^2) \tag{5.64e}$$

For the purposes of numerical computation, the elastic properties of the two subdomains were chosen to be identical and equal to $E = 1000$ and $\nu = 0.25$. The specific value of dimensions were $L = 100$ and $D = 20$, and the tip load value was $P = 8$.

Figure 5.28 shows the vertical displacement and its relative error with respect to absolute values of the maximum deflection $u_{max} = max|u_y|$. Overall, the error introduced by the enforcement of non-homogeneous essential boundary conditions was larger than the error near the coupling field. Only smooth variations about the expected value of the field were observed near the coupling interface. The same analysis was also carried out using three patch with a T-junction. The solution shown in Figure 5.28.

### 5.5.4 L-shaped Domain

Consider an L-shaped domain decomposed into three patches. The geometric dimensions, boundary conditions and discretizations are described in Figure 5.29a and Figure 5.29b. In

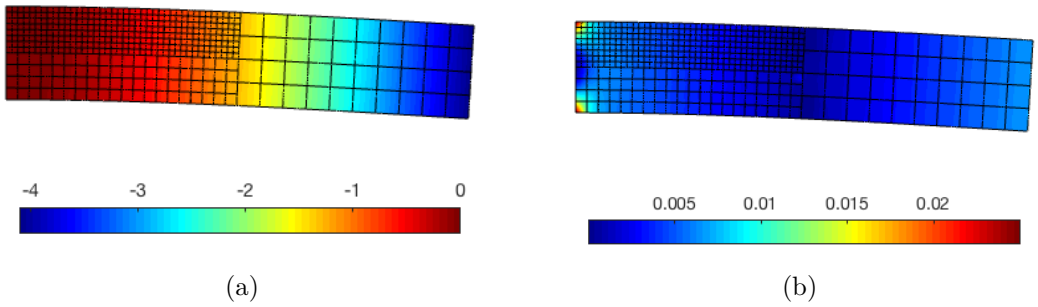


(a) (b)

**Figure 5.28.** (a) Vertical displacements $u_y$ and (b) its relative error $u_y/|u_{max}|$ in the Timoshenko beam using three patches

total, the model contained 2400 NURBS "elements" (non-zero knot spans) that resulted in 6784 degrees of freedom. The problem was also solved using the commercial finite element code ABAQUS for comparison. The finite element sizes vary from 0.002 at the corner to 0.03 far away from the corner. The mesh contains a total of 3834 quadratic elements, resulting in 14590 degrees of freedom (Figure 5.29c). The finite element model does not have decomposed sub-domains or a coupling interface. The simulation results are compared in Figure 5.30. Since p-stitching naturally assures compatibility at the interface, displacements are continuous across the coupling interfaces as expected. Since the singular stress at the corner is sensitive to mesh size. It is not accurate to compare the stress solution unless a convergence study is carried. Overall, the displacement and stress distribution contours show consistency with the finite element solution.

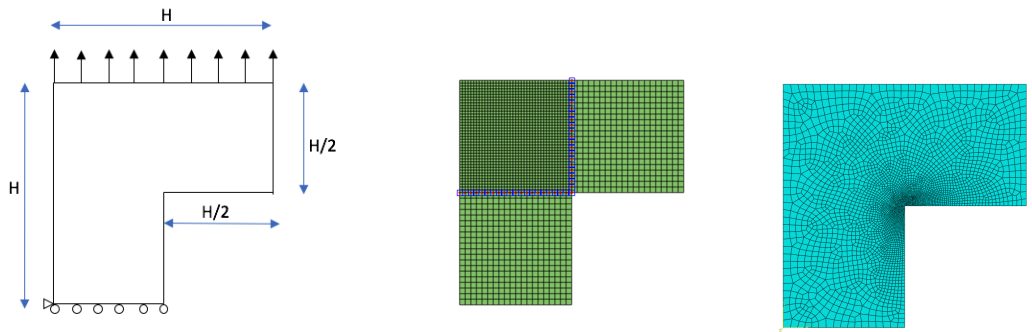


(a) (b) (c)

**Figure 5.29.** (a) Geometry and boundary condition (b) NURBS descretization (c) FEM mesh in ABAQUS

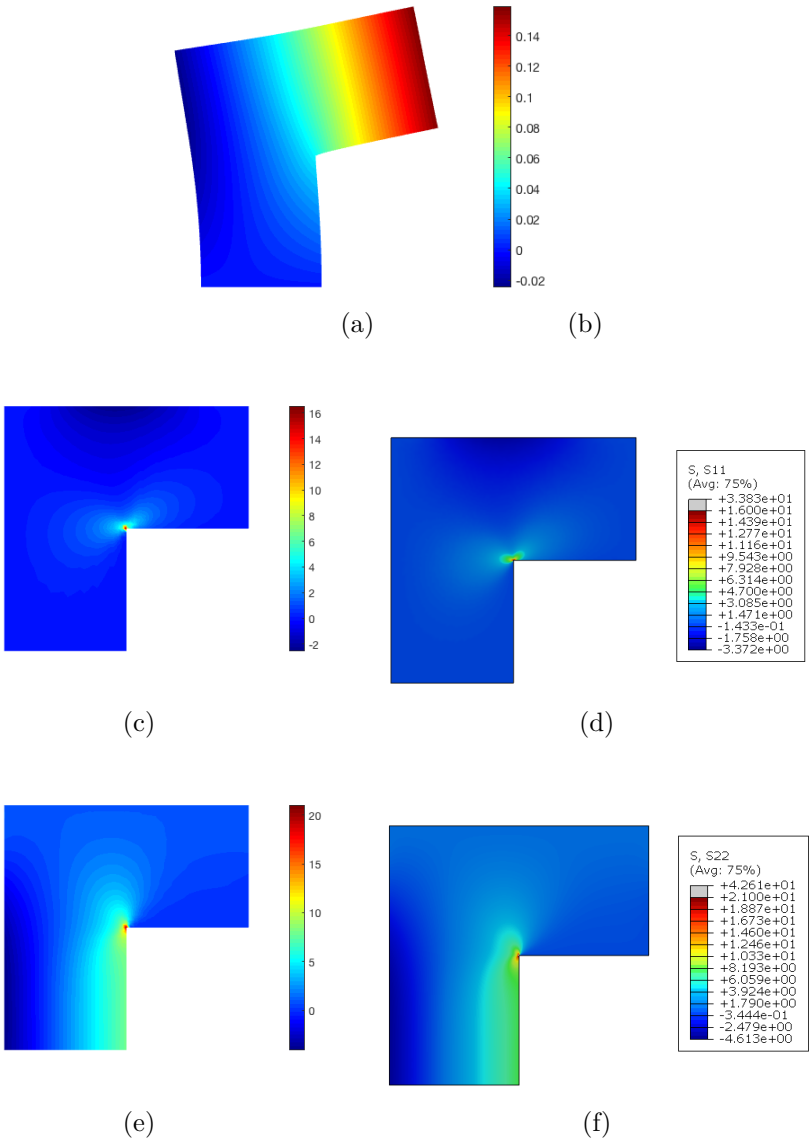


**Figure 5.30.** Simulation result: $u_y$ obtained by (a) the present method (b) ABAQUS; $\sigma_{xx}$ obtained by (c) the present method (d) ABAQUS; $\sigma_{yy}$ obtained by (e) the present method (f) ABAQUS

## 5.6 Summary

In this chapter, a technique to couple parametric subdomains with non-matching discretizations was developed. Explicit edge enrichments were used to stitch two adjacent patches. It was then extended to problems in which multiple patches join at T-junctions or

extraordinary vertices. A hierarchical enriching strategy over vertex, edge, face and body was developed.

The condition to ensure arbitrary smoothness was derived. By choosing proper weight function to blend the enrichment, one can achieve the expected smoothness. The weights need to satisfy: a value of 1 on the interface and 0 at the edge of blending region. For higher smoothness, the corresponding directional derivative should be 0 at both the enrichment and at the edge of blending region.

Patch tests were conducted on two-patch, three-patch, four-patch and multi-patch domains with extraordinary vertices. convergence studies on with both straight and curved edges were carried out. In general, solutions accurate to function precision are achieved when coupling patches with orthogonal straight edges, but the accuracy degrades with increased curvature of the coupling edges. Also, the solution error does depend on the accuracy of quadrature near curved boundaries, but the overall solution was in very good agreement with the reference one.

Lastly, the patch test solution on a generalized multi-patch domain with extraordinary vertices was demonstrated. The p-stitching procedure enables one to construct efficient discretizations for problems with large local gradients in the solution. It also provides a viable approach to stitching B-rep solid models for isogeometric analysis, without having to generate alternative single-patch spline approximations.

# 6. ENRICHED ISOGEOMETRIC ANALYSIS FOR CORNER SINGULARITIES

Singular stress is often observed at re-entrant corners and at the tips of cracks. They are critical concerns for the reliability of engineering structures. There are many theoretical studies on sharp corner singularity. Existing theories have shown that stress field at sharp corners is proportional to $r^{1-\lambda}$, where $r$ represents the distance to the sharp corner and $1-\lambda$ indicates the strength of the singularity. As a special case, crack has a singularity of $\lambda = 1/2$.

To numerically model the singular field, one needs large numbers of DOFs using FEM. Enriched analysis is a promising tool since it makes use of knowledge of a priori form as the basis function, which is a good approximation of the near field. When using the EIGA form to represent the singular stress field near the sharp corner, the theoretical solution near the sharp corner is needed. For general bi-material corner with one or two surface bonded, there is no explicit form of solution. Fortunately, the general solution form contains an angular function, whose coefficients can be determined easily by solving a eigenvector problem. Starting with Seweryn's general displacement solution [51], the stress field can be represented with an unknown constant, which can be used to explicitly represent generalized stress intensity factors (SIFs).

In this chapter, a computational framework of enriched isogeometric analysis for corner singularity is proposed. The framework is applied on three different types of singularities: homogeneous angular corner, bi-material wedge with two surface bonded and interface crack. The proposed method takes advantage of a priori known field and thus needs relatively fewer degrees of freedom to get accurate fields. The developed method also allows direct extraction of generalized stress intensity factors without needing a posteriori evaluation of path independent integrals for decisions on crack propagation.

## 6.1 Isogeometric Enrichments for Singular Fields

Due to the singular stress near the re-entrant corner or crack tip, large numbers of degrees of freedom are required to capture the near field using FEM. Besides, post-processing

technique is often necessary to extract stress intensity factor. To reduce the computational cost and avoid post-processing, Chen et al [65] proposed a general approach that enables accurate estimation of stress intensity factor with relatively coarse and uniform mesh by using the analytical asymptotic solution around the notch/crack tip.

Following the idea of The enriched isogemetric Analysis (EIGA)[134], the field near sharp corner is used to construct a hierarchical compositional field. In general, the singular field around the material re-entrant corner or crack tip is captured by a vertex enrichment.

For elasto-static analysis, the enriched displacement field is approximated by the following form:

$$\boldsymbol{u} = (1 - w_t(d))\boldsymbol{u}_c(\boldsymbol{x}) + w_t(d)[\boldsymbol{u}_t + \Psi_s(r,\theta)\bar{K}] \tag{6.1}$$

in which $\boldsymbol{u}_c$ is the continuous displacement field of the underlying domain, $\boldsymbol{u}_t$ is the displacement associated with the multi-material junction and $\Psi_s(r,\theta)\bar{K}$ is the enriching field from the asymptotic solution.

The value of $\Psi_s(r,\theta)$ depends on the angle $\theta$ with respect to a reference axis. The detailed form of $\Psi_s(r,\theta)$ will be discussed later. The $\theta = 0$ line is usually chosen to be the $x'$ axis for local coordinates. As shown in Figure 6.1, the local $x'$ axis is chosen to coincide with the symmetry axis of the material. In the case of fracture, $x'$ is usually set to be parallel to the crack surface. Point $\boldsymbol{P}$ has local polar coordinates $(\theta, r)$, while $\phi$ denotes the angle between global and local systems. The displacement field in the local polar coordinate can expressed by the following matrix-vector product:

$$\left\{ \begin{array}{c} \boldsymbol{u}_r \\ \\ \boldsymbol{u}_\theta \end{array} \right\} = [\boldsymbol{\Psi}'_s] \left[\bar{K}_I, \bar{K}_{II}, ...\bar{K}_{n\lambda}\right] \tag{6.2}$$

where,

$$[\boldsymbol{\Psi}'_s(r,\theta)] = \left[\boldsymbol{\Psi}'_{s_1}, \boldsymbol{\Psi}'_{s_{\mathrm{II}}}, \cdots, \boldsymbol{\Psi}'_{s_{n_\lambda}}\right] = \left[ \begin{array}{c} r^{\lambda_{\mathrm{I}}} f(\theta), r^{\lambda_{\mathrm{II}}} f(\theta), \cdots, r^{\lambda_{n_\lambda}} f(\theta) \\ \\ r^{\lambda_{\mathrm{I}}} g(\theta), r^{\lambda_{\mathrm{II}}} g(\theta), \cdots, r^{\lambda_{n_\lambda}} g(\theta) \end{array} \right] \tag{6.3}$$

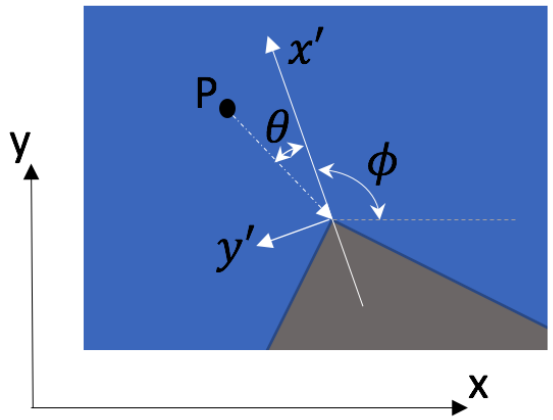


**Figure 6.1.** Illustration of conversion from local polar coordinates to global cartesian coordinate

Here, $\bar{K}_J$ is the unknown vector associated with the vertex, which is proportional to the generalized stress intensity factor (SIF) relating to the $J$-th mode of stress singularity, and $n_\lambda$ is the number of non-trivial singularities. The prime symbol signifies the local displacement field evaluated in the polar coordinate system. To evaluate the displacement in global Cartesian coordinate, a rotational transformation matrix is used, which is defined as:

$$\boldsymbol{T}(\theta) = \begin{bmatrix} \cos\theta & \sin\theta \\ -\sin\theta & \cos\theta \end{bmatrix} \tag{6.4}$$

$\boldsymbol{T}$ is an orthogonal matrix. Any displacement field in polar coordinate can be converted to global Cartesian coordinate by:

$$\begin{Bmatrix} \boldsymbol{u}_x \\ \boldsymbol{u}_y \end{Bmatrix} = [\boldsymbol{T}(\theta+\phi)]^T \begin{Bmatrix} \boldsymbol{u}_{r'} \\ \boldsymbol{u}_{\theta'} \end{Bmatrix} \tag{6.5}$$

Comparing the displacement in polar coordinates and global Cartesian coordinates, $[\Psi_s]$ can be represented by:

$$[\Psi_s] = [\boldsymbol{T}]^T [\Psi'_s] \tag{6.6}$$

The values of $\bar{K}_J$ are obtained by solving the boundary value problem with the applied far-field loading. The discretized equations are developed below for numerical analysis. The discretization of each component of displacement fields $\boldsymbol{u}_c, \boldsymbol{u}_t$ are discretized as:

$$\boldsymbol{u}_c = \sum_{\mathrm{i}}^{n_c} R_{c_\mathrm{i}} \boldsymbol{q}_{c_\mathrm{i}} = [R_c]\{\boldsymbol{q}_c\}, \tag{6.7a}$$

$$\boldsymbol{u}_t = \sum_{\mathrm{i}}^{n_t} R_{t_\mathrm{i}} \boldsymbol{q}_{t_\mathrm{i}} = [R_t]\{\boldsymbol{q}_t\} \tag{6.7b}$$

where, $R_{c_\mathrm{i}}$ and $R_{t_\mathrm{i}}$ are the NURBS basis functions of the underlying domain and the vertex enrichment.

The asymptotic displacement corresponding to the vertex enrichment is represented by:

$$\Psi_s \boldsymbol{u}_s = \sum_{\mathrm{i}=1}^{n_t} R_{t_\mathrm{i}} \Psi_{s_\mathrm{i}}(r,\theta) \boldsymbol{q}_{s_\mathrm{i}} = [R_t][\Psi_s(r,\theta)]\{\boldsymbol{q}_s\} \tag{6.8}$$

Combining the above equations, the displacement can be expressed in matrix form as $\boldsymbol{u} = N\boldsymbol{q}$ in which $N$ and $\boldsymbol{q}$ are

$$N = \Big[(1-w_t)R_c,\ w_t R_t,\ w_t R_t \Psi_s\Big], \tag{6.9a}$$

$$\boldsymbol{q} = [\boldsymbol{q}_c, \boldsymbol{q}_t, \boldsymbol{q}_s]^T \tag{6.9b}$$

The corresponding strain field is given by

$$\boldsymbol{\epsilon} = B\boldsymbol{q} \tag{6.10}$$

The matrix $B$ takes the following form:

$$B = \begin{bmatrix} (1-w_t)[\nabla R_c]^T - [R_c]^T[\nabla w_t]^T \\ w_t[\nabla R_t]^T + [R_t]^T[\nabla w_t]^T \\ w_t[\Psi_s]^T[\nabla R_t]^T + w_t[\nabla \Psi_s]^T[R_t]^T + [\Psi_s]^T[R_t]^T[\nabla w_t]^T \end{bmatrix}^T \tag{6.11}$$

Usually the vertex enrichment is on a point and $[R_t] = I$, $[\nabla R_t] = O$. It should be noted that even though strain is stored as a vector, it is a second-order tensor. Therefore, transformation of strain needs to follow tensor transformation rules. The transformation is denoted as $\nabla \Psi_s = T_\epsilon^{-1} \Psi'_s$.

The transformation equations from Cartesian coordinates to polar coordinates for strain is:

$$\begin{aligned} \epsilon_{x'} &= \epsilon_x \cos^2\theta + \epsilon_y \sin^2\theta + \gamma_{xy} \sin\theta\cos\theta \\ \epsilon_{y'} &= \epsilon_x \sin^2\theta + \epsilon_y \cos^2\theta - \gamma_{xy} \sin\theta\cos\theta \\ \gamma_{x'y'} &= 2\left(\epsilon_y - \epsilon_x\right)\sin\theta\cos\theta + \gamma_{xy}\left(\cos^2\theta - \sin^2\theta\right) \end{aligned} \tag{6.12}$$

From this relation, the transformation matrix for strain is defined as:

$$T_\epsilon = \begin{bmatrix} c^2 & s^2 & 2sc \\ s^2 & c^2 & -2sc \\ -sc & sc & c^2 - s^2 \end{bmatrix} \tag{6.13}$$

with $c$ denoting $cos(\theta)$ and $s$ denoting $sin(\theta)$. The above equations are substituted into the discretized form of governing equation:

$$K\boldsymbol{q} = \boldsymbol{f} \tag{6.14}$$

where

$$\begin{aligned} \mathbf{K} &= \int_\Omega [\mathbf{B}]^T [\mathbf{D}][\mathbf{B}] d\Omega, \\ \boldsymbol{f} &= \int_\Omega [\mathbf{N}]^T \{\bar{\boldsymbol{b}}\} d\Omega + \int_{\Gamma_t} [\mathbf{N}]^T \{\bar{\boldsymbol{t}}\} d\Gamma \end{aligned} \tag{6.15}$$

The results include the $\boldsymbol{q}_s$, which can be used to compute the generalized stress intensity factor (SIF) explicitly. Moreover, the enriched field takes advantage of a priori known solution and thus needs relatively fewer degrees of freedom to capture the singular field. In this chapter, three different types of corner singularities- homogeneous sharp corner, bi-material corner and interface crack will be analyzed using enriched isogeometric analysis.

## 6.2 Stress analysis for homogeneous sharp corner

Similar to fracture, stress singularity is also observed at the vicinity of sharp corners. The analysis of stress singularity for sharp corners dates back to Brahtz[135]. Williams[49] applied airy stress function method to the singular stress problem for notches with arbitrary angles. Based on Williams' work, further exploration was developed by Vasilopoulos[136], Rosel[137]. All of the above work utilize Airy stress functions, from which displacement field is obtained by integration and through compatibility condition. Instead, Seweryn and Molski[51] developed an analysis procedure from general solution of displacement field, which is more convenient than Williams' method since it only needs differentiation while integration in Williams' method will introduce constants of integration to be resolved through boundary conditions.

The strain displacement relation in polar coordinates is as follows:

$$\begin{aligned} \varepsilon_{rr} &= \tfrac{\partial u_r}{\partial r} \\ \varepsilon_{\theta\theta} &= \tfrac{u_r}{r} + \tfrac{1}{r}\tfrac{\partial u_\theta}{\partial \theta} \\ \gamma_{r\theta} &= \tfrac{1}{r}\tfrac{\partial u_r}{\partial \theta} + \tfrac{\partial u_\theta}{\partial r} - \tfrac{u_\theta}{r} \end{aligned} \tag{6.16}$$

The stress components for plane strain conditions are obtained by

$$\begin{aligned} \sigma_{rr} &= \tfrac{\mu}{(\kappa-1)}\left[(1+\kappa)\varepsilon_{rr} + (3-\kappa)\varepsilon_{\theta\theta}\right] \\ \sigma_{\theta\theta} &= \tfrac{\mu}{(\kappa-1)}\left[(1+\kappa)\varepsilon_{\theta\theta} + (3-\kappa)\varepsilon_{rr}\right] \\ \tau_{r\theta} &= \mu\gamma_{r\theta} \end{aligned} \tag{6.17}$$

The equilibrium equations in polar coordinates are

$$\frac{\partial \sigma_{rr_i}}{\partial r_i} + \frac{1}{r_i}\frac{\partial \tau_{r\theta_i}}{\partial \theta_i} + \frac{\sigma_{rr_i} - \sigma_{\theta\theta_i}}{r_i} = 0, \tag{6.18a}$$

$$\frac{\partial \tau_{r\theta_i}}{\partial r_i} + \frac{1}{r_i}\frac{\partial \sigma_{\theta\theta_i}}{\partial \theta_i} + 2\frac{\tau_{r\theta_i}}{r_i} = 0 \tag{6.18b}$$

Combing all the three equations above, the equilibrium equation can be written in terms of displacements as:

$$\begin{aligned}(\kappa-1)\,f''(\theta)+(\kappa+1)\,(\lambda^2-1)\,f(\theta)+2\,(\lambda-\kappa)\,g'(\theta)=0\\(\kappa+1)\,g''(\theta)+(\kappa-1)\,(\lambda^2-1)\,g(\theta)+2\,(\lambda+\kappa)\,f'(\theta)=0\end{aligned}\tag{6.19}$$

Assume that the components of displacement have the following form:

$$u_r(r,\theta)=r^{\lambda}f(\theta),u_\theta(r,\theta)=r^{\lambda}g(\theta)\tag{6.20}$$

The angular functions $f$ and $g$ are given by the following general expression:

$$f(\theta)=A\cos(1+\lambda)\theta+B\sin(1+\lambda)\theta+C\cos(1-\lambda)\theta+D\sin(1-\lambda)\theta\tag{6.21}$$

$$g(\theta)=B\cos(1+\lambda)\theta-A\sin(1+\lambda)\theta+\frac{\kappa+\lambda}{\kappa-\lambda}D\cos(1-\lambda)\theta-\frac{\kappa+\lambda}{\kappa-\lambda}C\sin(1-\lambda)\theta\tag{6.22}$$

The general solution for the stress field is:

$$\begin{aligned}\sigma_r=&2\lambda r^{\lambda-1}\mu\left[(\kappa-\lambda)\,A\cos(1+\lambda)\theta+(\kappa-\lambda)\,B\sin(1+\lambda)\theta\right.\\&\left.+(3-\lambda)C\cos(1-\lambda)\theta+(3-\lambda)D\sin(1-\lambda)\theta\right]/(\kappa-\lambda)\\\sigma_\theta=&2\lambda r^{\lambda-1}\mu\left[-(\kappa-\lambda)\,A\cos(1+\lambda)\theta-(\kappa-\lambda)\,B\sin(1+\lambda)\theta\right.\\&\left.+(1+\lambda)C\cos(1-\lambda)\theta+(1+\lambda)D\sin(1-\lambda)\theta\right]/(\kappa-\lambda)\\\tau_{r\theta}=&2\lambda r^{\lambda-1}\mu\left[-(\kappa-\lambda)\,A\sin(1+\lambda)\theta+(\kappa-\lambda)\,B\cos(1+\lambda)\theta\right.\\&\left.+(1-\lambda)C\sin(1-\lambda)\theta-(1-\lambda)D\cos(1-\lambda)\theta\right]/(\kappa-\lambda)\end{aligned}\tag{6.23}$$

where, $\kappa$ is the Kolosov constant with a value of $(3-\nu)/(1+\nu)$ under plane stress condition and $3-4\nu$ under plane strain condition, and $\mu=\frac{E}{2(1+\nu)}$ is the shear modulus, with $E$ being the elastic modulus and $\nu$ the Poisson ratio of material.

In the above derivation, the exponent $\lambda$ on the displacement field solution determines the strength of singularity $1-\lambda$ on the stress fields. The constants associated with the

displacement field $(A, B, C, D)$ are in general to be determined from the solution to the boundary value problem.

However, in the usual solution process, these constants are first obtained as the eigenvector to a *local asymptotic problem* and are therefore determined only to within a constant. This in turn implies that the coefficients may, in general, be expressed as:

$$\{A, B, C, D\} = \bar{K}\{\bar{A}, \bar{B}, \bar{C}, \bar{D}\} \tag{6.24}$$

where, $\bar{K}$ is an unknown coefficient that is related to the generalized stress intensity factor as elaborated later, and $\{\bar{A}, \bar{B}, \bar{C}, \bar{D}\}$ result as the eigenvector of the asymptotic solution.

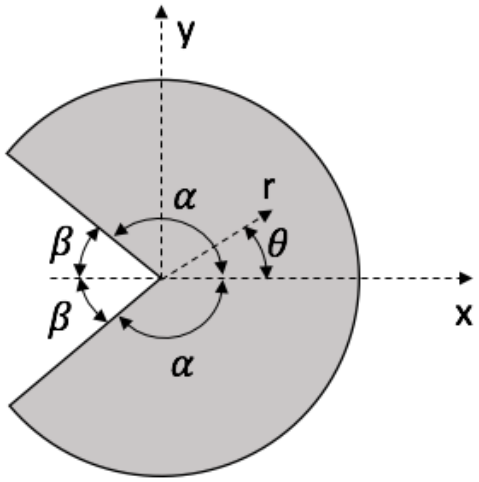


**Figure 6.2.** Sharp corner with opening angle $2\beta$ in polar coordinates $(r,\theta)$.

Figure 6.2 shows a homogeneous sharp corner with opening angle $2\beta$. Usually, two singularities are expected due to symmetric and anti-symmetric loading conditions. Let $\lambda^I$ and $\lambda^{II}$ denote for symmetric and anti-symmetric modes respectively. Besides, two sets of coefficients and unknowns in Eq. (6.24) are necessary to represent the field. It should be noted that stress singularity only exists when $0 < \lambda < 1$, which equals $\alpha > 90^o$ for symmetric mode, and $\alpha > 128.73^o$ for anti-symmetric mode. It is also worth pointing out that the singularity of strength is $1 - \lambda$, and therefore, higher $\lambda$ implies weaker singularity,

which is different from that in Williams' definition. The value of $\lambda$ depends on the opening angle $\beta$ within the range $[0, \pi)$. The value of $\lambda$ should be determined by the boundary condition at the local region.

For symmetric case, the boundary condition is:

$$\begin{aligned} u_\theta = \tau_{r\theta} = 0 \ for \ \theta = 0 \\ \sigma_\theta = \tau_{r\theta} = 0 \ for \ \theta = \alpha \end{aligned} \tag{6.25}$$

the singularity is determined by the following characteristic equation:

$$\lambda sin(2\alpha) + sin(2\lambda\alpha) = 0 \tag{6.26}$$

For the anti-symmetric case, the boundary condition is:

$$\begin{aligned} u_r = \sigma_\theta = 0 \ for \ \theta = 0 \\ \sigma_\theta = \tau_{r\theta} = 0 \ for \ \theta = \alpha \end{aligned} \tag{6.27}$$

the corresponding characteristic equation is:

$$\lambda sin(2\alpha) - sin(2\lambda\alpha) = 0 \tag{6.28}$$

The unknown $\bar{K}_J$ is proportional to the generalized stress intensity factor. For an arbitrary angle wedge, the generalized stress intensity factor (SIF) can be used to assess the risk of failure. For instance, Seweryn[138] proposed a brittle fracture criterion for sharp notches. Here, the generalized stress intensity factors are obtained by multiplying the unknowns $\bar{K}_J$ by a predetermined constant. Following [138], the SIF for Material 1 in Figure 6.6 is defined as:

$$\begin{aligned} K_I = \lim_{r \to 0} [(2\pi r)^{1-\lambda_I} \sigma_\theta(r, \theta)](\theta = 0) \\ K_{II} = \lim_{r \to 0} [(2\pi r)^{1-\lambda_{II}} \tau_{r\theta}(r, \theta)](\theta = 0) \end{aligned} \tag{6.29}$$

Based on Eq. (6.23) and Eq. (6.24), the stresses $\sigma_\theta$ and $\tau_{r\theta}$ can be derived as:

$$\begin{aligned}\sigma_\theta =& \frac{1}{r^{1-\lambda}}\frac{2\lambda\mu}{\kappa-\lambda}F_{\theta\theta}\bar{K}_I \\ \tau_{r\theta} =& \frac{1}{r^{1-\lambda}}\frac{2\lambda\mu}{\kappa-\lambda}F_{r\theta}\bar{K}_{II}\end{aligned} \tag{6.30}$$

where

$$\begin{aligned}F_{\theta\theta} &= -(\kappa-\lambda)\bar{A}\cos(1+\lambda)\theta - (\kappa-\lambda)\bar{B}\sin(1+\lambda)\theta + (1+\lambda)\bar{C}\cos(1-\lambda)\theta + (1+\lambda)\bar{D}\sin(1-\lambda)\theta \\ F_{r\theta} &= [\,-(\kappa-\lambda)\bar{A}\sin(1+\lambda)\theta + (\kappa-\lambda)\bar{B}\cos(1+\lambda)\theta + (1-\lambda)\bar{C}\sin(1-\lambda)\theta - (1-\lambda)\bar{D}\cos(1-\lambda)\theta\end{aligned} \tag{6.31}$$

By comparing Eq. (6.29) and Eq. (6.30), the generalized SIF may be obtained from the unknowns $\bar{K}$ as follows:

$$\begin{aligned}K_I &= (2\pi)^{1-\lambda}\tfrac{2\lambda\mu}{\kappa-\lambda}F_{\theta\theta}\Big|_{\theta=0}\bar{K}_I \\ K_{II} &= (2\pi)^{1-\lambda}\tfrac{2\lambda\mu}{\kappa-\lambda}F_{r\theta}\Big|_{\theta=0}\bar{K}_{II}\end{aligned} \tag{6.32}$$

Thus, the SIF is directly obtained by scaling the solution by a predetermined constant without needing any post-processing step.

The above definition of stress intensity factor can be compared with a critical value to assess the risk of fracture. For mode I Load condition, similar to Irwin's fracture criterion, a general fracture criterion for a sharp notch is given as:

$$K_I \geq K_{Ic}(\lambda_I) \tag{6.33}$$

where the exponent $\lambda_I$ depends on both the Possion's ratio and the vertex angle $\alpha$. Determining the values of the $K_{Ic}$ of different $\alpha$ by experiment is too expensive. Fortunately, they can be related to fracture toughness $K_{I0c}$ and material strength $\sigma_c$. One relation proposed by Seweryn[138] is:

$$K_{Ic} = (1-\lambda)\sigma_c(\frac{2K_{I0c}}{\sigma_c})^{2\lambda_I} \tag{6.34}$$

The form of the theoretical solution was applied on a notched plate under symmetric tension (Section 6.2). Only half of the structure was modeled for simplicity. The notch tip was enriched by the EIGA form. Section 6.2 shows the distribution of Von Mises stress with the coarsest mesh. The singular stress was captured near the sharp corner. By doubling

the mesh density, the convergence of the generalized SIF was also studied. Since the load was symmetric, only $K_I$ existed. The generalized SIFs converged to values of $K_I = 3.12$. Although no physical units were used in this specific example, the SIFs have units of $[Stress] \cdot [Length]^{1-\lambda}$ in a general problem.

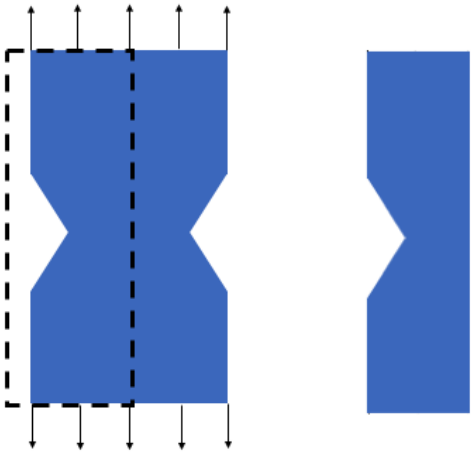

**Figure 6.3.** Notched plate subject to mode I load

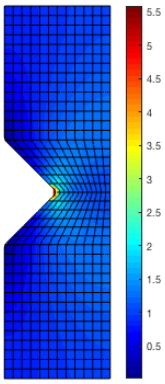


**Figure 6.4.** Von-Mises stress distribution in the plate with V-shaped Notch

## 6.3 Stress Analysis of Bi-Material Corner with Two Bonded Interfaces

In engineering structures, bi-material or even multi-material wedges are common. Luo and Subbarayn [52] extended the theory in [51] for multi-material corners. Figure 6.6 shows

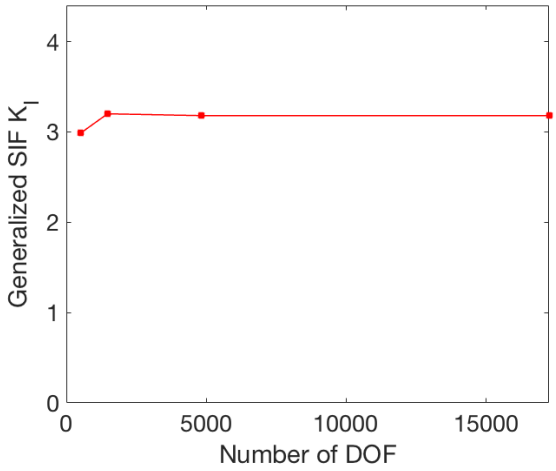


**Figure 6.5.** Convergence of generalized stress intensity factor for V-shaped notch.

two materials bonded perfectly. Eq. (6.20) are still applied to each material, but with different coefficients $A_{\mathrm{i}}, B_{\mathrm{i}}, C_{\mathrm{i}}, D_{\mathrm{i}}(\mathrm{i}=1,2)$:

$$\begin{aligned} u_{r_{\mathrm{i}}}(r,\theta_{\mathrm{i}}) &= r^{\lambda}[\bar{A}_{\mathrm{i}}\cos(1+\lambda)\theta_{\mathrm{i}} + \bar{B}_{\mathrm{i}}\sin(1+\lambda)\theta_{\mathrm{i}} + \bar{C}_{\mathrm{i}}\cos(1-\lambda)\theta_{\mathrm{i}} + \bar{D}_{\mathrm{i}}\sin(1-\lambda)\theta_{\mathrm{i}}]\bar{K} \\ u_{\theta_{\mathrm{i}}}(r,\theta_{\mathrm{i}}) &= r^{\lambda}[\bar{B}_{\mathrm{i}}\cos(1+\lambda)\theta_{\mathrm{i}} - \bar{A}_{\mathrm{i}}\sin(1+\lambda)\theta_{\mathrm{i}} \\ &\qquad + \frac{\kappa_{\mathrm{i}}+\lambda}{\kappa_{\mathrm{i}}-\lambda}\bar{D}_{\mathrm{i}}\cos(1-\lambda)\theta_{\mathrm{i}} - \frac{\kappa_{\mathrm{i}}+\lambda}{\kappa_{\mathrm{i}}-\lambda}\bar{C}_{\mathrm{i}}\sin(1-\lambda)\theta_{\mathrm{i}}]\bar{K} \end{aligned} \tag{6.35}$$

where $(\bar{A}_{\mathrm{i}}, \bar{B}_{\mathrm{i}}, \bar{C}_{\mathrm{i}}, \bar{D}_{\mathrm{i}})$ and $\lambda$ are predetermined and $\bar{K}$ is the unknown that is determined by solving the global boundary value problem.

The $x$ axis of the local coordinates are set to be the same as the symmetry axis of the material x-axis. Similar to homogeneous sharp corners, both symmetric and anti-loading loading modes are studied respectively.

For symmetric (opening) loading mode, the following conditions need to be satisfied:

$$\begin{aligned} u_{\theta 1} = \tau_{r\theta 1} = 0 \ for\ \theta = 0 \\ u_{\theta 2} = \tau_{r\theta 2} = 0 \ for\ \theta = \boldsymbol{\pi} \end{aligned} \tag{6.36}$$

While for anti-symmetric (shear) loading mode, the conditions become:

$$\begin{aligned} u_{r1} = \sigma_{\theta 1} = 0 \; for \; \theta = 0 \\ u_{r2} = \sigma_{\theta 2} = 0 \; for \; \theta = \pi \end{aligned} \tag{6.37}$$

For both modes, continuity conditions are required at the bonded interface.

$$u_{r1} = u_{r2}, \; u_{\theta 1} = u_{\theta 2}, \sigma_{\theta 1} = \sigma_{\theta 2}, \; \tau_{r\theta 1} = \tau_{r\theta 2} \; at \; \theta = \alpha \tag{6.38}$$

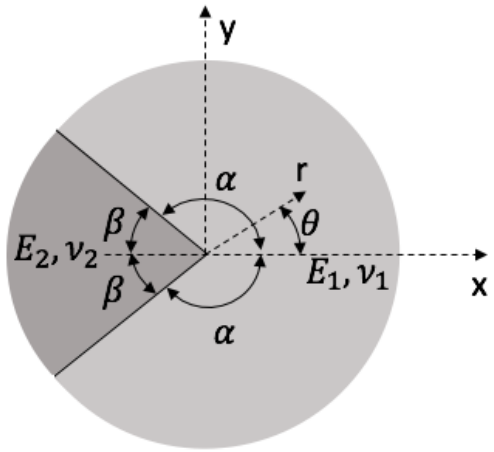


**Figure 6.6.** Sharp corner with opening angle $2\beta$ in polar coordinate ($r$,$\theta$)

The value of $\lambda$ is again obtained by forcing the determinant of coefficient matrix of characteristic equation to be zero, and the coefficients are the corresponding eigenvectors. Noting that there are nine unknowns but only eight equations, a scaling factor is necessary to represent the real field. Similar to homogeneous sharp notch, the following relation is defined:

$$\{A_{\mathrm{i}}, B_{\mathrm{i}}, C_{\mathrm{i}}, D_{\mathrm{i}}\} = \bar{K}\{\bar{A}_{\mathrm{i}}, \bar{B}_{\mathrm{i}}, \bar{C}_{\mathrm{i}}, \bar{D}_{\mathrm{i}}\} \tag{6.39}$$

where i = $1, 2$ represents the two materials. For each material, there are two sets of coefficients $\{A_{\mathrm{i}}, B_{\mathrm{i}}, C_{\mathrm{i}}, D_{\mathrm{i}}\}$ corresponding to symmetric and anti-symmetric loading condition.

Compared with the homogeneous sharp notch, bi-material with bonded interface exhibits weaker singularity.

Each of the above modes (symmetric or anti-symmetric) results in a set of eight equations in the constants $(\bar{A}_\mathrm{i}, \bar{B}_\mathrm{i}, \bar{C}_\mathrm{i}, \bar{D}_\mathrm{i}), \mathrm{i} = 1, 2$ as well as $\lambda$ upon application of the continuity and load conditions. To ensure a non-trivial solution to the constants $(\bar{A}_\mathrm{i}, \bar{B}_\mathrm{i}, \bar{C}_\mathrm{i}, \bar{D}_\mathrm{i}), \mathrm{i} = 1, 2$, the determinant of the eigenvalue problem must be zero, which leads to a set of transcendental equations in $\lambda$. Values of the strength of singularity $\lambda$ are the eigenvalues that are then numerically determined by solving the transcendental equations. Correspondingly, the constants $(\bar{A}_\mathrm{i}, \bar{B}_\mathrm{i}, \bar{C}_\mathrm{i}, \bar{D}_\mathrm{i})$ are the components of the associated eigenvector. For a bonded interfacial corner with more than two materials ($N > 2$), the above description is easily extended - the continuity conditions at all the interfaces result in $4N$ equations, and the eigenvalue-eigenvector problem needs to be similarly solved.

An example of bi-material corner with bonded interface is next illustrated. A heterogeneous square plate of size $l = 1$ is loaded with uniform tensile tractions under plane strain condition. The two materials are elastic with the property: $E_1 = 100, \nu_1 = 0.3$ and $E_2 = 1, \nu_1 = 0.3$.

The underlying domain is approximated by a bi-cubic NURBS patch and the vertex enrichment at the material corner has two singularity modes: $\lambda_I = 0.4416$ for symmetric mode and $\lambda_{II} = 0.08832$ for anti-symmetric mode. The coefficients corresponding to each material are obtained by solving the eigenvector problem and listed in Table 6.1

**Table 6.1**. Coefficients of angular function associated with bi-material corner with bonded interface obtained through asymptotic analysis.

| **Material** | **Mode** | $\bar{A}$ | $\bar{B}$ | $\bar{C}$ | $\bar{D}$ |
|---|---|---|---|---|---|
| 1 | I | -0.025995 | 0.140303 | 0.037942 | 0.204783 |
| | II | 0.075719 | 0.265855 | 0.163379 | -0.573638 |
| 2 | I | -0.806594 | 0 | 0.534479 | 0 |
| | II | 0 | 0.437278 | 0 | -0.613696 |

The boundary value problem was solved with uniformly refined discretization having 342, 726, 1,926, 6,054 and 21,222 degrees of freedom. As shown in Section 6.3, using the relation

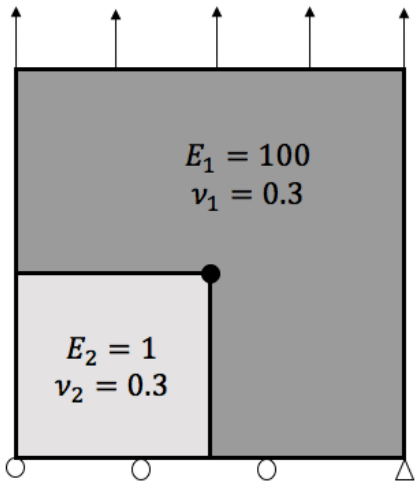


**Figure 6.7.** Boundary condtions on the structure with bi-material corner.

in Eq. (6.53), the generalized stress intensity factors converged to values of $K_I = 2.7120$ and $K_{II} = 0.3984$ with units of $[Stress] \cdot [Length]^{1-\lambda}$. As can be seen from the figure, the convergence to the solution is very rapid and achieved even under coarse discretizations.

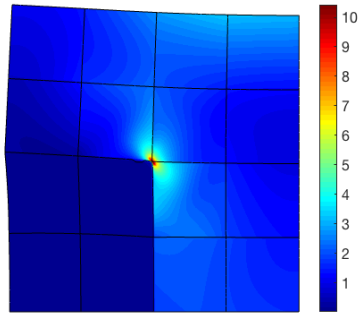


**Figure 6.8.** Von-Mises stress distribution near the bi-material corner.

## 6.4 Stress analysis for interface crack

Interface crack is another important problem in engineering application. It is a special case of the bi-material wedge, but with only one interface bonded Figure 6.10. When $\alpha = \pi$ and $\beta = \pi$, it becomes a problem of interfacial crack. This problem often results in a complex singularity with oscillation in the field near the crack tip.

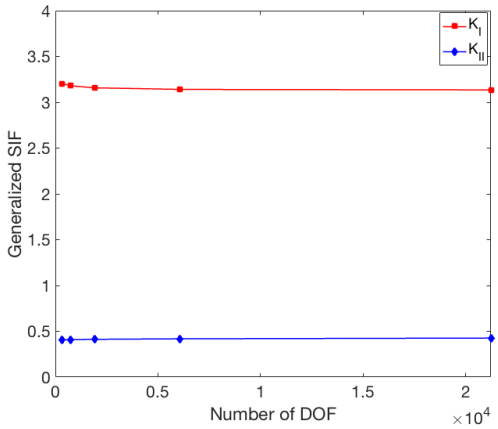


**Figure 6.9.** Convergence of generalized stress intensity factor for bi-material corner with bonded interface.

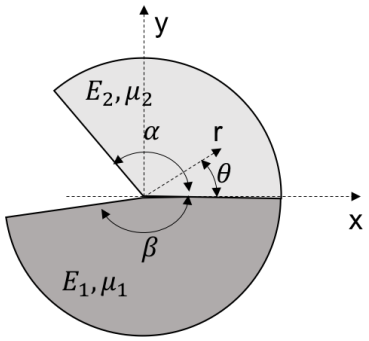


**Figure 6.10.** Bi-material corner with one bonded interface

In this section, the displacement approximation proposed by [51] is applied to determine the singularity and angular function. The approach used in Section 6.3 is applied but with different boundary conditions: continuity condition across the common interface and traction free condition at the free surfaces.

$$\begin{aligned} u_{\mathring{1}} = u_{\mathring{2}}, u_{\theta 1} = u_{\theta 2} \; at \; \theta = 0 \\ \sigma_{\theta 1} = \sigma_{\theta 2}, \tau_{r\theta 1} = \tau_{r\theta 2} \; at \; \theta = 0 \end{aligned} \tag{6.40}$$

and

$$\begin{aligned}\sigma_{\theta 1} = \tau_1 = 0, at\ \theta = \alpha \\ \sigma_{\theta 2} = \tau_2 = 0, at\ \theta = \beta\end{aligned} \tag{6.41}$$

For the special case of interface crack, substituting the above conditions for displacement and stress equation of each material results in eight equations. By solving the eigenvector problem, the following characteristic equation is obtained.

$$\cot^2 \lambda\pi + \left[\frac{\frac{\mu_1}{\mu_2}(1+\kappa_2) - (1+\kappa_1) - 2\left(\frac{\mu_1}{\mu_2} - 1\right)}{\frac{\mu_1}{\mu_2}(1+\kappa_2) + (1+\kappa_1)}\right]^2 = 0 \tag{6.42}$$

which is the same equation obtained using Wiliams's Airy function method. Further simplification leads to

$$cot(\pi\lambda) = \pm \mathrm{i}[\frac{\frac{\mu 1}{\mu 2}(1 - \kappa 2 - 1 + \kappa 1)}{\frac{\mu 1}{\mu 2}(1 + \kappa 2 + 1 + \kappa 1)}] \tag{6.43}$$

It is obvious that the equation only has complex solution except when $\mu 1 = \mu 2, \kappa 1 = \kappa 2$. In other words, any imhomogeneity leads to a complex singularity. Assuming

$$\lambda = \lambda_R + \mathrm{i}\lambda_I \tag{6.44}$$

Then the real and imaginary part of Eq. (6.43) result in two equations:

$$\frac{(\tan^2 \lambda_R\pi + 1)\tanh \lambda_I\pi}{\tan^2 \lambda_R\pi + \tanh^2 \lambda_I\pi} = \pm\frac{\frac{\mu_1}{\mu_2}(1+\kappa_2) - (1+\kappa_1) - 2\left(\frac{\mu_1}{\mu_2} - 1\right)}{\frac{\mu_1}{\mu_2}(1+\kappa_2) + (1+\kappa_1)} \tag{6.45}$$

$$\frac{\tan \lambda_R\pi\left(1 - \tanh^2 \lambda_I\pi\right)}{\tan^2 \lambda_R\pi + \tanh^2 \lambda_I\pi} = 0 \tag{6.46}$$

There could be two sets of conditions to satisfy Eq. (6.46):

The first one is based on the condition that $tan(\lambda_R \boldsymbol{\pi}) = 0$.

$$\begin{aligned} &\lambda_R = n, \quad n = 0, 1, 2, \ldots \\ &\lambda_I = \pm\tfrac{1}{\pi} \coth^{-1} \left[ \frac{\frac{\mu_1}{\mu_2}(1+\kappa_2) - (1+\kappa_1) - 2\left(\frac{\mu_1}{\mu_2} - 1\right)}{\frac{\mu_1}{\mu_2}(1+\kappa_2) + |(1+\kappa_1)} \right] \end{aligned} \tag{6.47}$$

Only when $n = 0$, singular stress will be produced at the crack tip. However, under such a condition, the stress near the crack tip is expressed as:

$$\sigma_{rr}, \sigma_{\theta\theta}, \sigma_{r\theta} \sim \frac{1}{r} \begin{pmatrix} \sin \\ \\ \cos \end{pmatrix} (\lambda_I \ln r) \tag{6.48}$$

This stress field will lead to infinite strain energy within any small region close to the tip, which is not admissible physically.

The second set is based on the condition that $\lambda_R \boldsymbol{\pi} = \infty$, under which Eq. (6.46) is also satisfied.

$$\begin{aligned} &\lambda_R = \tfrac{2n-1}{2}, \quad n = 1, 2, 3, \ldots \\ &\lambda_I = \pm\tfrac{1}{\pi} \tanh^{-1} \left[ \frac{\frac{\mu_1}{\mu_2}(1+\kappa_2) - (1+\kappa_1) - 2\left(\frac{\mu_1}{\mu_2} - 1\right)}{\frac{\mu_1}{\mu_2}(1+\kappa_2) + (1+\kappa_1)} \right] \end{aligned} \tag{6.49}$$

notice that

$$tanh^{-1}\frac{x}{b} = \frac{1}{2} ln \frac{b+x}{b-x} \tag{6.50}$$

the singularity is expressed by

$$\lambda = (n - \frac{1}{2}) \pm \mathrm{i}\epsilon, n = 1, 2... \tag{6.51}$$

where

$$\epsilon = \frac{1}{2\boldsymbol{\pi}} ln[\frac{\frac{\kappa 1}{\mu 1} + \frac{1}{\mu 2}}{\frac{\kappa 2}{\mu 2} + \frac{1}{\mu 1}}] \tag{6.52}$$

It is obvious that $n = 1$ leads to singularity $\lambda = 1/2 + \mathrm{i}\epsilon$. The $\pm$ sign does not matter since it flips if material 1 and 2 switch.

Substituting $\lambda$ into the matrix and solving the corresponding eigenvectors, one also gets complex values for complex eigen-function $f_r$ and $f_\theta$. The displacement field is thus represented as :

$$\begin{aligned} u_r &= r^\lambda (f_{rR} + \mathrm{i} f_{rI})(\bar{K}_R + \mathrm{i}\bar{K}_I) \\ u_\theta &= r^\lambda (g_{\theta R} + \mathrm{i} g_{\theta I})(\bar{K}_R + \mathrm{i}\bar{K}_I) \end{aligned} \tag{6.53}$$

where, the subscript $R$ and $I$ represents the real and imaginary parts respectively. $\bar{K} = \bar{K}_r + \mathrm{i}\bar{K}_\mathrm{i}$ is the complex unknown from which the generalized stress intensity factor (SIF) can be explicitly obtained. It is worth noting that the contact zone due to oscillation is ignored here.

The complex field has no physical meaning. As suggested by [51] and [139], the solution can be represented by a linear combination of real and imaginary part. Therefore, two coefficients $b_1$ and $b_2$ can be used to represent the field.

$$\boldsymbol{u}_{\mathrm{i}k} = b_1 \,\mathrm{Re}\,[\bar{K} r^\lambda f_{ik}] + b_2 \,\mathrm{Im}\,[\bar{K} r^\lambda f_{ik}],\ \mathrm{i} = r, \theta\ k = 1, 2 \tag{6.54}$$

It can be expanded as:

$$\begin{aligned} \boldsymbol{u}_{\mathrm{i}k} = r^{\lambda_R} (M_I(\mathrm{Re}(f_{\mathrm{i}k}) cos(\epsilon \ln(r)) - \mathrm{Im}(f_{\mathrm{i}k}) sin(\epsilon \ln(r)) \\ + M_{II}[\,\mathrm{Re}(f_{\mathrm{i}k}) cos(\epsilon \ln(r)) - \mathrm{Im}(f_{\mathrm{i}k}) sin(\epsilon \ln(r))]) \end{aligned} \tag{6.55}$$

where $M_I = b_1\bar{K}_1 + b_2\bar{K}_2$, $M_{II} = -b_1\bar{K}_2 + b_2\bar{K}_1$, and $f_{\mathrm{i}k}$ is the eigenfunction associated with the displacement. The unknowns $M_I$ and $M_{II}$ can be used to explicitly represent the generalized SIF. Note that the value of coefficient $b_1$ and $b_2$ can be arbitrarily selected regardless of geometry and loading condition (e.g., $b_1 = 1, b_2 = 0$, or $b_1 = 0.5, b_2 = 0.5$). The genralized SIF $K = K_I + \mathrm{i}K_{II}$ is defined in [97]:

$$(\sigma_{\theta\theta} + \mathrm{i}\tau_{r\theta})|_{\theta=0} = \frac{K r^{\mathrm{i}\varepsilon}}{(2\pi r)^{1/2}} = \frac{K_I + \mathrm{i}K_{II}}{(2\pi r)^{1/2}} r^{\mathrm{i}\varepsilon} \tag{6.56}$$

The value of $K$ can be obtained from $M_I + \mathrm{i}M_{II}$ by amplification and rotation [139], and thus the values of $b_1$ and $b_2$ are not important.

When $\alpha = \boldsymbol{\pi}$ and $\beta = \boldsymbol{\pi}$, by choosing $b_1 = 1$ and $b_2 = 0$, the solution is identical to that given in [62]:

$$\begin{aligned} u_x =& \sqrt{\frac{r}{2\boldsymbol{\pi}}} \frac{1}{4G_{\mathrm{j}}} \left[K_I \left(D_{\mathrm{j}} + 2\delta_{\mathrm{j}} \sin\theta \sin\Theta\right) - K_{II} \left(E_{\mathrm{j}} - 2\delta_{\mathrm{j}} \sin\theta \cos\theta\right)\right] \\ u_y =& \sqrt{\frac{r}{2\boldsymbol{\pi}}} \frac{1}{4G_{\mathrm{j}}} \left[-K_I \left(E_{\mathrm{j}} + 2\delta_{\mathrm{j}} \sin\theta \cos\Theta\right) - K_{II} \left(D_{\mathrm{j}} - 2\delta_{\mathrm{j}} \sin\theta \sin\Theta\right)\right] \end{aligned} \tag{6.57}$$

where

$$\begin{aligned} \delta_1 &= \mathrm{e}^{-(\boldsymbol{\pi}+\theta)\epsilon} \\ \delta_2 &= \mathrm{e}^{(\boldsymbol{\pi}+\theta)\epsilon} \\ \Theta &= \epsilon \log r + \tfrac{1}{2}\theta \\ D_{\mathrm{j}} &= \beta\gamma_{\mathrm{j}} \cos\tfrac{1}{2}\theta + \beta'\gamma'_{\mathrm{j}} \sin\tfrac{1}{2}\theta \\ E_{\mathrm{j}} &= \beta'\gamma_{\mathrm{j}} \cos\tfrac{1}{2}\theta - \beta\gamma'_{\mathrm{j}} \sin\tfrac{1}{2}\theta \end{aligned} \tag{6.58}$$

the quantities$\beta$, $\beta'$, $\gamma_{\mathrm{j}}$ and $\gamma'_{\mathrm{j}}$are given below:

$$\begin{aligned} \beta &= \tfrac{0.5\cos(\epsilon\log r)+\epsilon\sin(\epsilon\log r)}{0.25+\epsilon^2} \\ \beta' &= \tfrac{0.5\sin(\epsilon\log r)-\epsilon\cos(\epsilon\log r)}{0.25+\epsilon^2} \\ \gamma_{\mathrm{j}} &= \kappa_{\mathrm{j}}\delta_{\mathrm{j}} - \tfrac{1}{\delta_{\mathrm{j}}} \\ \gamma'_{\mathrm{j}} &= \kappa_{\mathrm{j}}\delta_{\mathrm{j}} + \tfrac{1}{\delta_{\mathrm{j}}} \end{aligned} \tag{6.59}$$

In the displacement field, $K_I$ and $K_{II}$ are the generalized SIFs, which are the unknowns in the EIGA form. The remaining part in Eq. (6.57) is the corresponding basis function.

If a crack face exists, the discontinuity needs to be included in the enriched field. In [65], The enriched field approximation of the displacement field takes the following form

$$\boldsymbol{u} = (1 - w_{\mathrm{e}})\boldsymbol{u}_c(\mathbf{x}) + (w_{\mathrm{e}} - w_t)[\boldsymbol{u}_{\mathrm{e}}(\mathcal{P}(\mathbf{x})) + \mathcal{H}(\mathbf{x})\boldsymbol{u}_H(\mathcal{P}(\mathbf{x}))] + w_t[\boldsymbol{u}_t + \Psi_s(r,\theta)\boldsymbol{u}_s] \tag{6.60}$$

where, $\boldsymbol{u}_{\mathrm{e}}$ is the displacement of the explicitly represented crack face, $\mathcal{H}\boldsymbol{u}_H$ is the discontinuous displacement of the crack opening, with $\mathcal{H}$ being Heaviside function, $w_{\mathrm{e}}$ and $w_t$ are the weight field associated with the edge enrichment and vertex enrichment.

This form can be also be applied for interface crack. However, for general multi-material wedge with arbitrary opening angle, it is not suitable. Therefore, the p-stitching technique introduced in Chapter 5 is used to enrich the region close to the bonded interface. The enriching entity is illustrated in Figure 6.11. The enriched displacement field is approximated as:

$$\boldsymbol{u}_{\mathrm{i}} = (1 - w_{\mathrm{e}})\boldsymbol{u}_c(\mathbf{x}) + (w_{\mathrm{e}} - w_t)[\boldsymbol{u}_{\mathrm{e}}(\mathcal{P}(\mathbf{x})) + d\boldsymbol{G}_{\mathrm{i}}(\mathcal{P}(\mathbf{x}))] + w_t[\boldsymbol{u}_t + \Psi_s(r,\theta)\boldsymbol{u}_s] \tag{6.61}$$

Where index $\mathrm{i} = 1, 2$ denotes different materials, $d$ is the signed distance to the stitching interface and $\boldsymbol{G}_{\mathrm{i}}$ is the associated gradient on either side. This form provides more flexibility for bonded materials with an arbitrary wedge angle. Also, interface crack propagation can be easily modeled by shrinking the stitching interface.

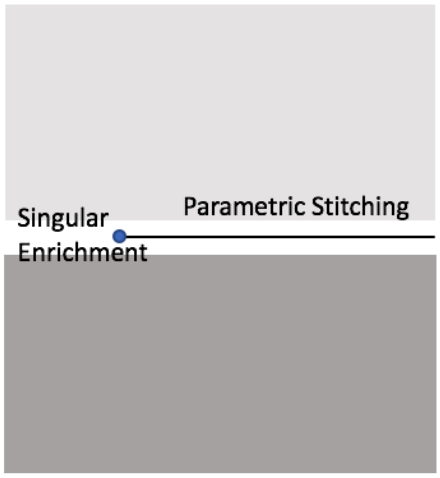


**Figure 6.11.** Illustration of enrichment for bi-material problem.

An interfacial crack example is illustrated in Figure 6.12 for a structure with the material property $E_1 = 200, \mu_1 = 0.3$ and $E_2 = 200, \mu_2 = 0.3$. The asymptotic solution Eq. (6.57) was used to enrich the displacement field near the tip.

The boundary value problem was also solved with uniformly refined discretization having 342, 726, 1,926, 6,054 and 21,222 degrees of freedom similar to that in Section 6.3. The generalized stress intensity factors converged to values of $K_I = 0.41$ and $K_{II} = -0.06$ with unit of $[Stress] \cdot [Length]^{1-\lambda}$. In the interface crack case, $K_I$ and $K_{II}$ are coupled with the same conjugate complex singularity. Figure 6.13 is the Mises stress distribution, which captures the singular stress at the crack tip. It can be seen from Figure 6.14, that the convergence to the solution is very rapid and achieved even under coarse discretizations.

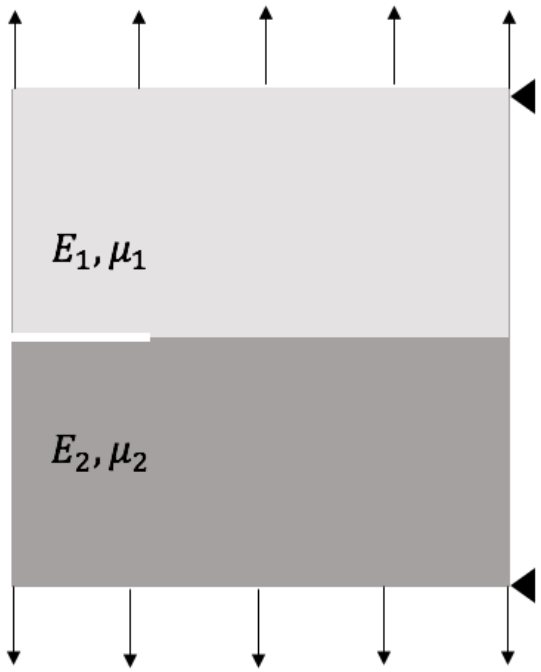


**Figure 6.12.** Boundary condition on the structure containing an interfacial crack.

Once $K_I$ and $K_{II}$ are determined, they can be used to evaluate the energy release rate as described in [55]:

$$G = \frac{1}{16}\left(\frac{\kappa_1 + 1}{\mu_1} + \frac{\kappa_2 + 1}{\mu_2}\right)\left(K_1^2 + K_2^2\right) \tag{6.62}$$

The critical value $G_c$, which depends on the mode mixty $(K_{II}/K_I)$, needs to be determined by experiment.

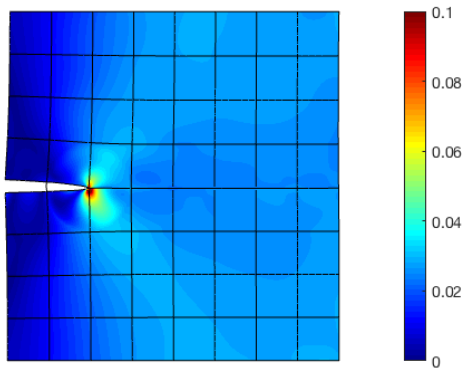


**Figure 6.13.** Von Mises Stress around the interface crack.

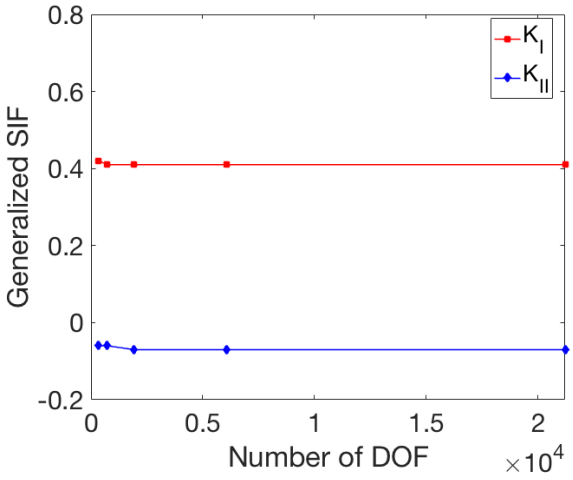


**Figure 6.14.** Convergence of generalized stress intensity factor for interface crack.

## 6.5 Numerical example: Iteraitve Global-local Analysis on BEOL Structure

The proposed method is a promising tool to model corner singularity. However, for a large scale problem, commercial codes are preferred due to their robustness and efficiency. If the singular behavior is local, the non-intrusive two-way coupling model in Chapter 3 can be used. The global model, without the specific nonlinear behavior, can be modeled using commercial software while the critical local region is modeled using the EIGA code.

The back end of line (BEOL) structure described in Section 3.5.3 was considered again. In reference [105], it was proposed that the displacement boundary conditions on the local region

may be decomposed into tension, bending, or shear, and considered one at a time in isolation. Through such an analysis, in the structure described in Section 3.5.3, shear displacements were observed to correlate most with cracks emanating from the passivation corner. To simulate such cracks, in this example, the local region described in Section 3.5.3 is now used as the global model with the bottom fixed, and the top was under displacement controlled shear load of $50\mu m$. The TEOS region above the upper right corner of aluminum was extracted as the local model (Figure 6.15). The local region was isogeometrically described using Non-Uniform Rational B-Spline (NURBS, [140]) representation with 1845 control points and 1440 integration cells. The red dot in Figure 6.15 represents the enrichment corresponding to the bi-material corner singularity, whose enriched form was given in Eq. (6.35). During analysis, integration was carried out cell-by-cell (each cell corresponded to the non-zero knot span). To map nodal values between the finite element mesh and the NURBS description of the local model, the projection matrix in Section 3.2.3 was calculated as before with the difference that the shape function of the local model was replaced by the NURBS basis function.

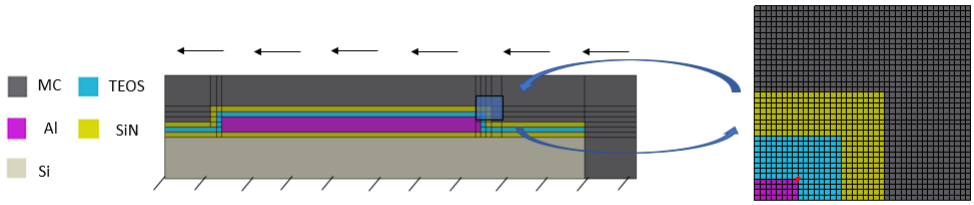


**Figure 6.15.** Corner singularity: model setup.

The global model was first run in Abaqus and the displacement on the interface was then mapped to the local model. Iterative coupling method was used to update the displacement until relative residual was below 1%. Figure 6.16a shows the nodal force vectors on the interface, where $GF$ indicates the global model force, $LF_{map}$ indicates the nodal force in local mesh mapped to global mesh through the mapping matrix. It is clear that the global and local forces are not balanced. After 20 iterations, equilibrium is nearly achieved as shown in Figure 6.16b. The relative residual decreases steadily at each iteration as shown in Figure 6.16c. The final distribution of principal stress is shown in Figure 6.16d. The

singular stress at the corner junction aluminum and TEOS was captured well by the corner enrichment.

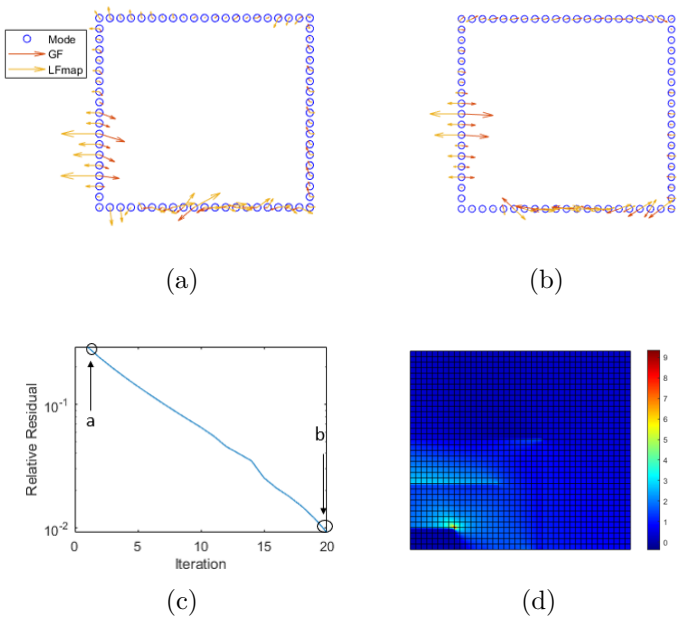


**Figure 6.16.** FE-IGA coupled analysis (a) Nodal force at the $1^{st}$ iteration (b) Nodal force at the $20^{th}$ iteration(c) Convergence of relative residual (d) Maximum principal stress distribution in the local model.

Figure 6.17 demonstrates the convergence of solution unknowns $\bar{K}_I$ and $\bar{K}_{II}$, which are proportional to the generalized stress intensity factors. In other words, higher $\bar{K}_I$ and $\bar{K}_{II}$ imply greater susceptibility to cracking. In the present example, mode I was dominant. The results show that $\bar{K}_I$ increased as iteration went on converging eventually. Since the initial stress intensity factors are lower than the converged values, a one-way global local model will underestimate the stress-intensity factors. Such an analysis will not be conservative on the potential for catastrophic fracture. The reason for this underestimation is the "stiff" behavior of the global model that could not capture the effect of the stress singularity at the corner. The mapped displacement in the local region was thus underestimated due to the "stiff" global model.

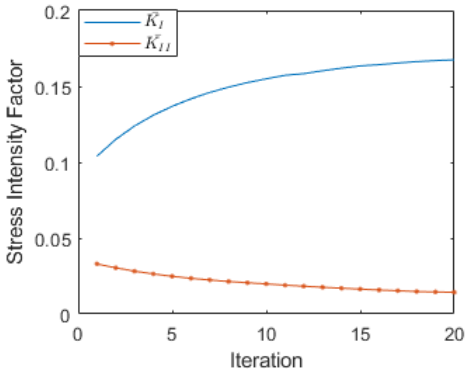


**Figure 6.17.** Convergence of the generalized stress intensity factors obtained directly using the EIGA procedure.

## 6.6 Summary

In this chapter, an isogeometric enriching approximation technique for modeling stress singularities at sharp corners was proposed. The displacement field given by Seweryn and Molski was extended to multi-material corners. The solution was applied to enrich corner singularities with predetermined angular functions. Combined with parametric stitching technique, singular enrichment was also used to solve interface crack problem. By taking advantage of the theoretical solution, the resulting solution system enables direct and efficient extraction of generalized stress intensity factors without post-solution evaluation of path-independent integrals. The proposed method was demonstrated by solving a homogeneous sharp corner problem, a bi-material problem with two interfaces bonded and an interface crack problem. Also, the technique is applied on a local model of BEOL structure using the iterative global-local model method. In conclusion, the numerical examples show that the method is capable of rapid convergence to the solution SIFs with relatively fewer degrees of freedom even with uniform and coarse discretizations.

# 7. CLOSURE

The focus of the thesis was on developing computational strategies for nonlinear multi-scale problems composed of multiple patches, with application to corner singularities. There are in total four topics relating to the theme that were described in the thesis.

## 7.1 Summary and Novel Contributions

The thesis research was first motivated with a multi-scale problem of importance to the microelectronics industry: plastic ratcheting-induced fracture in back end line (BEOL) structure. It was initially speculated that the singular stress at the local region on re-entrant corner may be the main cause of passivation fracture. A global-local analysis without a change in boundary conditions (one-way coupled model) may not be sufficient to capture the local field accurately due to lack of feedback to the global model, particularly when the local model response is nonlinear. An iterative computational strategy for code- and mesh-agnostic global-local analysis was then developed. Variational principles with intermediate framework were proposed to transfer nodal force between the sub-domains. Two different mapping techniques, namely global Lagrange multiplier (GLM) method and local Lagrange multiplier (LLM) method were studied. Overall, GLM was more accurate due to integration over the interface, but the need for integration made the technique computationally more expensive. The mapping of forces between the sub-domains allowed the calculation of the unbalanced force at the interface. The unbalance force was reduced iteratively until equilibrium was achieved. A procedure was developed to correct the displacement in a non-intrusive manner to allow the sub-domains to be modeled using commercial finite element software that may not provide access to the stiffness matrices. To accelerate the convergence, SR1 update and BFGS updates were applied. Several numerical examples were solved to demonstrate solutions over subdomains with different discretizations and even solved using different commercial finite element analysis codes.

Chapters 4–6 were applications of the Enriched Isogeometric Analysis (EIGA) technique. The first application of EIGA was to boundary condition application during immersed analysis. A direct and strong imposition of boundary conditions was proposed by using en-

richments with known function of gradient values. The enriching boundary contained extra degrees of freedom that were isoparametrically added to the enriching geometry and blended with the underlying domain approximation. The use of algebraic level sets enabled both the construction of the weight field and point classification. The former is necessary to capture the influence of boundaries on the underlying domain, while the latter helps classify quadrature points as being inside or outside the physical domain during analysis.

The proposed CAD-CAE integration approach eliminates the need for mesh generation, retains a geometric representation of the boundaries that are exact to the CAD model, and enables exact to CAD point containment queries during analysis. The accuracy of the proposed method was demonstrated through both patch tests as well as convergence analysis on a benchmark problem. In the patch test, decreasing the cell size lead to less error when using exponential weight function, while the cubic or quartic weight function yielded solutions that were accurate to machine precision. Optimal convergence was also observed in a perforated plate example.

Solid models generated by CAD systems consist of trimmed, disjoint patches. Therefore, the patches need to be stitched prior to their use directly for isogeometric analysis. A technique to couple multiple parametric subdomains with non-matching discretizations was proposed in Chapter 5. Explicit edge enrichments were used to stitch two adjacent patches. The strategy was then extended to stitching multiple patches that join at a T-junction or extraordinary vertex. A hierarchy of vertex, edge, face and body enrichments were proposed to achieve multi-patch stitching. The different patches were blended with weight functions that assured the satisfaction of partition of unity property of the approximations over the domain. It was shown that with appropriate conditions on the weight functions used for blending the enrichments, one can achieve the required smoothness in the fields between the patches. Patch tests were conducted on two-patch, three-patch, four-patch and multi-patch domains with extraordinary vertices. Convergence studies were conducted on patches with both straight and curved edges. In general, solutions accurate to function precision were achieved when coupling patches with orthogonal straight edges, but the accuracy degrades with increased curvature of the coupling edges. Also, the solution error does depend on the

accuracy of quadrature near curved boundaries, but the overall solution was in very good agreement with the reference one.

Finally, an isogeometric enriching approximation technique for modeling stress singularities in multi-material corners was described. The analytical solution method developed by Seweryn and Molski was extended to multi-material corners. A general approach to determine eigen-function for arbitrary bi-material corner was proposed. Cracks were then defined as partially stitched patches and the parametric stitching technique together with singular enrichments were used to analyze the singular stresses. The enriched solution enabled direct and efficient extraction of generalized stress intensity factors without the need for an a posteriori evaluation of path-independent integrals. The proposed method was demonstrated on a homogeneous sharp corner problem, a bi-material problem with two surfaces bonded and on an interface crack problem. Also, the developed technique was applied to a local model of BEOL structure using the iterative global-local analysis.

## 7.2 Recommendationa for Future Work

### 7.2.1 Non-Intrusive Coupling Algorithm on Multiple Geometrically Identical Sub-Structures using Machine Learning

Generally, the non-intrusive iterative global-local analysis developed in this thesis is not efficient when the non-linear region is large. A refined full model is more appropriate in this case. However, the computational cost will increase with a refined nonlinear analysis. For example, when modeling semiconductor packages with thousands of solder interconnects, millions or even tens of millions DOFs are needed to model the fracture propagation in solder joints. This computational cost is prohibitive for analysis on a desktop computer. However, fortunately, each solder joint (which forms the local model) is a repeated sub-structure. Every solder joint has identical geometry and material behavior. Therefore, the solder joint can be regarded as a non-linear super-element. Machine learning can thus be applied to capture the behavior of the solder joint to various applied loads.

Applying neural networks Zhang et al.[141] proposed a response surface model for predicting the fatigue life of solder joints in package structures. This is a potential approach

to improve the efficiency of solution for multi-scale problem with repeated local structures. The behavior of a representative local model could be captured by machine learning and later used to model the behavior of every solder joint. Even though the fitting process may be computationally expensive, it could help speed the analysis process, especially when the same local structure is repeated thousands of times.

### 7.2.2 Complex Solution for Arbitrary Wedge Angle Corners using EIGA

The asymptotic analysis of general angular corners yieds complex strengths of singularity. Seweryn[51] points out that both real and imaginary parts of the solution should satisfy the boundary condition and thus the solution may be represented by a linear combination of the both parts. Pageau[139] argues that in the complex case, the asymptotic field can be determined to within a multiplicative complex constant (amplification and rotation). The authors also proposed an approach to evaluate the general SIFs. The complex numerical solution to the angular corner of a multimaterial wedge is left as a future exercise.

For the complex case, the stress and displacement fields are determined to within a multiplicative complex constant (amplification plus rotation). However, there exits infinite number of ways to express the angular variations (eigenfunctions) of the stress and displacement fields with a complex scaling factor. Therefore, it is necessary to extract the generalized stress intensity factors from the arbitrary complex scaling factor. The proposed computational framework could also be extended for n-material wedges to evaluate generalized SIFs using EIGA.

### 7.2.3 Unified Failure Mechanism and Crack Propagation Simulation

The crack initiation condition at bi-material wedges or sharp corners is more complex than similar analysis of cracks. The wedge angle, material combination, interface property all are important to predictions of crack initiation.

For a structure containing sharp notches made of a homogeneous material, the critical energy state lies between fracture toughness of the material and the static strength[142]. The calculation of energy to advance a crack relies on the accurate description of stress, strain or

strain energy density distribution near the defect tip. Usually the fracture criterion involves both material strength and a characteristic length. Leguillon[142] proposed a criterion for v-shape notch, which combines the Griffith energy criterion for a crack, and the strength criterion for a straight edge. He also argued that the crack increment length for a wedge can not be infinitely small. Its lower bound is controlled by the wedge opening angle. The bound becomes zero for fracture problem. Strain energy density based criterion have also been proposed for propagation of cracks, either point-wise[143] or in an average sense[144]. Using enriched singular analysis for a sharp corner, the generalized stress intensity factor can be used to characterize the probability of crack advancement. However, there is little research on predicting the crack propagation direction at a sharp corner. When multiple materials join at a corner, there exists competition between crack penetration vs. deflection into an Interface. Tambat and Subbarayan [145] applied EIGA to simulate the path of a crack near an interface in layered strucutrus. However, this approach needs to evaluate the energy release rate of all possible new crack configurations to determine the likely path and is thus computationally expensive.

Configurational force (also termed material force) [146] may be a potential criterion to unify and predict the risk of crack initiation and the path of propagation. It is a thermodynamically consistent measure, which can unify crack initiation, risk of propagation and direction of propagation. Configurational force is a vector, whose direction is opposite to potential crack propagation direction while its amplitude may be used to determine crack initiation. However, the physical meaning of the critical configurational force that is proposed in [146] is unclear.

From a microscopic perspective, fracture is the result of microcracks or microvoids leading to microscopic damage that eventually form a macroscopic crack. The process should be governed by thermodynamic principles as well as statistical mechanics. [147] showed that the probability of nucleation depends on a theoretical estimate of critical volumetric energy density, which is directly related to the surface stress. The formation of new crack can be regarded as the accumulation of nucleated microscale defects. This provides a potential theoretical basis to connect configurational force with nucleation theory. In this manner, crack initiation criterion at any sharp corner may be unified using configurational force.

# REFERENCES


[1] G. B. Alers, K. Jow, R. Shaviv, G. Kooi, and G. Ray, "Interlevel dielectric failures in copper/low-k structures," *IEEE Transactions on Device and Materials Reliability*, vol. 4, no. 2, pp. 148–152, 2004.

[2] T. Gupta, *Copper interconnect technology*. Springer Science & Business Media, 2010.

[3] W.-S. Lei, A. Kumar, K. Mittal, and T. Ahsan, "Delamination and reliability issues in packaged devices," in *Adhesion in Microelectronics*, vol. 7, Wiley Online Library, 2014, pp. 267–312.

[4] Y. Ju, M. Saka, and H. Abe, "Detection of delamination in ic packages using the phase of microwaves," *NDT & E International*, vol. 34, no. 1, pp. 49–56, 2001.

[5] F. Renken and G. Subbarayan, "Nurbs-based solutions to inverse boundary problems in droplet shape prediction," *Computer methods in applied mechanics and engineering*, vol. 190, no. 11-12, pp. 1391–1406, 2000.

[6] D. Natekar, X. Zhang, and G. Subbarayan, "Constructive solid analysis: a hierarchical, geometry-based meshless analysis procedure for integrated design and analysis," *Computer-Aided Design*, vol. 36, no. 5, pp. 473–486, 2004. DOI: https://doi.org/10.1016/S0010-4485(03)00129-5. [Online]. Available: http://www.sciencedirect.com/science/article/pii/S0010448503001295.

[7] T. J. R. Hughes, J. A. Cottrell, and Y. Bazilevs, "Isogeometric analysis: CAD, finite elements, NURBS, exact geometry and mesh refinement," *Computer Methods in Applied Mechanics and Engineering*, vol. 194, no. 39, pp. 4135–4195, 2005. DOI: https://doi.org/10.1016/j.cma.2004.10.008.

[8] J. M. Melenk and I. Babuska, "The partition of unity finite element method: basic theory and applications," *Computer Methods in Applied Mechanics and Engineering*, vol. 139, no. 1-4, pp. 289–314, 1996.

[9] T. Strouboulis, K. Copps, and I. Babu***s***ka, "The generalized finite element method: an example of its implementation and illustration of its performance," *International Journal for Numerical Methods in Engineering*, vol. 47, no. 8, pp. 1401–1417, Mar. 2000, ISSN: 1097-0207. DOI: 10.1002/(SICI)1097-0207(20000320)47:8⟨1401::AID-NME835⟩3.0.CO;2-8. [Online]. Available: http://dx.doi.org/10.1002/(SICI)1097-

0207(20000320)47:8%7B%5C%%7D3C1401::AID-NME835%7B%5C%%7D3E3.0.CO%20http://2.0.0.8.

[10] N. Moës, J. Dolbow, and T. Belytschko, "A finite element method for crack growth without remeshing," *International Journal for Numerical Methods in Engineering*, vol. 46, no. 1, pp. 131–150, 1999.

[11] I. Babu*s*ka, "The finite element method with Lagrangian multipliers," *Numerische Mathematik*, vol. 20, no. 3, pp. 179–192, 1973. DOI: 10.1007/BF01436561.

[12] T. Zhu and S. Atluri, "A modified collocation method and a penalty formulation for enforcing the essential boundary conditions in the element free Galerkin method," *Computational Mechanics*, vol. 21, no. 3, pp. 211–222, 1998. DOI: 10.1007/s004660050296.

[13] M. Juntunen and R. Stenberg, "Nitsche's method for general boundary conditions," *Mathematics of Computation*, vol. 78, no. 267, pp. 1353–1374, 2009. DOI: 10.1090/S0025-5718-08-02183-2.

[14] T. W. Sederberg, D. C. Anderson, and R. N. Goldman, "Implicit representation of parametric curves and surfaces," *Computer Vision, Graphics, and Image Processing*, vol. 28, no. 1, pp. 72–84, Oct. 1984, ISSN: 0734-189X. DOI: 10.1016/0734-189X(84)90140-3.

[15] E. Catmull and J. Clark, "Recursively generated B-spline surfaces on arbitrary topological meshes," *Computer-Aided Design*, vol. 10, no. 6, pp. 350–355, Nov. 1978, ISSN: 0010-4485. DOI: 10.1016/0010-4485(78)90110-0. [Online]. Available: http://www.sciencedirect.com/science/article/pii/0010448578901100.

[16] D. Doo and M. Sabin, "Behaviour of recursive division surfaces near extraordinary points," *Computer-Aided Design*, vol. 10, no. 6, pp. 356–360, Nov. 1978, ISSN: 0010-4485. DOI: 10.1016/0010-4485(78)90111-2. [Online]. Available: http://www.sciencedirect.com/science/article/pii/0010448578901112.

[17] F. Cirak, M. J. Scott, E. K. Antonsson, M. Ortiz, and P. Schröder, "Integrated modeling, finite-element analysis, and engineering design for thin-shell structures using subdivision," *Computer-Aided Design*, vol. 34, no. 2, pp. 137–148, Feb. 2002, ISSN: 0010-4485. DOI: 10.1016/S0010-4485(01)00061-6. [Online]. Available: http://www.sciencedirect.com/science/article/pii/S0010448501000616.

[18] M. E. Mortenson, *Geometric Modeling*, 2nd Edition. New York, NY, USA: John Wiley & Sons, Inc., 1997, ISBN: 0-471-12957-7.

[19] D. R. Forsey and R. H. Bartels, "Hierarchical B-spline Refinement," *ACM SIGGRAPH Comput. Graph.*, vol. 22, no. 4, pp. 205–212, Jun. 1988, ISSN: 0097-8930. DOI: 10.1145/378456.378512.

[20] T. W. Sederberg, J. Zheng, A. Bakenov, and A. Nasri, "T-splines and T-NURCCs," *ACM Trans. Graph.*, vol. 22, no. 3, pp. 477–484, Jul. 2003, ISSN: 0730-0301. DOI: 10.1145/882262.882295.

[21] T. W. Sederberg, D. L. Cardon, G. T. Finnigan, N. S. North, J. Zheng, and T. Lyche, "T-spline Simplification and Local Refinement," *ACM Trans. Graph.*, vol. 23, no. 3, pp. 276–283, Aug. 2004, ISSN: 0730-0301. DOI: 10.1145/1015706.1015715.

[22] J. Deng, F. Chen, X. Li, *et al.*, "Polynomial splines over hierarchical T-meshes," *Graphical Models*, vol. 70, no. 4, pp. 76–86, Jul. 2008, ISSN: 1524-0703. DOI: 10.1016/j.gmod.2008.03.001.

[23] C. Giannelli, B. Jüttler, and H. Speleers, "THB-splines: The truncated basis for hierarchical splines," *Computer Aided Geometric Design*, Geometric Modeling and Processing 2012, vol. 29, no. 7, pp. 485–498, Oct. 2012, ISSN: 0167-8396. DOI: 10.1016/j.cagd.2012.03.025.

[24] T. Dokken, T. Lyche, and K. F. Pettersen, "Polynomial splines over locally refined box-partitions," *Computer Aided Geometric Design*, vol. 30, no. 3, pp. 331–356, Mar. 2013, ISSN: 0167-8396. DOI: 10.1016/j.cagd.2012.12.005.

[25] D. Thomas, L. Engvall, S. Schmidt, K. Tew, and M. Scott, "U-splines: Splines over unstructured meshes," *Preprint, https://coreform. com/usplines*, 2018.

[26] H.-J. Kim, Y.-D. Seo, and S.-K. Youn, "Isogeometric analysis for trimmed CAD surfaces," *Computer Methods in Applied Mechanics and Engineering*, vol. 198, no. 37, pp. 2982–2995, Aug. 2009, ISSN: 0045-7825. DOI: 10.1016/j.cma.2009.05.004.

[27] Y. Bazilevs, V. M. Calo, J. A. Cottrell, *et al.*, "Isogeometric analysis using T-splines," *Computer Methods in Applied Mechanics and Engineering*, Computational Geometry and Analysis, vol. 199, no. 5, pp. 229–263, Jan. 2010, ISSN: 0045-7825. DOI: 10.1016/j.cma.2009.02.036.

[28] M. R. Dörfel, B. Jüttler, and B. Simeon, "Adaptive isogeometric analysis by local h-refinement with T-splines," *Computer Methods in Applied Mechanics and Engineering*, Computational Geometry and Analysis, vol. 199, no. 5, pp. 264–275, Jan. 2010, ISSN: 0045-7825. DOI: 10.1016/j.cma.2008.07.012.

[29] E. Cohen, T. Martin, R. M. Kirby, T. Lyche, and R. F. Riesenfeld, "Analysis-aware modeling: Understanding quality considerations in modeling for isogeometric analysis," *Computer Methods in Applied Mechanics and Engineering*, Computational Geometry and Analysis, vol. 199, no. 5, pp. 334–356, Jan. 2010, ISSN: 0045-7825. DOI: 10.1016/j.cma.2009.09.010.

[30] R. Schmidt, J. Kiendl, K.-U. Bletzinger, and R. Wüchner, "Realization of an integrated structural design process: Analysis-suitable geometric modelling and isogeometric analysis," en, *Computing and Visualization in Science*, vol. 13, no. 7, pp. 315–330, Oct. 2010, ISSN: 1433-0369. DOI: 10.1007/s00791-010-0147-z.

[31] X. Li, J. Zheng, T. W. Sederberg, T. J. R. Hughes, and M. A. Scott, "On linear independence of T-spline blending functions," *Computer Aided Geometric Design*, Geometric Constraints and Reasoning, vol. 29, no. 1, pp. 63–76, Jan. 2012, ISSN: 0167-8396. DOI: 10.1016/j.cagd.2011.08.005.

[32] L. Beirão da Veiga, A. Buffa, D. Cho, and G. Sangalli, "Analysis-Suitable T-splines are Dual-Compatible," *Computer Methods in Applied Mechanics and Engineering*, Higher Order Finite Element and Isogeometric Methods, vol. 249-252, pp. 42–51, Dec. 2012, ISSN: 0045-7825. DOI: 10.1016/j.cma.2012.02.025.

[33] M. A. Scott, X. Li, T. W. Sederberg, and T. J. R. Hughes, "Local refinement of analysis-suitable T-splines," *Computer Methods in Applied Mechanics and Engineering*, vol. 213-216, pp. 206–222, Mar. 2012, ISSN: 0045-7825. DOI: 10.1016/j.cma.2011.11.022.

[34] F. Massarwi and G. Elber, "A B-spline based framework for volumetric object modeling," *Computer-Aided Design*, SPM 2016, vol. 78, pp. 36–47, Sep. 2016, ISSN: 0010-4485. DOI: 10.1016/j.cad.2016.05.003.

[35] J. C. Simo, P. Wriggers, and R. L. Taylor, "A perturbed Lagrangian formulation for the finite element solution of contact problems," *Computer Methods in Applied Mechanics and Engineering*, vol. 50, no. 2, pp. 163–180, Aug. 1985, ISSN: 0045-7825. DOI: 10.1016/0045-7825(85)90088-X.

[36] K. C. Park, C. A. Felippa, and U. A. Gumaste, "A localized version of the method of Lagrange multipliers and its applications," en, *Computational Mechanics*, vol. 24, no. 6, pp. 476–490, Jan. 2000, ISSN: 1432-0924. DOI: 10.1007/s004660050007.

[37] J. Nitsche, "Über ein Variationsprinzip zur Lösung von Dirichlet-Problemen bei Verwendung von Teilräumen, die keinen Randbedingungen unterworfen sind," de, *Ab-*

*handlungen aus dem Mathematischen Seminar der Universität Hamburg*, vol. 36, no. 1, pp. 9–15, Jul. 1971, ISSN: 1865-8784. DOI: 10.1007/BF02995904.

[38] T. Nguyen, K. Kar**c**iauskas, and J. Peters, "A comparative study of several classical, discrete differential and isogeometric methods for solving poisson's equation on the disk," *Axioms*, vol. 3, no. 2, pp. 280–299, 2014.

[39] M. Kapl, V. Vitrih, B. Jüttler, and K. Birner, "Isogeometric analysis with geometrically continuous functions on two-patch geometries," *Computers & Mathematics with Applications*, vol. 70, no. 7, pp. 1518–1538, 2015.

[40] A. Collin, G. Sangalli, and T. Takacs, "Analysis-suitable g1 multi-patch parametrizations for c1 isogeometric spaces," *Computer Aided Geometric Design*, vol. 47, pp. 93–113, 2016.

[41] D. Toshniwal, H. Speleers, and T. J. Hughes, "Smooth cubic spline spaces on unstructured quadrilateral meshes with particular emphasis on extraordinary points: Geometric design and isogeometric analysis considerations," *Computer Methods in Applied Mechanics and Engineering*, vol. 327, pp. 411–458, 2017.

[42] A. Blidia, B. Mourrain, and G. Xu, "Geometrically smooth spline bases for data fitting and simulation," *Computer Aided Geometric Design*, vol. 78, p. 101 814, 2020.

[43] D. Natekar, X. Zhang, and G. Subbarayan, "Constructive solid analysis: A hierarchical, geometry-based meshless analysis procedure for integrated design and analysis," *Computer-Aided Design*, vol. 36, no. 5, pp. 473–486, Apr. 2004, ISSN: 0010-4485. DOI: 10.1016/S0010-4485(03)00129-5.

[44] J. M. Melenk and I. Babu**s**ka, "The partition of unity finite element method: Basic theory and applications," *Computer Methods in Applied Mechanics and Engineering*, vol. 139, no. 1, pp. 289–314, Dec. 1996, ISSN: 0045-7825. DOI: 10.1016/S0045-7825(96)01087-0.

[45] T. Strouboulis, K. Copps, and I. Babu**s**ka, "The generalized finite element method," *Computer Methods in Applied Mechanics and Engineering*, vol. 190, no. 32, pp. 4081–4193, 2001. DOI: https://doi.org/10.1016/S0045-7825(01)00188-8. [Online]. Available: http://www.sciencedirect.com/science/article/pii/S0045782501001888.

[46] D. J. Benson, Y. Bazilevs, E. De Luycker, *et al.*, "A generalized finite element formulation for arbitrary basis functions: From isogeometric analysis to XFEM," *International*

*Journal for Numerical Methods in Engineering*, vol. 83, no. 6, pp. 765–785, 2010. DOI: 10.1002/nme.2864. [Online]. Available: http://dx.doi.org/10.1002/nme.2864.

[47] E. De Luycker, D. J. Benson, T. Belytschko, Y. Bazilevs, and M. C. Hsu, "X-fem in isogeometric analysis for linear fracture mechanics," *International Journal for Numerical Methods in Engineering*, vol. 87, no. 6, pp. 541–565, 2011.

[48] S. S. Ghorashi, N. Valizadeh, and S. Mohammadi, "Extended isogeometric analysis for simulation of stationary and propagating cracks," *International Journal for Numerical Methods in Engineering*, vol. 89, no. 9, pp. 1069–1101, 2012. DOI: 10.1002/nme.3277. eprint: https://onlinelibrary.wiley.com/doi/pdf/10.1002/nme.3277. [Online]. Available: https://onlinelibrary.wiley.com/doi/abs/10.1002/nme.3277.

[49] M. L. Williams, "Stress singularities resulting from various boundary conditions in angular corners of plates in extension," *Journal of applied mechanics*, vol. 19, no. 4, pp. 526–528, 1952, ISSN: 0021-8936.

[50] M. Williams, "On the stress distribution at the base of a stationary crack," *Journal of Applied Mechanics*, vol. 24, no. 1, M. Williams, Ed., pp. 109–114, 1956.

[51] A. Seweryn and K. Molski, "Elastic stress singularities and corresponding generalized stress intensity factors for angular corners under various boundary conditions," *Engineering Fracture Mechanics*, vol. 55, no. 4, pp. 529–556, 1996. DOI: https://doi.org/10.1016/S0013-7944(96)00035-5. [Online]. Available: http://www.sciencedirect.com/science/article/pii/S0013794496000355.

[52] Y. Luo and G. Subbarayan, "A study of multiple singularities in multi-material wedges and their use in analysis of microelectronic interconnect structures," *Engineering Fracture Mechanics*, vol. 74, no. 3, pp. 416–430, 2007. DOI: https://doi.org/10.1016/j.engfracmech.2006.04.032. [Online]. Available: http://www.sciencedirect.com/science/article/pii/S0013794406002116.

[53] A. Carpinteri and M. Paggi, "Asymptotic analysis in linear elasticity: From the pioneering studies by wieghardt and irwin until today," *Engineering Fracture Mechanics*, vol. 76, no. 12, pp. 1771–1784, 2009.

[54] M. L. Williams, "The stresses around a fault or crack in dissimilar media," *Bulletin of the Seismological Society of America*, vol. 49, no. 2, pp. 199–204, Apr. 1959, ISSN: 0037-1106. [Online]. Available: http://dx.doi.org/.

[55] B. Malyshev and R. Salganik, "The strength of adhesive joints using the theory of cracks," *International Journal of Fracture Mechanics*, vol. 1, no. 2, pp. 114–128, 1965.

[56] J. Rice and G. Sih, "Plane problems of cracks in dissimilar media," *Journal of Applied Mechanics*, vol. 32, no. 2, p. 418, 1965.

[57] M. Comninou, "Interface crack with friction in the contact zone," *Journal of Applied Mechanics*, vol. 44, no. 4, p. 780, 1977.

[58] J. Rice, "Elastic fracture mechanics concepts for interfacial cracks," *Journal of applied mechanics*, vol. 55, no. 1, pp. 98–103, 1988.

[59] J. W. Hutchinson and Z. Suo, "Mixed mode cracking in layered materials," *Advances in applied mechanics*, vol. 29, pp. 63–191, 1991.

[60] J. E. Akin, "The generation of elements with singularities," *International Journal for Numerical Methods in Engineering*, vol. 10, no. 6, pp. 1249–1259, Jan. 1976, ISSN: 1097-0207. DOI: 10.1002/nme.1620100605. [Online]. Available: http://dx.doi.org/10.1002/nme.1620100605.

[61] S. E. Benzley, "Representation of singularities with isoparametric finite elements," *International Journal for Numerical Methods in Engineering*, vol. 8, no. 3, pp. 537–545, Jan. 1974, ISSN: 1097-0207. DOI: 10.1002/nme.1620080310. [Online]. Available: http://dx.doi.org/10.1002/nme.1620080310.

[62] E. Chen, "Finite element analysis of a bimaterial interface crack," *Theoretical and Applied Fracture Mechanics*, vol. 3, no. 3, pp. 257–262, 1985.

[63] M.-C. Chen and K. Sze, "A novel hybrid finite element analysis of bimaterial wedge problems," *Engineering Fracture Mechanics*, vol. 68, no. 13, pp. 1463–1476, 2001.

[64] G. Yi, T. Yu, T. Q. Bui, and S. Tanaka, "Bi-material v-notched sifs analysis by xfem and conservative integral approach," *Computers & Structures*, vol. 196, pp. 217–232, 2018.

[65] C.-P. Chen, Y. Chen, and G. Subbarayan, "Singular enrichment for multi-material corners with application to assessing the risk of fracture in semiconductor devices," *Engineering Fracture Mechanics*, vol. 248, p. 107 739, 2021.

[66] E. F. Rybicki and M. F. Kanninen, "A finite element calculation of stress intensity factors by a modified crack closure integral," *Engineering fracture mechanics*, vol. 9, no. 4, pp. 931–938, 1977.

[67] J. RICE, "A path independent integral and the approximate analysis of strain concentration by notches and cracks," *Journal of Applied Mechanics*, vol. 35, pp. 379–386, 1968.

[68] X. Liu, Q. Xiao, and B. L. Karihaloo, "Xfem for direct evaluation of mixed mode sifs in homogeneous and bi-materials," *International Journal for Numerical Methods in Engineering*, vol. 59, no. 8, pp. 1103–1118, 2004.

[69] A. Leung and R. Su, "Mode i crack problems by fractal two level finite element methods," *Engineering Fracture Mechanics*, vol. 48, no. 6, pp. 847–856, 1994.

[70] M. Treifi, S. O. Oyadiji, and D. K. Tsang, "Computations of modes i and ii stress intensity factors of sharp notched plates under in-plane shear and bending loading by the fractal-like finite element method," *International Journal of Solids and Structures*, vol. 45, no. 25-26, pp. 6468–6484, 2008.

[71] J. D. Whitcomb, "Iterative global/local finite element analysis," *Computers & structures*, vol. 40, no. 4, pp. 1027–1031, 1991.

[72] K. Mao and C. Sun, "A refined global-local finite element analysis method," *International journal for numerical methods in engineering*, vol. 32, no. 1, pp. 29–43, 1991.

[73] T. Strouboulis, K. Copps, and I. Babu*s*ka, "The generalized finite element method," *Computer methods in applied mechanics and engineering*, vol. 190, no. 32-33, pp. 4081–4193, 2001.

[74] D.-J. Kim, J. Pereira, and C. A. Duarte, "Analysis of three-dimensional fracture mechanics problems: A two-scale approach using coarse-generalized fem meshes," *International journal for numerical methods in engineering*, vol. 81, no. 3, pp. 335–365, 2010.

[75] C. A. Duarte and D.-J. Kim, "Analysis and applications of a generalized finite element method with global–local enrichment functions," *Computer Methods in Applied Mechanics and Engineering*, vol. 197, no. 6-8, pp. 487–504, 2008.

[76] Y. Maday, C. Mavriplis, and A. T. Patera, *Nonconforming mortar element methods: Application to spectral discretizations*. Institute for Computer Applrefsications in Science and Engineering, NASA Langley ..., 1988.

[77] J. C. Simo, P. Wriggers, and R. L. Taylor, "A perturbed lagrangian formulation for the finite element solution of contact problems," *Computer methods in applied mechanics and engineering*, vol. 50, no. 2, pp. 163–180, 1985.

[78] J. Nitsche, "Über ein variationsprinzip zur lösung von dirichlet-problemen bei verwendung von teilräumen, die keinen randbedingungen unterworfen sind," in *Abhandlungen aus dem mathematischen Seminar der Universität Hamburg*, Springer, vol. 36, 1971, pp. 9–15.

[79] L. Gendre, O. Allix, P. Gosselet, and F. Comte, "Non-intrusive and exact global/local techniques for structural problems with local plasticity," *Computational Mechanics*, vol. 44, no. 2, pp. 233–245, 2009.

[80] C. Farhat and F.-X. Roux, "A method of finite element tearing and interconnecting and its parallel solution algorithm," *International Journal for Numerical Methods in Engineering*, vol. 32, no. 6, pp. 1205–1227, 1991.

[81] J. Mandel, "Balancing domain decomposition," *Communications in numerical methods in engineering*, vol. 9, no. 3, pp. 233–241, 1993.

[82] T. F. Chan and T. P. Mathew, "Domain decomposition algorithms," *Acta numerica*, vol. 3, pp. 61–143, 1994.

[83] Y. Liu, Q. Sun, and X. Fan, "A non-intrusive global/local algorithm with non-matching interface: Derivation and numerical validation," *Computer Methods in Applied Mechanics and Engineering*, vol. 277, pp. 81–103, 2014.

[84] A. Beckert and H. Wendland, "Multivariate interpolation for fluid-structure-interaction problems using radial basis functions," *Aerospace Science and Technology*, vol. 5, no. 2, pp. 125–134, 2001.

[85] M. Duval, J.-C. Passieux, M. Salaün, and S. Guinard, "Non-intrusive coupling: Recent advances and scalable nonlinear domain decomposition," *Archives of Computational Methods in Engineering*, vol. 23, no. 1, pp. 17–38, 2016.

[86] Z. Zhang, Z. Suo, Y. Liu, S. Irving, T. Luk, and D. Desbiens, "Methodology for avoidance of ratcheting-induced stable cracking (risc) in microelectronic devices," in *56th Electronic Components and Technology Conference 2006*, 2006, 7 pp.

[87] P. Alpern, P. Nelle, E. Barti, *et al.*, "On the Way to Zero Defect of Plastic-Encapsulated Electronic Power Devices—Part I: Metallization," *IEEE Transactions on Device and Materials Reliability*, vol. 9, no. 2, pp. 269–278, Jun. 2009, ISSN: 1530-4388. DOI: 10.1109/TDMR.2009.2018299. [Online]. Available: http://ieeexplore.ieee.org/document/4803755/.

[88] T. Smorodin, J. Wilde, P. Alpern, and M. Stecher, "A temperature-gradient-induced failure mechanism in metallization under fast thermal cycling," *IEEE Transactions on device and materials reliability*, vol. 8, no. 3, pp. 590–599, 2008.

[89] M. Huang, Z. Suo, Q. Ma, and H. Fujimoto, "Thin film cracking and ratcheting caused by temperature cycling," *Journal of Materials Research*, vol. 15, no. 6, pp. 1239–1242, 2000.

[90] M. Huang, Z. Suo, and Q. Ma, "Metal film crawling in interconnect structures caused by cyclic temperatures," *Acta Materialia*, vol. 49, no. 15, pp. 3039–3049, 2001. DOI: https://doi.org/10.1016/S1359-6454(01)00196-3. [Online]. Available: http://www.sciencedirect.com/science/article/pii/S1359645401001963.

[91] M. Huang, Z. Suo, and Q. Ma, "Plastic ratcheting induced cracks in thin film structures," *Journal of the Mechanics and Physics of Solids*, vol. 50, pp. 1079–1098, 2002.

[92] J. Zhu, S. Quander, and T. Reinikainen, "Global/local modeling for pwb mechanical loading," in *2001 Proceedings. 51st Electronic Components and Technology Conference (Cat. No. 01CH37220)*, IEEE, 2001, pp. 1164–1169.

[93] F. Che, H. Pang, W. Zhu, *et al.*, "Development and assessment of global-local modeling technique used in advanced microelectronic packaging," in *2007 International Conference on Thermal, Mechanical and Multi-Physics Simulation Experiments in Microelectronics and Micro-Systems. EuroSime 2007*, IEEE, 2007, pp. 1–7.

[94] G. Gustafsson, I. Guven, V. Kradinov, and E. Madenci, "Finite element modeling of bga packages for life prediction," in *2000 Proceedings. 50th Electronic Components and Technology Conference (Cat. No. 00CH37070)*, IEEE, 2000, pp. 1059–1063.

[95] D. B. Bogy, "Edge-bonded dissimilar orthogonal elastic wedges under normal and shear loading," *Journal of Applied Mechanics*, vol. 35, no. 3, pp. 460–466, 1968.

[96] D. B. Bogy, "Two edge-bonded elastic wedges of different materials and wedge angles under surface tractions," *Journal of Applied mechanics*, vol. 38, no. 2, pp. 377–386, 1971.

[97] J. R. Rice, "Elastic fracture mechanics concepts for interfacial cracks," *Journal of Applied Mechanics*, vol. 55, no. 1, pp. 98–103, 1988.

[98] A. I. Sauter and W. D. Nix, "Thermal stresses in aluminum lines bounded to substrates," *IEEE Transactions on Components, Hybrids, and Manufacturing Technology*, vol. 15, no. 4, pp. 594–600, Aug. 1992, ISSN: 0148-6411.

[99] D. Systemes, "Abaqus http://www. 3ds. com/products-services/simulia/products/abaqus," *Accessed June*, vol. 16, 2017.

[100] K. C. Park and C. A. Felippa, "A variational principle for the formulation of partitioned structural systems," en, *International Journal for Numerical Methods in Engineering*, vol. 47, no. 1-3, pp. 395–418, 2000, ISSN: 1097-0207. DOI: 10.1002/(SICI)1097-0207(20000110/30)47:1/3⟨395::AID-NME777⟩3.0.CO;2-9.

[101] C. Bernardi, Y. Maday, and F. Rapetti, "Basics and some applications of the mortar element method," *GAMM-Mitteilungen*, vol. 28, no. 2, pp. 97–123, 2005.

[102] J. E. Dennis Jr and R. B. Schnabel, *Numerical methods for unconstrained optimization and nonlinear equations*. Siam, 1996, vol. 16.

[103] J. Nocedal and S. Wright, *Numerical optimization*. Springer Science & Business Media, 2006.

[104] N. Moës and T. Belytschko, "Extended finite element method for cohesive crack growth," *Engineering fracture mechanics*, vol. 69, no. 7, pp. 813–833, 2002.

[105] C.-P. Chen, Y. Chen, G. Subbarayan, H.-Y. Lin, and S. Gurrum, "A mechanistic model for plastic metal line ratcheting induced beol cracks in molded packages," in *2020 19th IEEE Intersociety Conference on Thermal and Thermomechanical Phenomena in Electronic Systems (ITherm)*, IEEE, 2020, pp. 1121–1127.

[106] D. Chan, G. Subbarayan, and L. Nguyen, "Maximum-entropy principle for modeling damage and fracture in solder joints," *Journal of electronic materials*, vol. 41, no. 2, pp. 398–411, 2012.

[107] M. Cassale, "Integration of geometric analysis and structural analysis using trimmed patches," Ph.D. dissertation, PhD Thesis. Irvine: University of California, 1989.

[108] F. P. Renken and G. Subbarayan, "NURBS-based solutions to inverse boundary problems in droplet shape prediction," *Computer Methods in Applied Mechanics and Engineering*, vol. 190, no. 11, pp. 1391–1406, 2000, ISSN: 0045-7825. DOI: https://doi.org/10.1016/S0045-7825(00)00168-7.

[109] P. Kagan and A. Fischer, "Integrated mechanically based cae system using b-spline finite elements," *Computer-Aided Design*, vol. 32, no. 8-9, pp. 539–552, 2000.

[110] D. Natekar, X. Zhang, and G. Subbarayan, "Constructive solid analysis: A hierarchical, geometry-based meshless analysis procedure for integrated design and analysis," *Computer-Aided Design*, vol. 36, no. 5, pp. 473–486, 2004. DOI: 10.1016/S0010-4485(03)00129-5.

[111] Y. Zhang, W. Wang, and T. J. Hughes, "Solid T-spline construction from boundary representations for genus-zero geometry," *Computer Methods in Applied Mechanics and Engineering*, vol. 249, pp. 185–197, 2012. DOI: 10.1016/j.cma.2012.01.014.

[112] X. Wang and X. Qian, "An optimization approach for constructing trivariate B-spline solids," *Computer-Aided Design*, vol. 46, pp. 179–191, 2014. DOI: 10.1016/j.cad.2013.08.030.

[113] H. Al Akhras, T. Elguedj, A. Gravouil, and M. Rochette, "Isogeometric analysis-suitable trivariate NURBS models from standard B-rep models," *Computer Methods in Applied Mechanics and Engineering*, vol. 307, pp. 256–274, 2016. DOI: 10.1016/j.cma.2016.04.028.

[114] C. S. Peskin, "The immersed boundary method," *Acta Numerica*, vol. 11, pp. 479–517, 2002. DOI: 10.1017/S0962492902000077.

[115] W.-K. Liu, S. Li, and T. Belytschko, "Moving least-square reproducing kernel methods (i) methodology and convergence," *Computer Methods in Applied Mechanics and Engineering*, vol. 143, no. 1-2, pp. 113–154, 1997. DOI: 10.1016/S0045-7825(96)01132-2.

[116] W. K. Liu, S. Jun, and Y. F. Zhang, "Reproducing kernel particle methods," *International Journal for Numerical Methods in Fluids*, vol. 20, no. 8-9, pp. 1081–1106, 1995. DOI: 10.1002/fld.1650200824.

[117] G. Ventura, "An augmented lagrangian approach to essential boundary conditions in meshless methods," *International Journal for Numerical Methods in Engineering*, vol. 53, no. 4, pp. 825–842, 2002. DOI: 10.1002/nme.314.

[118] A. Tambat and G. Subbarayan, "Isogeometric enriched field approximations," *Computer Methods in Applied Mechanics and Engineering*, vol. 245, pp. 1–21, 2012. DOI: 10.1016/j.cma.2012.06.006.

[119] A. Biswas and V. Shapiro, "Heterogeneous material modeling with distance fields," *Computer Aided Geometric Design*, vol. 21, pp. 215–242, 3 2004. DOI: 10.1016/j.cagd.2003.08.002.

[120] K. Upreti, T. Song, A. Tambat, and G. Subbarayan, "Algebraic distance estimations for enriched isogeometric analysis," *Computer Methods in Applied Mechanics and Engineering*, vol. 280, pp. 28–56, 2014. DOI: 10.1016/j.cma.2014.07.012.

[121] K. Upreti and G. Subbarayan, "Signed algebraic level sets on NURBS surfaces and implicit boolean compositions for isogeometric CAD–CAE integration," *Computer-Aided Design*, vol. 82, pp. 112–126, 2017. DOI: 10.1016/j.cad.2016.09.006.

[122] J. M. Melenk and I. Babu***s***ka, "The partition of unity finite element method: Basic theory and applications," *Computer Methods in Applied Mechanics and Engineering*, vol. 139, no. 1-4, pp. 289–314, 1996. DOI: 10.1016/S0045-7825(96)01087-0.

[123] T. Strouboulis, I. Babu***s***ka, and K. Copps, "The design and analysis of the generalized finite element method," *Computer Methods in Applied Mechanics and Engineering*, vol. 181, no. 1-3, pp. 43–69, 2000. DOI: 10.1016/S0045-7825(99)00072-9.

[124] T. Belytschko, Y. Y. Lu, and L. Gu, "Element-free Galerkin methods," *International Journal for Numerical Methods in Engineering*, vol. 37, no. 2, pp. 229–256, 1994. DOI: 10.1002/nme.1620370205.

[125] M. E. Mortenson, *Geometric Modeling*. CUMINCAD, 1997.

[126] L. Piegl and W. Tiller, *The NURBS Book*. Springer Science & Business Media, 2012.

[127] A. Biswas and V. Shapiro, "Approximate distance fields with non-vanishing gradients," *Graphical Models*, vol. 66, no. 3, pp. 133–159, 2004. DOI: 10.1016/j.gmod.2004.01.003.

[128] B. A. Payne and A. W. Toga, "Distance field manipulation of surface models," *IEEE Computer Graphics and Applications*, no. 1, pp. 65–71, 1992. DOI: 10.1109/38.135885.

[129] T. W. Sederberg, "Implicit and parametric curves and surfaces for computer aided geometric design," Ph.D. dissertation, Purdue University, 1983.

[130] V. Shapiro, "Theory of R-functions and applications: A primer," Cornell University, Technical Report, 1991.

[131] M. Ruess, D. Schillinger, A. I. Oezcan, and E. Rank, "Weak coupling for isogeometric analysis of non-matching and trimmed multi-patch geometries," *Computer Methods in Applied Mechanics and Engineering*, vol. 269, pp. 46–71, 2014. DOI: 10.1016/j.cma.2013.10.009.

[132] N. Troyani, C. Gomes, and G. Sterlacci, "Theoretical stress concentration factors for short rectangular plates with centered circular holes," *Journal of Mechanical Design*, vol. 124, no. 1, pp. 126–128, 2002. DOI: 10.1115/1.1496769.

[133] S. Timoshenko and J. N. Goodier, *Theory of elasticity*, eng, 2nd ed.., ser. Engineering societies monographs. New York: McGraw-Hill, 1951.

[134] A. Tambat and G. Subbarayan, "Isogeometric enriched field approximations," *Computer Methods in Applied Mechanics and Engineering*, vol. 245-246, pp. 1–21, 2012, ISSN: 00457825. DOI: 10.1016/j.cma.2012.06.006.

[135] J. Brahtz, "Stress distribution in wedges with arbitrary boundary forces," *Physics*, vol. 4, no. 2, pp. 56–65, 1933.

[136] D. Vasilopoulos, "On the determination of higher order terms of singular elastic stress fields near corners," *Numerische Mathematik*, vol. 53, no. 1, pp. 51–95, 1988.

[137] R. Rösel, "On the wedge/notch eigenvalues," *International journal of fracture*, vol. 33, no. 1, pp. 61–71, 1987.

[138] A. Seweryn, "Brittle fracture criterion for structures with sharp notches," *Engineering Fracture Mechanics*, vol. 47, no. 5, pp. 673–681, 1994.

[139] S. S. Pageau, K. S. Gadi, S. B. Biggers, and P. F. Joseph, "Standardized complex and logarithmic eigensolutions for n-material wedges and junctions," *International Journal of Fracture*, vol. 77, no. 1, pp. 51–76, 1996.

[140] L. Piegl and W. Tiller, *The NURBS Book*, 2nd. Springer-Verlag New York, 1997, ISBN: 3-540-61545-8.

[141] L. Zhang, G. Subbarayan, B. Hunter, and D. Rose, "Response surface models for efficient, modular estimation of solder joint reliability in area array packages," *Microelectronics Reliability*, vol. 45, no. 3-4, pp. 623–635, 2005.

[142] D. Leguillon, "Strength or toughness? a criterion for crack onset at a notch," *European Journal of Mechanics-A/Solids*, vol. 21, no. 1, pp. 61–72, 2002.

[143] G. Sih and B. Macdonald, "Fracture mechanics applied to engineering problems-strain energy density fracture criterion," *Engineering Fracture Mechanics*, vol. 6, no. 2, pp. 361–386, 1974.

[144] P. Lazzarin and F. Berto, "Some expressions for the strain energy in a finite volume surrounding the root of blunt v-notches," *International Journal of fracture*, vol. 135, no. 1-4, pp. 161–185, 2005.

[145] A. Tambat and G. Subbarayan, "Simulations of arbitrary crack path deflection at a material interface in layered structures," *Engineering Fracture Mechanics*, vol. 141, pp. 124–139, 2015.

[146] C. Miehe, E. Gürses, and M. Birkle, "A computational framework of configurational-force-driven brittle fracture based on incremental energy minimization," *International Journal of Fracture*, vol. 145, no. 4, pp. 245–259, 2007.

[147] P. Vaitheeswaran, A. Udupa, S. Sadasiva, and G. Subbarayan, "Interface balance laws, phase growth and nucleation conditions for multiphase solids with inhomogeneous surface stress," *Continuum Mechanics and Thermodynamics*, vol. 32, no. 4, pp. 987–1010, 2020.

[148] C. E. Shannon, "A mathematical theory of communication," *The Bell system technical journal*, vol. 27, no. 3, pp. 379–423, 1948.

[149] E. T. Jaynes, "Information theory and statistical mechanics," *Physical review*, vol. 106, no. 4, p. 620, 1957.

[150] D. Bhate, K. Mysore, and G. Subbarayan, "An information theoretic argument on the form of damage accumulation in solids," *Mechanics of Advanced Materials and Structures*, vol. 19, no. 1-3, pp. 184–195, 2012.

[151] P. Towashiraporn, G. Subbarayan, and C. Desai, "A hybrid model for computationally efficient fatigue fracture simulations at microelectronic assembly interfaces," *International Journal of Solids and Structures*, vol. 42, no. 15, pp. 4468–4483, 2005.

[152] R. de Borst, "Fracture in quasi-brittle materials: A review of continuum damage-based approaches," *Engineering fracture mechanics*, vol. 69, no. 2, pp. 95–112, 2002.

[153] W. Brekelmans and J. De Vree, "Reduction of mesh sensitivity in continuum damage mechanics," *Acta Mechanica*, vol. 110, no. 1, pp. 49–56, 1995.

[154] A. Hillerborg, M. Modéer, and P.-E. Petersson, "Analysis of crack formation and crack growth in concrete by means of fracture mechanics and finite elements," *Cement and concrete research*, vol. 6, no. 6, pp. 773–781, 1976.

[155] Z. P. Ba*z*ant and B. H. Oh, "Crack band theory for fracture of concrete," *Matériaux et construction*, vol. 16, no. 3, pp. 155–177, 1983.

[156] Z. k. P. Baz ant and B. H. Oh, "Rock fracture via strain-softening finite elements," *Journal of engineering mechanics*, vol. 110, no. 7, pp. 1015–1035, 1984.

[157] G. Pluvinage and J. Capelle, "On characteristic lengths used in notch fracture mechanics," *International Journal of Fracture*, vol. 187, no. 1, pp. 187–197, 2014.

# A. MULTI-SCALE ANALYSIS OF PACKAGE AND SOLDER JOINT FRACTURE SIMULATION

Fatigue fracture is one of the major failures of solder joints in semiconductor assemblies. Under thermal cycling, solder joints undergo cyclic loading due the coefficient of thermal expansion (CTE) mismatch. Among various kind of fatigue fracture models, Coffin-Manson model may be the most frequently used one. It is an empirical model with little physical basis. It is based on an observed correlation to predict the life of an intact joint without tracking the crack initiation and propagation process. Generally, assumptions in linear elastic fracture mechanics (LEFM), such as isotropy, small-scale yielding are often unrealistic for solder joints. The microstructural uncertainties, especially the heterogeneous constituents, brings more difficulties in simulating the behavior of solder joints.

The maximum entropy fracture model (MEFM) is a thermodynamically consistent and information theory inspired (non-empirical) damage accumulation theory for ductile solids. The model uses a single damage accumulation parameter to relate the damage leading to fracture to accumulated entropic dissipation. It is a promising tool to predict the fatigue damage in solder joints under cycling loading.

## A.1 The Maximum Entropy Fracture Model

The model is based on Shannon's idea of Information entropy [148] and Jaynes' work on maximum entropy principle [149]. An expression for damage is derived, which accounts for the uncertainties at the lower length scales. Dissipation of energy in the form of crack propagation is related to damage using continuum thermodynamics and J2 plasticity theory. For the sake of completeness, the maximum entropy fracture model[150] is briefly described below:

The notion of entropy in Shannon's theory is abstract. He argues that to be able to measure uncertainty, a function must satisfy three conditions: continuity, montonicity and composition. The only function which satisfies all the three condition is :

$$H = -k\Sigma_{\mathrm{i}}^{n} p_{\mathrm{i}} ln p_{\mathrm{i}} \tag{A.1}$$

with $n$ being the number of possible events and $p_{\mathrm{i}}$ the probability of an event occurring. It is worth noting that Shannon's function has similar form to Boltzmann's H-function and the Gibbs entropy function.

$$s = -k_B \Sigma_{\mathrm{i}}^{n} p_{\mathrm{i}} ln p_{\mathrm{i}} \tag{A.2}$$

where $s$ is entropy, and $k_B$ is the Boltzmann's constant. Gibbs' equation has a physical significance to it, whereas Shannon's derivation is purely a mathematical argument with no connection to any physical behavior. Jaynes[149] used information entropy as a starting point to derive well known relations in statistical mechanics without the need for physically limiting assumptions. He argues that given a system with a probabilistically defined state, the maximum entropy method should be used to find the probability distribution. To this extent a solder joint may be in any one of its $n$ possible microstructural states $x_{\mathrm{i}}$ with a probability of $p_{\mathrm{i}}$ of being in that particular microstructural state. Here, microstructural states refer to a thermodynamic ensemble. The discrete probabilities will sum to unity.

$$\sum_{\mathrm{i}}^{n} p_{\mathrm{i}} = 1 \tag{A.3}$$

Assume that damage is only associated with energy, the expected energy measure at any point $x_{\mathrm{i}}$ is:

$$\psi(x) \ = \sum_{\mathrm{i}}^{n} p_{\mathrm{i}} \psi_{\mathrm{i}} \tag{A.4}$$

The probability $p_{\mathrm{i}}$ can be obtained by minimizing the entropy function with constraint Eq. (A.3) and Eq. (A.4):

$$p_{\mathrm{i}} = exp(\frac{-\mu\psi_{\mathrm{i}} - \lambda - k}{k}) \tag{A.5}$$

where $\mu$ and $\lambda$ are the Lagrangian multipliers corresponding to the two constraints. By choosing the appropriate quantity $\psi$, which could be the plastic dissipation, total damage is defined as the accumulative function:

$$D = \int_o^t f(0) exp(-\int_0^t \frac{W_t}{\rho k_\psi T} d\tau) dt) \tag{A.6}$$

Finally, by assuming constant inelastic dissipation rate, and using the condition $D(\text{inf}) = 1$ the damage has a simplified mathematical form

$$D = 1 - exp(-\frac{W_t}{\rho k_\psi T}) \tag{A.7}$$

where, $k_\psi$ is a parameter associated with damage, $W_t$ is the inelastic dissipation, $\rho$ is the density of the material, and $T$ is temperature.

The above form is very similar to the damage estimated by equivalent inelastic strain in [151]:

$$D = 1 - exp[-(\frac{\xi}{\xi_c})^\beta] \tag{A.8}$$

where, $\xi$ is the inelastic strain with $\xi_c$ being a characteristic value.

## A.2 Numerical Implementation

A user defined field (USDFLD) subroutine in FORTRAN was written and linked with ABAQUS® to calculate the damage. Eq. (A.7) is used to evaluate damage at any time by extracting inelastic strain energy density. In ABAQUS, two variables EPDDEN and ECDDEN, which represent energy dissipated per unit volume in the element by plastic deformation and creep respectively, are extracted. However, evaluating the inelastic dissipation at each cycle is computationally very expensive. A linear extrapolation scheme to accelerate the process was thus developed. Two sequential thermal cycles were simulated using Abaqus. The increment in inelastic dissipation from the first to the second cycle was tracked. The

change in dissipation was then extrapolated using a single term Taylor series expansion to a predetermined number $\Delta N = N_{n+1} - N_n$ of cycles using the following equation:

$$W_{n+1}W_n + \frac{\partial W}{\partial N}|_n(\Delta N) \tag{A.9}$$

$W_{n+1}$ is then substituted into Eq. (A.7) to evaluate the probability of failure $D$ at every material point using the maximum entropy fracture model. As $D$ increased, linear decrease of modulus was imposed on the solder. The crack path is represented by the loci of critically damaged elements. The modulus is linearly decreased with $D$:

$$E = (1 - D)E_0 \tag{A.10}$$

where $E_0$ is the initial modulus for the intact material. To avoid singular system during computation, the stiffness is reduced to 1% of the initial value when $D$ is 1. The critical damage was set to be $D > 0.95$ in the current study.

### A.3 Mesh Dependence Mitigation

The MEFM described above can be used to simulate fatigue fracture propagation. In the method, fracture propagation is represented by sequence of elements with critical damage. In this approach, the crack is not necessary to be defined a priori. There is no necessity to insert pre-existing crack either.

However, such a smeared crack model suffers from mesh dependence issues[152]. That is, the extent of crack propagation and energy release varies with element size. As damage occurs, strain softening tends to localize within a small band whose width is sensitive to the FE mesh size. The width of the band is small so sometimes the volumetric energy released in this band due to local damage is referred to surface energy. The band width, as an internal characteristic length of the material, is determined by the ratio of volumetric energy and surface energy.

From the perspective of numerical simulation, the potential energy stored in the whole element is released as a result of damage. In the model, energy dissipation is proportional

to the element size. Since the crack is represented by damaged elements, smaller element leads to faster fracture propagation due to less stored energy release. Ideally, the size of the element should be the same as the intrinsic characteristic length of the the material. However, this length scale is not readily known.

To mitigate the mesh dependence in strain-softening model, a characteristic length is usually introduced[153], [154]. Bazant and Oh [155], [156] proposed a crack band model with an intrinsic material property embedded into numerical method to mitigate mesh dependence issue. Usually, the characteristic length parameter is either intrinsic to material and connected to the fracture process zone, or a characteristic of the effective stress distribution within a specific volume[157].

A brief illustration of process zone and charateritic length is shown in Appendix A.3. Let $\Omega$ represent the volume of process zone and $\Gamma$ represent the surface area of crack. $\bar{W}_{Omega}$ denotes the average inelastic dissipation per volume in the process zone, and $\bar{W}_{\Gamma}$ is average dissipation density per area on the fictitious crack surface $\Gamma$.

The energy dissipated through the newly generated crack surface should be equivalent to the energy stored in the process zone.

$$\bar{W}_{\Omega}\Omega \approx \bar{W}_{\Gamma}\Gamma \tag{A.11}$$

The above quantity can be further simplified to:

$$\bar{W}_{\Gamma} \approx \bar{W}_{\Omega}\frac{\Omega}{\Gamma} = \bar{W}_{\Omega}l_c \tag{A.12}$$

with $l_c$ being the characteristic length, which connects volumetric energy density and surface energy density.

From the perspective of numerical simulation, damage is localized in one layer of elements and thus the energy dissipation relates to the element size. To mitigate this effect, the mesh size is incorporated into the damage equation. It is assumed that the energy dissipated

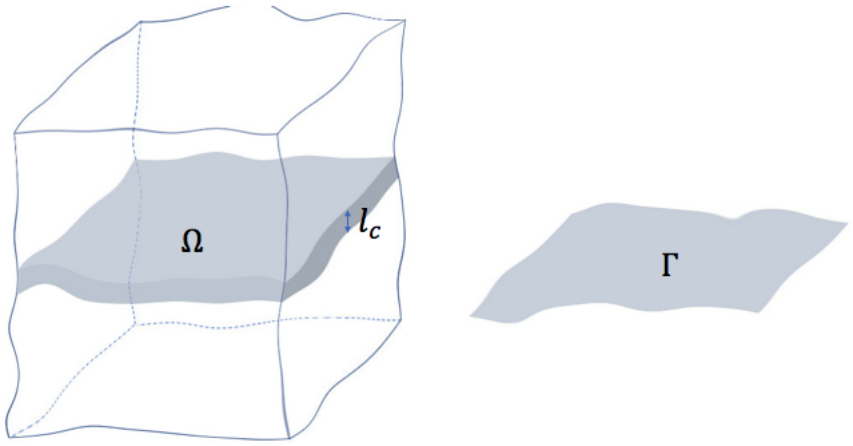


**Figure A.1.** Illustration of process zone and crack surface.

within the contiguous damaged elements should be equivalent to that dissipated through the crack surface:

$$\bar{W}_{\Gamma_{elem}}\Gamma = \bar{W}\Omega_{elem} \tag{A.13}$$

$$\bar{W}_{\Gamma} \approx \bar{W}\frac{\Omega_{elem}}{\Gamma_{elem}} \tag{A.14}$$

Comparing Eq. (A.14) and Eq. (A.12), the relation between inelastic dissipation density in the process zone and critical element is:

$$\bar{W}l_{elem} = \bar{W}_{\Omega}l_c \tag{A.15}$$

$$\bar{W}_{\Omega} \approx \bar{W}\frac{l_{elem}}{l_c} \tag{A.16}$$

In finite element implementation, the maximum entropy model is:

$$D = 1 - exp(-\frac{l_{elem}W}{l_c\rho kT}) = 1 - exp(-\frac{cW}{\rho kT}) \tag{A.17}$$

where $c = \frac{l_{elem}}{l_c}$ is a normalized element size. $l_c$ is the characteristic length of the fracture, with $l_{elem}$ being the equivalent element size, which is defined as cube root of a element volume for 3D elements, square root of the area for 2D elements.

A simplified 2D test example is demonstrated to show the mesh dependence of the current method. The material property is as shown below: It is assumed that solder has a yield

**Table A.1**. Properties of materials.

| **Mateiral** | $E$ (GPa) | $\nu$ | $\alpha(ppm/K)$ |
|---|---|---|---|
| Si | 5 | 0.4 | 2.61 |
| Cu | 117 | 0.37 | 16.7 |
| PCB | 5 15 | 0.11 | 14.5 |
| Solder | 32 46 | 0.33 | 23 |

stress of 22MPa and ultimate stress of 35 MPa and under thermal cycling between 398K and 233K. At the lowest temperature, it can be seen that the solder joint is under shear with the maximum stress on the upper right corner. As thermal cycling goes on, plastic accumulation finally leads to crack.

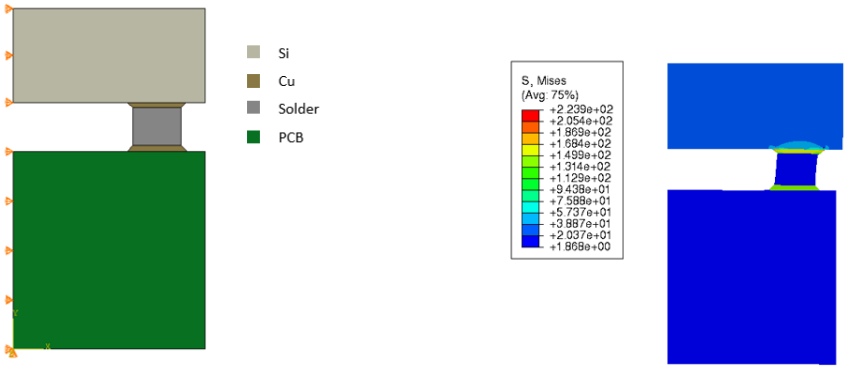


(a) (b)

**Figure A.2.** (a) Simplified 2D test setup and (b) Von Mises Stress Distribution (Deformation 50 times amplified).

The problem is modeled by three levels of mesh size $5\mu m$, $10\mu m$, $20\mu m$. For simplicity, the chracteristic length is assumed to be $l_c = 5\mu m$. The results without mitigation technique in Appendix A.3 shows that cracks finer mesh propagates faster than in coarser mesh. This is

because crack generation is the result of energy dissipation within the bulk element. Larger element needs more energy dissipation to damage and thus needs more cycles to crack.

The mitigation technique introduced a scaling factor to remedy this effect, as can be seen in Appendix A.3. The mesh dependence is significantly reduced. To quantitatively evaluate the improvement, the relative crack length is defined as the ratio of number cracked elements ($D > 0.95$) over the total number of elements in the row. Appendix A.3 clearly demonstrates the effect of the mitigation technique. The case of $h = 5\mu m$ is used as a reference, by choosing $l_c = 5\mu m$, The result is identical whether using mitigation or not. But, for $h = 10\mu m$ and $h = 20\mu m$, without mitigation, the crack initiation time has an error of 70% and 230% respectively. By using the mitigation technique, the errors are reduced to 0% and $-10\%$. It can also seen that the the curves diverge at the later stage of crack, but the mitigation technique still works well when the relative crack length is below 0.7.

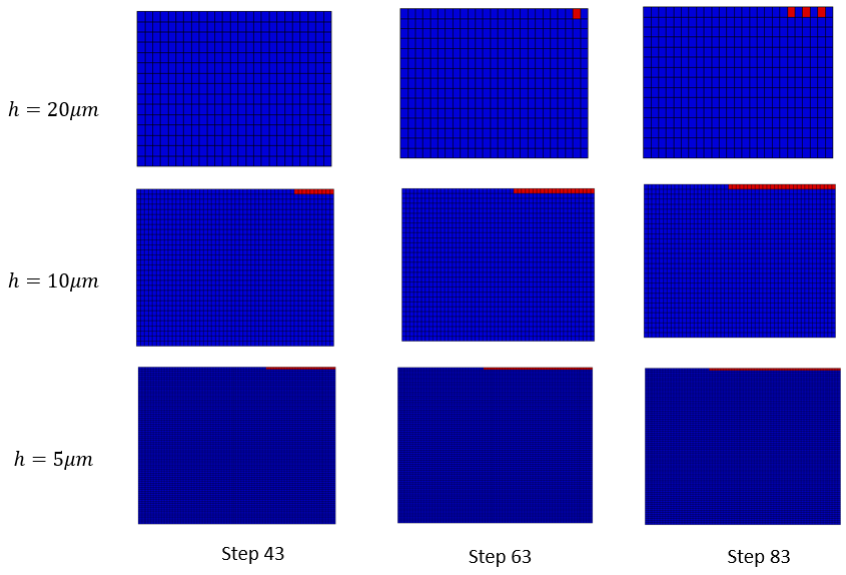


**Figure A.3.** Comparison of crack propagation without mitigation.

## A.4 Extrapolation to accelerate

Different $\Delta N$ were used to test the acceleration technique. It could be seen in Appendix A.4 that higher $\Delta N$ may result in faster crack propagation. But, the difference in

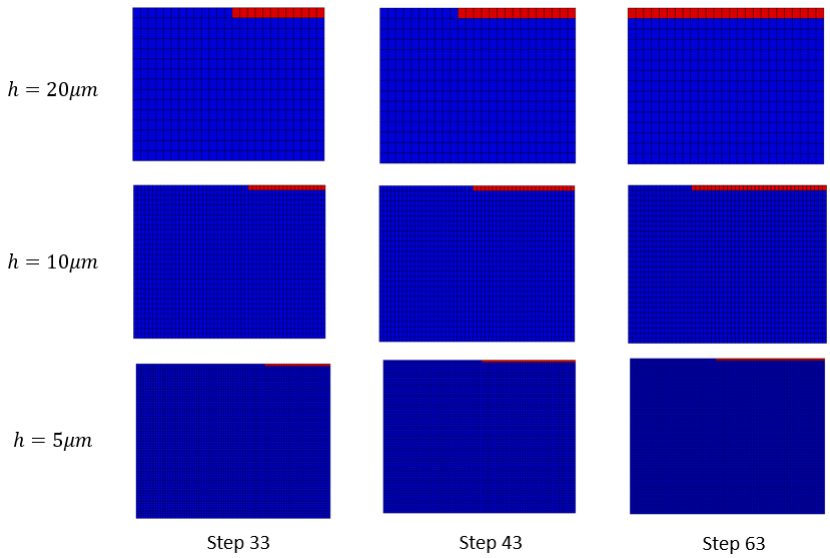


**Figure A.4.** Comparison of crack propagation with different mesh sizes.

crack length for $\Delta N = 20$, $\Delta N = 50$,$\Delta N = 100$ are small. Especially when relative crack length is below 0.6, the three curves are almost identical.

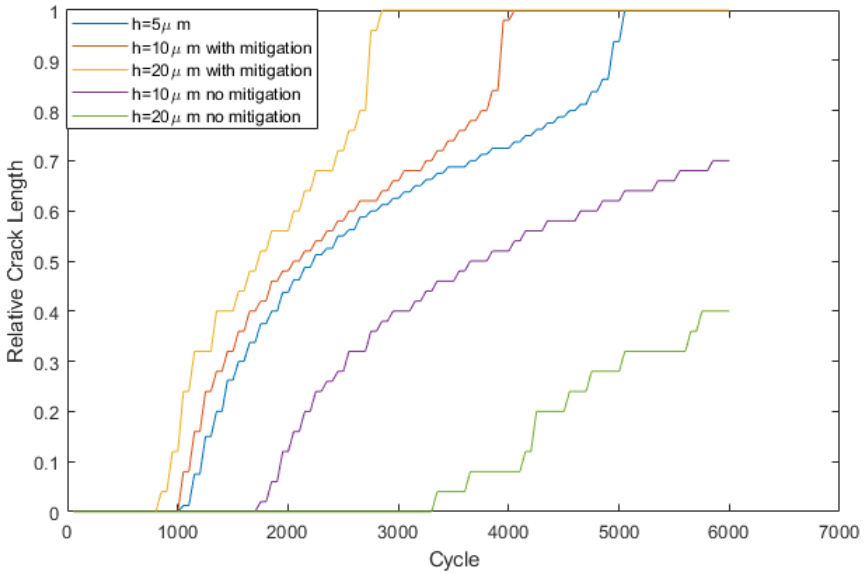


**Figure A.5.** Comparison of relative crack length with different mesh sizes.

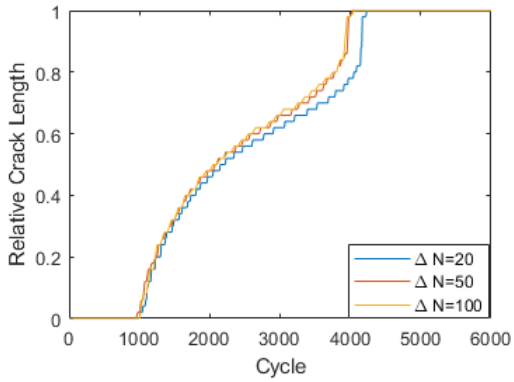


**Figure A.6.** Comparison of crack propagation with different acceleration time step.